Exploring the Limits of the Standard Model with the ATLAS Experiment at the LHC

Inauguraldissertation

der Philosophisch-naturwissenschaftlichen Fakultät
der Universität Bern

vorgelegt von

Lea Halser

aus Deutschland

CERN-THESIS-2023-305
09/10/2023

Leiter der Arbeit:

Prof. Dr. Michele Weber

Albert Einstein Center for Fundamental Physics
Laboratorium für Hochenergiephysik
Physikalisches Institut

Exploring the Limits of the Standard Model with the ATLAS Experiment at the LHC

Inauguraldissertation

der Philosophisch-naturwissenschaftlichen Fakultät
der Universität Bern

vorgelegt von

Lea Halser

aus Deutschland

Leiter der Arbeit:

Prof. Dr. Michele Weber

Albert Einstein Center for Fundamental Physics
Laboratorium für Hochenergiephysik
Physikalisches Institut

Von der philosophisch-naturwissenschaftlichen Fakultät
angenommen.

Bern, 9. Oktober 2023

Der Dekan
Prof. Dr. Marco Herwegh

Abstract

The high-energy proton-proton collisions at the Large Hadron Collider at CERN provide a unique environment to address open questions in the fundamental description of matter and its interactions: the Standard Model. These collisions are the most likely place on Earth to produce massive particles beyond the Standard Model and to observe them with detectors such as the ATLAS experiment. The work presented in this thesis describes the exploration of two different beyond the Standard Model signatures in a supersymmetric framework, using the full Run 2 dataset of $140\,\text{fb}^{-1}$ proton-proton collisions at $\sqrt{s} = 13\,\text{TeV}$. The first is a third-generation squark-pair decaying to a final state with one top-quark, one bottom-quark, and missing transverse energy. The second targets pair-produced gluinos that decay to an all-hadronic final state via an R-parity-violating coupling. Despite the use of dedicated search strategies, including standard cut-and-count methods and machine learning, no deviation from the Standard Model prediction is observed. The non-observation in the data constrains the lower limits on the masses of the supersymmetric particle up to 2.2 TeV for gluinos at the 95% confidence level. The third-generation squark analysis gives expected exclusion limits up to 1.0 TeV for the squark masses. In preparation for the extended lifetime of the Large Hadron Collider through the High-Luminosity phase, the ATLAS experiment will upgrade its tracking detector with a new, all-silicon Inner Tracker. Dedicated irradiation studies were performed at the Bern cyclotron on service components for the Inner Tracker Pixel data transmission chain. The tests presented in this thesis show that the components can withstand the total ionising dose expected for the lifetime of the High Luminosity phase and recommendations for their use are given. The results from the various studies presented in this thesis highlight the importance of continuing the exploration of beyond the Standard Model physics such as supersymmetry at the Large Hadron Collider, using the increasing statistics of the forthcoming High-Luminosity Large Hadron Collider.

Acknowledgements

In October 2013, I attended my first physics lecture at the Ludwig-Maximilians-University in Munich. Nobody would have guessed (least of all me) that now, 10 years later, I would be submitting my PhD thesis in particle physics at the University of Bern. This path has been supported and shaped by many people, whom I would like to thank here.

I would like to thank Michele for being the supervisor and mentor during my PhD years, for inviting me to join the ATLAS group in Bern, for supporting me to find my way and for always keeping his door open.
Thank you to Saverio as my second supervisor and the members of his group for all cyclotron-related matters and beyond.
I would also like to thank Prof. Dr. Thomas Becher for being the chair of my defence committee and Dr. Rosa Simoniello for reading and evaluating my thesis as an external reviewer.

Special thanks go to the Bern ATLAS Team (BAT) in its past and present configuration for creating an inspiring and motivating working environment.
As promised: Cheers John for answering all my questions, whether from the dark corner of B94 or from CERN and for following my work day by day. Many thanks to Laura, John, Isidre, Aaron and Silke for discussing questions, providing endless constructive comments on this document, helping out whenever needed and becoming friends and mentors. Thank you Roman, Armin, Daniele, Megh and Meinrad for going through the ups and downs of being PhD students together. I am so grateful to have found such good friends to share Friday beers, Minigolf sessions and Luce pizzas with! :)

I would like to acknowledge Marcella, Ursula, and the LHEP (electronic) workshop.
I am grateful to the ATLAS RPV Multijet team for their collaborative efforts and for all the amazing work that has been put together.
Thanks to the Bern CERN office in b40 for hosting me for nine months.
I would also like to express my appreciation to my mentor, Philipp, who I connected with through the SPS WiP mentoring program.
During my Master's studies at the Niels Bohr Institute and CERN, I had the privilege of meeting numerous wonderful people. Among them, Tamara and Markus introduced me to the world of particle physics with their enthusiasm, sparking my interest to continue on this path. Thank you Berti and Candy for promoting girls going into science!!

Jana, Sara, Rebecca, Kathi, Julia, Jo-Jo, Jan, Ida, and Klara: your friendship means the world to me and I am so grateful that I have met you - with and without physics background, at CERN or at home, wherever that may be.
Dear Timo, thank you for always being at my side, for trying to read my analysis chapter, for being the stable base in my life, and the excellent culinary contributions in the last months. I am looking forward to the adventures that lie ahead of us. :)
Lastly, I would like to thank my family, my parents and my brother Luis, who always support my way, from North to South with understanding, guidance, interest and love.

Lea

Contents

Chapter 1

Introduction

The Standard Model (SM) of particle physics offers the most comprehensive theoretical framework for describing matter and the interactions of matter surrounding us. It explains the smallest fundamental units of matter, elementary particles, and describes how they interact through electromagnetic, weak, and strong forces.

Over the past 130 years, the development of this theoretical framework has progressed alongside the discovery of new elementary particles. A detailed chronology of these discoveries can be seen in Figure 1.1. The evolution began with J.J. Thomson's discovery of the electron in 1897 [1], and has continued to this day. In the earlier stages, discoveries like the anti-electron and muons were predominantly made with cosmic-ray observations [2, 3]. Yet, from the 1950s onwards, particle accelerators became the primary tool for identifying most elementary particles. A milestone was achieved in 1962 when the first elementary particle, the muon neutrino, was detected using the Alternating Gradient Synchrotron (AGS), a proton accelerator used to prepare a neutrino beam at the Brookhaven National Laboratory [4]. Over the years, improving collider and detector technologies pushed the frontiers of energy and intensity, paving the way for further particle discoveries. The 1970s and 1980s, often referred to as the golden era of particle physics, were dominated by accelerators such as the linear accelerator at the Stanford Linear Accelerator Complex (SLAC). With this accelerator, the substructure of protons was revealed, providing evidence for the existence of up-, down-, and strange-quarks. Furthermore, the electron-positron collider SPEAR at SLAC facilitated the discovery of the charm-quark in 1974 and the tau-lepton in 1975 [5, 6]. The proton antiproton collider Sp$\bar{p}$S at CERN unveiled the electroweak gauge bosons $W^{\pm}$ and Z in 1983 [7–10]. Then, only 50 years after the muon neutrino was found with a particle accelerator, the last missing piece of the SM as we know it today, was found with the Higgs boson at the Large Hadron Collider (LHC) in 2012 [11, 12].

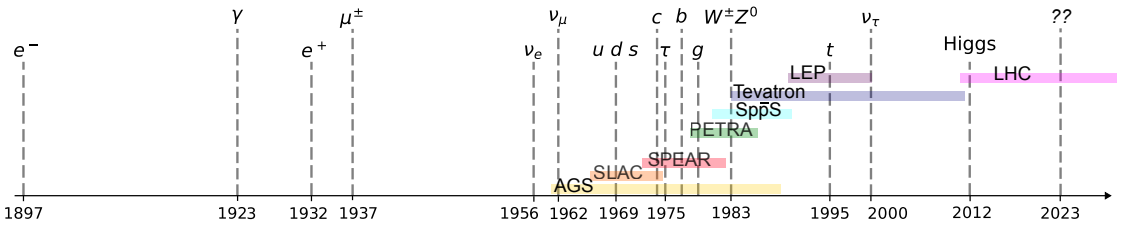

Figure 1.1: Chronological overview of the discoveries of elementary particles of the Standard Model as we know it today. Additionally shown are collider experiments and their operation periods as "stand-alone" experiments, with no claim to be a complete representation of all main particle accelerators.

Despite its great success in describing physics at the level of known elementary particles, the SM is not a complete description of all fundamental matter and forces in the Universe. As such, several significant questions remain unanswered within its framework.
One example of many phenomena that are not covered by the SM is dark matter. Cosmological observations show that the energy density in our Universe comprises 31% matter and 69% dark energy. However, baryonic matter, which is the matter described within the SM, accounts for just 5% of this [13]. The elusive 26% is attributed to dark matter. Despite its significant contribution to the Universe's energy content, dark matter has never been directly detected, leaving its composition a mystery. Many theories attempt to describe dark matter in a more general description of fundamental particle physics by extending the SM through the introduction of additional particles. One such extension of the SM is Supersymmetry (SUSY), whose theoretical formulation dates back to the 1970s [14–19]. It predicts supersymmetric partners for every SM particle, which differ by half-an-integer of spin. SUSY provides not only excellent candidates for dark matter, but also answers to other remaining questions, such as the mechanism to stabilise the Higgs boson's observed mass, generally known as the naturalness problem [20–22].
Extensive search programmes over many decades of collider physics have shown no experimental evidence or indications of these new particles so far [23]. This leads to the interpretation that new supersymmetric particles might exist at mass scales surpassing the electroweak scale of SM particles and are characterised by low production cross-sections.

To access the TeV mass scales of the new, potentially weakly interacting particles, particle accelerators with large centre-of-mass energies and high luminosities are utilised. The world's largest particle accelerator to date is the Large Hadron Collider (LHC) at CERN [24]. It collides protons at record centre-of-mass energies up to 13.6 TeV. While astrophysical phenomena, such as gamma-ray bursts, can produce particles at much higher energies - there is no place on Earth where protons are brought to collisions at higher energies than at the LHC. Therefore, the LHC collisions are the most promising for potential discoveries of new particles at the TeV scale.
In 2018, the LHC completed its second physics run (Run 2) with a total luminosity of $140\,\text{fb}^{-1}$of proton-proton collisions. This is the largest dataset of high-energy collisions ever recorded, and - despite many already published search results - there is still a lot of unexplored data with potential for new discoveries.

In my doctoral thesis I am exploring the limits of the Standard Model by looking for two distinct supersymmetric particle signatures in the full Run 2 LHC dataset, recorded with the ATLAS experiment [25].
The first signature is a search for pair-produced third-generation SUSY quarks. In many SUSY models, the third-generation squarks are predicted to be among the lightest SUSY particles and have therefore comparably high production cross-sections at the LHC. Historically, in third-generation analyses the $bb + E_{\text{T}}^{\text{miss}}$ and $tt + E_{\text{T}}^{\text{miss}}$ final states are considered separately from exclusive $\tilde{b} \to b + \tilde{\chi}_1^0$ ($\tilde{t} \to t + \tilde{\chi}_1^0$) or $\tilde{b} \to t + \tilde{\chi}_1^\pm$ ($\tilde{t} \to b + \tilde{\chi}_1^\pm$) decays of the bottom- (top-)squark pair. Lower limits on the top- and bottom-squark masses have been set beyond the TeV scale by ATLAS [26–29] and CMS [30–33] in these "symmetric" final states, where both squarks decay in the same pattern. In this thesis, I am exploring the "asymmetric" final state, where a priori assumptions are made to allow both decays ($\tilde{b} \to b + \tilde{\chi}_1^0$, $\tilde{b} \to t + \tilde{\chi}_1^\pm$) with a 50% branching ratio. This allows top- and bottom-squark masses to be probed simultaneously and covers different model assumptions. This "mixed" final state contains one bottom-quark, one top-quark, and

missing transverse energy from the neutralino, $\tilde{\chi}_1^0 : tb + E_{\mathrm{T}}^{\mathrm{miss}}$. This model has been studied before by the ATLAS collaboration with early Run 2 data with a luminosity of 36.6 fb^{-1}. Lower exclusion limits on the squark masses up until 860 GeV (for neutralino masses below 250 GeV) at a confidence level (CL) of 95% are observed, leaving unexplored regions. Especially for a low-mass difference between the squark and neutralino mass, discovery potential remains [34]. The CMS collaboration excluded squark masses below 1150 GeV for neutralino masses below 500 GeV at 95% CL using the full Run 2 with 137 $\mathrm{fb}^{-1}$of recorded data [33]. My work particularly focuses on this low-mass difference or "compressed" region. I am presenting a dedicated search strategy, examining multiple high-level variables to enhance sensitivity within the SUSY particle mass range.

The second analysis is looking for a specific SUSY model with R-parity violation (RPV). As a consequence of RPV, SUSY particles can decay exclusively into SM particles. The search presented in this thesis is focusing on pair-produced gluinos. These can either decay directly into SM final states comprising three jets each or undergo a cascade decay, where the gluino decays to an intermediate neutralino before decaying to SM particles, leading to five jets each.
The RPV multijet all-hadronic final state has been studied previously by the ATLAS [35–37] and CMS [38–40] collaborations. ATLAS placed lower limits on the masses of directly decaying gluinos to 917 GeV at 95% CL [36], while CMS reported a lower limit of the gluino mass of 1.5 TeV at 95% CL [40]. In cascade gluino decays, the limits in the gluino-neutralino mass plane observed by the ATLAS experiment were found to exclude gluino masses up to 1.85 TeV at 95% CL [37], but leaving an unexplored region for gluino masses of $\sim$ 1.1 TeV with a lighter intermediate neutralino mass. The same unexplored corridor was left by the CMS collaboration, which excluded cascade decaying gluinos up to 1.0 TeV [38]. While in R-parity-conserving models the gluino mass has been excluded up to 2.45 TeV in certain model scenarios [41], a low-mass RPV-decaying gluino still leaves unexplored regions. This is a strong motivation for me to make use of the full Run 2 dataset and explore uncovered regions in the RPV gluino decay with ATLAS, replacing the unknown particle "??", to be discovered in 2023, in Figure 1.1 with the gluino or a third-generation squark.

In the future, both analyses will benefit from higher statistics, to increase the sensitivity to even higher particle masses. This will be achieved by the High-Luminosity LHC (HL-LHC), which will increase the LHC's total integrated luminosity up to 3000 fb^{-1} by the end of its lifetime in 2040. Higher luminosity is achieved by higher number of particle collisions per bunch crossing, which will require dedicated detector upgrades to withstand the high particle densities in those environments.
One of these upgrades is the new ATLAS Inner Tracker (ITk), a fully semiconductor-based tracking detector, replacing the current Inner Detector. The ATLAS ITk has finer granularity, is closer to the collision point, and will withstand higher radiation levels, while keeping the material budget of the detector low. The data transmission chain to read out the ITk Pixel detector is designed, tested, and partially manufactured at the Laboratory for High Energy Physics at the University of Bern. The main component of the readout-system, the Optosystem, is located a few metres away from the collision point to limit radiation damage of the components.
Despite the distance, the components are subject to doses of 15 Mrad over the 10-year lifespan of the HL-LHC. I am presenting here studies of the effect of radiation on the ITk Pixel service components by utilising the 18-MeV medical cyclotron in Bern as an irradiation facility. In this work, I describe the irradiation campaigns for various

components, such as cables, connectors, filters, and shielding materials, including the irradiation setups and testing procedures. The results are compared with specifications and recommendations for their usage in the ATLAS ITk Pixel detector are given.

This thesis is organised as follows: Chapter 2 introduces the Standard Model of particle physics and outlines the limitations of the model. An elegant solution to those limitations is described: Supersymmetry. The chapter concludes with experimental constraints on Supersymmetry to date.
Following this, Chapter 3 gives an overview of the Large Hadron Collider and the ATLAS experiment, as well as physics object reconstruction and identification.
A general overview of physics analyses is given in Chapter 4, including a description of the recorded dataset, Monte Carlo event generation, and general concepts of analysis strategies. The subsequent two sections, Chapter 5 and Chapter 6 discuss two searches for Supersymmetry with the ATLAS detector. Chapter 5 describes the search for third-generation squarks, Chapter 6 covers the search for R-parity-violating Supersymmetry in all-hadronic final states.
Chapter 7 gives first an overview of the planned HL-LHC phase and the ATLAS Inner Tracker upgrade, as well as the data-transmission chain, the Optosystem. It then discusses the expected radiation levels for several service components of the Optosystem and illustrates irradiation campaigns of these components that were conducted at the Bern cyclotron.
Finally, Chapter 8 summarises the findings of the studies I performed during the four years of my PhD, draws conclusions and gives a short outlook for future studies to be followed up.

Integration of Artificial Intelligence in Scientific Writing

The natural language processing model chatGPT (chat Generative Pre-trained Transformer), developed by OpenAI, was launched in November 2022.
chatGPT is designed to understand and generate human-like text based on the input it receives via "prompts", resulting in a conversation between the human user and the model. It is trained on information from the internet up until September 2021, including books, websites, and other texts to obtain a broad understanding of language and knowledge.

For the writing process of this thesis, I used chatGPT to gain a better understanding of theoretical and experimental concepts through summaries of certain topics such as detector technologies, or reconstruction techniques. I frequently asked to summarise in a limited number of sentences well-established concepts in experimental high-energy physics to help me understand and explain those concepts. I used chatGPT to rephrase my written text or to embed information it provided me into existing text. I used the model to find relevant resources and to extract key information from those. The way I used chatGPT is as a tool to improve my writing and get support with technicalities like LaTeX or other coding-related issues. However, I did not use the model to generate creative or novel ideas for the studies I present here.

While it is a powerful tool to generate summarising text passages, it is also prone to generate incorrect text. Often, the replies of chatGPT miss the key ideas or describe topics not in their full extent. It is very good in describing non relevant facts in a language containing many professional sounding words which give a wrong impression of confidence. I also found that it is not very good at logically structuring paragraphs or even chapters. In my experience, chatGPT and other similar models are a helpful tool when it comes to generating text with very precise commands - but it is not capable of giving correct and precise answers to specific, technical or vague questions. While it provides useful starting points for writers, the understanding of concepts and logical description of the same still requires a human thinking process.

Asking chatGPT to write one sentence about the fundamental question that is addressed in particle physics, "what are we made of?", it replies with

> "Certainly:
> Probing the deepest layers of the universe, particle physics seeks to unravel the enigma of 'What are we made of?' by dissecting the subatomic symphony that constructs our reality."
> *OpenAI. (2023). ChatGPT (August 3 version).*

This answer leaves the human part of this conversion with a smile, wondering which training data shows in this formulation. Even though there is a great potential in the integration of AI in scientific writing, it still requires a lot of fine-tuning from human minds.

Usage of Natural Units

If not stated otherwise, the natural units are used in this thesis. Natural units define the system of units used in particle physics, wherein the fundamental constants c (speed of light) and $\hbar$ (reduced Planck constant) are set to unity:

$$c = \hbar = 1.$$

From this follows that all quantities such as energy, momentum, mass and time expressed in natural units are given in units of electron Volt (eV),

$$1\,\mathrm{eV} = 1.602 \times 10^{-19}\mathrm{J},$$

corresponding to the energy an electron receives when passing through a 1 V potential.

Chapter 2
The Standard Model and Beyond

The foundation of elementary particle physics is the Standard Model (SM). It describes known matter and interactions by introducing two types of particles: matter particles (*fermions*) and mediators, which transmit interactions between particles (*bosons*).

2.1 The Standard Model of Elementary Particles

All known matter is constructed out of quarks and leptons, which are the two families of fermions, but make up only 5% of the total energy content of the Universe. Cosmological observations and assumptions suggest that the remaining 95% consist of dark matter (26%) and dark energy (69%), which are not described in the SM and have not been directly observed so far [23].
Three of the fundamental forces in nature, the weak, electromagnetic, and strong force are transmitted by the gauge bosons of the SM. However, the SM does not include the description of the gravitational force.

The gauge group $SU(3)_C \times SU(2)_L \times U(1)_Y$ is the symmetry group of the SM, which characterises the local symmetries of the strong, weak, and electromagnetic forces. This gauge group is responsible for regulating the behaviour of the particles and forces in the model. Quantum field theory (QFT) provides the mathematical framework describing these particles and forces in the SM [42].

All elementary particles of the SM have - to our current knowledge - no further substructure and are therefore considered to be the indivisible elementary building blocks of matter, thus fundamental.

2.1.1 Fermions

Fermions make up the known matter in our Universe. All fermions have a half-integer spin and follow Fermi-Dirac statistics [43, 44]. Fermions differ in their quantum numbers and properties, such as mass, charge, flavour, and colour. Due to these characteristics, they can be divided into different categories. All fermions are either leptons or quarks, which both are further divided into three generations. Figure 2.1 summarises all fermions and their most accurately measured properties. For every fermion exists an anti-fermion with opposite electric charge (for charged fermions) and opposite helicity.

Each lepton generation is a doublet of one charged, massive lepton and one corresponding neutral neutrino of the same "flavour",

$$\begin{pmatrix} e \\ \nu_e \end{pmatrix}, \quad \begin{pmatrix} \mu \\ \nu_\mu \end{pmatrix}, \quad \begin{pmatrix} \tau \\ \nu_\tau \end{pmatrix}. \tag{2.1}$$

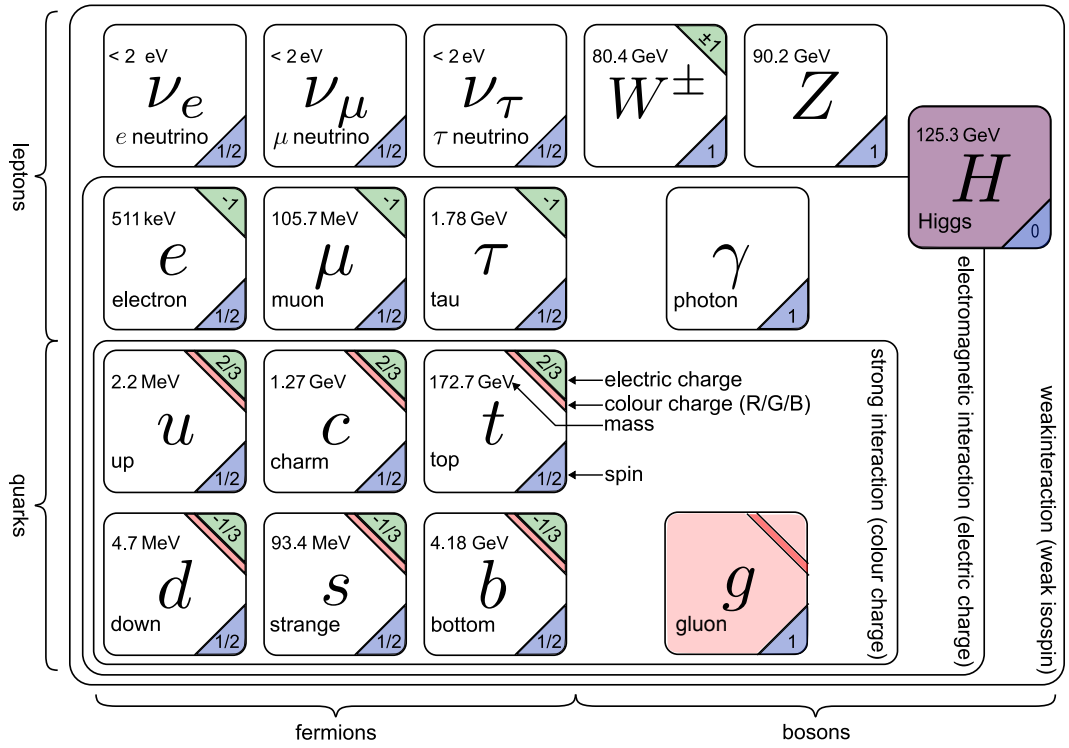

Figure 2.1: Elementary particles of the SM we know today. For every particle, the name, mass, spin, colour charge and electrical charge is given. For fermions, the generations are given, while for each boson, the corresponding force is stated. The graviton has not been observed yet, and is therefore without any characteristics. The graphic is adapted and modified from [45].

The electron is as light as 511 keV, while the third-generation lepton, the tau, is more than three orders of magnitudes heavier, 1.776 GeV. The neutrinos were believed to be massless for a very long time. However, the discovery of neutrino oscillations provided evidence that neutrinos have a non-zero mass [46, 47]. But it is yet unclear how the neutrino masses can be introduced exactly in the SM and what their exact masses and the hierarchy of their mass ordering are. The massive, charged leptons interact via the weak and electromagnetic force, the massless, neutral neutrinos interact only weakly.

Quarks come in six different "flavours": up (u), down (d), charm (c), strange (s), top (t), and bottom (b), which are grouped into three generations as pairs with increasing mass, same as for the leptons. Each generation consists of a doublet with one up-type (u, c, t) and one down-type quark (d, s, b),

$$\begin{pmatrix} u \\ d \end{pmatrix}, \quad \begin{pmatrix} c \\ s \end{pmatrix}, \quad \begin{pmatrix} t \\ b \end{pmatrix}. \tag{2.2}$$

All up-type quarks have a positive electric charge of $+2/3\ e$, down-type quarks have $-1/3\ e$, where e is the elementary charge a proton carries. Their masses span several orders of magnitude, from the lightest up-quark with 2.2 MeV to the heaviest particle in the Standard Model, the top-quark with 172.70 ± 0.30 GeV.

Contrary to the leptons, quarks carry one additional quantum number, the colour charge: a quark is either red, green or blue. Quarks can only exist in colour neutral bound states

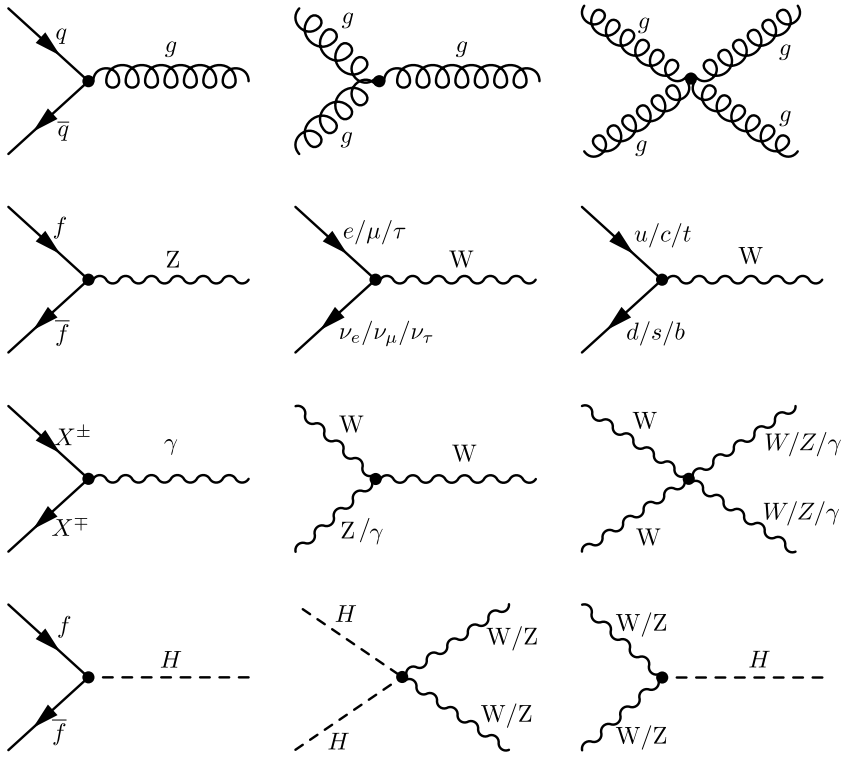

Figure 2.2: A selection of allowed vertices in the SM. The first row shows strong interaction vertices involving gluons and quarks, the second row weak vertices between fermions and the electroweak gauge bosons W and Z. The third row shows the electromagnetic vertex with two charged particles $X^\pm$ (fermions or bosons) and a photon, as well as electroweak vertices between electroweak gauge bosons only. Finally, the last row shows Higgs interaction vertices. Higgs self-interaction vertices are not shown.

and not as free particles, which is known as *confinement*. Bound states of quarks are called *hadrons*. There are two types of hadrons: *baryons* and *mesons*. Baryons consist of three quarks (or three antiquarks), examples are the lightest baryons, proton (uud) and neutron (udd). To be colourless, (and obey the Pauli exclusion principle) the three quarks in a baryon need to have three different colours. Mesons are bound states of a quark-antiquark pair with the same colour and anti-colour. The pions are the lightest mesons, π^+ ($u\bar{d}$), π^- ($d\bar{u}$), and π^0 ($1/\sqrt{2}(u\bar{u} - d\bar{d})$ [42, 48].

All known elements and their isotopes, summarised in the table of nuclides, are composed of a nucleus surrounded by electrons. The atomic nuclei are built upon protons and neutrons. This means that all ordinary matter around us consists of leptons and quarks of the first generation.

2.1.2 Bosons

In addition to fermions, the SM includes integer spin gauge bosons, which are responsible for transmitting the fundamental forces between fermions and obey Bose-Einstein statistics [49, 50]. There are four known fundamental forces: the electromagnetic force, the weak force, the strong force, and gravity. Each force is associated with at least one spin-1 boson. The hypothetical graviton (boson associated with gravity) is not incorporated into the SM due to its non-observation so far and the difficulty to reconciling QFT and

general relativity. The energy dependent coupling strengths of the forces span over several magnitudes, depending on the available energy.

The photon (γ) is the carrier of the electromagnetic force, which is described by Quantum Electrodynamics (QED). Requiring local gauge invariance of the Lagrangian of a free Dirac spinor ($\psi(x)$), which describes the wave functions of fermions, under the underlying $U(1)$ symmetry results in introducing the spin-1 gauge field A_μ. Its interaction vertex to charged fermions corresponds to the third term in

$$\begin{aligned}\mathcal{L}_{\text{QED}} &= i\bar{\psi}(x)\gamma^\mu\partial_\mu\psi(x) - m\bar{\psi}(x)\psi(x) \\ &- eQA_\mu(x)\bar{\psi}(x)\gamma^\mu\psi(x) \\ &- \frac{1}{4}F_{\mu\nu}(x)F_{\mu\nu}(x).\end{aligned} \tag{2.3}$$

This gauge field A_μ corresponds to the photon. The coupling strength between a photon and a fermion with charge Q in an interaction vertex, as shown in Figure 2.2, is proportional to the electromagnetic fine structure constant α_{EM} via

$$g_{\text{EM}} = Q \cdot \sqrt{4\pi\alpha_{\text{EM}}}. \tag{2.4}$$

The introduction of the kinetic term of the photon, the fourth term of the QED Lagrangian in Eq. (2.3), requires the gauge field to be massless in order to preserve the local gauge invariance. Following Noether's theorem on symmetries [51], the electric charge is the conserved quantity in the symmetry group of electromagnetic interactions.

The strong force holds atomic nuclei together and is mediated by the gluons g. It is described by Quantum Chromodynamics (QCD), which is invariant under a local phase transformation in $SU(3)_C$, the three dimensional colour phase. Similar to the procedure discussed for QED, new terms need to be introduced to the Lagrangian to preserve this gauge invariance. These terms give rise to eight gauge fields, corresponding to the eight generators of the $SU(3)_C$ symmetry, which are identified as eight gluons. Due to the non-abelian nature of QCD (meaning the generators do not commute), the gluons themselves carry colour charge. One possible combination for the colour charge of gluons is $r\bar{g}, r\bar{b}, b\bar{g}, b\bar{r}, g\bar{b}, g\bar{r}, 1/\sqrt{2}(r\bar{r} - g\bar{g})$, and $1/\sqrt{6}(r\bar{r} + g\bar{g} + b\bar{b})$. Because gluons carry the charge to which they couple, a self-interaction term is present in the QCD Lagrangian. At every strong interaction vertex, colour is conserved.

Like all gauge couplings in the SM, the gauge coupling of the strong force, g_S, depends on the energy scale of the interaction, the momentum transfer Q^2. This is known as running of the coupling constants. Because QCD is based on a non-Abelian gauge group, the strong coupling constant α_S increases with large distances, thus smaller energies - contrary to electromagnetic and the weak coupling constants. The consequence is that QCD needs to be treated differently for the two opposite regimes, the high energy and the low energy regime. Figure 2.3 shows measurements of various experiments measuring α_S as a function of Q^2, which follows

$$\alpha_s(Q^2) = \frac{g_S^2}{4\pi} = \frac{1}{\beta_0 \log\left(\frac{Q^2}{\Lambda^2_{\text{QCD}}}\right)}, \tag{2.5}$$

with β_0 describing the number of bosonic and fermionic loops and Λ^2_{QCD} the energy scale below which non-perturbative QCD dominates. At high energies, the running

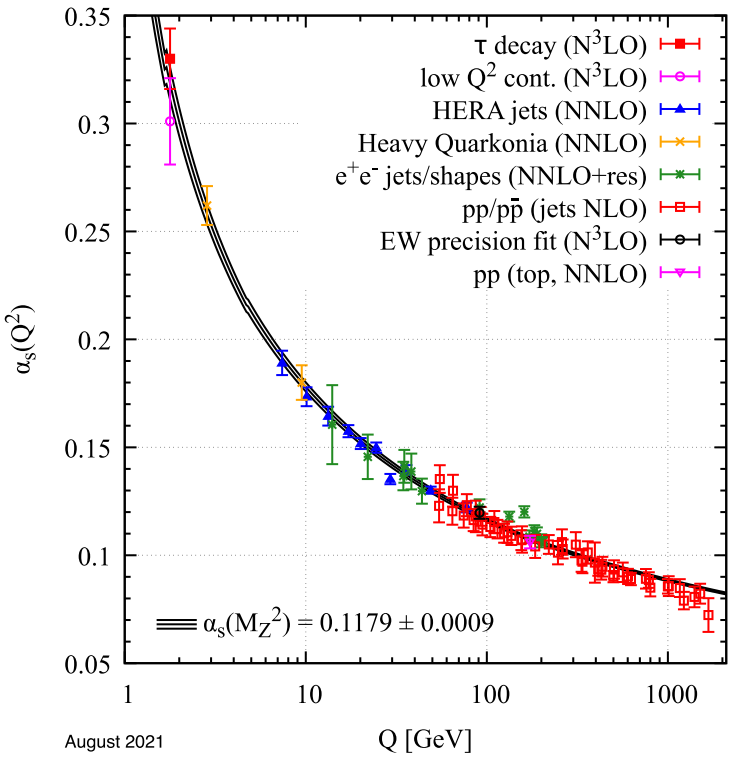

Figure 2.3: Measurements of the strong coupling α_S as a function of momentum transfer Q. At $\sim 1\,\text{GeV}$, α_S is ~ 1, and thus perturbative calculations cannot be applied for QCD at this energy regime [23].

coupling constant, $\alpha_S = g_S^2/4\pi$, is small enough (~ 0.1) such that QCD can be described perturbatively. In this regime, quarks and gluons can be considered as *quasi-free* particles, which is known as *asymptotic freedom*. In the low energy regime (thus high α_S values), perturbative theory cannot be applied and quarks and gluons are not considered quasi-free. An observed phenomenon in this regime is *hadronisation*, which is typically observed in hadron collider experiments. While a quark-antiquark pair from an interaction is moving apart from each other, the energy density between those two quarks is increasing until enough energy density is available to create another quark-antiquark pair. This process is repeated until the energy is no longer sufficient and colour-neutral bound quark states (mesons and baryons) are formed.

The weak force is described by an $SU(2)_L$ symmetry group, which couples only to left-handed fermions (right-handed anti-fermions). Two of the three mediators, the charged $W^\pm$ bosons, are responsible for processes such as the nuclear β-decay via charged current (CC) weak interactions, e.g.

$$d \to u + e^- + \bar{\nu}_e.$$

The two charged W bosons are related to the gauge fields W^1, W^2, W^3 of the $SU(2)_L$ symmetry group via

$$W^\pm = \frac{1}{\sqrt{2}}\left(W^1 \mp iW^2\right). \tag{2.6}$$

The third weak gauge boson, W^3 cannot exactly be associated with the Z^0 boson, the third mediator of the weak forces described by the SM. Observations showed that Z^0

couples to left- and right-handed anti-fermions, contrary to the W^3 which couples only to left-handed fermions.
To address this, Glashow, Salam and Weinberg proposed the unification of the electromagnetic and weak interaction into the electroweak interaction [52–54]. The theory proposes that the electromagnetic and weak nuclear forces are one single force. In the early universe, as the temperature cooled down, they separated. It predicts four gauge fields, W^1, W^2, W^3 and B^0 from the symmetry group $SU(2)_L \times U(1)_Y$, where Y is the hypercharge $Y = 2(Q - T_3)$ with the electric charge Q and T_3, the third component of the isospin. In the unification, the two neutral electroweak gauge bosons, γ and Z^0, are a linear combination of W^3 and a newly introduced field B^0,

$$\begin{pmatrix} Z^0 \\ \gamma \end{pmatrix} = \begin{pmatrix} \cos(\theta_W) & \sin(\theta_W) \\ -\sin(\theta_W) & \cos(\theta_W) \end{pmatrix} \cdot \begin{pmatrix} B^0 \\ W^3 \end{pmatrix} \tag{2.7}$$

with the electroweak mixing angle θ_W, the Weinberg angle.

The last missing piece was discovered in 2012: the Higgs boson, a massive, spin-0 scalar boson. Its existence confirms the existence of the associated Higgs field, which is responsible for the generation of the masses of the particles in the SM. Through the process of spontaneous symmetry breaking, described by the Brout-Englert-Higgs (BEH) mechanism [55–57], the Higgs field gives mass to the gauge bosons of the electroweak sector. To preserve gauge invariance within the description of the electro-weak sector, massless gauge bosons are predicted. The BEH mechanism allows the W and Z bosons to be massive, as observed by experiments, while preserving the gauge invariance. The BEH mechanism also introduces Yukawa coupling terms between the Higgs field and the fermions. The stronger this coupling to the Higgs field, the higher the mass. The observation of the Higgs boson at the LHC, by the ATLAS and CMS experiments confirmed the predicted theory of the Brout-Englert-Higgs-mechanism [11, 12]. In July 2023, ATLAS published the most precise measurement of the Higgs boson's mass to date, $125.11 \pm 0.11\,\text{GeV}$ [58].

Figure 2.4 shows the impressive prediction ability of the SM in the form of multiple measurements of SM parameters with the ATLAS experiment. One can see that none of the observables deviate largely from the theoretical prediction of the SM. Therefore, one can conclude that the theoretical description of the SM is a huge success of particle physics.

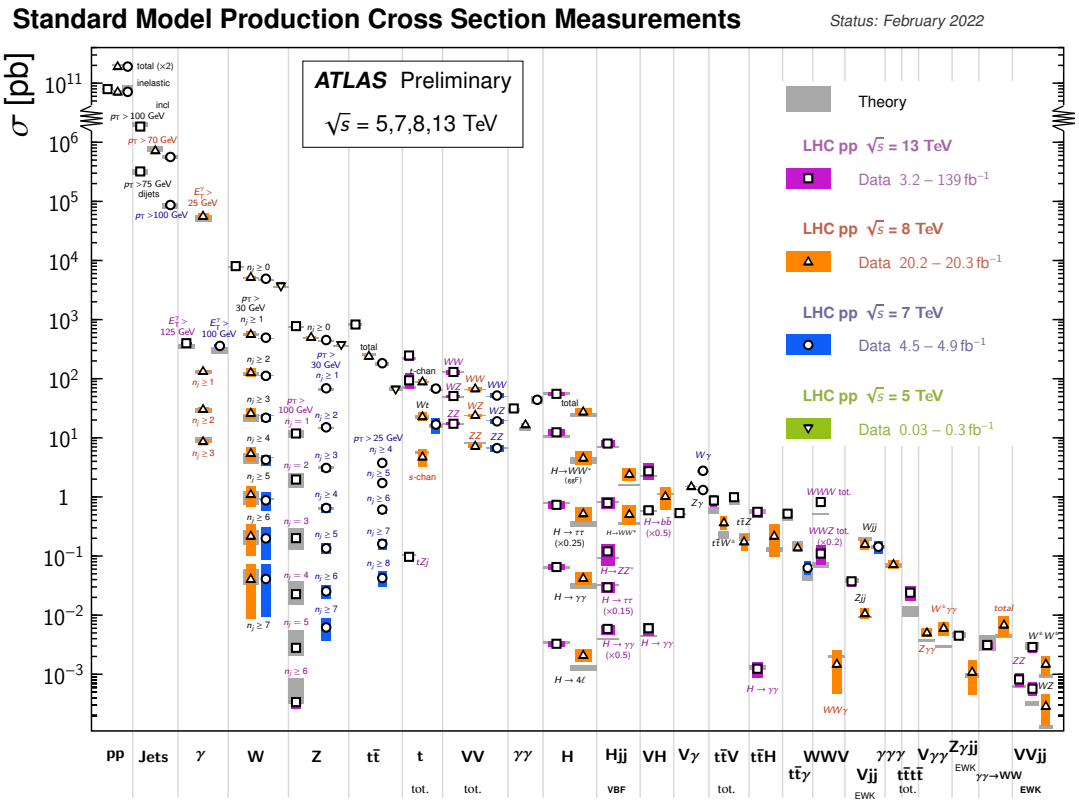

Figure 2.4: Summary of most recent SM total production cross-section measurements from the ATLAS experiment compare to the corresponding theoretical expectations [59].

2.1.3 Limitations of the Standard Model

Despite its astonishing number of successful experimental confirmations, summarised in Figure 2.4, the SM is not a complete description of all fundamental interactions and particles observed in the universe.

One of the biggest open questions is the nature of *dark matter* (DM), which makes up approximately 26% of the Universe's mass-energy density [60]. While dark matter has been indirectly observed through its gravitational effects on visible matter, its actual composition remains unknown. Various theoretical models have been proposed to explain the nature of dark matter, including weakly interacting massive particles (WIMPs) or axions, but so far, no direct experimental evidence has been found [23].

Another unanswered question is the *hierarchy problem*, which concerns the large discrepancy between the energy scale at which the Higgs boson is observed and the Planck scale, which is the scale at which gravity becomes as strong as the other fundamental forces. The Higgs boson's mass is highly sensitive to quantum corrections, which easily cause it to become much larger than the electroweak scale. This leads to the questions of why the Higgs boson's mass is not significantly larger than what has been observed and how this mass is "fine-tuned" to its observed value [42].

In the original formulation of the SM, the assumption was made that only left-handed neutrinos exist, due to the non-observation of weak interactions involving right-handed neutrinos. However, the Yukawa term to generate fermion masses requires left- and right-handed fermions, which lead to the assumption that *neutrinos are massless*. But the experimental observation of neutrino oscillations has shown that they do have small, but non-zero masses [46, 47]. Several mechanisms have been proposed to explain the origin of neutrino masses, among them are Dirac neutrinos or the Seesaw mechanism. Up until today, there is no experimental proof of which mechanism is the correct one, as no experimental evidence has been found so far [23].

The *matter-antimatter asymmetry* in the universe, namely the question why there is more matter than antimatter in the universe, is not fully explained in the SM. The SM predicts that matter and antimatter should have been produced in equal amounts during the Big Bang, but observations show that the observable universe is composed almost entirely of matter. Several mechanisms have been proposed to explain this asymmetry, including contributions from CP-violating or baryogenesis, but the exact mechanism that led to the observed matter-antimatter asymmetry is still unknown [61].

The vast majority of these unanswered questions could be solved by introducing new particles, which extend our known set of elementary particles. These particles are at higher masses than the observed ones, thus large-scale high energy experiments are needed to search for them [23]. An elegant solution is the supersymmetric extension of the SM: it provides not only a well-defined dark matter candidate, it also solves the hierarchy problems. This extension, Supersymmetry, is introduced in the following section and is a main subject of this thesis.

2.2 Supersymmetric Extension of the Standard Model

Supersymmetry (SUSY) is a theoretical framework that proposes a new type of symmetry between fermions and bosons, thus the spin of elementary particles [62]. Through transformation under this new symmetry by the operator Q, every SM particle gets a new "superpartner" with a spin differing by half an integer. This means Q transforms bosons into fermions and vice versa via

$$Q\,|\text{Boson}\rangle = |\text{Fermion}\rangle\,, \text{ and } Q\,|\text{Fermion}\rangle = |\text{Boson}\rangle\,. \tag{2.8}$$

Except for their spin, the new super partners, "sparticles", have the same quantum numbers as their SM counterpart.

By introducing the new symmetry, the particle content is doubled. Spartners of SM leptons are spin-0 scalar bosons, called *sleptons* (scalar leptons, $\tilde{\ell}$), for example the selectrino being the supersymmetric electron. The supersymmetric partners of quarks are spin-0 *squarks* (scalar quarks $\tilde{q}$), such as the top squark (sometimes informally called *stop*). The electroweak SM gauge fields, W^1, W^2, W^3, and B^0, are transformed into spin-1/2 fermions, the *gauginos*: the three *winos*, $\tilde{W}^i$, and the *bino*, $\tilde{B}^0$. In order to remain invariant under electroweak gauge symmetry transformations, the SM Higgs sector is extended to two chiral Higgs doublets which differ in their hypercharge component $Y = \pm 1/2$. The superpartners of extended SM Higgses are called *higgsinos*. The remaining vector boson superpartners are the eight coloured *gluinos* $\tilde{g}$.

SUSY breaking needs to be introduced due to the non-observation of supersymmetric particles at the same mass as their SM partners. This, with the additional electroweak symmetry breaking, allows for additional mixing between the electroweak gauginos and the higgsinos, which result in two *charginos* $\tilde{\chi}^{\pm}_{1,2}$ and four *neutralinos* $\tilde{\chi}^0_{1-4}$. The charginos arise from the mixing of charged higgsinos and winos. The neutralinos are combinations of the neutral higgsinos and neutral electroweak gauginos, winos and binos. The neutralino $\tilde{\chi}^0_1$ is often considered to be the lightest supersymmetric particle (LSP).

The left- and right-handed SM fermions get assigned individual left- and right-handed superpartners, gauge eigenstates $\tilde{f}_R$, $\tilde{f}_L$, which form the supersymmetric mass eigenstates $\tilde{f}_1$, $\tilde{f}_2$ through mixing. The mixing depends on the mass of the SM particles, and is therefore only relevant for the third-generation squarks, such as $\tilde{t}_1$ ($\tilde{b}_1$) and $\tilde{t}_2$ ($\tilde{b}_2$) for the top- (bottom-)squarks and $\tilde{\tau}_1$,$\tilde{\tau}_2$ for staus.
For lighter generations, the left- and right-handed gauge eigenstates are the same as their mass eigenstates. The supersymmetric particles do not possess spin degrees of freedom to be classified as left-handed or right-handed, therefore the left- and right-handedness is related only to their SM partners.

All particles, of the SM and its SUSY extension, can be grouped into *supermultiplets*. A SM particle and its spartner make up a supermultiplet, either doublets or singlets. Multiplets containing SM fermions are *chiral* (or matter, scalar), while SM vector boson multiplets are *gauge* (or vector) supermultiplets. Due to the different behaviour of right- and left-handed fermions under weak $SU(2)$ symmetry transformations, they are also treated separately in the context of SUSY. While left-handed fermions and their superpartners are grouped in chiral doublets, the right-handed fermions do not have superpartners with matching quantum numbers within the same supermultiplet. They are treated separately as singlets.

The superpartners of the Higgs bosons are spin-1/2 fermions, therefore they are grouped into chiral supermultiplets. The two doublets correspond to a left- and right-handed part, H_u and H_d, which each consists of a charged and neutral component $(H_u^+ H_u^0), (H_d^+ H_d^0)$. The observed SM Higgs boson at 125 GeV is constructed as a linear combination of H_u^0 and H_d^0 [62].

Theoretically, various supersymmetric extensions to the SM can be introduced, which may involve different compositions of superpartners. The model with the minimum amount of new particles is called the Minimal Supersymmetric Standard Model (MSSM). In this model, the mass eigenstates are not given by the particles described above. Table 2.1 summarises all gauge and mass eigenstates of the MSSM, yet undiscovered.

Names	Spin	Gauge eigenstates	Mass eigenstates
Squarks	0	$\tilde{u}_L, \tilde{u}_R, \tilde{d}_L, \tilde{d}_R$	(same)
	0	$\tilde{c}_L, \tilde{c}_R, \tilde{s}_L, \tilde{s}_R$	(same)
	0	$\tilde{t}_L, \tilde{t}_R, \tilde{b}_L, \tilde{b}_R$	$\tilde{t}_1, \tilde{t}_2, \tilde{b}_1, \tilde{b}_2$
Sleptons	0	$\tilde{e}_L, \tilde{e}_R, \tilde{\nu}_e$	(same)
	0	$\tilde{\mu}_L, \tilde{\mu}_R, \tilde{\nu}_\mu$	(same)
	0	$\tilde{\tau}_L, \tilde{\tau}_R, \tilde{\nu}_\tau$	$\tilde{\tau}_1, \tilde{\tau}_2, \tilde{\nu}_\tau$
Neutralinos	1/2	$\tilde{B}^0, \tilde{W}^0, \tilde{H}_u^0, \tilde{H}_d^0$	$\tilde{\chi}_1^0, \tilde{\chi}_2^0, \tilde{\chi}_3^0, \tilde{\chi}_4^0$
Charginos	1/2	$\tilde{W}^\pm, \tilde{H}_u^+, \tilde{H}_d^-$	$\tilde{\chi}_1^\pm, \tilde{\chi}_2^\pm$
Gluino	1/2	$\tilde{g}$	(same)

Table 2.1: Mass states of all supersymmetric partners to the known and observed SM particles in Minimal Supersymmetric Standard Model with their spin and gauge eigenstates that form the mass eigenstates [62].

2.2.1 R-parity

The supersymmetric extension of the SM doubles the particle content of the model. However, the introduction of these new particles leads to possible SM interactions that have not been observed.
R-parity is a multiplicative quantum number assigned to each particle, defined as

$$R = (-1)^{3(B-L)+2s} = \begin{cases} +1 & \text{for SM} \\ -1 & \text{for SUSY,} \end{cases} \tag{2.9}$$

with baryon number B, lepton number L, and spin s. All SM particles are assigned an R-parity of $+1$, while their superpartners carry an R-parity of -1. R-parity conservation, if imposed, has significant consequences:

- It prevents the rapid proton decay via $p \to e^+ + \pi^0$, depicted in Figure 2.5. If it occurred, it would be a powerful indication of beyond the SM (BSM) physics.

However, there is no experimental evidence for the proton decay, which sets a lower limit on the proton's half-life of about $> 3.6 \times 10^{29}$ years [23], many orders of magnitude longer than the age of the universe. This suggests that if proton decay does occur, it is an extremely rare event. Due to R-parity conservation, B and L numbers are simultaneously conserved and therefore the proton decay is prevented.

- The LSP is stable, as it cannot decay into only SM particles due to the conservation of R-parity. This stable, neutral, and colourless LSP is a potential candidate for dark matter [62]. This particle interacts only weakly with SM particles out of which the ATLAS detector is built, and therefore they leave the detector volume undetected.
- SUSY particles must be produced in pairs. This is because the initial particles in these processes are SM particles with R-parity of +1, and the total R-parity must be conserved in the reaction. Similarly, SUSY particles must decay into an odd number of SUSY particles, ensuring that the final state of the decay also includes a stable LSP.

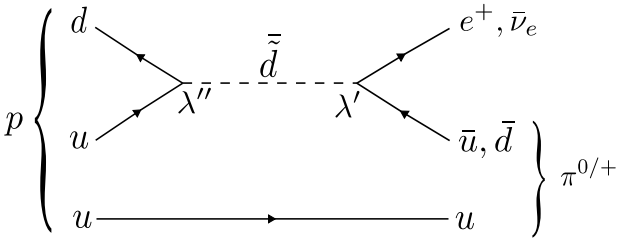

Figure 2.5: Potential proton decay via two R-parity-violating couplings. While λ'' violates baryon number conservation, λ' violates lepton number conservation. The decay of the stable proton is prohibited by imposing an R-parity conservation, or in an R-parity-violating model, allowing only one of the two couplings, λ'' or λ, to be non-zero.

The proton decay shown in Figure 2.5 violates both, the baryon- and the lepton number, at the two vertices with the R-parity-violating (RPV) couplings λ' and λ''. Within the SM, baryon and lepton numbers are accidentally conserved at all vertices.

In R-parity-conserving (RPC) models, all coupling terms in the SUSY Lagrangian, which violate B or L, are set to zero. These terms include

$$W_{\Delta L=1} = \frac{1}{2}\lambda^{ijk} L_i L_j \bar{e}_k + \lambda'^{ijk} L_i Q_j \bar{d}_k + \mu'^{i} L_i H_u, \tag{2.10}$$

$$W_{\Delta B=1} = \frac{1}{2}\lambda''^{ijk} \bar{u}_i \bar{d}_j \bar{d}_k, \tag{2.11}$$

where Eq. (2.10) are the lepton number and Eq. (2.11) the baryon number violating terms. The indices i, j, k run from 1 to 3 and represent the three generations of fermions in the SM, the three λ^{ijk} are dimensionless Yukawa couplings, μ'^{i} are the trilinear couplings. The remaining components are chiral superfields, where L_i and Q_i are lepton and quark doublets, $\bar{e}_i$, $\bar{d}_i$ and $\bar{u}_i$ are electron, down- and up- quark singlets and H_i denotes the Higgs doublet that couples to up-type quarks in the MSSM [63].

The coupling constants are [63]:

- λ^{ijk} between two leptons and one slepton,
- λ'^{ijk} between one lepton and two quarks, of whose one (either the lepton or one of the quarks) is a sparticle,
- λ''^{ijk} between two up-type and one down-type quarks, where one of the three quarks is a sparticle,
- μ'^{i} mixing the lepton and Higgs superfields.

RPV SUSY models allow large values for individual couplings, while keeping the others low enough to prevent the proton from decaying. In this thesis, I am discussing two different SUSY searches, one that conserves R-parity, and one that violates it. To investigate these scenarios, "simplified" models are used. Such models reduce the extensive parameter space inherent to SUSY theories by setting specific assumptions on parameters such as cross-sections, branching ratios and the sparticle masses to limit the parameter space. Typically, the considered process is assumed to have a branching ratio of 100%, which allows the isolated study and interpretation of distinct signatures.

2.2.2 Implications of Supersymmetry

The introduction of SUSY carries profound implications for our understanding of particle physics and cosmology. It offers promising answers to many of the to-date open questions of the SM, which were discussed in Section 2.1.3.

SUSY offers an elegant solution to the hierarchy problem in the SM. As previously discussed, the Higgs boson mass, m_H, receives quantum corrections from fermionic and bosonic loops, as shown in Figure 2.6.

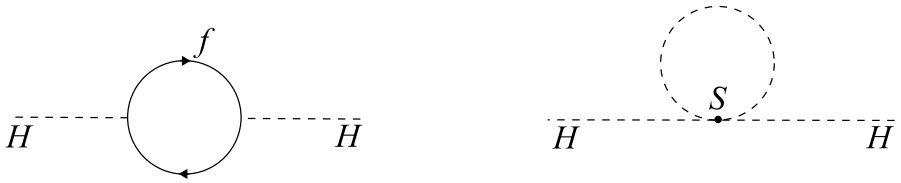

Figure 2.6: Leading order loop corrections to the Higgs boson mass from fermionic (a) and bosonic (b) contributions [62].

The leading order correction with the highest contribution to the Higgs boson mass from a fermionic loop is given by:

$$\Delta m_H^2 = -\frac{1}{8\pi^2}\lambda_f^2\Lambda^2 + \dots \,, \tag{2.12}$$

where λ_f is the Yukawa coupling of the fermion f with mass m_f to the Higgs-field, and Λ is the cutoff scale, which could be as high as the Planck scale. These corrections to the Higgs boson mass can be very large, as Λ can be much larger than the electroweak scale, leading to the hierarchy problem. In SUSY, for each fermionic loop, there is a corresponding bosonic loop from the superpartner, and vice versa. The corrections from

the superpartners have the opposite sign to the SM particles, leading to a cancellation of each of the corrections. For example, the correction to the Higgs boson mass from a supersymmetric scalar loop (shown in Figure 2.6(b) for scalar S), corresponding to the term given in Eq. (2.12), is given by:

$$\Delta m_H^2 = \frac{1}{16\pi^2}\lambda_S \Lambda^2 + ... \tag{2.13}$$

It is worth noting that the cancellation is only perfect if the masses of the particles and their superpartners are equal. Since we have not yet observed any superpartners at the same mass scale as the Standard Model particles, SUSY is a broken symmetry. For the description of a softly broken supersymmetry, additional parameters are needed to define the masses separately. The resulting non-exact cancellation of the mass corrections requires additional fine-tuning of the mass values.

For cosmology, SUSY's implications for dark matter are particularly significant. In R-parity-conserving SUSY models, the LSP is stable and only weakly interacts with ordinary matter. This makes it an excellent candidate for dark matter, which is estimated to constitute approximately 80% of the matter in the universe. As mentioned before, the lightest of the neutralinos, the superpartners of neutral gauge and Higgs bosons, is often considered the most plausible candidate for the LSP.

Furthermore, SUSY models would also enable the unification of the three gauge couplings at a high energy scale, providing a pathway towards a possible Grand Unified Theory (GUT), which is an appealing feature beyond the scope of the SM. The gauge couplings in the SM have different strengths at low energies. However, as the energy scale increases (equivalently, as the distance scale decreases), these couplings approach, but unfortunately they do not meet at a single point. This is shown in Figure 2.7. Newly introduced SUSY particles could contribute to the running of the gauge couplings, changing their trajectories towards a single meeting point at the "Grand Unification scale", also shown in Figure 2.7 [62].

2.2.3 Experimental Constraints on SUSY

Since the theoretical introduction of SUSY in the 1970s, particle accelerators have played a crucial role in the active search for an experimental confirmation of SUSY. With each new generation of larger and more powerful accelerators, the reach into the realm of SUSY widens. There are two primary approaches to search for new physics: one is through the observation of deviations from the predictions of SM processes, such as discrepancies in precision measurements or rare processes. The other approach involves direct searches for the production of BSM particles at colliders. Both approaches are crucial in the comprehensive exploration of SUSY and provide complementary information about the potential existence of supersymmetric particles.

Despite these extensive search programmes over many decades, direct evidence for SUSY has not been observed so far. The Large Electron Positron (LEP) collider operated at CERN from 1989 to 2000. LEP's experiments, namely ALEPH, DELPHI, L3, and OPAL, played a significant role in setting early constraints on SUSY [64]. Another collider, Tevatron, was running at Fermilab in the United States from 1983 to 2011 and was a proton-antiproton collider. Experiments at the Tevatron, including CDF and DØ,

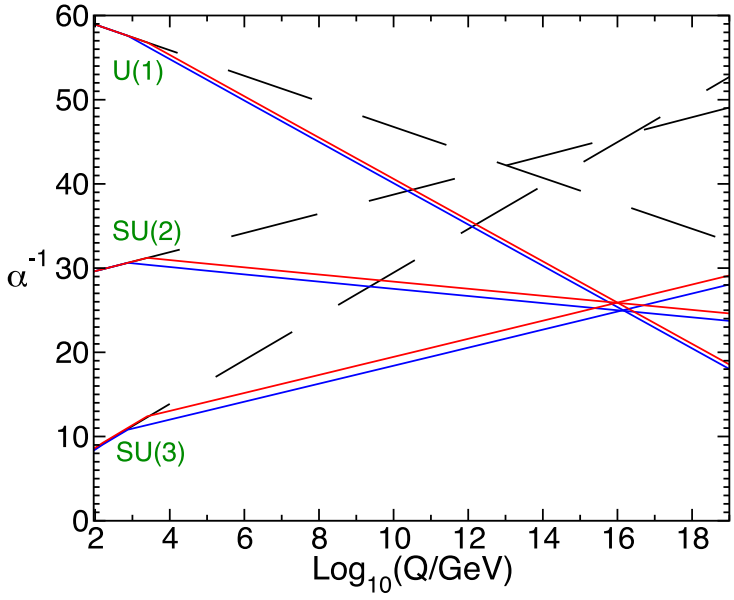

Figure 2.7: Evolution of the fundamental coupling constants with increasing energy. The black dashed line shows the evolution without SUSY, the red and blue curves are including SUSY and lead to a meeting point of all forces at $\sim 10^{16}$ GeV. This scale is slightly lower when the masses of the newly introduced particles are raised (red curve) [62].

also conducted searches for supersymmetric particles and set important limits on SUSY models [65]. Flavour physics experiments, including LHCb at the LHC [66] and Belle II in Japan [67], have explored rare decays and flavour-changing processes, constraining SUSY loop contributions [68]. Additionally, various smaller non-collider experiments, dedicated to dark matter detection, magnetic moment measurements, etc. have indirectly probed diverse SUSY scenarios.

The LHC, which is introduced in the next chapter, collides protons at a record centre-of-mass energy of up to 13 TeV (13.6 TeV since 2022). Therefore, it is - to date - the most likely place on Earth to produce and observe high-mass SUSY objects in a laboratory. Figure 2.8 shows that coloured SUSY particles, such as gluinos and squarks, have the highest pair production cross-sections and are therefore the most promising candidates when it comes to direct SUSY searches at the LHC.

This thesis discusses two SUSY searches for pair-produced, coloured sparticles: the search for a gluino pair, decaying into an all-hadronic final state via an R-parity-violating λ'' coupling and the pair production of top/bottom squarks, decaying asymmetrically into a final state with a top-quark, a bottom-quark and missing transverse momentum. Schematic diagrams for both simplified models are displayed in Figure 2.9.

The absence of SUSY particles so far is by no means a sign that SUSY does not exist - but rather a motivation to explore all of the available data, investigate new methods to search for it, and explore potential improvement of the experiments - which is the aim of this thesis.

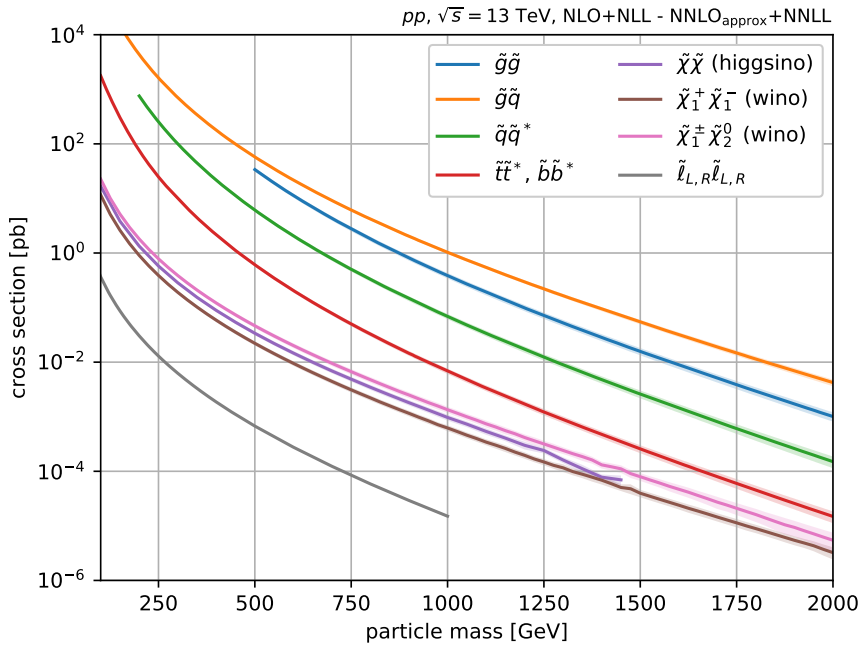

Figure 2.8: SUSY cross-sections for sparticle pair production at a centre-of-mass energy of $\sqrt{s} = 13\,\text{TeV}$ at the LHC as a function of the sparticle masses. Reproduced from [69].

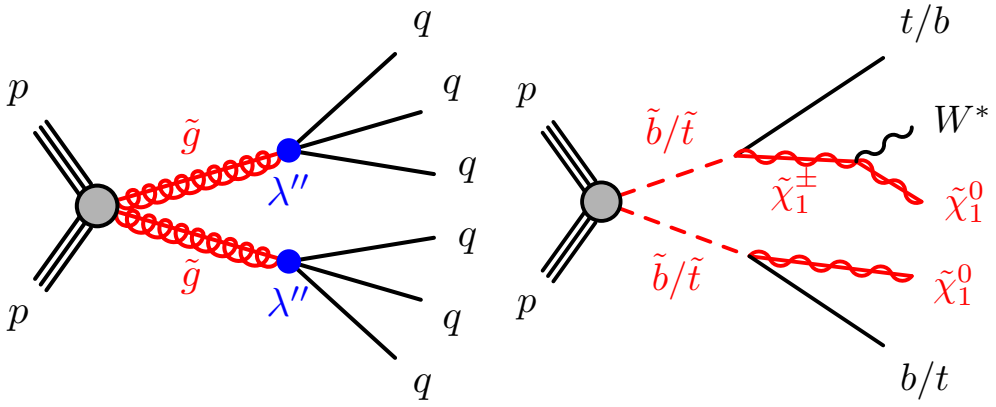

(a) RPV multijet signature

(b) $tb + E_{\text{T}}^{\text{miss}}$ signature

Figure 2.9: The diagrams show the two simplified SUSY models, which are targeted in this thesis. The gluino pair production search is targeting an R-parity-violating model. The stop/sbottom pair production is searched in an R-parity-conserving model, where the neutralinos are considered to be the lightest supersymmetric particles.

Chapter 3

The Large Hadron Collider and the ATLAS Experiment

The searches for BSM physics presented in this thesis use data from the ATLAS experiment at the Large Hadron Collider (LHC). ATLAS detects particles from high-energy proton-proton or heavy ion (Lead or Xenon ions) collisions that are delivered by the LHC, the largest particle accelerator of the world, located at the Conseil Européen pour la Recherche Nucléaire (CERN). This chapter provides an overview of LHC and ATLAS.

3.1 The Large Hadron Collider

The LHC [24] is the world's most powerful particle accelerator. It is a 26.7 km long circular particle accelerator (synchrotron) and is located about 100 m below the French-Swiss border at CERN near Geneva, Switzerland. Figure 3.1 presents the area in which the LHC is located with the accelerator complex overlaid. The LHC employs electromagnetic fields to increase the energy of subatomic particles (protons or heavy ions) to relativistic energies.
Radiofrequency (RF) cavities produce high-frequency electromagnetic waves that provide the accelerating forces necessary to increase the kinetic energy of the particles. The resulting electromagnetic field gradient within the cavities allows for efficient energy transfer to the particles, leading to high accelerating gradients and achieving particle energies up to several TeV. The LHC's superconducting magnets guide and focus the accelerated particles as they travel through the accelerator ring, enabling the particles to collide with each other at the intersection points of the detector experiments. In total, 1 232, 15 m-long super-conductive dipole magnets provide a nominal magnetic field of 8.3 T, which is necessary to keep the protons on their circular orbit [70]. Another 392 quadrupole magnets are used for the focusing of the beam. In 2023, the highest centre-of-mass energy for proton-proton collisions ever achieved is 13.6 TeV. In the heavy-ion programme, the maximum energies per nucleon ever reached are 5.36 TeV for Lead-Lead collisions, 8.16 TeV for proton-Lead collisions, and 5.44 TeV for Xenon-Xenon collisions.

Prior to the installation of the LHC, the tunnel and experimental caverns housed the Large Electron Positron (LEP) collider [72] and its main experiments, which ceased their physics programmes in 2000 after having operated for 11 years. The main physics results contributed significantly to the study of the electroweak gauge bosons, Z and W [23, 73]. It took over a decade to construct the LHC and the experiments for which it provides proton collisions. The LHC delivered its first collisions at $\sqrt{s} = 7$ TeV in March 2010.

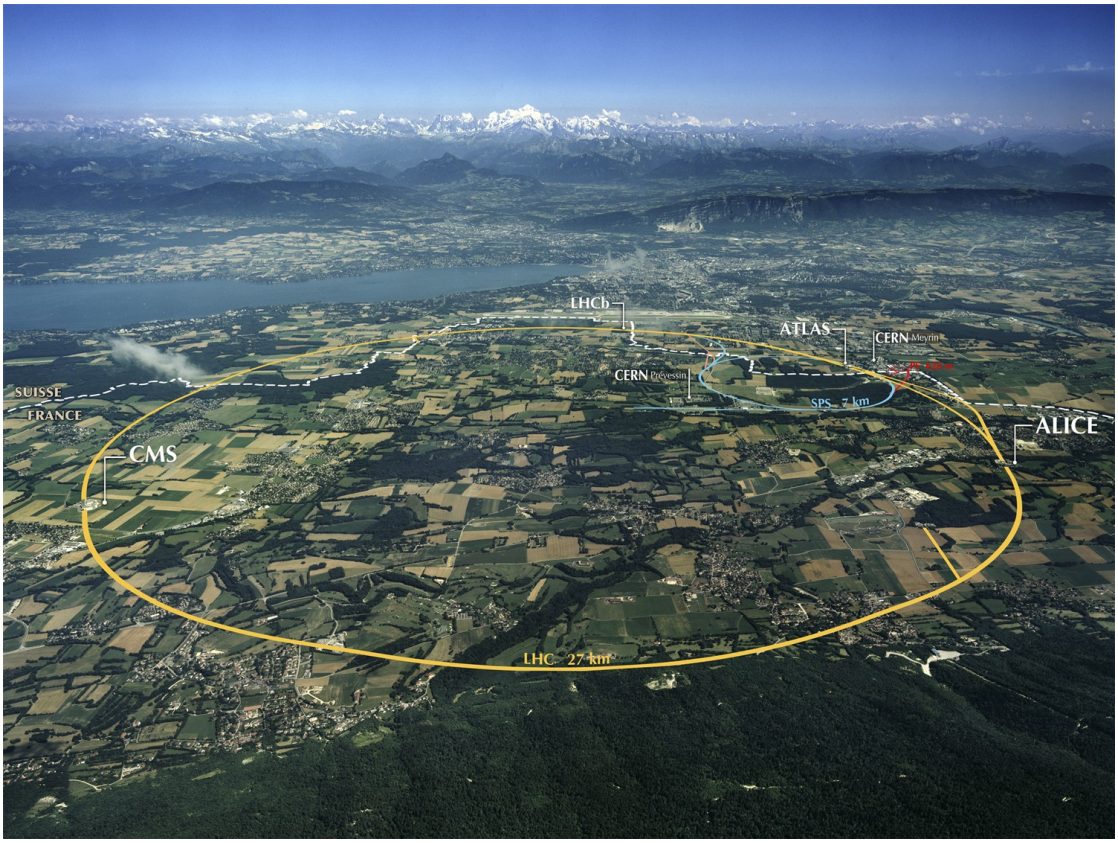

Figure 3.1: Location of CERN, the LHC, and its four main experiments (ATLAS, ALICE, CMS and LHCb) in the area around the French-Swiss border region close to Geneva [71].

As illustrated in Figure 3.2, the LHC is divided into eight sectors that are separated by eight junction points, four of which are surrounded by the main LHC experiments: A Toroidal Lhc ApparatuS (ATLAS), located at Point 1, A Large Ion Collider Experiment (ALICE) at Point 3, the Compact Muon System (CMS) experiment at Point 5, and LHC beauty (LHCb) at Point 8. The accelerating radio frequency system is situated at Point 4. Both, ATLAS [25] and CMS [74], are multi-purpose detectors, whose main goal is to observe and study elementary particles, such as the Higgs boson, and new physics, with their onion-like arrangement of subdetectors around the collision points. The asymmetric LHCb [66] detector was designed for forward-directed flavour physics studies, such as the precise study of flavour-physics. The fourth detector, ALICE [75], is dedicated to heavy ion collisions. Its physics objective is to study quark-gluon plasma, which is created when protons and neutrons from heavy ions collide and the quarks are no longer bound to the gluons for a short period of time.

3.1.1 The LHC acceleration complex

The LHC accelerator complex is a chain of 5 individual accelerators that gradually increase the energy of the protons up to their maximum energy of 6.8 TeV (in 2022) [77]. Figure 3.3 shows the LHC accelerator complex.

The injection of protons starts with hydrogen atoms from a bottle of hydrogen. During the first two physics runs (Run 1, 2010-2012 and Run 2, 2015-2018), the electrons were

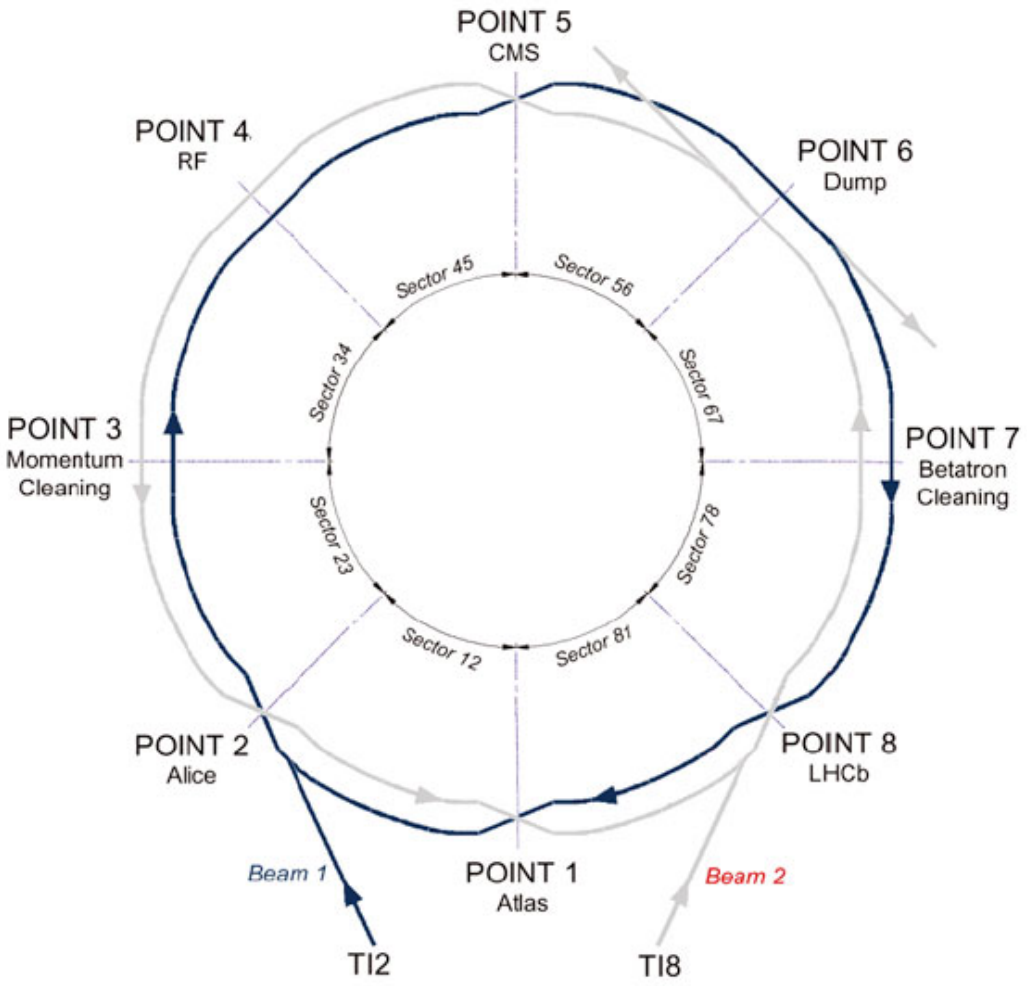

Figure 3.2: Schematic of the eight sectors and four interaction points of the LHC, showing the location of the experiments ATLAS, ALICE, CMS and LHCb, as well as the location of the radio frequency (RF) cavities and other important components of the machine. Image from [76].

removed from the hydrogen and the remaining protons began their acceleration path towards their collision energy in the linear accelerator, LINAC 2, up to 50 MeV. For Run 3, LINAC 2 was replaced by LINAC 4 [79]. This is a linear accelerator that accelerates negative hydrogen ions (H^-) up to 160 MeV, and protons are extracted by a stripper foil at the injection into the next accelerator. The replacement of LINAC 2 is one of the main upgrades for the upcoming High-Luminosity LHC phase, which is discussed in Section 7.

After the initial acceleration in a linac, the protons are injected into the first circular collider of the chain, the Proton Synchrotron Booster (BOOSTER). Here, the protons are accelerated to 2 GeV (1.4 GeV until 2018).
The next acceleration step is the Proton Synchrotron (PS), which accelerates the proton bunches up to 26 GeV. The PS is CERN's oldest synchrotron, which has been in operation since 1959. Once the protons are at the maximum energy that can be reached with the PS, they are transferred into the Super Proton Synchrotron (SPS). Here, the protons

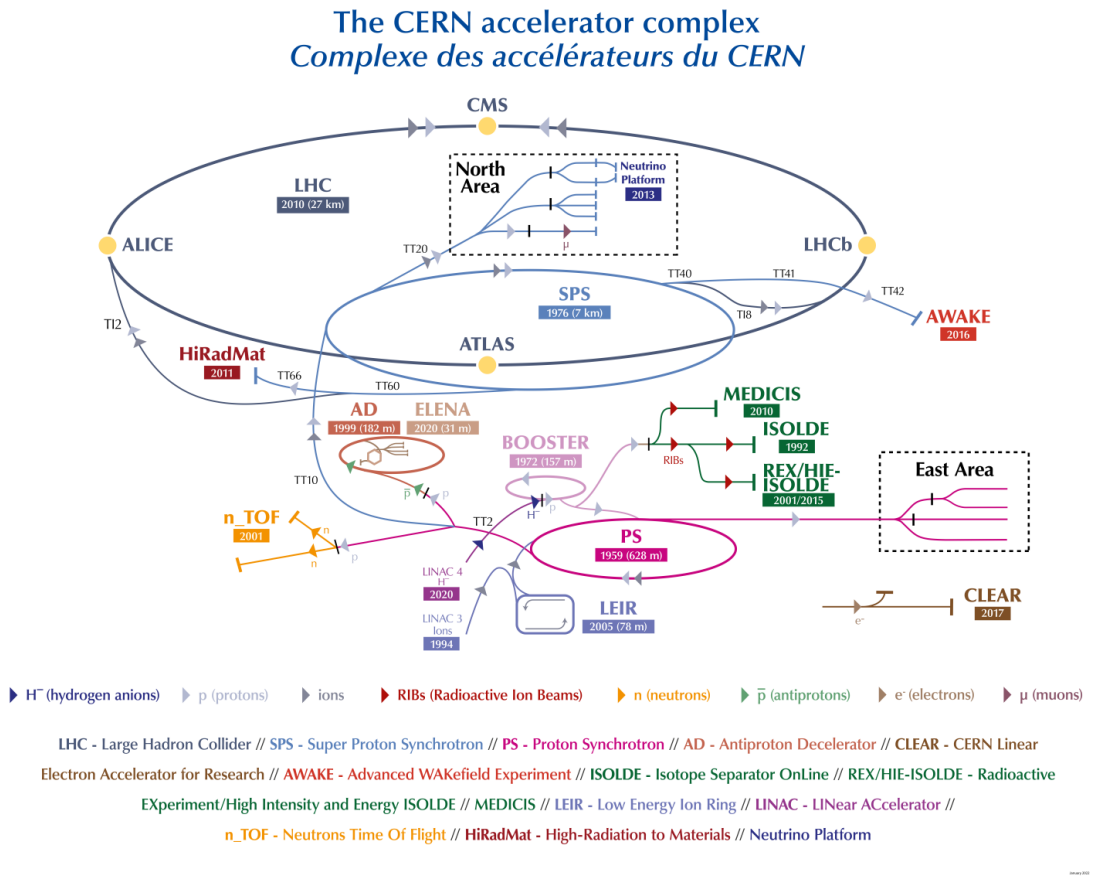

Figure 3.3: The acceleration complex of the LHC. The protons start their journey as H^- ions and are accelerated to 450 GeV by iterative acceleration in LINAC4, BOOSTER, PS and SPS, and then injected into the LHC ring [78].

are accelerated to 450 GeV, which is the injection energy for the LHC. The protons are injected into the LHC in both directions of travel according to a predefined filling pattern. Once the LHC is "full", the protons are further accelerated to the maximum energy of 6.8 TeV (6.5 TeV until 2018).

As a consequence of the acceleration mechanism, which is based on radiofrequency electric fields, the protons are not a continuous beam in the LHC, but constrained in bunches of protons. One bunch contains up to 1.2×10^{11} protons at the start of a physics run. During Run 2, the LHC was filled with up to 2 808 individual bunches per proton beam, with a revolution frequency of 11 245 Hz [80].

Once the LHC ring is filled with bunches, the energy is ramped up to the maximum proton energy. After the so-called "flat-top" period, the proton beams get squeezed and adjusted with the quadrupole magnets along the ring to ensure the highest possible luminosity, which is introduced in Section 3.1.2. Finally, stable beams are declared and the LHC experiments can start taking data with a collision frequency of 40 MHz, corresponding to a bunch spacing of 25 ns. A nominal proton physics fill is usually kept around 20 hours, before the remaining protons are dumped into the beam-dump. Figure 3.4 shows the online-monitoring interface, 'Page 1', which shows the evolution of luminosity and

intensity of the proton beams over 24 hours. Additionally, important beam parameters, such as the beam energy, intensity, and the β^* values are given at every moment in time. The β^* is a measure of the amplitude of particle oscillations in the transverse plane at the interaction point and is optimised by the quadrupole magnets of the LHC.

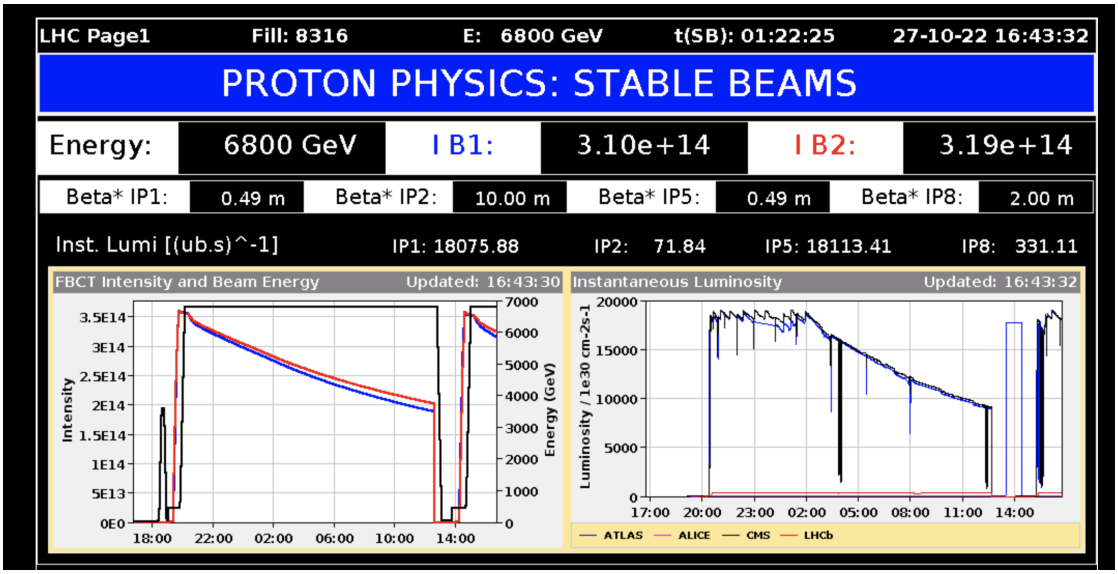

Figure 3.4: Snapshot of LHC Page 1, showing a full fill during the data taking period in 2022. The energy per beam (6 800 GeV), the intensities per beam (IB1, IB2), the β^* values at every interaction point and the instantaneous luminosity at every interaction point are given. Page 1 can always be accessed under https://op-webtools.web.cern.ch/vistar/vistars.php.

3.1.2 Luminosity

Luminosity $\mathcal{L}$ is a measure of the rate at which particular processes are produced within the collisions of an accelerator. It is defined as the number of collisions per second per unit of area and is an important parameter for particle physics experiments because it describes the number of events that can be observed and studied. The time-integrated luminosity L of a particle accelerator, measured in inverse femto-barn (fb^{-1}), is proportional to the number of produced particles N via a particular process $pp \to X$ with a given production cross-section $\sigma_{pp\to X}$,

$$N_{pp\to X} = L \cdot \sigma_{pp\to X} = \int \sigma_{pp\to X} \cdot \mathcal{L} \, \mathrm{d}t. \tag{3.1}$$

Therefore, the higher the luminosity, the greater the number of particle collisions, which increases the probability of detecting rare events (such as the discussed SUSY processes in this thesis),. This consequently allows for more precise measurements of the properties of known elementary particles. The instantaneous luminosity $\mathcal{L}$ can be calculated as

$$\mathcal{L} = \frac{N_a N_b f_{\mathrm{Rev}}}{2\pi\sigma_a\sigma_b}, \tag{3.2}$$

with N_i the number of particles per bunch i, the revolution frequency f_{Rev}, and the

beam area in x- and y-direction of the bunches σ_i [70]. The indices $i = a, b$ denote the counter-rotating bunches.

The curves in Figure 3.5(a) show that the data acquisition periods in 2011 at $\sqrt{s} = 7\,\text{TeV}$ and 2012 at $\sqrt{s} = 8\,\text{TeV}$ mark the LHC Run 1, which ended at the end of 2012 with a delivered total luminosity of $5.51\,\text{fb}^{-1}$ at 7 TeV and $28.31\,\text{fb}^{-1}$ at 8 TeV. The observation of the Higgs boson in 2012 by the ATLAS and CMS experiments demonstrates the enormous scientific importance of the LHC. After the Long Shutdown 1 (LS1), the LHC came back online in June 2015, marking the start of Run 2. In Run 2, the LHC delivered $156\,\text{fb}^{-1}$ of proton-proton collisions at a centre-of-mass energy of $\sqrt{s} = 13\,\text{TeV}$. The trend over the years is shown in Figure 3.5(b). ATLAS recorded $147\,\text{fb}^{-1}$ of which $140\,\text{fb}^{-1}$ are considered as "good" physics data, which is used for the two analyses presented in this thesis. Compared to the $139\,\text{fb}^{-1}$ stated in Figure 3.5(b), the final value for the full Run 2 luminosity was updated to $140\,\text{fb}^{-1}$ in 2022 [81].
LS2 started at the end of 2018 and lasted until spring 2022, when the LHC launched its third physics run, Run 3, with $\sqrt{s} = 13.6\,\text{TeV}$. Throughout one year, the machine delivered more than $40\,\text{fb}^{-1}$, which is the green curve in Figure 3.5(a).

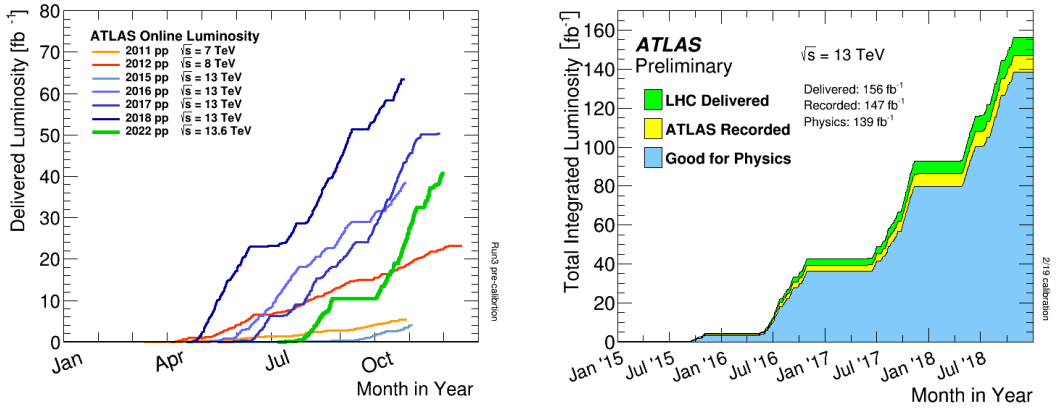

(a) (b)

Figure 3.5: Delivered luminosity in all years of LHC operation (a) and delivered luminosity by the LHC and observed by the ATLAS experiment (b). Figures taken from [82].

Run 3 will continue until 2025, followed by LS3. This period will be used to upgrade the accelerator, but also to prepare the experiments for the High-Luminosity phase of the LHC, HL-LHC, which is scheduled to start in 2029. Within 11 years, HL-LHC is expected to deliver up to $3\,000\,\text{fb}^{-1}$ with a maximum collision energy of $\sqrt{s} = 14\,\text{TeV}$ by the end of its physics programme in 2040. Figure 3.6 shows the timeline of the entire physics program of the accelerator from the start in 2011 until the foreseen end in 2040.

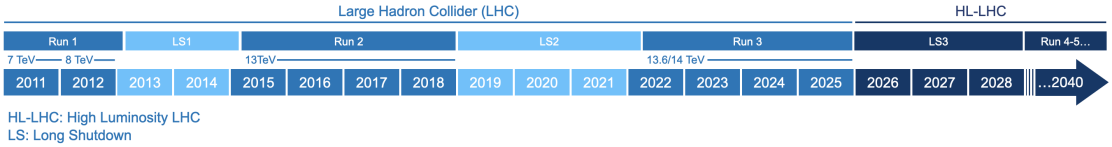

Figure 3.6: Timeline of LHC and HL-LHC, starting with the beginning of Run 1 in March 2010. The LHC physics programme is expected to run until 2040. Image adapted from [83].

3.2 The ATLAS Detector

One of the main users of LHC collisions is the ATLAS experiment. It is located around the Interaction Point 1 (IP1) along the LHC ring, 100 m underground, as shown in Figure 3.2.

ATLAS is one of the two multi-purpose detectors at the LHC, consisting of four main sub-systems: the Inner Detector (ID), the electromagnetic and hadronic calorimeters (ECAL, HCAL), the Muon Spectrometer (MS), and the magnet system with an inner solenoid and the outer toroidal structure, shown in Figure 3.7. Together with the on-detector infrastructure for signal and command transfer, cooling and powering, the entire detector spans 46 m in length and 25 m in height, weighing approximately 7 000 tonnes. The purpose of this machine is to record trajectories and energies from particles that are produced in proton-proton collisions at the centre of the detector.

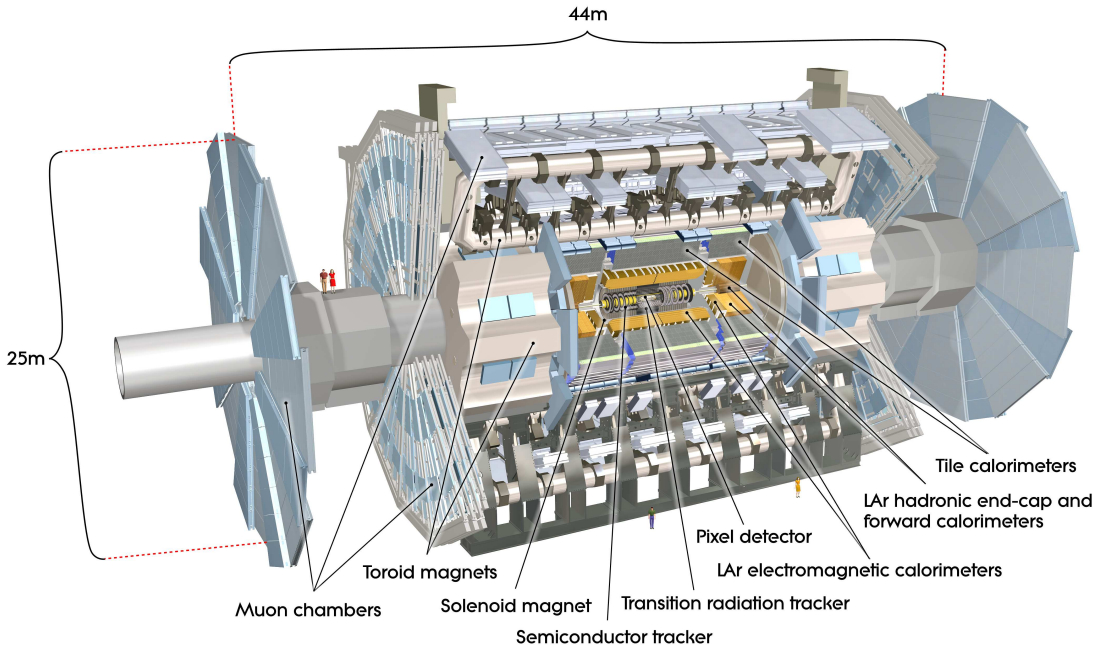

Figure 3.7: Schematic of the the ATLAS detector with the subsystems of the four different detector components: the Inner Detector with its PIX detector, SCT tracker and TRT tracker, the two calorimeters, the Tile and Liquid Argon calorimeter, toroid and solenoid magnets forming the magnet systems and the Muon Detectors. The two figures between the muon wheels on the left are to scale with average-height humans [25].

ATLAS uses a right-handed coordinate system, where the nominal interaction point serves as the origin. The z-axis runs parallel to the beam axis, while the x-axis is directed towards the centre of the LHC ring. The y-axis is pointing upwards to establish a right-handed coordinate system with the x- and z-axes.
The angle ϕ is the azimuthal angle around the beam pipe in the transverse plane, with respect to the x-axis. The polar angle θ measures the particle's direction in the transverse plane relative to the z-axis. Generally, the pseudorapidity η is used to describe the angular distribution of particles with respect to the z-axis. It is defined as

$$\eta = -\ln \tan\left(\frac{\theta}{2}\right), \tag{3.3}$$

with the polar angle θ between the particle's momentum and the positive z-axis, but assuming the mass of the particle to be zero. This is an approximation for relativistic particles for which their mass is negligible compared to their momentum. A $\eta = 0$ corresponds to the transverse plane, perpendicular to the beam direction. The larger the η value is, the more the particle's trajectory is in the forward direction, with $\eta = 4$ corresponding to $\sim 2^\circ$ in θ and $\eta = \infty$ parallel to the z-axis. The use of pseudorapidity instead of the true rapidity y is convenient because the distance in η between two particles, $\Delta\eta$, is a Lorentz invariant quantity.

3.2.1 Inner Detector

The Inner Detector (ID) [84, 85] of ATLAS is situated in close proximity to the interaction point, with a distance of only 3.25 cm, making it the closest detector component to the collision zone. To precisely determine the origin of particle trajectories, the tracking detector meets highest requirements in terms of spatial resolution within all subsystems. It covers a range in pseudorapidity up to $|\eta| < 2.5$. The ID, as shown in Figure 3.8, is composed of three subcomponents: the silicon-based Pixel detector (PIX) including the Insertable B-Layer (IBL) [86], the silicon strip detector (SCT), and the transition radiation tracker (TRT).

PIX and SCT are based on semiconductor detectors. This technology makes use of pn-junctions, where n-doped (with free extra electrons) and p-doped (with extra free positive charges, or holes) semiconductor materials, silicon for example, are brought next to each other. Through diffusion, the free charge carriers will be attracted by the ions of the opposite side of the junction, meaning the n-doped material will have a positive net charge and the p-doped side a negative net charge. Thus, an electric field from the n-doped to the p-doped side is created in which no free charge carriers are present: the active depletion region. If a charged particle passes through the depletion region, electron-hole pairs are created and are separated in the electric field. The increased current flow can be read out. The depletion area, which is the active area of a semiconductor detector, can be increased by applying a reverse bias. The big advantage of semiconductor detectors is that their granularity can be very high, depending on the size of the individual pixel (or strip) size. Usually, innermost tracking detector components use semiconductor technology, while larger surface detectors further outside are based on other technologies for cost and material budget reasons.

The silicon PIX detector is composed of three layers in the barrel region, and three endcaps on each side. During LS1, the IBL was installed as the fourth, innermost layer

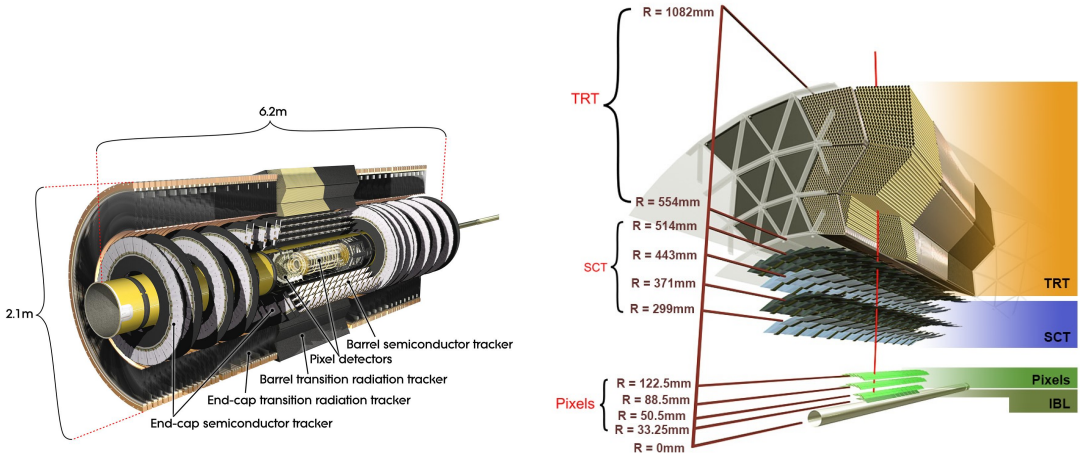

(a) (b)

Figure 3.8: Schematics of ATLAS Inner Detector with all outer barrel discs (a) [25] and a cross-section of the central barrel components (b) [87], including the IBL.

of the PIX detector [86]. The PIX detector is 0.25 m in diameter, and 1.4 m long [84, 85]. The size of the IBL pixels is as small as $50 \times 250\,\mu m^2$, while the pixels of the outer layers have a size of $50 \times 400\,\mu m^2$.

Placed around the PIX detector, is the SCT detector, which consists of 4 barrel layers, and 9 discs at both ends of the detector. Its 6.2 million readout channels are distributed over an area of 1.05 m in diameter and almost 6 m in length. Along the silicon surface, there is a readout strip every 80 µm [84].

The outermost part of the ID is the TRT detector, which is a drift-tube detector, thus a different detector technology than the PIX and SCT detectors. It is composed out of 298 000 individual drift tubes, each of them 144 cm (barrel region) or 39 cm (endcaps) long and four millimetres in diameter [84]. The straws are filled with Xenon gas, which ionises when a relativistic, charged particle traverses the tube. The TRT detector has interleaved Mylar foils between the drift tubes to additionally produce transition radiation for electron identification. The transition radiation, emitted by charged particles crossing the interface between two media with differing dielectric constants, depends on the Lorentz factor γ. Therefore, the yields of emitted photons can be used to distinguish between electrons and hadrons [25, 88].

3.2.2 Calorimeters

Calorimeters are used to measure the energy of particles. Ideally, all particles (except muons and neutrinos) should be completely stopped within the calorimeter volume. ATLAS uses two different calorimeter systems. The liquid-argon (LAr) calorimeter [89] is located just outside the thin solenoid magnet surrounding the ID and is dedicated to measuring the energy of electromagnetic particle showers. Around the LAr calorimeter is the scintillator-tile calorimeter [90], designed to determine the energy of hadron-induced showers. Both calorimeters are shown in Figure 3.9. Particle showers induced by electrons or photons are smaller in spatial scale than hadronic showers. The LAr ECAL has a finer granularity and is closer to the collision point than the Tile HCAL calorimeter.

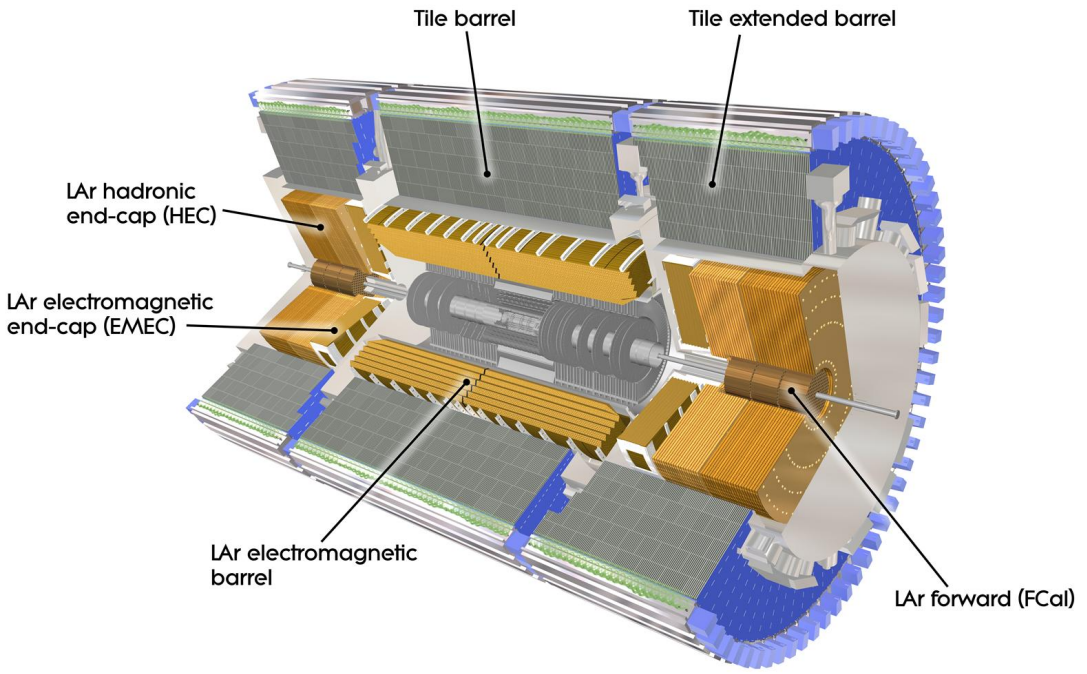

Figure 3.9: These schematics show the layout of the calorimeter system in the ATLAS detector. The calorimeter system consists of several components, including the liquid argon (LAr) electromagnetic calorimeter and the hadronic tile calorimeter, for the barrel, endcap, and forward regions [25].

The ECAL is a Lead/liquid-argon sampling calorimeter that is used to measure the energy of electrons and photons. It consists of three parts: a barrel section covering the central region, and two endcap sections in the forward regions. The pseudorapidity of the barrel and end-cap (EMEC) region is covered the the range $0 < |\eta| < 3.2$, and extended by the LAr forward calorimeter (FCal) up to $|\eta| < 4.9$ [25].

Electrons and positrons travelling through matter lose energy through ionisation. Above a certain threshold, namely the material-dependent critical energy E_c, high-energy electrons lose energy mainly through bremsstrahlung at a rate of $1/e$ per radiation length X_0 [cm] travelled. The radiation length depends on the stopping material. The electrons and positrons produced in the LHC typically have energies in the order of GeV. To stop 30 GeV particles in iron, at least $20\,X_0$ are required. This corresponds to 35 cm of iron with a radiation length of 1.757 cm [23, 91]. This determined the design choice of the LAr calorimeter, which varies between $22\,X_0$ and up to $38\,X_0$ for different areas of the LAr detector [89, 92]. The ATLAS LAr detector uses an accordion-shaped sandwich structure, alternating passive layers of Lead with active layers of liquid-argon. The Lead absorbs the energy of the incoming electron or photon, producing a shower of secondary particles that interact with the liquid-argon. The liquid-argon is ionised by the secondary particles, producing an electrical signal that is read out. The amplitude of the signal is proportional to the energy deposited by the particle in the ECAL.

In general, hadrons do not lose all of their energy as they pass through the electromagnetic calorimeter's layers. To stop these particles and thus measure their full energy, a HCAL

is built around the ECAL. Hadrons lose energy through nuclear interactions, which are non-trivial to describe and use numerical approximations. For simplicity, the interaction length λ_I can be defined for different materials. It is defined as the length for which the probability that a hadron does not interact with the material is $1/e$. Compared to the radiation length X_0 of iron (1.757 cm), λ_I is almost one order of magnitude larger (16.77 cm). Studies showed that 11 λ_I are sufficient to absorb almost all of the particle's energy hadrons in the detector volume [90].

The ATLAS HCAL is built on several layers of steel, with plastic scintillator-tiles sandwiched between the layers. Hadrons induce a secondary particle shower within the steel plates. These charged particles penetrate through the plastic-scintillator layers, where scintillation and fluorescence processes generate signals (photons) that are read out via wavelength-shifting optical fibres and photomultiplier tubes. The tile detector uses 420 000 individual scintillator-tiles and covers a pseudorapidity range of $0 < |\eta| < 3.2$ with its barrel and end-cap calorimeters (HEC). The FCal also provides hadronic coverage up to $|\eta| < 4.9$ [25]. Because of the passive steel layers, it is the heaviest component of ATLAS, weighing almost 3 000 tonnes. The entire ATLAS detector is estimated to weigh 7 000 tonnes.

3.2.3 Muon Spectrometer

The ATLAS muon spectrometer [93] consists of different types of gas detectors: monitored drift tubes (MDTs), cathode strip chambers (CSCs), thin gap chambers (TGC), and resistive plate chambers (RPCs), which can be seen in Figure 3.10. The RPC and TGC detectors allow for fast and precise timing measurements of the muons in a pseudorapidity range up to $|\eta| < 2.4$, while the CSC and MDT detectors are precision tracking detectors up to $|\eta| < 2.7$. Together, these four detectors allow for the identification and precise measurement of muons produced in the LHC collisions [25].

The MDTs are long, thin-walled aluminium drift tubes filled with a gas mixture of Argon and Carbon-dioxide and are used in both the barrel and endcap regions. The CSCs are located in the endcap regions, at the Small Wheels, and are multi-wire proportional chambers filled with a gas mixture of Argon, Carbon-dioxide, and a small amount of Oxygen-gas. During the LS2, they were replaced by the New Small Wheels [94], which use small-strip Thin Gap Chambers (sTGC) and Micromegas detectors (MM). The RPCs are another type of gaseous detectors made up of two parallel plates filled with a gas mixture of Tetrafluoromethane (CF_4) and isobutane gas, used in the barrel region. Lastly, the TGCs consist of two metal plates with a narrow gap between them filled with a gas mixture of Carbon-dioxide, Argon, and n-pentane gas, placed in the endcap regions of the detector.

3.2.4 Magnet System

Magnetic fields are used in the tracker and muon spectrometer regions to determine the momenta of traversing particles. With the radii of the tracks (R) and the magnetic field strength (B), the momentum (p) can relativistically be determined via

$$p\,[\text{GeV}] = 0.3 \cdot B\,[\text{T}] \cdot R\,[\text{m}]. \tag{3.4}$$

The ATLAS detector has two magnet systems [95]: the central solenoid around the ID and the large toroidal magnets for the muon spectrometer.

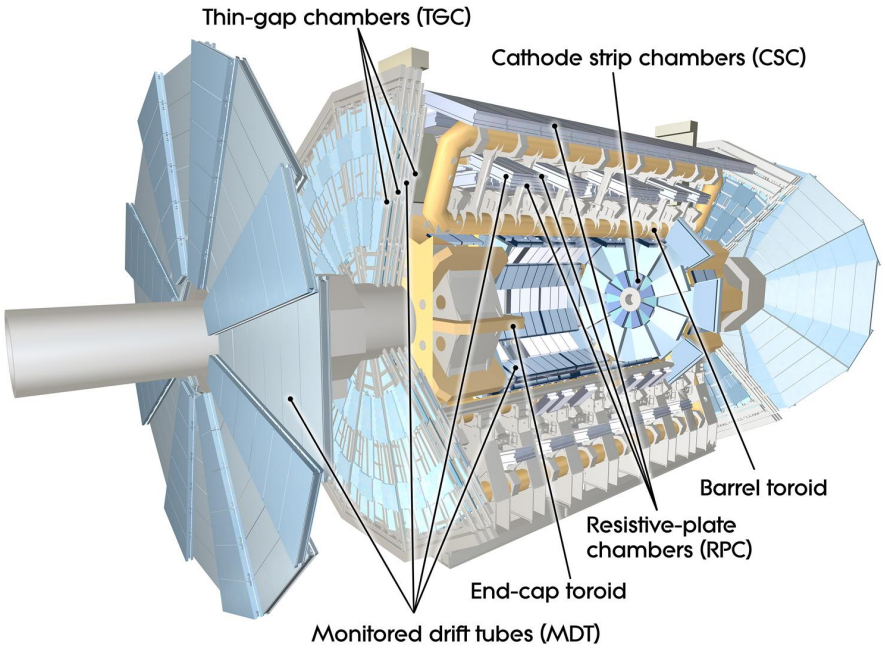

Figure 3.10: Image of the ATLAS muon spectrometer, showing the arrangement of the monitored drift tubes (MDTs), cathode strip chambers (CSCs), resistive plate chambers (RPCs), and thin gap chambers (TGCs) in the barrel and endcap regions of the detector [25].

The central solenoid surrounds the ID with its cylindrical structure. It has a length of 5.6 m and a remarkable thickness of only 4.5 cm, providing a homogeneous magnetic field of 2 T. Its field lines are parallel to the beam axis, as shown in Figure 3.11.

The ATLAS detector has a unique design in which the eight air-core toroid magnets used in the barrel region are separate structures, each 25.1 metres long. This distinctive design choice for the ATLAS detector gives the experiment its name. The corresponding smaller endcap magnet coils are enclosed in the same volume one at each end of the detector. The magnetic field strength varies between $0.5 - 1.0$ T and the field lines of the superconducting toroidal magnets are perpendicular to the beamline, as shown in Figure 3.11 [25].

3.2.5 Trigger

The ATLAS detector collects a large amount of data during its operation. With an LHC collision rate of 40 MHz, the data rate is about several terabytes per second. To handle this large amount of data, the ATLAS detector uses a trigger system to reduce the amount of data to be recorded and analysed [25]. The ATLAS trigger system consists of two levels: the Level-1 (L1) trigger and the high-level trigger (HLT) [97].

The L1 trigger [98] is a hardware-based system that selects events of interest, using information from the detector's calorimeters and muon chambers. It consists of custom electronics and firmware located in the ATLAS cavern, close to the detector. If an event passes the L1 trigger selection, it is accepted and forwarded to the next stage of the trigger system, the HLT. The L1 trigger reduces the event rate from the LHC's maximum

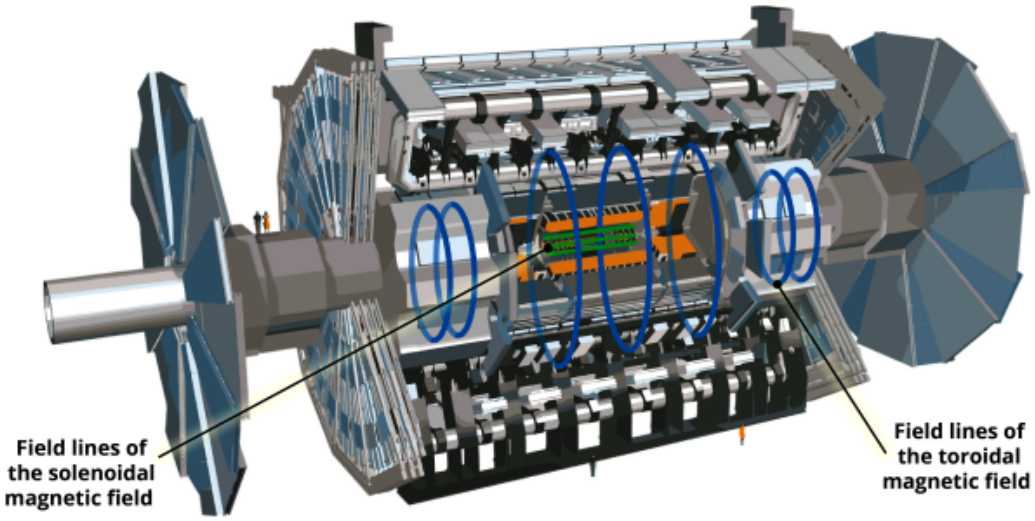

Figure 3.11: Magnetic field lines in the ATLAS detector, showing the strong magnetic fields produced by the central solenoid (green) and toroidal magnets (blue) in the barrel and endcap regions of the detector [96]. The field lines of the solenoid magnet are parallel to the beam pipe and are enclosed around the cylindrical volume of the magnet's structure, which can not be seen on this image.

of 40 million bunch crossings per second (40 MHz) down to about 100 000 events per second (100 kHz).

The HLT [99, 100] is a software-based system that further reduces the event rate to a manageable level for storage and analysis. The HLT consists of two trigger levels that use increasingly sophisticated algorithms to identify events of interest. The first HLT level, called L2, uses more advanced reconstruction algorithms than the L1 trigger to identify particles and measure their properties. The L2 trigger reconstructs tracks and clusters from the detector data, using more refined selection criteria than the L1 trigger. The second HLT level, called the Event Filter (EF), uses the full detector information to reconstruct all particles, including those missed by the L2 trigger. The EF trigger uses even stricter selection criteria to identify the most interesting events to save for further study. The HLT selection criteria are designed to identify events that have the potential to be interesting for physics analysis, such as events containing rare particles or phenomena. The selection criteria are based on the properties of the reconstructed particles, such as their energy, momentum and direction, and are optimised for different physics analyses. The HLT reduces the event rate to about 1 000 events per second for permanent storage, which corresponds to roughly 1 GB/s [101].

3.3 Particle and Event Reconstruction with ATLAS

The information from tracking, calorimeters and the muon spectrometer are combined, grouped, and reconstructed to identify particles and measure their properties. Figure 3.12 gives an overview of signatures for different particles.
Electrons, as charged particles, leave a track in the ID. The bending radius scales with their momentum, as explained in Section 3.2.4. Electrons lose energy via bremsstrahlung as they pass through the electromagnetic calorimeter. The through this process created photons undergo conversion into e^+e^- pairs after a mean free path of $9/7\,X_0$. The electrons emit further bremsstrahlung photons. This process continues building up a cascade of electrons, positrons and photons, until the energy of the electrons (positrons) is below the critical energy. This results in a remarkable energy deposition in the calorimeter, an electromagnetic shower.
Photons, as neutral particles, do not leave a trace in the inner detector. However, they interact in the electromagnetic calorimeter, producing an electron-positron pair which undergoes the same process as just described. An electromagnetic shower induced by electrons or positrons is built up, but without the associated trace in the inner detector.
Protons, as charged particles, will also leave a trace in the ID. They primarily interact in the hadronic calorimeter, where they deposit most of their energy within a hadronic shower. Similarly, neutrons leave a significant energy deposition in a hadronic shower, but do not show a trace in the ID. Muons leave a trace in the ID and pass through the calorimeters with minimal interaction due to their relatively large mass and the resulting low energy loss via bremsstrahlung. They are mainly detected in the outermost part of the detector, the muon spectrometer. Neutrinos interact very weakly and do not leave a directly detectable signal in the detector. However, they can be inferred by a missing transverse momentum calculation, which adds up the energy and momentum of all detected particles and finds an imbalance in the transverse plane.

The main physics objects used in the analyses discussed in this thesis are jets, electrons, muons and the missing transverse momentum. In general, physics analyses use two different categories of physics objects: objects defined with primary, loose "baseline" requirements, and objects with stricter "signal" criteria. Signal objects are defined to have a higher purity and are used to set selection criteria for events, while baseline objects are used for vetoing, where a good suppression of objects with lower reconstruction quality is targeted. An example is the R-parity-violating (RPV) multijet analysis with an all-hadronic final state, where signal jets are the main objects in the analysis. Therefore, the quality of the signal jets should be very high, introducing less systematic uncertainties. Baseline leptons are defined to set vetoes on those, in order to suppress as many leptons (with minimum selection criteria) as possible.
Another use case for baseline objects is the Overlap Removal (OR) procedure, which is performed to avoid double counting of objects found as candidates for different object categories. This procedure is introduced in Section 3.3.6.

3.3.1 Tracks and Vertices

To reconstruct tracks in ATLAS, an inside-out followed by outside-in strategy is used. First, tracks are "seeded" with hits from the innermost layers (PIX and SCT) by finding three distinct points in space. These candidates are then evaluated based on specific criteria such as momentum ($p_{\mathrm{T}} > 500\,\mathrm{MeV}$), centrality ($|\eta| < 2.5$), number of hits (at least seven silicon hits), shared modules (less than one), and "holes" (less than two silicon

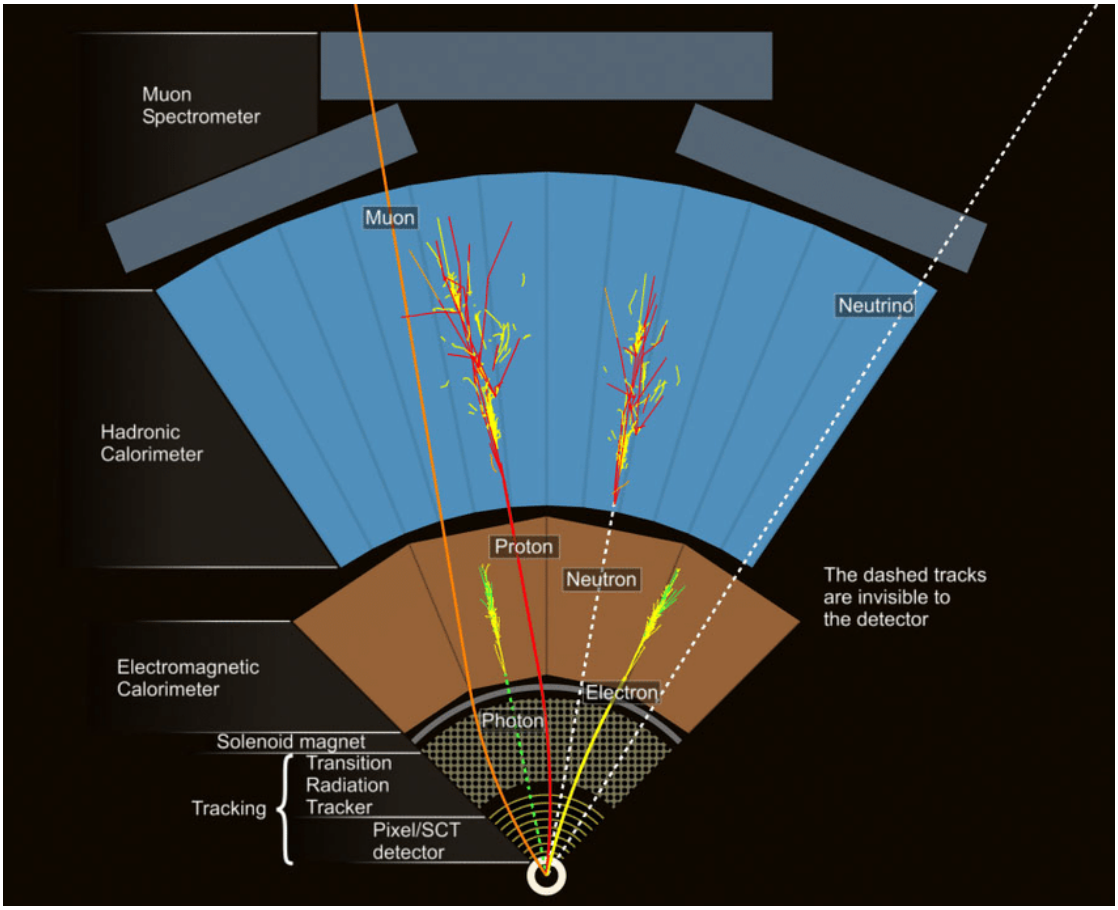

Figure 3.12: Schematic of the trajectories of common particles in the ATLAS detector. Charged particles such as electrons, protons and muons leave curved tracks in the ID volume. Neutral particles, such as photons and neutrons, do not leave any traces but can be identified by their decay in the calorimeters. Muons and neutrinos are the only particles known to leave the detector volume. Neutrinos can only be reconstructed as a missing transverse momentum track, as they do not interact with the detector material. Taken from [102].

holes). The track is then extended outwards and the projection is matched to hits in the TRT. The quality of the extension is assessed by the track fit and a track score [103, 104].

Following this, an outside-in tracking path reconstructs standalone TRT track segments seeded by the electromagnetic calorimeter. Potentially they are extended back into the silicon detectors by associating them with unused hits from the inside-out path. If no silicon hits can be assigned, the track is still kept and identified as a track from a converted photon. The combined outcome of these processes yields the final set of standard tracks [105, 106].

These reconstructed tracks are then used to identify vertices. Vertices are the locations at which the initial partons collide and new particles are produced. They are reconstructed through a two-step process. Firstly, a primary vertex finding algorithm associates the reconstructed tracks to vertex candidates. Secondly, a vertex fitting algorithm [107] determines the vertex position and its corresponding error matrix, while also refitting the

associated tracks to originate from the reconstructed interaction point. On average, 30 interactions per bunch crossing at the LHC were registered during data-taking in 2018. The vertex corresponding to the hardest process and is the vertex with the highest sum of transverse momenta, $\sum p_{\mathrm{T}}^2$, for its associated tracks. This vertex is called the Primary Vertex (PV). The remaining vertex candidates are considered to be pile-up vertices [106, 108]. Pile-up describes additional proton-proton collisions that occur during the same or nearby bunch crossings, and can complicate the event reconstruction process, see Section 4.2.

Secondary vertices may be produced from the decay of heavier particles produced in the collision. For example, a B-hadron, due to its relatively long lifetime before decaying, travels a short distance from the PV before decaying into other particles, creating a secondary vertex [109].

For each vertex, the longitudinal and transverse impact parameters, z_0 and d_0, represent the closest distances of a particle track to the vertex in the longitudinal and transverse directions respectively. Requirements on these parameters used for physics object definitions.

3.3.2 Jets

Quarks and gluons from high-energy collisions hadronise into traces of many baryons and mesons, which are generally detected as particle streams, referred to as *jets*.

The Particle Flow (PFlow) algorithm [110] attempts to provide a granular and detailed reconstruction of physics objects by using information from all the sub-detectors in the ATLAS detector. Rather than treating energy clusters independently, it uses information about individual particles to construct a more accurate representation of the objects. The key feature of PFlow objects is that it attempts to optimally assign the detected signals to the particles that produced them (the initial parton), leading to improved energy resolution for jets. Both analyses presented in this thesis use jets based on PFlow objects, which is the standard recommendation for physics analyses in ATLAS.

The Jet Energy Scale (JES) is calibrated from several effects, such as energy losses due to detector inefficiencies, pile-up from additional proton-proton interactions, and non-linear detector response. JES correction factors are derived and applied to adjust the jet energies accordingly, aiming for a more accurate representation of the true jet energy [111].

Once the PFlow objects, track-associated clusters, are reconstructed, the anti-k_t jet clustering algorithm [112] is applied to cluster these objects into jets, which is the standard jet reconstruction in ATLAS.
It is a sequential reconstruction algorithm that uses measures inversely proportional to the transverse momentum of the objects, k_t: the "hardness" of each object and the distance measure d_{iB}. In each iteration of the algorithm, all available measures$d_{i,j}$ and d_{iB} are calculated:

$$d_{i,j} = \min\left(k_{t_i}^{2p}, k_{t_j}^{2p}\right) \cdot \frac{\Delta R_{i,j}^2}{R^2} \tag{3.5}$$

$$d_{iB} = k_{t_i}^{2p} \tag{3.6}$$

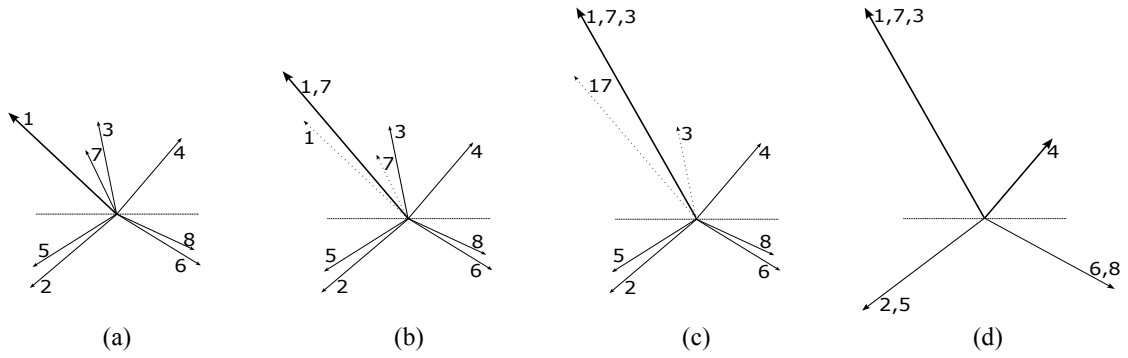

Figure 3.13: Steps of the anti-k_t jet reconstruction algorithm. The measures $d_{i,j}$ and d_{iB} are calculated for all objects in (a), whereas the distances to the objects 1 with highest momentum result in minimal values. Therefore, object 1 is combined with object 7 (b), which results in object 1,7. This is furthermore combined with object 3 into object 1,7,3 (c). There are no more objects within R, therefore 1,7,3 is a *jet*. This procedure is repeated until all objects are found to be in conglomerates whose minimal measure is d_{iB}, meaning they are isolated (d).

with R the cone radius defined in the algorithm, $p = -1.0$ specifically for the anti-k_t algorithm and the distance $\Delta R_{i,j}$ between objects i and j in the η-ϕ-plane,

$$\Delta R_{i,j} = \sqrt{\left(\eta_i - \eta_j\right)^2 + \left(\phi_i - \phi_j\right)^2}. \tag{3.7}$$

The principle of the algorithm is best illustrated with the example in Figure 3.13. For all $n = 8$ objects, the d_{iB} and $d_{i,j}$ are calculated and the minimum among all these measures is identified.
If the minimum is a distance measure $d_{i,j}$, the two objects i and j are combined into a "new" objects i, j and used in the next step of the iteration with $d_{(i,j)B}$ (as shown Figure 3.13(a) and (b) for the two objects 1 and 7 combined into 1,7).
If the minimum is a hardness measure, d_{iB}, it is identified as an isolated jet and removed from the list of remaining objects (combined objects), which are left for further iteration (shown for object 1,7,3 in Figure 3.13(c)). The algorithm continues until all objects (or jets) are isolated and no more candidates for potential combination are left, seen in Figure 3.13(d).
Figure 3.14 shows the comparison of jet shapes for four different jet-finding algorithms, all defined with different values for p in Eq. (3.5). The metric for the anti-k_t algorithm presented here favours clustering together objects with high transverse momentum p_{T} that are close to each other in the η-ϕ-plane, resulting in collimated jets. The final shape of an anti-k_t jet is a cone with radius R around the centre-of-mass of the combined jets. Standard ATLAS jets are defined as anti-k_t R=0.4 jets, while so-called "large-R jets" are reconstructed with R=1.0.

The presence of collinear and infrared divergences leads to infinities in the calculations of cross-sections. To avoid these divergences, cutoffs are introduced to regulate the calculations, such as requiring a minimum p_{T} for the objects that are included in a jet. However, the use of such cutoffs can lead to inconsistencies and dependence on the choice of cutoff parameter. The anti-k_t algorithm is designed to be infrared and collinear (IRC) safe, which means that it is less sensitive to the presence of low-energy particles or

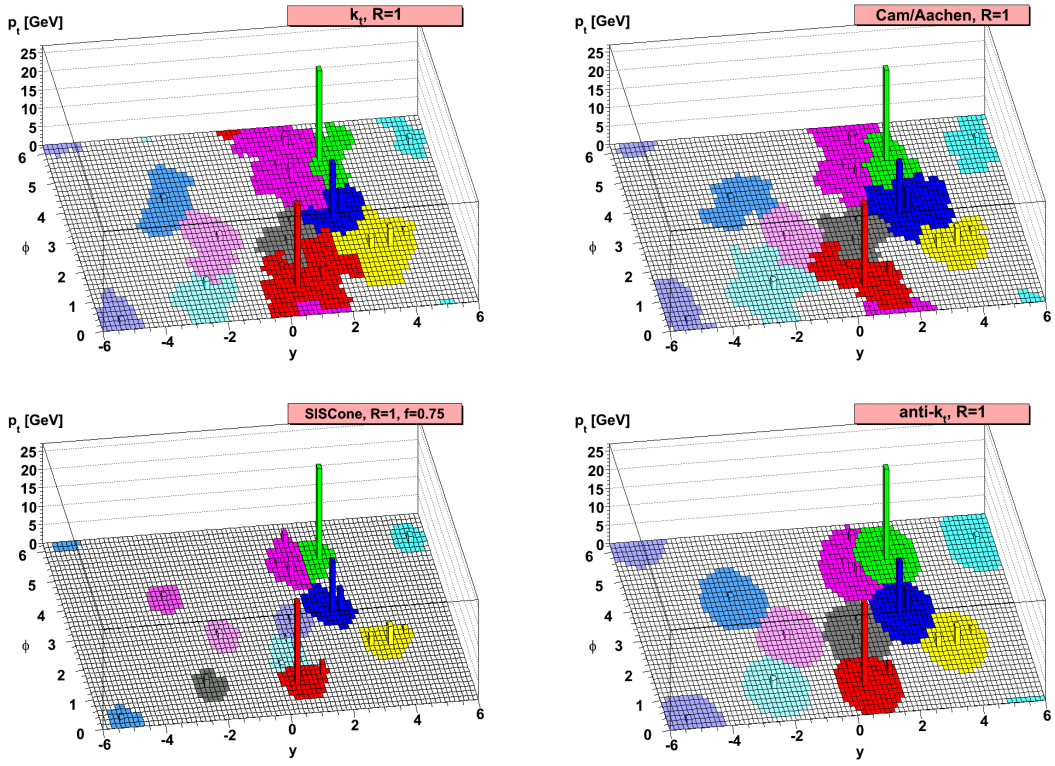

Figure 3.14: Comparison of final jet shapes in the y-ϕ plane for different jet-finding algorithms for a generated parton-level event. The z-axis shows the p_{T} of the particles in the event. The anti-k_t algorithm (bottom right) with $p = -1.0$ results in circular shaped jets centred around the hardest objects. The k_t algorithm (top left) defines $p = 1.0$, Cambridge/Aachen algorithm (top right) $p = 0$. Image taken from [112].

particles that are collinear with other particles. Because of the use of the distance metric, the algorithm is less likely to cluster together low-p_{T} particles with high-p_{T} particles, even if they are collinear, because the distance metric gives more weight to the p_{T} of the particles than to their total momentum. Additionally, the use of a distance parameter, R, in the algorithm allows for some control over the size of the jets and the degree to which low-energy particles are clustered together with high-energy particles.

Once the jets are reconstructed, the Jet Vertex Tagger (JVT) algorithm [113] is used to determine the compatibility of the jet with the primary collision vertex and to distinguish it from jets originating from pile-up interactions. The JVT discriminant is calculated based on track information and other parameters to assess the likelihood of the jet originating from the primary vertex. Jets failing the JVT criteria may be rejected or flagged as coming from pile-up interactions.

Both analyses presented in this work, use jets in their event selections. These jets are categorised as "baseline" if they satisfy $p_{\mathrm{T}} > 20\,\mathrm{GeV}$ and $|\eta| < 2.8$. In order to discriminate pile-up jets from those of the hard scatter, the JVT is applied. The jet is retained if JVT > 0.5 or it has $p_{\mathrm{T}} > 60\,\mathrm{GeV}$ or $|\eta| < 2.4$. These jets are then categorised as "signal" jets if they pass the overlap removal (OR) described in Section 3.3.6.
The RPV multijet analysis additionally requires its signal jets to have $p_{\mathrm{T}} > 50\,\mathrm{GeV}$.

b-tagged Jets

When a b-quark is produced in a collision, it hadronises and forms a B-hadron, which is a bound state of a b-quark and other lighter quarks. The B-hadron decays, but due to its relativistic Lorentz boost γ and "long" lifetime τ (around 1.5 ps [23]), the decay products, or daughter particles, can travel a significant distance d before decaying. For a B-hadron with a mass of $\sim 5\,\mathrm{GeV}$ and a momentum of 50 GeV, the distance can be approximated via

$$d = \beta\gamma c\tau \approx 4.5\,\mathrm{mm}.$$

This results in a jet with a secondary, displaced vertex, i.e., the point of origin of the jet is significantly displaced from the point of the initial proton-proton collision. Figure 3.15 gives an illustration how the PV and secondary vertex (SV) are related. Additionally, B-hadron induced jets often contain charged leptons, such as electrons or muons, due to the decay modes of B-hadrons. These distinct features allow for the application of algorithms to identify or "tag" these b-jets in the detector, a process known as b-tagging [114].

The jets used in the analysis presented here are identified as b-tagged with the DL1r algorithm [116]. It utilises a deep neural network architecture to process various input variables associated with a jet, such as impact parameters, secondary vertex information, and other discriminant variables. These variables are used to train the neural network to classify jets as b-tagged or non-b-tagged. The DL1r algorithm provides a discriminant output, which represents the likelihood that a jet contains a B-hadron. A higher value of the DL1r discriminant corresponds to a higher likelihood of the jet being b-tagged. In the analyses, jets are labelled as b-jets if they pass the "standard" 77% efficiency working point with $p_{\mathrm{T}} > 20\,\mathrm{GeV}$, $|\eta| < 2.5$ and satisfy the standard JVT requirements described above.

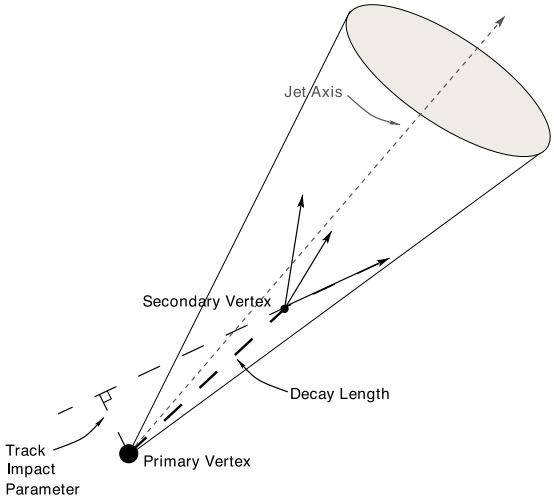

Figure 3.15: Illustration of displaced, secondary vertex. Relativistic, heavy flavour hadrons, such as B-hadrons, have a noticeable decay length in the order of a few mm before hadronising. This distance between the primary and secondary vertex can be measured and used to tag these jets as "b-jets". Image taken from [115].

3.3.3 Electrons

To reconstruct electron candidates, the tracks within the ID are associated with energy clusters in the ECAL. They can easily be identified by tracks originating from the PV and ending in a shower in the ECAL, as also discussed in Figure 3.12. "Baseline" electron candidates are reconstructed from an isolated electromagnetic calorimeter energy deposit matched to an ID track [117] and are required to possess $p_{\mathrm{T}} > 10\,\mathrm{GeV}$ and $|\eta| < 2.47$. They satisfy the loose likelihood-based identification criteria, referring to a set of selection requirements defined in likelihood-based algorithms, including the presence of hits in the innermost B-layer of the pixel detector and loose thresholds on shower shape and track-cluster matching variables, described in [117, 118]. The longitudinal impact parameter relative to the primary vertex is required to be $z_0 \sin\theta < 0.5\,\mathrm{mm}$. "Signal" electrons are additionally required to have $d_0/\sigma(d_0) < 0.5$, and satisfy stricter likelihood-based identification and isolation criteria.

3.3.4 Muons

Muons deposit a small fraction of their energy in all subsystems, but are known to be the only detectable particles that leave the detector volume. For their reconstruction, an ID track is matched with a MS track or segment [119]. An initial selection on "baseline" muons requires that they pass the "medium" track quality requirements, have $p_T > 10$ GeV, are within $|\eta| < 2.7$, and have $z_0 \sin(\theta) < 0.5\,\mathrm{mm}$ [120]. Adding additional, more stringent requirements to the muon selections defines the "signal" muons. These are required to satisfy isolation criterion as well as having $d_0/\sigma(d_0) < 3$ and satisfying $z_0 \sin(\theta) < 0.5\,\mathrm{mm}$ [120, 121].
The tbMET analysis uses signal and baseline leptons as described for the event selection, discussed in Section 6.2. The RPV multijet analysis uses only baseline leptons, with the criteria listed here,for vetoing them, see Section 6.2.

3.3.5 Missing Transverse Momentum

Missing transverse momentum represents the imbalance in the momentum in the transverse plane of the detector caused by undetected particles, particularly neutrinos or possibly BSM particles. While the missing transverse momentum vector is denoted $\vec{E}_{\mathrm{T}}^{\mathrm{miss}}$, its magnitude is commonly called "missing transverse energy", and denoted with $E_{\mathrm{T}}^{\mathrm{miss}}$. In this thesis, $E_{\mathrm{T}}^{\mathrm{miss}}$, describes the magnitude of the missing transverse momentum vector. The $E_{\mathrm{T}}^{\mathrm{miss}}$ is reconstructed in two distinct parts [122, 123]:

$$\vec{E}_{\mathrm{T}}^{\mathrm{miss}} = \underbrace{-\sum_{i \in \text{Hard Objects}} \vec{p}_{\mathrm{T}}^{\,i}}_{\vec{E}_{\mathrm{T}}^{\mathrm{miss,\,Hard}}} \underbrace{-\sum_{i \in \text{Soft Signals}} \vec{p}_{\mathrm{T}}^{\,i}}_{\vec{E}_{\mathrm{T}}^{\mathrm{miss,\,Soft}}} . \tag{3.8}$$

The first component corresponds to the contribution from well-defined and fully calibrated physics objects, known as hard objects, originating from the primary hard-scatter vertex. These hard objects include identified particles such as leptons and jets. The second component, referred to as the soft term, encompasses detector signals associated with the primary hard-scatter vertex but not attributed to any defined physics objects. The $E_{\mathrm{T}}^{\mathrm{miss}}$ is the magnitude of the $\mathbf{E}_{\mathrm{T}}^{\mathrm{miss}}$ vector, which is determined as the negative vector sum of these two components, representing the overall imbalance of transverse momentum in the event.

3.3.6 Overlap Removal

It can happen that an object is identified as two different physics objects. The overlap removal (OR) procedure ensures that each particle or physics object is uniquely assigned to a specific analysis object, avoiding duplicated or misleading measurements and is applied to baseline objects. It is a subsequent, analysis-specific procedure. Table 3.1 lists the steps for the "standard" and "b-jet aware" OR removals, which are used in the RPV multijet and $tb + E_{\mathrm{T}}^{\mathrm{miss}}$ analyses respectively.

Reject	Against	Criterium (standard)	Criterium (b-jet aware)
electron	electron	shared ID track, $p_T(1) < p_T(2)$	same
muon	electron	calo-muon and shared ID track	same
electron	muon	shared ID track	same
jet	electron	$\Delta R < 0.2$	$\Delta R < 0.2$ and not a b-jet
electron	jet	$\Delta R < 0.4$	same
jet	muon	NumTrack > 3 and (ghost-associated or $\Delta R < 0.2$)	NumTrack > 3 and (ghost-associated or $\Delta R < 0.2$) and not a b-jet
muon	jet	$\Delta R < 0.4$	same

Table 3.1: Sequential procedure for the overlap removal. Listed is the standard procedure, and the b-jet aware procedure, which sets additional requirements for rejecting b-tagged jets against other particles.

Chapter 4

Searches for Supersymmetry with ATLAS

This thesis describes two different searches for Supersymmetry (SUSY), which are based on the same Run 2 ATLAS data set.
The first analysis is focusing on the search for pair-produced, third-generation squarks, the superpartners of the top- and bottom-quarks, which decay into a $tb + E_{\mathrm{T}}^{\mathrm{miss}}$ final state.
The second analysis is looking for pair-produced massive gluinos, which decay via an R-parity-violating coupling into an all-hadronic final state with at least six jets.
While both searches target different signal models, they use the common analysis methods. These are described in the following sections before moving to the specifics of the two distinct searches.
The following sections describe the ATLAS Run 2 data set including the pile-up profile, the foundations of Monte Carlo (MC) event generation, the basic steps of an analysis strategy, as well as common statistical methods and the treatment of systematic uncertainties.

4.1 ATLAS Run 2 Data Set

The analyses discussed in this thesis use data from high-energy pp collisions at the LHC during Run 2, which took place between 2015 and 2018. The centre-of-mass energy of the collisions during this period was 13 TeV. The total amount of data, measured in terms of integrated luminosity, is 140 ± 1.2 fb^{-1}, as shown in Figure 3.5. The uncertainty in the combined 2015–2018 integrated luminosity is 0.83% [124], obtained using the LUCID-2 detector [125] for the primary luminosity measurements, complemented by measurements with the ID and calorimeters.

The value of 140 fb^{-1}corresponds to the standard "AllGood" physics good run list (GRL). This list contains all the luminosity blocks of each data-taking period where the detector was fully operational and the data was taken with high efficiency, so that the data meets the imposed data quality requirements for physics analyses.

4.2 Pile-up and Underlying Events

In the high-intensity environment of the LHC, multiple proton-proton collisions occur within a single bunch crossing, leading to what is known as *pile-up*. A single event can contain particles from several interactions, not just the one interaction of interest, the so-called "hard-scatter" event. Depending on the settings of the LHC, the average number

of collisions per bunch crossing, $\langle\mu\rangle$, varies. It is calculated for each bunch separately via

$$\mu = L_{\text{bunch}} \times \frac{\sigma_{\text{inel}}}{f_{\text{Rev}}}, \tag{4.1}$$

with the instantaneous luminosity per bunch L_{bunch}, the revolution frequency of the LHC f_{Rev}, and the cross-section for inelastic scattering σ_{inel}. The cross-section for inelastic pp collisions at a centre-of-mass energy of several TeV is around 100 mb. This is nine orders of magnitude more than the total Higgs production cross-section, shown in Figure 2.4. The average number of interactions per bunch crossing was measured to be 33.7, for the total data-taking period of Run 2, which is shown in Figure 4.1 along with the different pile-up profiles corresponding to the individual years of the data-taking period.

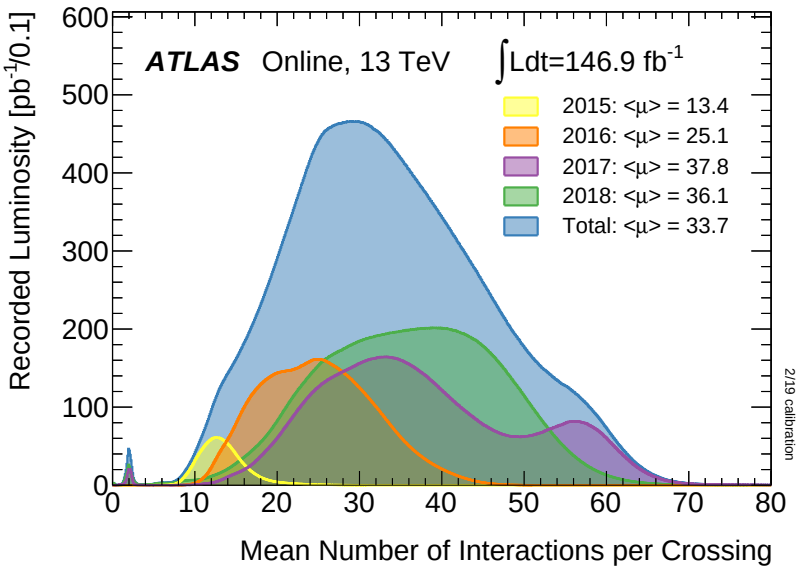

Figure 4.1: Average number of interactions per bunch crossing in the ATLAS detector for the different years during the Run 2 data-taking period [126].

The *underlying event*, on the other hand, refers to the rest of the pp collision that is not part of the hard-scattering process. Even though the hard scatter - involving only a pair of partons - is the primary focus of an analysis, the remaining partons in the proton do not simply disappear. They interact via the strong force, leading to additional particle production that forms the low p_{T} underlying event.

These additional interactions can add significant complexity to the data, as particles from pile-up and underlying events can be superimposed on the particles of interest from the hard interaction.

4.3 MC Event Generation

The analysis of the LHC data is based on Monte Carlo (MC) event generators, simulating pp collisions. MC event generators are advanced computational tools employing stochastic techniques to simulate the chain of processes occurring in particle collisions. These MC simulations are used to study kinematics of BSM signal models, and estimate the SM background contributions. The entire process is simulated, starting from the initial

interaction of two partons until the cascades of particles produced in the hadronisation process. The generated events are then propagated through a detector response simulation, followed by their digitalisation, detection, and reconstruction, which is outlined in the following.

The process of MC event generation begins with the calculation of the matrix element for the hard scattering event, determining the production cross-sections for a given process. To perform this calculation, parton distribution functions (PDFs), which describe the likelihood of finding a specific type of parton carrying a particular fraction (the Bjorken scale x) of the proton's momentum, are taken into account additionally. Figure 4.2 shows the PDFs for two different negative four-momentum-transfer squared (Q^2) of the proton at next-to-next-to-leading (NNLO) order [127]. From these distributions one can infer that parton interactions including one or two gluons have the highest probabilities at low Bjorken-x. The choice of PDF is considered as an important source of systematic uncertainties, which are discussed in Section 4.6.

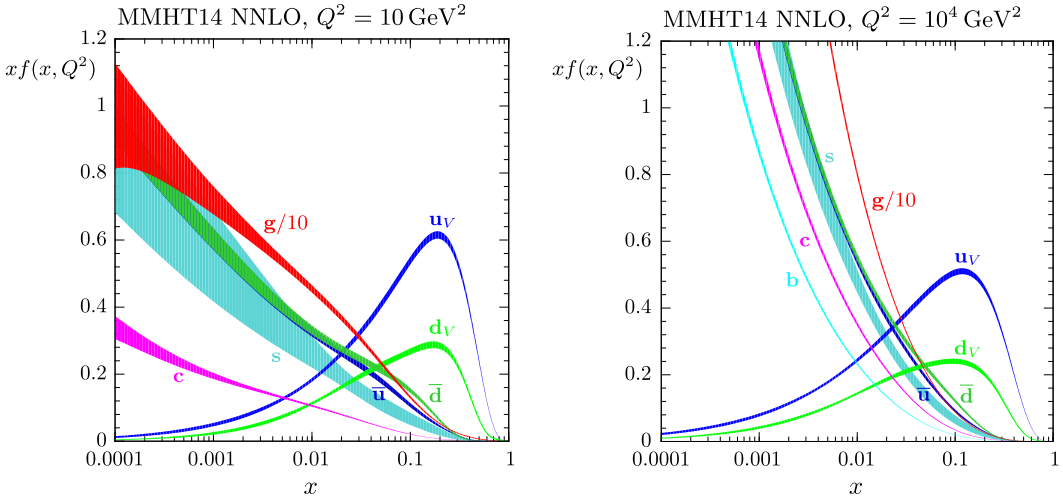

Figure 4.2: Parton distribution function for partons of a proton with a low negative four-momentum-transfer squared, $Q^1 = 10^2\,\text{GeV}^2$ (left) and a high Q^2 of $10^4\,\text{GeV}$ [127]. The functions represent the probability for certain types of partons to carry a certain fraction of the proton's momentum, described by the Bjorken-x, given Q^2.

Following the hard scattering event, the process of parton showering (PS) begins. It describes the evolution of the initial partons into a cascade of lower-energy partons, the soft emission and splitting of gluons and quarks. The phenomenon is described by the Dokshitzer-Gribov-Lipatov-Altarelli-Parisi (DGLAP) equations [128–130], describing strong processes such as $q \to qg$ and $g \to qq$, which are taken into account by MC techniques in the PS event generators. The process continues until the energy scale of the partons is low enough that non-perturbative effects become important. A related type of emission is the hard initial state (ISR) and final state radiation (FSR) of gluons and quarks, depending whether the radiation is emitted before or after the hard scatter process.

At this non-perturbative or confinement scale, partons are bound into observable particles such as protons, neutrons, pions, kaons, etc., a process known as hadronisation. As discussed in Section 2.1.2, QCD does not allow free partons. Therefore, the parton showers must eventually hadronise into colour-neutral particles.

Figure 4.3 illustrates all stages of MC event generation. The central blue lines show the initial partons of two colliding protons (green). The big, red circle marks the hard scatter process where in this case two gluons interact and produce a $t\bar{t}$ pair and a Higgs boson (red dashed line), which are all marked as smaller red circles. The PS is shown as red quark and gluon lines and the final hadronisation process is represented by the green lines and blobs. The yellow lines mark electromagnetic emission, which can be radiated off by any charged particles or - as in in this specific event shown - be the final decay product of one constituent of the event (here, one top-quark decays into a leptonically decaying W boson). The purple lines are the previously discussed underlying event, where other partons from the proton interact with each other.

Typically the whole generation of a physics process can be split into two types of MC event generation:

- MC generators allow for **matrix element calculations** of the hard-scatter with high precision, like next-to-next-to-next-to-leading order (NNNLO) for certain processes, including ISR/FSR.
- As discussed in Section 2.1.2, QCD phenomena such as **parton showering and hadronisation**, but also pile-up, can not be computed perturbatively, therefore additional generators with phenomenological approaches are used to mimic the evolution of the physics processes [131].

Some generators (for example Sherpa [132]) can do both, whereas others (e.g. Powheg [133, 134]) are interfaced specifically with dedicated Parton Shower algorithms (e.g. Pythia [135]). In cases where different generators are combined, the phase space between the matrix element and parton shower calculations needs to be matched to ensure there's no double-counting. This process is done by so-called matching algorithms.

Finally, the generated events are passed through a detailed **detector simulation**, GEANT4, taking into account the geometry and materials of the detector and the response to different particles interacting with the detector material [136].
After digitisation of the detector responses, the MC samples are stored in the same format as data and can be treated identically, except that the MC samples contain the so-called "truth" information of the particles which were generated in the event [131]. The truth information describes the properties of the simulated particles at the generator level, before they undergo any detector effects or reconstruction procedures. It includes various attributes of the particles such as their type (ID), momentum, energy, and direction (in η and ϕ). Usually, it also includes the full decay history, indicating which particles are the parents and listing all children in each decay process.
This truth information is of importance for example in the RPV multijet analysis, where reconstructed jets are matched with the truth quark originating from a supersymmetric particle. This is discussed in detail in Section 6.4.1.
Additionally, the generation of the simulated event samples includes the effect of multiple pp interactions per bunch crossing, as well as the effect on the detector response due to interactions from bunch crossings before or after the one containing the hard interaction. For the two specific analyses, the nominal MC generators used are listed in Table 4.1 for background and signal samples.

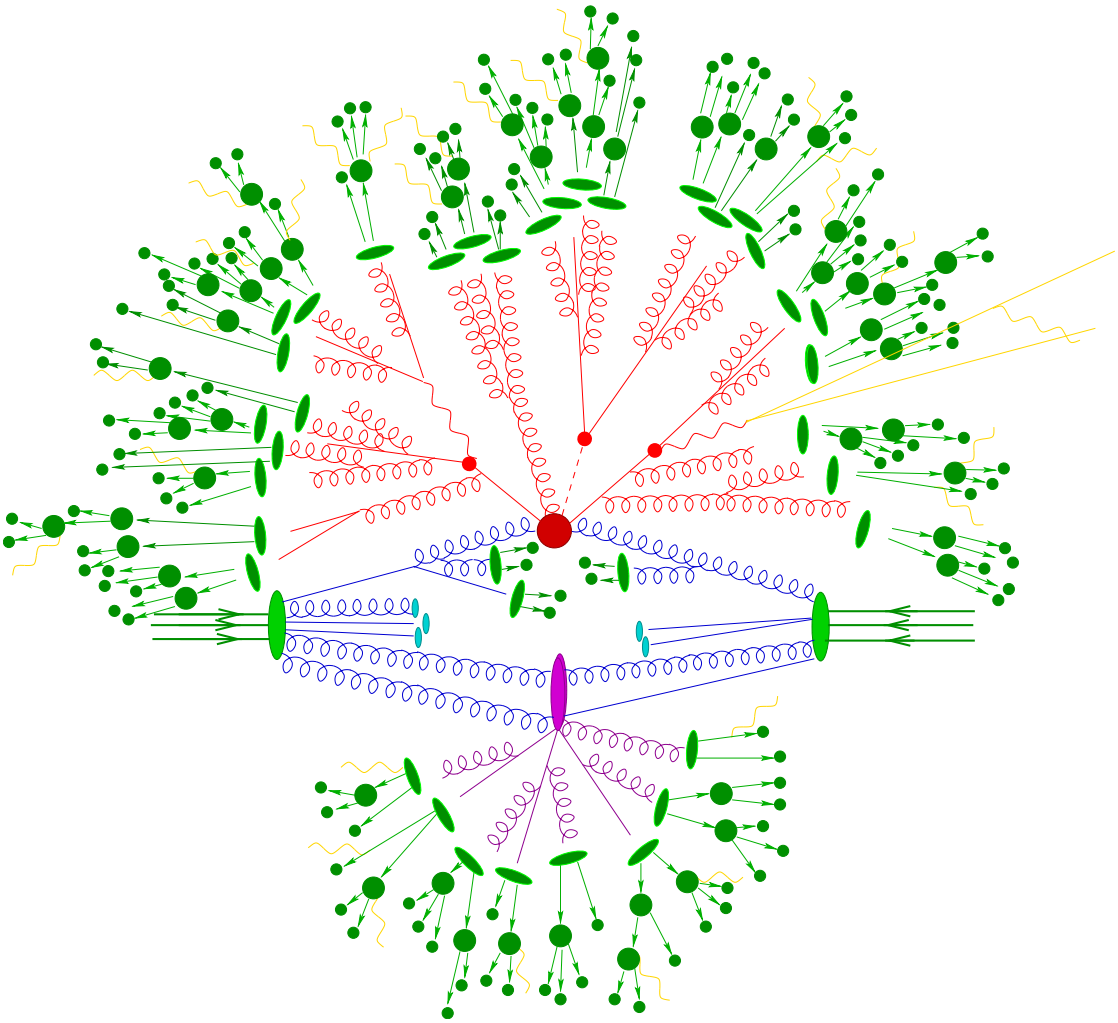

Figure 4.3: Steps of MC event generators colour coded: the hard scatter process is marked by the red dot, which is initiated by two gluons from the proton. All initial partons are blue. The two gluons produce a $t\bar{t}H$ event. All particles emit final state radiation (red). Once all particles fall below an energy threshold, hadronisation starts (green lines). The purple lines show an underlying event between two partons of the same proton, which also hadronise. Schematic taken from [132].

Physics Process	ME Event generator	Parton shower and hadronisation	PDF set	UE tune	Cross-section normalisation
$tb + E_{\mathrm{T}}^{\mathrm{miss}}$ signals	MadGraph5_aMC@NLO [137]	Pythia8 [138]	NNPDF2.3LO [139]	A14 [140]	NNLO+NNLL [141–147]
RPVMJ signals	MadGraph5_aMC@NLO	Pythia8	NNPDF2.3LO	A14	NNLO+NNLL
$t\bar{t}$	Powheg-Box [v2] [133, 134, 148, 149]	Pythia [8.230] [135]	NNPDF3.0NLO [150]	A14	NNLO+NNLL
Single top	Powheg-Box [v2]	Pythia [8.230]	NNPDF3.0LO	A14	NNLL [151, 152]
$t\bar{t} + Z/W$	MadGraph5_aMC@NLO	Pythia [8.210] [135]	NNPDF3.0NLO	A14	NLO [153]
W/Z+jets	Sherpa [2.2.1] [154]	Sherpa [155]	NNPDF3.0NLO	Sherpa default	NNLO [156]
Diboson	Sherpa [2.2.1]-[2.2.2] [154]	Sherpa	NNPDF3.0NLO	Sherpa default	NLO
W/Z	Sherpa [2.2.1]	Sherpa	NNPDF3.0NLO	Sherpa default	NNLO [157]
Dijets	Pythia [8.230]	Pythia [8.230]	NNPDF2.3LO	A14	LO

Table 4.1: Overview of the nominal signal and simulated background samples for the $tb + E_{\mathrm{T}}^{\mathrm{miss}}$ and RPV multijet analyses.

4.4 Analysis Strategy

The typical analysis strategy for searches involves the definition of control, validation, and signal regions (CR, VR, SR).
SRs are defined using only MC simulated background and signal samples. The SR, as the name suggests, are regions in the phase space of observed variables, which contain high numbers of signal events, while the SM background events are suppressed. Combinations of selections on discriminating variables are considered and iteratively improved. These regions are typically optimised such that a maximal significance Z_0 is observed, which is a measure of the excess of signal events above the expected SM background [158]. The higher the significance, the better the signal to background ratio is. Figure 4.4 shows an illustration of what an idealised discriminating variable would look like. The optimal selection within the region towards the right of the arrow is found with the significance for different selection values on an arbitrary variable, "Variable 1". No data is used to avoid biasing the selections, the analysis is "blinded".

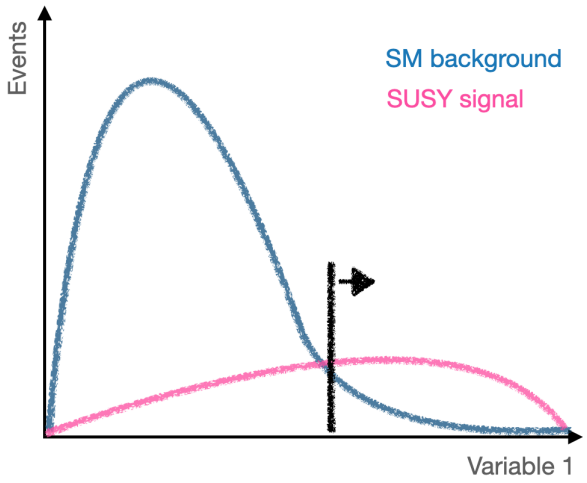

Figure 4.4: Illustration showing an example for an idealised discriminating variable to separate background from signal.

CRs with low signal contamination are defined to compare the MC modelling of the dominant SM processes in the SRs with data. Following this, VRs, which are kinematically closer to the SRs than the CRs, are used to validate the background extrapolation from the prediction in the CR to the SR. Once the results of the background estimation method are satisfying, the SR selections are applied to data - the analysis is unblinded.

SUSY searches are targeting a certain model with varying parameters, such as the masses of the SUSY particles. This may result in kinematic differences over the range of different mass regions. The range of SUSY particle's masses which are investigated in a search is called a "search grid". SUSY searches typically define more than one SR to target specific kinematic regions of the signal under investigation.

Once the SRs are optimised, the background composition is probed. In order to estimate how well the dominant background processes are modelled by MC, CRs are defined. These are enriched in the type of background they are targeting and low in signal contamination. While being close enough to probe the background in similar kinematic conditions, the

CRs are orthogonal to the SR. Orthogonal here means that the two regions are defined in two non-overlapping regions of the phase space of the considered variables. The orthogonality is necessary in order to include both regions in a final fit, described in Section 4.5. Figure 4.5 shows an illustration how SR, CR and VR could be located in a 2D plane with two arbitrary variables.

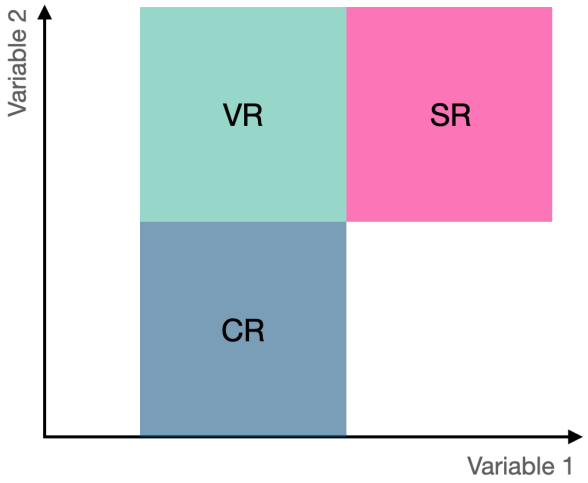

Figure 4.5: Illustration showing potential CR, VR, and SR in a 2D phase space of two arbitrary variables. All regions are orthogonal.

From the CR, a scaling factor μ_i can be extracted for the expected number of background events of type i in the SR, $N_{\mathrm{SR}}^{\mathrm{ex},i}$, via

$$N_{\mathrm{SR}}^{\mathrm{ex},i} = \frac{N_{\mathrm{CR}}^{i}}{\mathrm{MC}_{\mathrm{CR}}^{i}} \cdot \mathrm{MC}_{\mathrm{SR}}^{i}, \tag{4.2}$$

$$= \mu_i \cdot \mathrm{MC}_{\mathrm{SR}}^{i}, \tag{4.3}$$

with the number of background events of type i in the CR predicted by Monte Carlo, $\mathrm{MC}_{\mathrm{CR}}^{i}$, and observed in data, N_{CR}^{i}, as well as predicted in the SR in MC, $\mathrm{MC}_{\mathrm{SR}}^{i}$. These scaling factors are extracted from a background-only fit of MC to data in the CRs, as discussed in Section 4.5.

VRs are defined to validate the prediction of the background contamination in the SRs. Typically, VRs are kinematically in-between CRs and SRs. All CR and SR are required to be orthogonal, if they are subject to the same likelihood fit.

4.5 Statistical Analysis

To statistically analyse and interpret the results of the two searches presented in this thesis, the HistFitter framework is used [159]. The framework performs profile likelihood fits using the expected numbers of events from MC in the CR and SR, the observed events in data, and the systematic uncertainties, which are described in Section 4.6.

For this, the likelihood function $L(n, \theta^0 | \mu_{\mathrm{sig}}, b, \theta)$, describing the probability of observing a particular dataset given a set of model parameters, is built. This function is the product

of three terms [159]:

$$L(n, \theta^0|\mu_{\text{sig}}, b, \theta) = \mathcal{P}_{\text{SR}} \times \mathcal{P}_{\text{CR}} \times \mathcal{C}_{\text{syst}} \tag{4.4}$$

$$= P(n_S|\lambda_S(\mu_{\text{sig}}, b, \theta)) \times \prod_{i \in CR} P(n_i|\lambda_i(\mu_{\text{sig}}, b, \theta)) \times C_{\text{syst}}(\theta^0, \theta), \tag{4.5}$$

with the Poisson probability $\mathcal{P}_{\text{SR}}$ of observing n_S events in the signal region given an expectation value λ_S, which depends on the signal strength μ_{sig}, expected background contribution b, and nuisance parameters θ. The product over all Poisson probabilities $\mathcal{P}_{\text{CR}}$ of observing n_i events given Poisson expectation values λ_i in the CR i also dependent on μ_{sig}, b, and θ. The Gaussian constraint term, $\mathcal{C}_{\text{syst}}$, quantifies the deviation of θ from its nominal values θ^0 encapsulating systematic uncertainties [160], which are typically defined as Gaussians with θ^0 set to zero [159].

The model parameters include the signal strength (μ_{sig}), which represents the number of SUSY events, the background rate (b), and the nuisance parameters (θ), which account for systematic uncertainties. These parameters are fitted to maximise the likelihood function (or equivalently minimise -ln($L(n, \theta^0|\mu_{\text{sig}}, b, \theta)$), according to the Neyman-Pearson lemma), providing the best fit to the observed data [161]. Additionally, the fit provides a measure of the uncertainty on these parameters, taking into account both the statistical uncertainties and the systematic uncertainties captured by the nuisance parameters.

Two types of fits are usually performed: a *background-only fit* and a *signal + background fit*. In the background-only fit, the signal strength is set to zero ($\mu_{\text{sig}} = 0$), assuming that there are no SUSY events. This fit yields the parameters that best describe the background contributions to the data, serving as a baseline expectation in the absence of new physics. It only takes information from the CRs and fits the scaling factors μ_i from Eq. (4.2) for specific SM backgrounds i. The scaling factors are used to predict the number of background events in the SR, which is first validated in the VR.

The signal+background fit allows for a non-zero signal strength. This fit adjusts all parameters, including the signal strength, to achieve the best agreement between the model and the data. The signal+background fit can be *model-dependent* or *model-independent.*
In a model-dependent fit, a specific theoretical model for the signal is assumed, such as a specific SUSY model, and the fit adjusts the parameters of this specific model along with the background parameters. Depending whether the background-only fit concluded with an excess or not, the model-dependent fit can be used to either measure the signal strength μ_{sig} or use the results to set exclusion limits on the model under consideration. In contrast, a model-independent fit does not assume a specific signal model. Instead, it looks for a general excess of events above the estimated background without specifying a particular shape or rate for the signal.

4.6 Systematic Uncertainties

There are two types of systematic uncertainties which are important in the statistical interpretation: theoretical uncertainties, arising from modelling of physics processes, and uncertainties originating from the experimental setup: the detector.
Theoretical modelling uncertainties in SUSY searches at the LHC origin from various sources, such as

- Uncertainties related to the choice of parton distribution functions, as discussed in Section 4.3.
- The modelling of initial and final state radiation, depending on the choice of the strong coupling constant (α_S).
- Variations of the QCD scales, which are introduced in the theoretical calculations to regulate the behaviour of the strong force at short distances (renormalisation scale μ_R) and to separate the contributions from short-distance and long-distance physics (factorization scale, μ_F).
- The scale at which matrix element matching between the scale of the matrix element generation and PS are calculated respectively.
- The subtraction method for interference terms, such as $t\bar{t}$ in the single-top processes, which is explained in more detail in Section 5.4.

Typically, these modelling systematics are estimated by comparing results obtained using different MC generators or different settings of the same generator. For each source of systematic uncertainty, weights are introduced to scale the simulated events up and down, usually within one standard deviation around their mean value θ^0, as introduced in Eq. (4.4). These weights are then propagated through the analysis to evaluate their impact on the final result. In the fit, these systematic uncertainties are treated as nuisance parameters and are adjusted to maximise the likelihood, taking into account the constraints from control regions.
Experimental systematic uncertainties originate from the limitations and characteristics of the experimental process and the detector. Among these are

- Jet Energy Scale (JES) and Jet Energy Resolution (JER) uncertainties, which are connected to the calibration and resolution of jets in the detector. The measured energy of a jet may differ from its true energy. The JES is a correction applied to each jet to account for this, and the JES uncertainty reflects the limited knowledge of this correction. Similarly, the JER is a measure of the detector's ability to measure the jet energy precisely, and the JER uncertainty accounts for possible inaccuracies in this measurement [111, 162].
- Systematics introduced from the Jet Vertex Tagger, discussed in Section 3.3.2. These take into account the efficiency to correctly identify jets from the primary interaction and reject those from pile-up, as well as uncertainties in the rate of falsely tagging a primary jet as a pile-up jet (the "mistag" rate).
- Soft term contributions to E_T^{miss} from low-momentum objects, that might not be associated with any reconstructed object. These introduce uncertainties to the overall missing transverse momentum calculation.
- Lepton efficiency uncertainties, coming from various factors, including trigger

efficiency, reconstruction algorithms, energy calibration, and particle identification algorithms.

- The b-tagging related uncertainties. The results of the b-tagging algorithm can vary between data and simulation, leading to systematic uncertainties in terms of efficiency and miss-tagging rate [163].
- The level of pile-up can vary from event to event and uncertainties in its modelling can affect the reconstructed objects and event selection.Therefore, a re-weighting of the MC events to the data is included as systematic uncertainty.
- The luminosity uncertainty, which directly impacts the calculation of production cross-sections and is discussed in Section 4.1.

These detector-related systematic uncertainties are included as Gaussian distributed nuisance parameters in the likelihood function, Eq. (4.4), and their impact on the final results is assessed as part of the statistical interpretation. Reducing the impact of systematic uncertainties is one of the key components of precision measurements with the ATLAS detector. For searches which expect low numbers of signal events, statistical uncertainties play a large role. The two searches summarised in the next two chapters include the systematic uncertainties described above.

Chapter 5

Search for Third-generation Squarks

This chapter describes the full Run 2 $tb + E_{\mathrm{T}}^{\mathrm{miss}}$ analysis, searching for pair-produced, third-generation squarks decaying into a top-quark, a bottom-quark and $E_{\mathrm{T}}^{\mathrm{miss}}$ from the undetectable SUSY particles, as shown in Figure 5.1. From the work presented here, my main contributions include:

- the Signal Region B definition and optimisation
- the studies with different single-top MC samples, validating DR vs. DS
- the setup of statistical framework, fit and interpretation

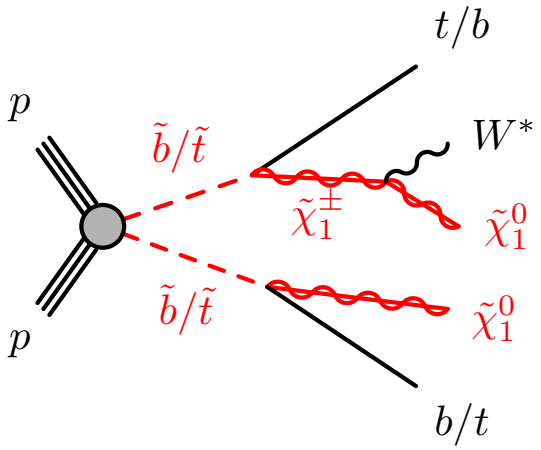

Figure 5.1: Asymmetric top-/bottom-squark decay into $E_{\mathrm{T}}^{\mathrm{miss}}$, top-, and a b-quark from the undetectable $\tilde{\chi}_1^0$. One leg of the decay is a cascade decay via an intermediate $\tilde{\chi}_1^{\pm}$.

As shown in Figure 5.2, this asymmetric signature has already been studied with data from Run 1 at $\sqrt{s} = 8\,\mathrm{TeV}$ [164] as well as early data from Run 2 at $\sqrt{s} = 13\,\mathrm{TeV}$ corresponding to $36.1\,\mathrm{fb}^{-1}$ [34]. As can be seen from the exclusion curve, especially the one-lepton (1L) final state from the top decay leaves uncovered corridors in the region where the $\tilde{\chi}_1^0$ and $\tilde{b}/\tilde{t}$ masses are close - the so-called "compressed" mass region. This region is located below the diagonal line indicating the minimal kinematically allowed mass difference corresponding to the top-quark mass, 175 GeV.
The $tb + E_{\mathrm{T}}^{\mathrm{miss}}$ 1L signature has been excluded for all mass points below the pink line in the 2D plane for the neutralino and sbottom masses, up to $m(\tilde{b}_1) = 825\,\mathrm{GeV}$ for $m(\tilde{\chi}_1^0) = 100\,\mathrm{GeV}$. The previous analysis had very little exclusion power in the

compressed region. Therefore, there is a strong motivation to perform an analysis with two dedicated regions for the compressed and bulk regions to improve the detection potential of the signal search; as discussed here.

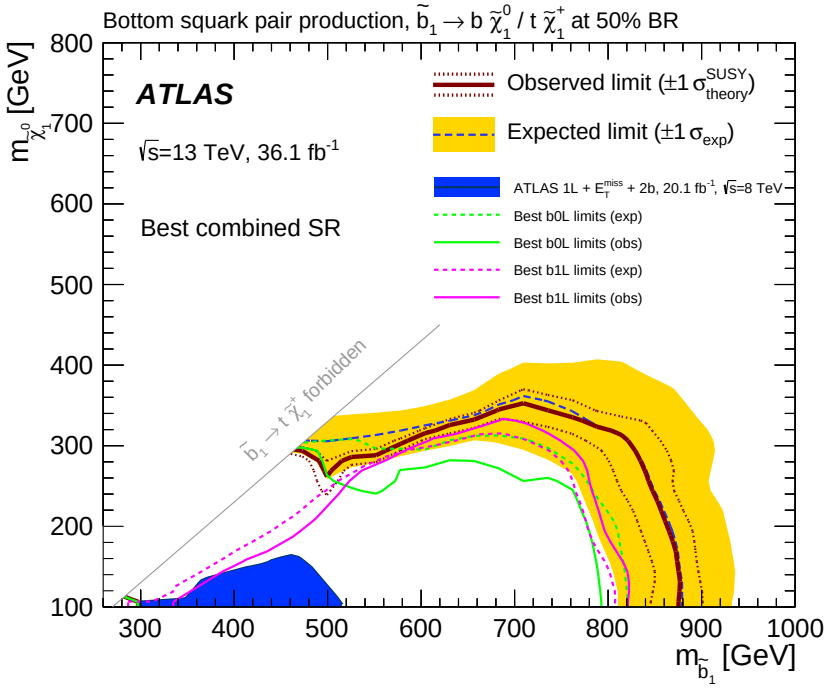

Figure 5.2: Exclusion contour from the early Run 2 $tb + E_{\mathrm{T}}^{\mathrm{miss}}$ analysis using 36.1 fb^{-1}data [34]. Shown are the two exclusion curves for the 1L and zero-lepton (0L) channels, as well as the combination of both. For comparison, the figure also shows the Run 1 exclusion, using 20.1 fb^{-1}of data at $\sqrt{s} = 8$ TeV [34].

The main SM background processes, which can result in the same or a similar final state, include $t\bar{t}$ production, single-top production, production of a W boson in association with jets (W+jets), and the $t\bar{t}$ production with a Z or W boson ($t\bar{t}Z$, $t\bar{t}W$), as well as diboson production. Other processes, which are combined in the category "Others" include processes such as $t\bar{t}$ production with a Higgs boson associated ($t\bar{t}H$), Z boson in association with jets (Z+jets), rare top processes (tZ and tWZ production), Higgs production, and dijet production. These processes do not individually contribute significantly in this search.

The $t\bar{t}$ process has, among all background processes relevant for this work, one of the highest production cross-section at the LHC. For a $tb + E_{\mathrm{T}}^{\mathrm{miss}}$ final state with 2 b-quarks, one lepton, and missing transverse momentum, one top-quark needs to decay hadronically, the other leptonically, which is called a semi-leptonic top decay.
The single-top production combines three different processes as shown in Figure 5.3. The t-channel process in Figure 5.3(b) is highly suppressed when requiring two b-jets in the final state because the proton's PDF predicts low probability of two third-generation quarks from the initial proton's interacting with each other as can be seen in Figure 4.2. Therefore, mostly the s-channel and Wt production contribute to the single-top SM background [165]. The Wt process needs to be corrected for $t\bar{t}$ interferences, for which a dedicated study is presented in Section 5.4.
Another process, which is relevant for this analysis is the $t\bar{t}$ production with an associated

Z boson, decaying invisibly into two neutrinos.
For those three main backgrounds, dedicated control regions are defined to estimate their contribution in the signal regions.

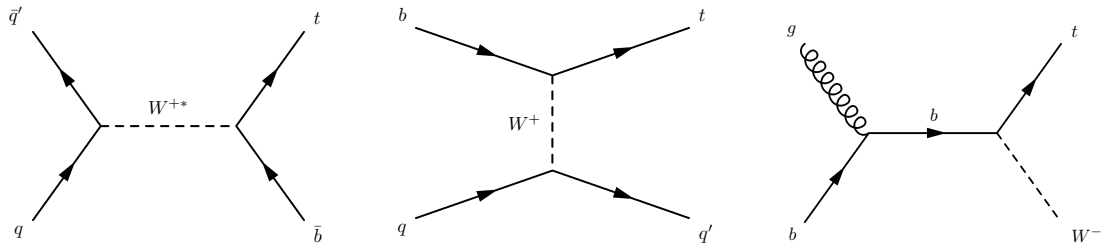

(a) s-channel (b) t-channel (c) Wt production

Figure 5.3: Production processes for-single-top.

After introducing and motivating the signal phenomenology in the next section, the analysis strategy is outlined in Section 5.2, including the signal region definitions, background estimation, and interpretation of statistical fit results.

5.1 Signal Phenomenology

The analysis focuses on the production of top- and bottom-squarks, the SUSY partners of the top- and bottom-quarks. These supersymmetric particles are mainly produced by strong interactions via direct production or by the decay of a gluino pair. The production cross-sections for both third-generation squarks are comparable, indicating similar production rates in high-energy proton-proton collisions.
This analysis is looking for squark decays into a neutralino and a top- or bottom-quark,

$$\tilde{t} \to t + \tilde{\chi}_1^0, \ \tilde{b} \to b + \tilde{\chi}_1^0, \tag{5.1}$$

or into a chargino and a bottom or top-quark,

$$\tilde{t} \to b + \tilde{\chi}_1^\pm, \ \tilde{b} \to t + \tilde{\chi}_1^\pm. \tag{5.2}$$

In the latter decay mode, the chargino further decays into an off-shell W^* boson and a neutralino,

$$\tilde{\chi}_1^\pm \to \tilde{\chi}_1^0 + W^*. \tag{5.3}$$

In this simplified model we set a fixed mass difference of 1 GeV between the chargino and the neutralino. This assumption is motivated by models in which the chargino and neutralino are wino-like, and therefore nearly degenerate in mass. Due to the small mass difference, the resulting W^* boson as a decay product is very soft and therefore basically undetectable. Despite the small chargino-neutralino mass difference, the mass difference between the top-/bottom-squarks and neutralino can be much larger, and is considered "compressed" if it is small enough to make the detection of the decay products challenging.

Of particular interest is the "asymmetric decay" scenario, where the two top-/bottom-squarks decay differently. The two decays in Eq. (5.1) and Eq. (5.2) are assumed to have the same branching ratio of 50%. Thus, in 50% of the events the top-/bottom-squark pair

decays asymmetrically. Events where the sparticle pair decays exclusively via Eq. (5.1) ($bb + E_{\mathrm{T}}^{\mathrm{miss}}$) or Eq. (5.2) ($tt + E_{\mathrm{T}}^{\mathrm{miss}}$) account for 25% of all events for each of the two cases. These symmetric decays are not the focus of the analysis I present here.

The $tb + E_{\mathrm{T}}^{\mathrm{miss}}$ final state is historically further divided by the decay channels of the top-quark into the 0L channel for hadronically decaying tops and the 1L channel for leptonic top decays. This analysis focuses on the 1L channel, for which the final state consists of one lepton, two b-tagged jets and $E_{\mathrm{T}}^{\mathrm{miss}}$ from the LSPs, the neutrino, and the off-shell W boson. The W^* is undetectable and thus contributes to the missing transverse momentum. Therefore, the top-/bottom-squarks are interchangeable in the model discussed here.

The SUSY particle mass configurations are systematically scanned over a wide range using a 2D search grid for the $\tilde{t}/\tilde{b}$ and $\tilde{\chi}_1^0$ masses. The mass points which were generated for this analysis are shown in Figure 5.4, along with the number of generated events for each mass point. The figure also shows where we define the distinction between the "compressed" and "bulk" region of signal points in the grid, which is outlined in Section 5.2.

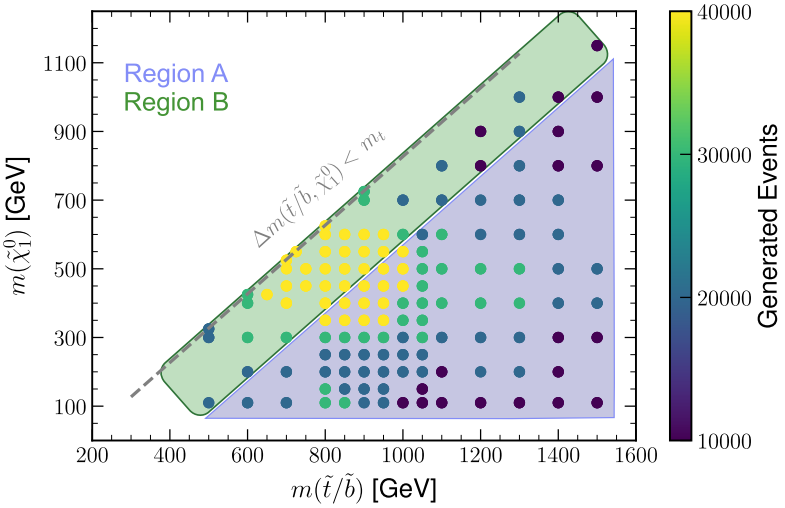

Figure 5.4: Mass grid of generated MC signal points in the 2D plane of top-/bottom-squark and neutralino mass. It is shown where the bulk (Region A) and compressed (Region B) regions are and how many events per mass point are generated. The kinematically disfavoured region with .a mass difference between the SUSY particles below the top mass is also indicated.

5.2 Analysis Strategy

The general analysis strategy splits the two-dimensional mass grid for $\tilde{t}/\tilde{b}$ and neutralinos, shown in Figure 5.4, into two distinct regions: the compressed region and the bulk region. We set the distinction between the two regions at a mass difference between the top-/bottom-squark and the neutralino of 400 GeV.

In the compressed region, where the mass difference between the $\tilde{t}/\tilde{b}$ and the $\tilde{\chi}_1^0$ is small (≤ 400 GeV), the decay products have a relatively low momentum - compared to the

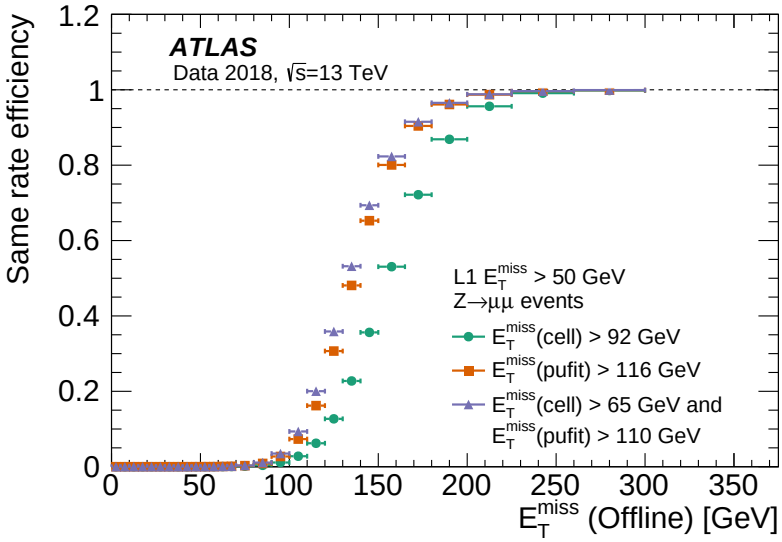

Figure 5.5: $E_{\mathrm{T}}^{\mathrm{miss}}$ trigger turn-on curve as a function of the reconstructed missing transverse momentum [167]. Applying an offline selection of $E_{\mathrm{T}}^{\mathrm{miss}}$ $geq250\,\mathrm{GeV}$ ensures a trigger efficiency which is almost 100%.

bulk region. This situation presents challenges in detection due to reduced $E_{\mathrm{T}}^{\mathrm{miss}}$ and potentially softer b-tagged jets, which makes identification more difficult.

The bulk region involves contrary scenarios with a substantial mass difference between the top-/bottom-squarks and the neutralino. This significant mass gap yields decay products with higher momentum, leading to increased $E_{\mathrm{T}}^{\mathrm{miss}}$ and simplified detection.

By splitting the signal grid into those two categories, regions are defined which target mass points from the one or the other region. In order to benefit from this strategy in the statistical interpretation, both regions are orthogonal to each other - allowing a combined fit in both regions simultaneously. Both signal regions have different background contributions, therefore control regions were defined separately for both scenarios.

5.2.1 Trigger Strategy

We performed studies on the signal efficiency of the MC generated $tb + E_{\mathrm{T}}^{\mathrm{miss}}$ signals to investigate the most suitable trigger for the analysis. Due to the expected final state signature with large amount of missing transverse momentum, the $E_{\mathrm{T}}^{\mathrm{miss}}$ trigger was chosen [166, 167]. An offline $E_{\mathrm{T}}^{\mathrm{miss}}$ threshold of greater than 250.0 GeV is applied, which is inferred from Figure 5.5. This threshold ensures high trigger efficiency and therefore removes uncertainties due to low trigger efficiencies.
The turn-on curve of the $E_{\mathrm{T}}^{\mathrm{miss}}$ trigger, shown in that figure, is obtained by considering $Z \to \mu\mu$ events. Muons are passing through the calorimeters without depositing large amount of energy, thus they can be considered invisible at the calorimeter level and are used to calculate the efficiency of the $E_{\mathrm{T}}^{\mathrm{miss}}$ trigger.

Previous analyses often used a 1L trigger to optimise signal efficiency in the compressed region. However, the neutralino masses have been excluded for values up until 300 GeV as shown in Figure 5.2.
Additionally, our compressed region requires the leading-p_{T} jet to be tagged as an ISR jet.

In addition to ensuring that both SRs are orthogonal, this selection also has implications on the kinematic distribution of the events. Recoiling from the high p_{T} ISR jet, the neutralinos are boosted in the same direction (opposite to the ISR jet). This implies that the missing momenta of such an event are not isotropically distributed and therefore a higher transverse component is observed.
Thus, enough $E_{\mathrm{T}}^{\mathrm{miss}}$ is expected for the $E_{\mathrm{T}}^{\mathrm{miss}}$ trigger efficiency of the signal points and we decided to use the $E_{\mathrm{T}}^{\mathrm{miss}}$ trigger for both SRs.

While for the signal regions, exclusively the $E_{\mathrm{T}}^{\mathrm{miss}}$ trigger is used, a single lepton (muon or electron) trigger is used for control and validation regions requiring more than one lepton. In those regions, a selection on the lepton transverse momentum greater than 27 GeV is applied to ensure full trigger efficiency [166, 168, 169].

5.2.2 1L Pre-selection

Preliminary signal and background investigations have been carried out on events meeting 1L pre-selection criteria. Potential discrimination variables and kinematic distributions are studied. The pre-selections require that the events must satisfy the $E_{\mathrm{T}}^{\mathrm{miss}}$ triggers as described above, have a transverse missing momentum greater than 250 GeV, exactly two b-tagged jets, and only one light (electron or muon) signal lepton with $p_T \geq 10$ GeV, ensuring a well reconstructed lepton. These criteria are summarised in the Table 5.1 and are sufficiently loose to identify the most discriminating variables for constructing high-sensitivity signal regions and suitable control and validation regions.

Selection Criteria	Value
Trigger selection	Passed MET Trigger
$E_{\mathrm{T}}^{\mathrm{miss}}$ [GeV]	≥ 250
$n_{b\text{-jets}}$	$= 2$
$n_{\mathrm{lep}(e,\mu)}$ baseline	$= 1$
$n_{\mathrm{lep}(e,\mu)}$ signal	$= 1$
p_{T}(lep) [GeV]	≥ 10

Table 5.1: 1L pre-selection requirements

The MC signal and background distributions for kinematic variables, such as $E_{\mathrm{T}}^{\mathrm{miss}}$, the jet's and lepton's p_{T}, and the number of jets at pre-selection level are shown in Figure 6.5 together with the data. The lower panels of the plots compare the full Run 2 data with the MC samples.

From these distributions one can infer that at pre-selection level, the shape of the distribution for signal and background events look very similar. To achieve a better discrimination between signal and background, additional higher level variables are introduced and presented at preselection level in the following.

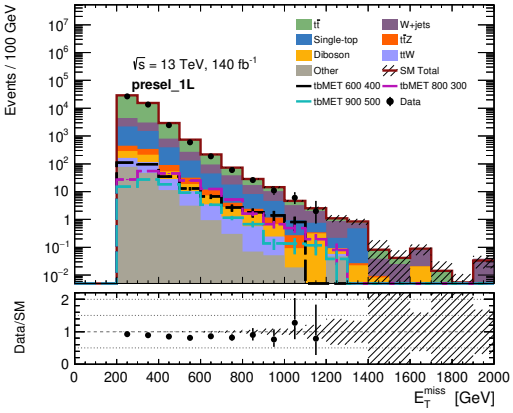

(a) Missing transverse energy $E_{\mathrm{T}}^{\mathrm{miss}}$

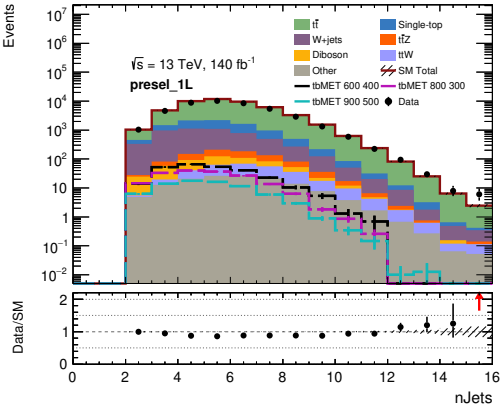

(b) Number of jets

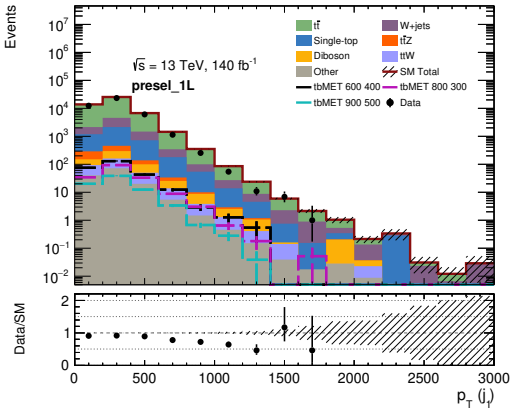

(c) Leading jet p_{T}

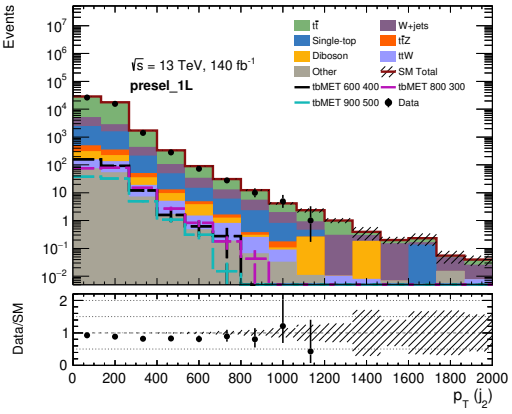

(d) Sub-leading jet p_{T}

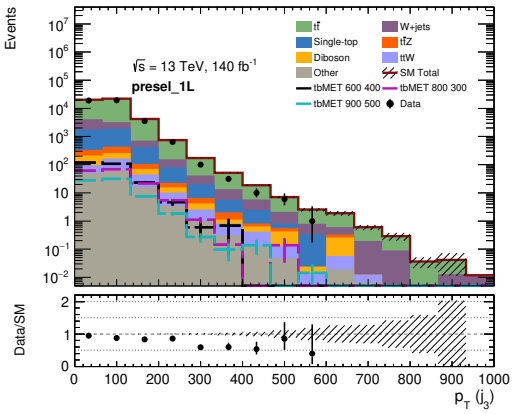

(e) Third-leading jet p_{T}

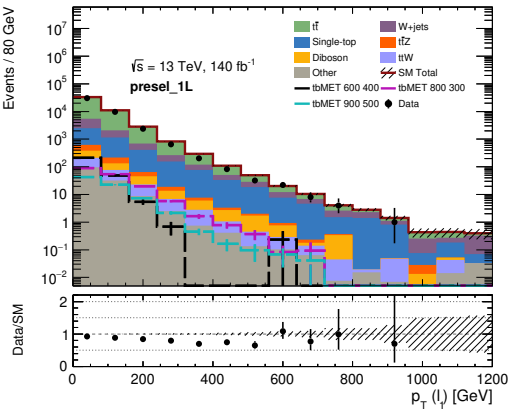

(f) Leading lepton p_{T}

Figure 5.6: Kinematic variable distributions at 1L pre-selection level for representative signal and various background SM processes, as well as data. The MC simulation is scaled to the 140 fb^{-1} of the shown data. The lower panel presents the data and MC agreement as a ratio. The error bars indicate statistical uncertainties.

5.2.3 Discriminating Variables

A set of higher-level discriminating variables are constructed from the physics objects introduced in Section 3.3. The purpose of these variables is to suppress SM backgrounds in the SR while enhancing the BSM signature targeted in the search. Furthermore, the variables are used to isolate dominant SM processes in CRs and VRs to demonstrate effective modelling and are discussed in the following.

$\mathcal{S}(E_{\mathrm{T}}^{\mathrm{miss}})$: the object based $E_{\mathrm{T}}^{\mathrm{miss}}$ significance [170] is a variable designed to evaluate the contribution to $E_{\mathrm{T}}^{\mathrm{miss}}$ from weakly interacting particles. The $E_{\mathrm{T}}^{\mathrm{miss}}$ value might have a large contribution from detector noise, pile-up, or mis-measurements of the energy of the particles. The $E_{\mathrm{T}}^{\mathrm{miss}}$ significance helps discriminating between $E_{\mathrm{T}}^{\mathrm{miss}}$ coming from such sources, and $E_{\mathrm{T}}^{\mathrm{miss}}$ coming from true weakly interacting particles. It is defined as

$$\mathcal{S}(E_{\mathrm{T}}^{\mathrm{miss}}) = \frac{E_{\mathrm{T}}^{\mathrm{miss}}}{\sqrt{\sigma_{\mathrm{L}}^2\left(1-\rho_{\mathrm{LT}}^2\right)}}, \tag{5.4}$$

where σ_{L}^2 the variance in the longitudinal direction of the $E_{\mathrm{T}}^{\mathrm{miss}}$ vector and ρ_{LT} represents the correlation factor of the longitudinal and transverse measurements of the objects contributing to the $E_{\mathrm{T}}^{\mathrm{miss}}$ vector. A high $E_{\mathrm{T}}^{\mathrm{miss}}$ significance is more likely to indicate a real physical process, such as the production of SUSY particles, than detector noise or other spurious sources of $E_{\mathrm{T}}^{\mathrm{miss}}$. This can be seen in Figure 5.7(a), where signals peak at slightly higher values of $\mathcal{S}(E_{\mathrm{T}}^{\mathrm{miss}})$.

H_{T}: the scalar sum of the all transverse jet momenta in an event, is defined via

$$H_{\mathrm{T}} = \sum_i p_{\mathrm{T},i}^{\mathrm{jet}}, \tag{5.5}$$

with $p_{\mathrm{T,i}} = |\vec{p}_{\mathrm{T},i}|$ for all jets. H_{T} is a representation of the total hadronic activity in the event, and as such, it can give an estimate of the overall energy scale of the event. Selecting events with high H_{T} can help suppress background processes, which often lead to lower H_{T}. It is shown in Figure 5.7(b).

m_{eff}: the effective mass, which is defined as the scalar sum of the p_{T} of the leading n jets in an event and $E_{\mathrm{T}}^{\mathrm{miss}}$,

$$m_{\mathrm{eff}} = \sum_{i \leq n} p_{\mathrm{T,i}}^{\mathrm{jet}} + E_{\mathrm{T}}^{\mathrm{miss}}. \tag{5.6}$$

The effective mass is sensitive to the mass scale of the process under consideration. In SUSY processes, where one often expects the production of several high-p_{T} particles, m_{eff} can be large. Therefore, it can help in discriminating potential SUSY events from SM background events, which typically have lower m_{eff}. The variable is shown in Figure 5.7(c).

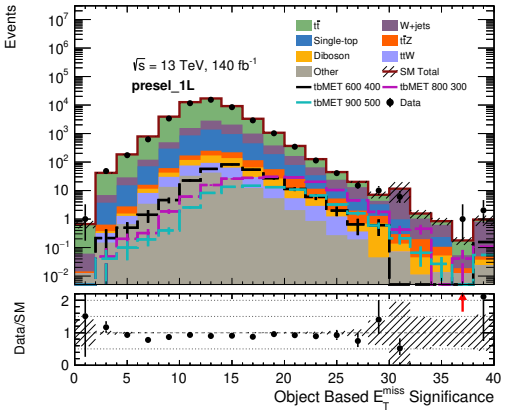

(a) Object based $E_{\mathrm{T}}^{\mathrm{miss}}$ significance

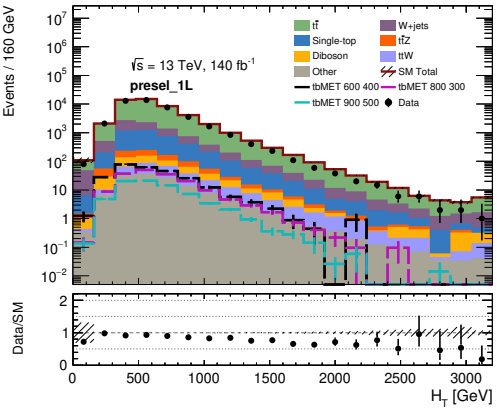

(b) H_{T}

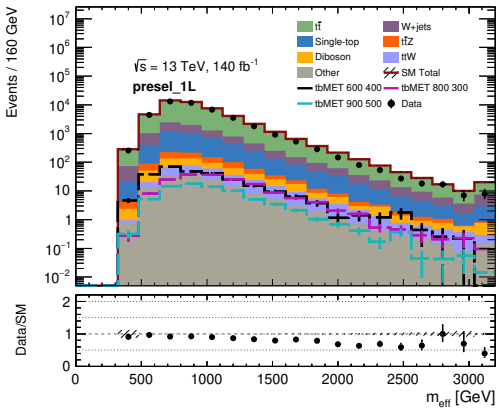

(c) Effective mass m_{eff}

Figure 5.7: Distributions of high-level discriminating variables at 1L pre-selection level for representative signal and various background SM processes, as well as data. The MC simulation is scaled to the 140 fb^{-1} of the shown data. The lower panel presents the data and MC agreement as a ratio. The error bars indicate statistical uncertainties.

$\boldsymbol{m_{ij}}$: the invariant mass of a pair of particles i and j is another important variable, which is calculated using their energy and momentum via

$$m_{ij}^2 = (E_i + E_j)^2 - (|p_i + p_j|)^2. \tag{5.7}$$

Specific cases of the invariant mass are considered in this analysis:

- $\boldsymbol{m_{bb}}$**:** the invariant mass of the two leading b-jets in an event. This variable can help isolate the $t\bar{t}$ contributions. It can also discriminate between $t\bar{t}$ and single-top events, shown in Figure 5.8 (a). The two b-tagged jets from an $t\bar{t}$ event are likely to have a higher m_{bb} than two b-tagged jets from a single-top event.
- $\boldsymbol{m_{\ell\ell}}$**:** the invariant mass of two leptons. This variable is only used for control regions, to identify events where two leptons are originating from a Z boson. In this case the invariant mass of the two leptons peaks at the Z mass. This is discussed in Section 5.4.

- $\boldsymbol{m_{b\ell}^{\min}}$**:** the minimum invariant mass between the lepton and one of the two b-jets,

$$m_{b\ell}^{\min} = \min_{i=1,2} \left(m_{\ell b_i} \right). \tag{5.8}$$

The lepton-b-jet system from a leptonically decaying top-quark will have an invariant mass corresponding at most the mass of the top-quark. Therefore, looking at the minimum invariant mass of the lepton and b-jet pairs can help isolating $t\bar{t}$ events. This can be seen in Figure 5.8(b). While in an $t\bar{t}$ event both b-tagged jets originate from a top-quark (and therefore the minimum must be from a top-quark decay), the minimum for all processes which include only one top is most likely formed with the lepton from top-decay and a b-tagged jet not originating from a top-decay.

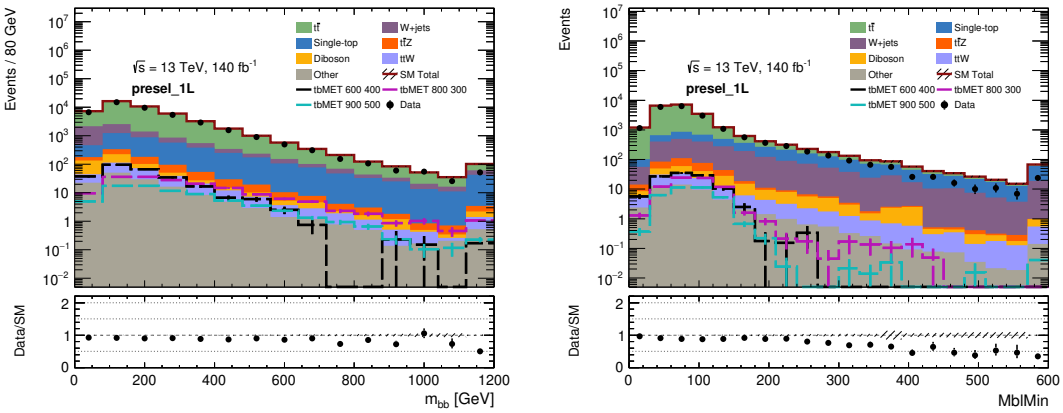

(a) Invariant mass m_{bb}

(b) Min. invariant mass $m_{b\ell}^{\min}$

Figure 5.8: Distributions of high-level discriminating variables at 1L pre-selection level for representative signal and various background SM processes, as well as data. The MC simulation is scaled to the 140 fb^{-1} of the shown data. The lower panel presents the data and MC agreement as a ratio. The error bars indicate statistical uncertainties.

$\boldsymbol{m_{\mathrm{T}}}$**:** The transverse mass [171] is defined for a pair of particles originating from the same parent particle, of which one is undetected, such as a neutrino or a neutralino. For a particle i and $E_{\mathrm{T}}^{\mathrm{miss}}$ from the undetected particle it is defined as

$$m_{\mathrm{T}} = \sqrt{2 p_{\mathrm{T}}^{i} E_{\mathrm{T}}^{\mathrm{miss}} \cos\left(\Delta\phi_{i, E_{\mathrm{T}}^{\mathrm{miss}}}\right)}. \tag{5.9}$$

The transverse mass can be best explained with leptonic W boson decays. The neutrino leaves the detector undetected and contributes therefore to the $E_{\mathrm{T}}^{\mathrm{miss}}$. The transverse mass computed from the lepton and the $E_{\mathrm{T}}^{\mathrm{miss}}$ shows a distinctive edge at the W boson mass, clearly visible in Figure 5.10(a) for processes with W-decays: $t\bar{t}$, W+jets, and single-top. Setting a lower limit on m_{T} above the W mass helps significantly reducing SM processes with W bosons. Signal events are expected to have a much larger $E_{\mathrm{T}}^{\mathrm{miss}}$ contribution from the neutralinos and therefore they peak at higher values.
Two specific versions of m_{T} are considered:

- $\boldsymbol{m_{\mathrm{T}_b}^{\min}\left(b\text{-jet}_{1-2}, E_{\mathrm{T}}^{\mathrm{miss}}\right)}$**:** The smallest transverse mass of one of the two the b-jets and $E_{\mathrm{T}}^{\mathrm{miss}}$ respectively, which peaks around the top mass for $t\bar{t}$ events. Therefore it is a useful variable to suppress $t\bar{t}$ SM background events, shown in Figure 5.10(b).

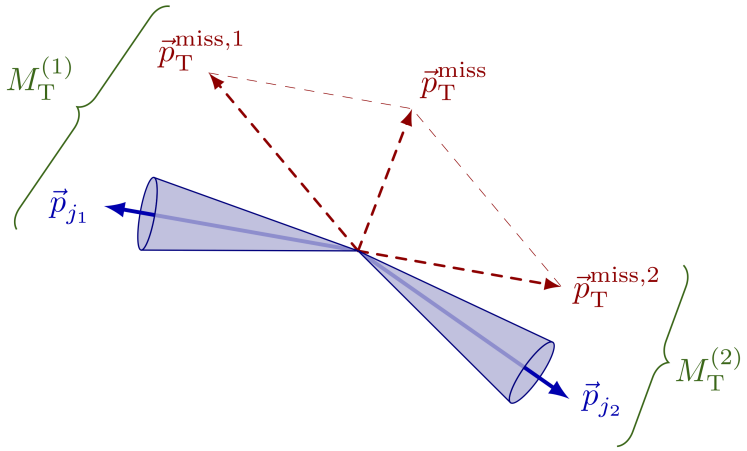

Figure 5.9: Illustration for the M_{T2} variable, which is a modified version of the transverse mass. It reconstructs the transverse mass of a pair of heavy particles, identically decaying into a visible and invisible part by minimising the maximal M_T when decomposing the vector of missing transverse momentum, $\vec{p}_{\mathrm{T}}^{\,\mathrm{miss}}$, into two components, $\vec{p}_{\mathrm{T}}^{\,\mathrm{miss,1}}$ and $\vec{p}_{\mathrm{T}}^{\,\mathrm{miss,2}}$. Image from [174].

- $\boldsymbol{m_{\mathrm{T}_j}^{\mathrm{min}}\left(\mathbf{jet_{1-2}}, \boldsymbol{E}_{\mathrm{T}}^{\mathrm{miss}}\right)}$**:** The minimum transverse mass of the jets in an event and $E_{\mathrm{T}}^{\mathrm{miss}}$, which yields the same result as $m_{\mathrm{T}_b}^{\mathrm{min}}\left(b\text{-jet}_{1-2}, E_{\mathrm{T}}^{\mathrm{miss}}\right)$, but is more generic. The distribution shown in Figure 5.10(c) looks very similar to Figure 5.10(b), because the two leading jets are required to be b-tagged.

$\boldsymbol{M_{\mathrm{T2}}}$**:** the stransverse mass [172, 173] is an extension of the transverse mass. It can be used to reconstruct the mass of a pair of identical, heavy particles, which decay symmetrically into an invisible and visible particle, as shown in Figure 5.9. The variable is defined as

$$M_{\mathrm{T2}} = \min_{\vec{p}_{\mathrm{T}}^{\,\mathrm{miss,1}} + \vec{p}_{\mathrm{T}}^{\,\mathrm{miss,2}} = \vec{p}_{\mathrm{T}}^{\,\mathrm{miss}}} \left[\max(M_{\mathrm{T}}^{(1)}, M_{\mathrm{T}}^{(2)})\right], \tag{5.10}$$

with the missing transverse momentum, $\vec{p}_{\mathrm{T}}^{\,\mathrm{miss}}$, which is decomposed into two components, $\vec{p}_{\mathrm{T}}^{\,\mathrm{miss},i}$ in a way, that two transverse masses with the two visible particles in the event can be constructed, M_{T}^{i}. From all possible combinations, the composition of $\vec{p}_{\mathrm{T}}^{\,\mathrm{miss},i}$ which results in the most equal M_{T}^{i} values is chosen, and M_{T}^{i} calculated.

$\boldsymbol{am_{\mathrm{T2}}}$**:** the asymmetric stransverse mass [175] is used for asymmetric decaying particles, such as the two charginos in the tb+$E_{\mathrm{T}}^{\mathrm{miss}}$ analysis. In the calculation of the transverse mass, the masses of the visible and invisible particles are considered to be identical within each side of the decay. Introducing additional parameters for varying masses of the undetectable particles in Eq. (5.10), results in the asymmetric mass depending on additional parameters,

$$am_{\mathrm{T2}} = am_{\mathrm{T2}}(m_{j1}, m_{j2}, m_{\tilde{\chi}}, m_{\tilde{\kappa}}, \vec{p}_{\mathrm{T,j1}}, \vec{p}_{\mathrm{T,j2}}, \vec{\boldsymbol{p}}_{\mathrm{T}}^{\,\mathrm{miss}}), \tag{5.11}$$

with m_{j1} and m_{j1} being (potential) different masses of the visible particles. The masses $m_{\tilde{\chi}}$ and $m_{\tilde{\kappa}}$ are the (also potential) different masses of the invisible particles with the transverse momenta of the visible particles, $\vec{p}_{\mathrm{T,j1}}, \vec{p}_{\mathrm{T,j2}}$. Figure 5.10(d) shows the asymmetric stransverse mass. The asymmetric stransverse mass in this analysis is used

to suppress the $t\bar{t}$ background rather than targeting the mass of the SUSY particles, because their masses are unknown. For this, the masses of the invisible particles are set to the masses of the invisible neutrinos, for which zero is assumed. Therefore, the $t\bar{t}$ distribution peaks at the top-mass, as can be seen in Figure 5.10(d). A lower limit on am_{T2} has great suppression power.

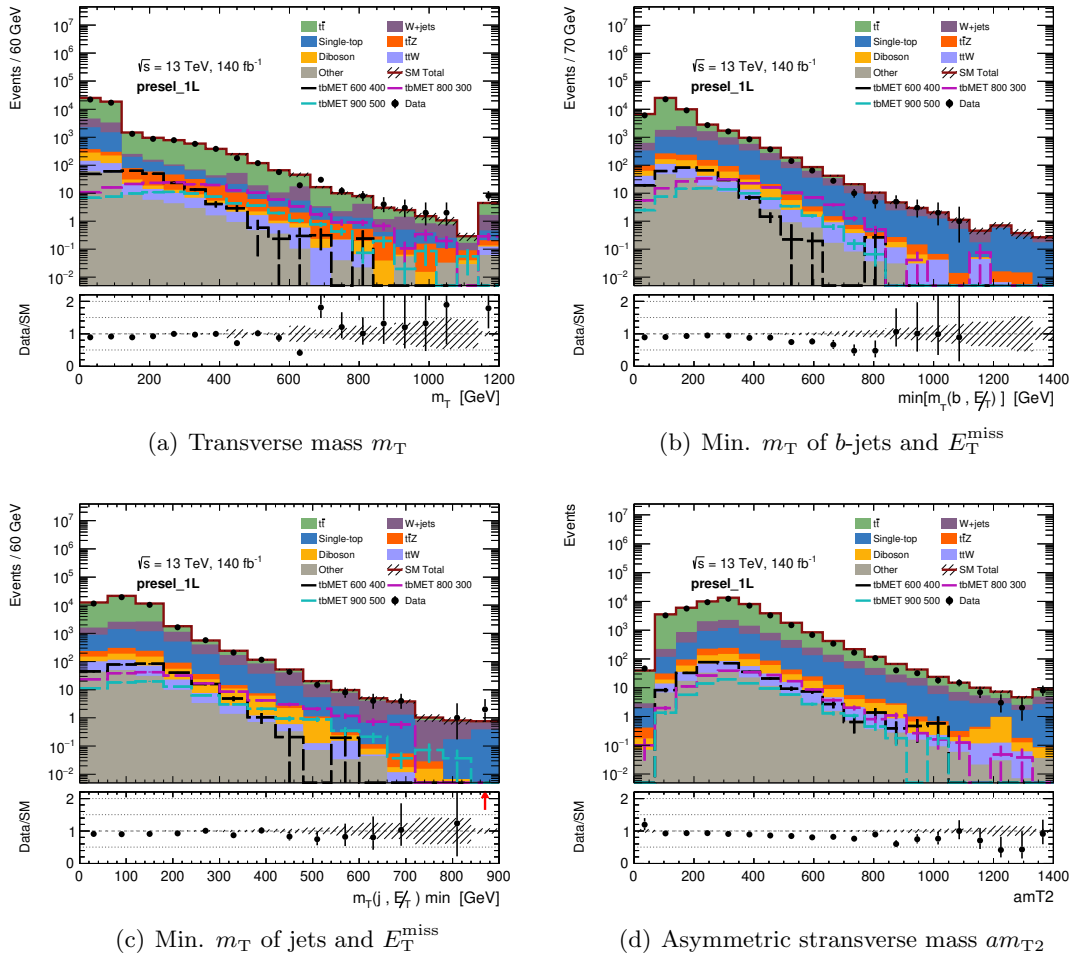

(a) Transverse mass m_{T}

(b) Min. m_{T} of b-jets and $E_{\mathrm{T}}^{\mathrm{miss}}$

(c) Min. m_{T} of jets and $E_{\mathrm{T}}^{\mathrm{miss}}$

(d) Asymmetric stransverse mass am_{T2}

Figure 5.10: Distributions of high-level discriminating variables at 1L pre-selection level for representative signal and various background SM processes, as well as data. The MC simulation is scaled to the 140 fb^{-1} of the shown data. The lower panel presents the data and MC agreement as a ratio. The error bars indicate statistical uncertainties.

5.3 Signal Region Definitions

We define two signal regions to target the signal model in Figure 5.1, focusing on different kinematics caused by the mass difference between $\tilde{t}/\tilde{b}$ and $\tilde{\chi}_1^0$.

Signal region A (SRA) is optimised for signals of the "bulk region" in which the mass difference $\Delta m\left(\tilde{t}/\tilde{b}, \tilde{\chi}_1^0\right)$ is at least 400 GeV as shown in Figure 5.4. Contrary, Signal Region B (SRB), which I defined, targets the signal points with a mass difference $\Delta m\left(\tilde{t}/\tilde{b}, \tilde{\chi}_1^0\right)$ of less than 400 GeV, the "compressed" region. This region goes down to a minimum mass difference of

$$\Delta m\left(\tilde{t}/\tilde{b}, \tilde{\chi}_1^0\right) \geq 175\,\text{GeV}. \tag{5.12}$$

Below this critical limit, the top-quark in the decay cannot be produced on shell and would require a different analysis strategy, which is beyond the scope of this search.

Both regions are optimised with a conventional cut-and-count method. For this, we studied several variables and found the optimal combination of selections, which results in high signal sensitivities, as explained in Section 4.4. Table 5.2 summarises the selections for both signal regions.

Selection	SRA	SRB
$E_{\text{T}}^{\text{miss}}$ [GeV]	≥ 250	≥ 400
n_{lep} baseline	$= 1$	$= 1$
n_{lep} signal	$= 1$	$= 1$
$n_{b\text{-jets}}$	$= 2$	$= 2$
n_{jets} signal	≥ 2	≥ 3
leading-p_{T} jet	is b-tagged	not b-tagged
p_{T} (j_1) [GeV]	≥ 100	≥ 200
p_{T} (j_2) [GeV]	≥ 100	≥ 100
p_{T} (ℓ_1) [GeV]	> 27	≥ 10
$\min[\Delta\phi(\text{jet}_{1-4}, E_{\text{T}}^{\text{miss}})]$	> 0.4	> 0.4
am_{T2} [GeV]	> 350	> 280
$E_{\text{T}}^{\text{miss}}$ significance	> 16	> 15
H_{T} [GeV]	> 300	-
$m_{\text{T}_j}^{\text{min}}$ [GeV]	> 200	-
m_{eff} [GeV]	>1000	> 800
m_{T} [GeV]	> 200	> 150
m_{bl}^{min} [GeV]	< 170	< 170
$m_{\text{T}_b}^{\text{min}}$ [GeV]	> 300	> 200

Table 5.2: Selection criteria for the definition of SRA and SRB. The variables which are used to define the regions are explained in Section 5.2.3.

The primary distinguishing selection between SRA and SRB lies in the b-tag of the leading transverse momentum jet. For compressed scenarios, the leading p_{T} jet is not

b-tagged, because it does not originate from the decay of the top-/bottom-squark pair, but from an ISR jet. Therefore, the b-jet is softer, and thus less efficiently b-tagged. For SRB, this suggests a relaxation of the requirement of exactly two b-tagged jets to at least one b-tagged jet. However, our studies with MC signal samples have shown that in scenarios where an ISR jet is present, requiring two b-jets still leads to a higher significance, because two b-tagged jets provide better SM background suppression power. As a result, SRB requires at least three jets, while SRA seeks a minimum of two jets resulting from the SUSY decay.

Both regions set selection criteria based on the transverse mass (m_{T}). For this variable to effectively discriminate from Standard Model (SM) processes with top-quarks by computing correctly the W mass value, the variable m_{bl}^{min} must be less than 170 GeV, targeting the b-quark-$E_{\mathrm{T}}^{\mathrm{miss}}$ system, thus the top-quark.
In both signal regions, we also apply a lower bound on the minimum transverse mass of a bottom-quark ($m_{\mathrm{T}_b}^{\mathrm{min}}$) to reduce top-antitop contributions. In Figure 5.10(b) it can be seen, that a selection of at least $m_{\mathrm{T}_b}^{\mathrm{min}} > 200\,\mathrm{GeV}$ removes the majority of the $t\bar{t}$ dominated region. The differing values arise from the optimisation in each region.
For similar reasons a threshold for am_{T2} is set in both regions, primarily to suppress $t\bar{t}$ backgrounds. The effective mass for signal points is anticipated to be large, due to the final state comprising a significant proportion of missing transverse energy ($E_{\mathrm{T}}^{\mathrm{miss}}$), and at least two high momentum (b-tagged) jets. The remaining kinematic selection criteria on the lepton's and jet's p_{T} were determined through our iterative optimisation processes for the individual regions.

The number of predicted events are summarised in Table 5.3 for SRA and SRB. Figure 5.11 shows the background and signal contributions in the regions for the $E_{\mathrm{T}}^{\mathrm{miss}}$ and number of jets distributions as well as the integrated significance Z_{N}. The distribution in Z_{N} shows how additional selections on the shown variable would affect the integrated significance in the region. In the two shown variables no further improvement by harder selections is to be expected. The signal points with lower top-/bottom-squark masses have generally a higher production cross-section which leads to higher expected number of events and thus stronger significances. In SRA, up to 12.35 signal events are expected for the signal mass-point $m(\tilde{t}/\tilde{b}, \tilde{\chi}_1^0) = (850{,}200)\,\mathrm{GeV}$, while the total SM background contribution is suppressed down to 6.06 events. The SRB region shows up to 23.06 signal events for the signal mass-point $m(\tilde{t}/\tilde{b}, \tilde{\chi}_1^0) = (600{,}200)\,\mathrm{GeV}$ and the total background contribution sums up to an expectation of 16.70 events. For both regions, the two additionally shown mass points with higher top-/bottom-squark mass predict lower number of signal events. These numbers translate into expected significances, thus sensitivity to new physics, using the standard ATLAS definition for significance [158]. To exclude a mass point, a significance of at least 3σ is required. Both regions show sufficient high significance to ensure good sensitivity in the mass point regions we are targeting.
Notably the background composition is different in both regions. The SM background composition in SRA is dominated by single-top, followed by $t\bar{t}Z$. For SRB, the dominant process is $t\bar{t}$, also followed by $t\bar{t}Z$, which is shared between the two regions. As shown in the pre-selection distributions in Figure 6.5-5.10, the MC samples are not perfectly modelling the data. Therefore, we apply a background estimation method to reduce uncertainties arising from that imperfect modelling when predicting the number of SM background events in the SRs. The background estimation for both regions is discussed in Section 5.4.

		Yield SRA	Yield SRB
$m(\tilde{t}/\tilde{b}, \tilde{\chi}_1^0)$:	(850,200) GeV	12.35 ± 0.83	
	(900,150) GeV	10.58 ± 0.63	
	(950,300) GeV	6.78 ± 0.34	
$m(\tilde{t}/\tilde{b}, \tilde{\chi}_1^0)$:	(600,300) GeV		23.06 ± 2.95
	(500,300) GeV		15.80 ± 3.86
	(700,400) GeV		11.20 ± 1.09
	Single-top	2.67 ± 0.38	2.50 ± 0.37
	$t\bar{t}Z$	2.02 ± 0.22	5.18 ± 0.46
	W+jets	0.95 ± 0.67	2.29 ± 0.62
	Diboson	0.15 ± 0.04	0.82 ± 0.09
	$t\bar{t}$	0.11 ± 0.03	4.94 ± 0.30
	$t\bar{t}W$	0.08 ± 0.03	0.61 ± 0.16
	Other	0.07 ± 0.03	0.36 ± 0.06
	SM	6.06 ± 0.80	16.70 ± 0.93

Table 5.3: Expected SM background yields in SRA and SRB, including three signal points, representative for each of the SRs. The predicted number of events are given with statistical uncertainty only.

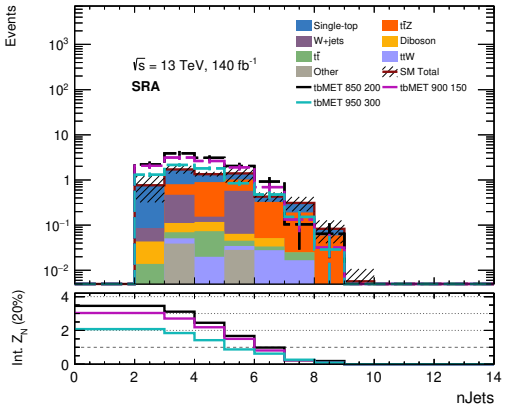

(a) SRA: Number of jets

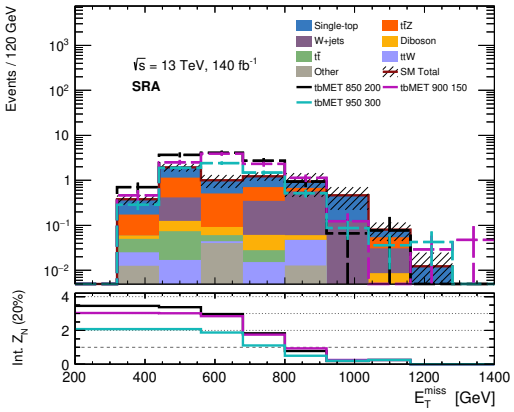

(b) SRA: $E_{\mathrm{T}}^{\mathrm{miss}}$

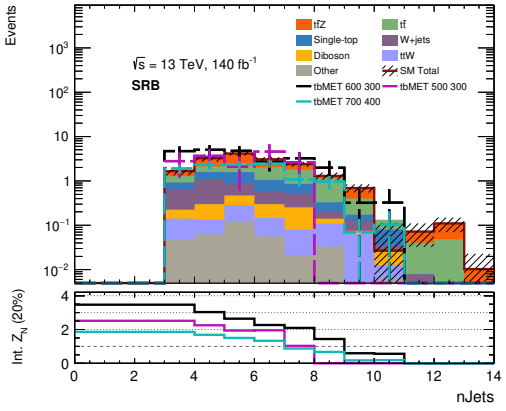

(c) SRB: Number of jets

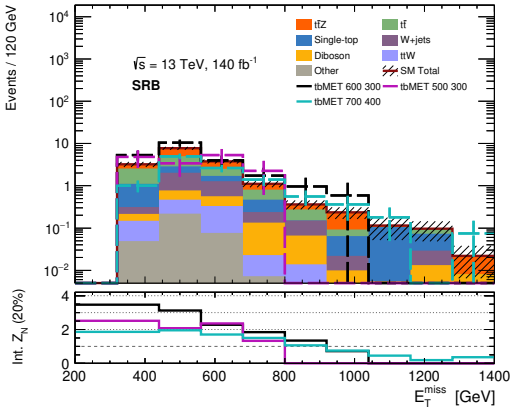

(d) SRB: $E_{\mathrm{T}}^{\mathrm{miss}}$

Figure 5.11: Distributions of two variables, $E_{\mathrm{T}}^{\mathrm{miss}}$ and the number of jets, for SRA and SRB. The MC simulation is scaled to 140 fb^{-1}. The solid coloured histograms indicate the different SM background contributions, with the hatched area representing the total statistical uncertainty. The lines show the distributions from three different representative signal points in each of the two SRs. The lower panel displays the standard recommended ATLAS significance of each bin, Z_{N}, with a flat 20 % uncertainty applied.

5.4 Background Estimation

In this section, the MC-based background estimation method is described. We defined orthogonal CRs for the most dominant SM backgrounds in the two SRs. Background-only fits to data are performed simultaneously in the CRs per SR. Through that fit to data, normalisation factors are obtained, as introduced in Section 4.5 and afterwards validated through application to dedicated VRs.
For SRA and SRB, the background-only fit is done separately. In the following, I first describe the CRs, then I present the background-only fit results, define VRs and show the validation of those results in the VRs.

5.4.1 Control Region Definitions

The background composition differs between the two SRs as they target two different final state kinematics. Both regions are found to have two main SM background contributions. The two most significant backgrounds in SRA are single-top and $t\bar{t}Z$. As shown in Table 5.3 they account for 44% (single-top) and 33% ($t\bar{t}Z$) of the total SM background events. SRB is dominated by the $t\bar{t}Z$ (31%) and $t\bar{t}$ (30%) processes, as listed in Table 5.3. We defined three CRs, one for $t\bar{t}Z$, single-top, and $t\bar{t}$ respectively.

$t\bar{t}Z$ Control Region

The $t\bar{t}Z$ process is contributing to SRA and SRB. We defined one common CR, which is used in both regions. In the $t\bar{t}Z$ process, the Z boson decays invisibly into two neutrinos and the two tops decay semi-hadronically. Therefore, the final state looks very similar to the SUSY process.

In contrast to all other 1L CR and SR defined in this analysis, we defined a three-lepton (3L) CR for $t\bar{t}Z$, requiring the Z boson to decay into visible leptons (e,μ). The two visible leptons from the Z boson are then re-interpreted as mimicking the invisible neutrinos for which an additional variable is defined:

$\boldsymbol{E_{\mathrm{T}}^{\mathrm{miss}+\ell}}$**:** the lepton corrected $E_{\mathrm{T}}^{\mathrm{miss}}$, for which the p_{T} of the two leptons from the Z decay are added inversely to the $E_{\mathrm{T}}^{\mathrm{miss}}$ via

$$E_{\mathrm{T}}^{\mathrm{miss}+\ell} = E_{\mathrm{T}}^{\mathrm{miss}} - \sum_{i=1,2} p_{\mathrm{T},\ell_i}. \tag{5.13}$$

To ensure that the two correct leptons (the ones from the decay of the Z) are used, we check that they are of the same flavour, have opposite signs and are the closest pair in ΔR among the three leptons.

The selections for the $t\bar{t}Z$ CR, CR-ttZ, are listed in Table 5.4. We use the invariant mass of the two leptons of opposite sign and same flavour, $m_{\ell\ell}$ and select a window around the Z mass of 90 GeV to isolate $t\bar{t}Z$ events. Events in this region pass the 1L HLT triggers, which require either one lepton or one muon, as discussed in Section 5.2. The p_{T} of the leading lepton is chosen to satisfy the trigger plateau requirement, the two sub-leptons are above 10 GeV to ensure good reconstruction.

Table 5.5 summarises the yields for all defined CR. Figure 5.12 shows the agreement between data and MC prediction in the region for the invariant mass of the two leptons coming from the Z decay. The table and figure show that the region is sufficiently pure

in the $t\bar{t}Z$ background with 55% of the total SM background. Since the SUSY signal has only one lepton in the final state, no contamination of the signal is expected nor observed. The agreement between data and the MC prediction is within 10% in the CR.

Selection	ttZ-CR
Trigger	1ℓ
n_{lep} baseline	$= 3$
n_{lep} signal	$= 3$
n_{jets} signal	≥ 2
$n_{b\text{-jets}}$	$= 2$
p_{T} (ℓ_1) [GeV]	> 27
p_{T} (ℓ_2) [GeV]	> 10
p_{T} (ℓ_3) [GeV]	> 10
$m_{\ell\ell}$ [GeV]	[86,96]

Table 5.4: Selections for $t\bar{t}Z$ control region.

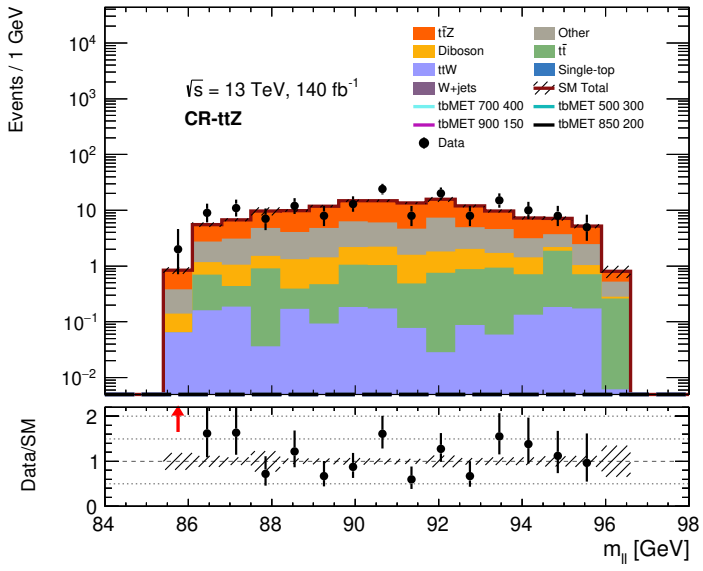

Figure 5.12: Distribution of invariant mass of the two leptons from the Z boson in the 3L $t\bar{t}Z$ CR. The coloured, solid histograms show the SM backgrounds scaled to 140 fb^{-1}. The hatched area represents the statistical error on the prediction. The black points show the data with statistical error bars. The lower panel contains the ratio of data over SM prediction.

		Yield CRA-st	Yield CRB-ttbar	Yield CR-ttZ
$m(\tilde{t}/\tilde{b}, \tilde{\chi}_1^0)$:	(850, 200)	1.51 ± 0.30		0.00 ± 0.00
	(900, 150)	1.24 ± 0.23		0.00 ± 0.00
	(950, 300)	0.88 ± 0.13		0.00 ± 0.00
$m(\tilde{t}/\tilde{b}, \tilde{\chi}_1^0)$:	(500, 300)		9.81 ± 3.17	0.00 ± 0.00
	(600, 300)		2.71 ± 1.01	0.00 ± 0.00
	(700, 400)		1.46 ± 0.39	0.00 ± 0.00
	Single-top	21.31 ± 1.10	12.60 ± 1.22	0.00 ± 0.00
	$t\bar{t}Z$	1.48 ± 0.21	2.59 ± 0.31	81.35 ± 0.67
	W+jets	8.81 ± 1.26	12.44 ± 1.38	0.00 ± 0.00
	Diboson	0.47 ± 0.10	1.01 ± 0.40	11.49 ± 0.29
	$t\bar{t}$	11.65 ± 0.62	142.93 ± 2.47	9.89 ± 1.12
	$t\bar{t}W$	0.34 ± 0.09	1.26 ± 0.24	1.82 ± 0.25
	Other	0.43 ± 0.09	0.74 ± 0.07	40.75 ± 2.55
	SM	44.49 ± 1.80	173.57 ± 3.13	145.29 ± 2.89
	Data	42.00 ± 6.48	139.00 ± 11.79	160.00 ± 12.65

Table 5.5: Composition of Control Regions, with both the SM background and three signal points, representative for each of the SRs. Only statistical uncertainties are given for the expected event numbers.

Single-top Modelling: Diagram Removal vs. Diagram Subtraction

Before defining the single-top CR, I did a study comparing different available single-top MC samples. The modelling of single-top processes is challenging due to the interference terms at NLO with LO $t\bar{t}$ processes. Figure 5.13 shows the two processes, which both lead to a final state with two b-quarks and two W bosons.

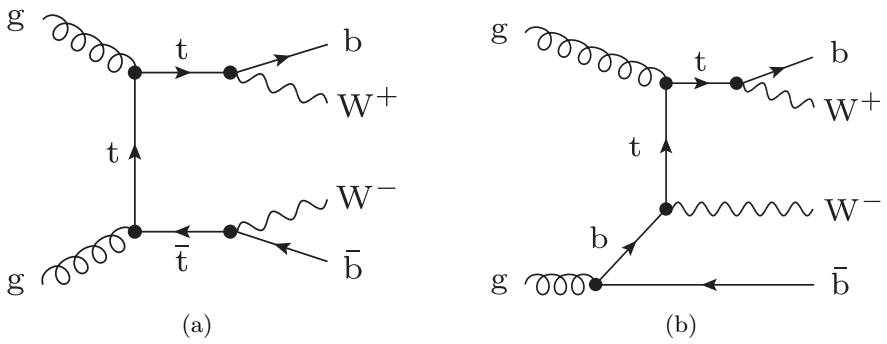

Figure 5.13: Two diagrams interfering: the $t\bar{t}$ LO process (a) and single-top Wt production with an extra b-jet at NLO (b). Image taken and adapted from [176].

Since the $tb + E_{\mathrm{T}}^{\mathrm{miss}}$ final state requires two b-tagged jets, a lepton and $E_{\mathrm{T}}^{\mathrm{miss}}$- the interference terms become non negligible for this search, in which the $t\bar{t}$ and single-top SM background processes are modelled individually. Therefore, a correction of the perturbation term is typically applied, which can be done in two ways, via the diagram removal or diagram subtraction scheme [176, 177].

In the **Diagram Removal** (DR) scheme, all diagrams that could contribute to both single-top and $t\bar{t}$ production, such as the NLO process in Figure 5.13(b) are removed from the matrix element calculation of the single-top production cross-section. This effectively means that all overlapping diagrams contribute to $t\bar{t}$ and not to single-top production.

The **Diagram Subtraction** (DS) scheme, on the other hand, attempts to more evenly distribute the interference between the two processes. In this scheme, the overlapping diagrams are still included in the single-top process, but a counter term is subtracted from the matrix element calculation to account for the interference with $t\bar{t}$. The counter term is defined to cancel out the contribution of these diagrams in the limit where the b-quark-W system is around the top-quark mass. For processes beyond this region, the DS scheme usually leads to worse performance than the DR scheme.

To explore the difference and to assess whether an additional systematic uncertainty needs to be included in the statistical analysis, I compare the single-top CR, defined in the next subsection, with the single-top processes generated by both schemes. This is shown in Figure 5.14. For these figures, the selection on m_{bl}^{min} and am_{T2} are removed compared to the CR defined in Table 5.6 to get a sufficiently high enough number of events for the study. Shown is am_{T2} for both Wt samples, with the DS scheme (a) and the DR scheme (b) applied.

The DS scheme has a worse data-MC agreement than the DR scheme. While the data to MC prediction agreement in the shown region with the DR samples is 0.93, it changes to 1.39 for the region with the DS sample, adding a disagreement of 30%. I made a similar observation when applying the DR and DS samples for the CR-st definition. The ratio

changed from 0.94 to 1.64, thus even a larger change is observed. In the single-top CR, a selection on the $m_{\mathrm{T_b}}^{\mathrm{min}}$ similar to the SR is set with a lower limit of 200 GeV. With this selection, the CR targets a kinematic regions, were the invariant mass of the W boson and b-tagged quark might be beyond the top-quark mass, which is outside the region for which DS performs better. Therefore, only the DR scheme is considered in the following.

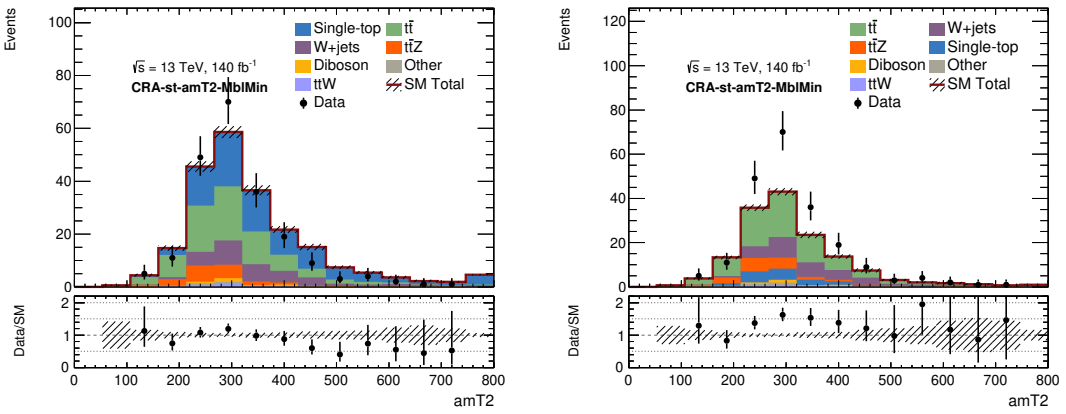

(a) Wt sample with DR scheme

(b) Wt sample with DS scheme

Figure 5.14: Distribution of background and three representative signal events in the single-top CR. While we observe good agreement between data and the MC prediction using the single-top samples based on the DR scheme (a), the agreement is 30% worse with the DS (b) scheme.

Single-top Control Region

The selections for the single-top CR, CRA-st, are listed in Table 5.6, which summarises both 1L CRs in this analysis. To ensure orthogonality between CRA-st and SRA, a $E_{\mathrm{T}}^{\mathrm{miss}}$ significance window is selected which is below the SR selection. In order to suppress events which are dominated by processes where the $E_{\mathrm{T}}^{\mathrm{miss}}$ is mimicked by mis-measurements, as discussed in Section 5.2.3, a window instead of an upper limit for the $E_{\mathrm{T}}^{\mathrm{miss}}$ significance is chosen. Figure 5.15 shows the distribution of the various background and signal processes for the $E_{\mathrm{T}}^{\mathrm{miss}}$ significance and the minimum transverse mass between the b-quark and $E_{\mathrm{T}}^{\mathrm{miss}}$, which is slightly relaxed compared to the SR. Table 5.5 summarises the yields in the single-top CR. This table shows a reasonable agreement between data and MC, with a data-to-MC ratio of 0.94. A signal contamination of up to 3.5% is expected in the CR, which is considered to be small enough. The purity of single-top events in the single-top CR is 48%.

$t\bar{t}$ Control Region

SRB is dominated by the SM $t\bar{t}$ process, where one of the W bosons from the top-quarks decays leptonically into a single lepton and a neutrino, while the other undergoes hadronic decay. The selection criteria for a dedicated $t\bar{t}$ CR are summarised in Table 5.6. These criteria require the presence of one lepton and incorporate kinematic variables similar to those in SRB. Orthogonality to the SR and CR is guaranteed by selecting a window within the transverse mass, m_{T} variable, in which $t\bar{t}$ is dominant, and inverting the selection of the $E_{\mathrm{T}}^{\mathrm{miss}}$ significance to reduce signal contamination. A lower limit on the

Selection	CRA-st	CRB-ttbar
$E_{\mathrm{T}}^{\mathrm{miss}}$ [GeV]	> 250	> 250
n_{lep} baseline	$= 1$	$= 1$
n_{lep} signal	$= 1$	$= 1$
$n_{b\text{-jets}}$	$= 2$	$= 2$
n_{jets} signal	≥ 2	≥ 3
leading-p_{T} jet	is b-tagged	not b-tagged
p_{T} (j_1) [GeV]	> 100	> 200
p_{T} (j_2) [GeV]	-	> 100
p_{T} (ℓ_1) [GeV]	> 27	> 10
$\min[\Delta\phi(\mathrm{jet}_{1-4}, E_{\mathrm{T}}^{\mathrm{miss}})]$	> 0.4	> 0.4
am_{T2} [GeV]	> 350	> 280
$E_{\mathrm{T}}^{\mathrm{miss}}$ significance	$[13, 16]$	$[8, 15]$
m_{eff} [GeV]	-	> 800
m_{T} [GeV]	> 90	$[100, 150]$
m_{bl}^{min} [GeV]	< 170	< 170
$m_{\mathrm{T}_b}^{\mathrm{min}}$ [GeV]	> 200	> 120

Table 5.6: Summary of the selections defining the 1L CRs.

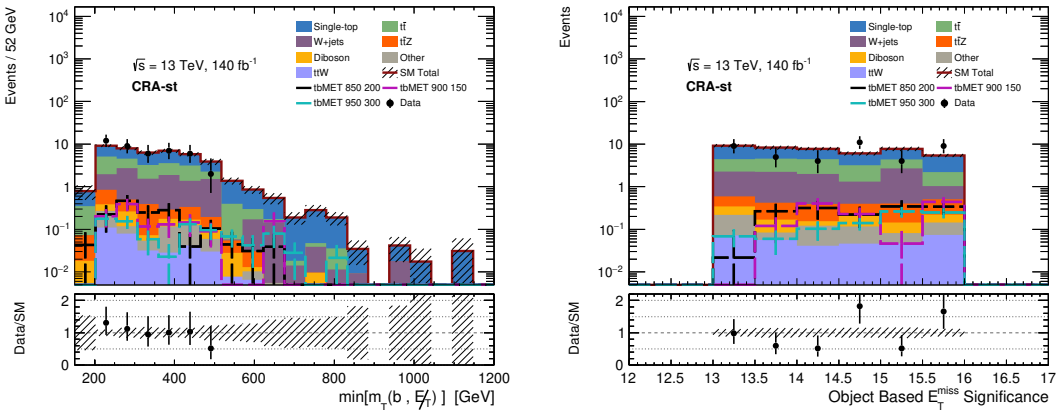

(a) $m_{\mathrm{T}_b}^{\mathrm{min}}$ (b) $E_{\mathrm{T}}^{\mathrm{miss}}$ significance

Figure 5.15: Distributions in single-top CR, CRA-st, for $m_{\mathrm{T}_b}^{\mathrm{min}}$ (a) and the $E_{\mathrm{T}}^{\mathrm{miss}}$ significance (b). In each subfigure the coloured, solid histograms show the SM backgrounds scaled to $140\,\mathrm{fb}^{-1}$. The hatched area represents the statistical uncertainty on the prediction. The black points show the data with statistical error bars. Overlaid are dashed lines of three representative signal points. The lower panel shows the ratio of data over SM prediction.

$E_{\mathrm{T}}^{\mathrm{miss}}$ significance is set to avoid the badly modelled low $E_{\mathrm{T}}^{\mathrm{miss}}$ significance regions which are dominated by mis-measurements in the soft term, as discussed in Eq. (5.4).
The $t\bar{t}$ CR is depicted in Figure 5.16, and the yield values are reported in Table 5.5. A

low signal contamination of 6% is observed, while a high $t\bar{t}$ purity of 82% of the total SM prediction is achieved. The data to MC ratio in the CR is 0.80.

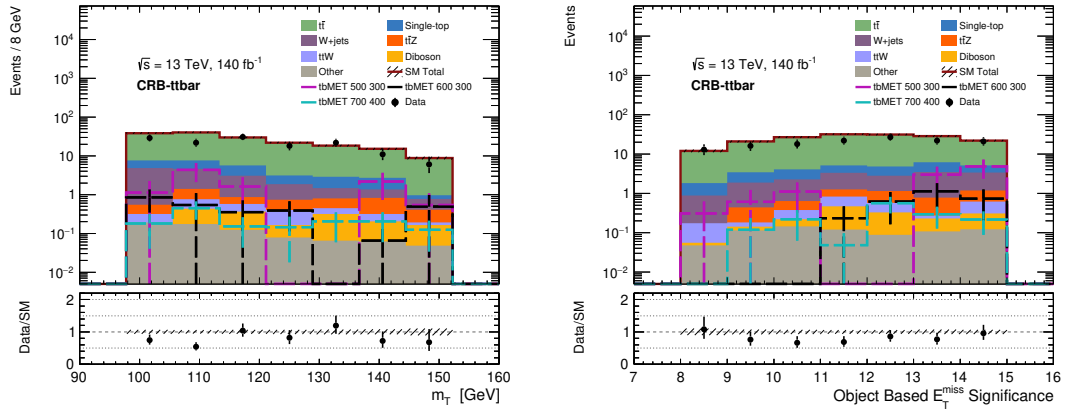

(a) m_{T} (b) $E_{\mathrm{T}}^{\mathrm{miss}}$ significance

Figure 5.16: Distributions in CRB-ttbar for m_{T} (a) and $E_{\mathrm{T}}^{\mathrm{miss}}$ significance (b). In each subfigure the coloured, solid histograms show the SM backgrounds scaled to 140 fb^{-1}. The hatched area represents the statistical error on the prediction. The black points show the data with statistical error bars. Overlaid are dashed lines of representative signal points. The lower panel contains the ratio of data over SM prediction.

5.4.2 Background-only fit

The background-only fit returns the background normalisation factors summarised in Table 5.7. For SRA, normalisation factors for single-top and $t\bar{t}Z$ are fitted simultaneously, while for SRB $t\bar{t}$ and $t\bar{t}Z$ normalisation factors are the results of the fit.

Table 5.8 and Table 5.9 show the total nominal, ("MC expected SM events") as listed with its components in Table 5.5, and fitted background yields in all control regions. The overall data-MC agreement has been significantly improved through the normalisation factors as expected.

Region	Normalisation Factor	Value
SRA	μ(single-top)	0.87 ± 0.30
	$\mu(t\bar{t}Z)$	1.18 ± 0.16
SRB	$\mu(t\bar{t})$	0.75 ± 0.08
	$\mu(t\bar{t}Z)$	1.21 ± 0.16

Table 5.7: Normalisation factors for backgrounds obtained with separate background-only fits in region A and B. Only statistical uncertainties are included in the fit.

tb+$E_{\mathrm{T}}^{\mathrm{miss}}$ CRA	CRAst	CRttZ
Observed events	42	160
Fitted bkg events	41.96 ± 6.45	159.98 ± 12.64
Fitted W events	8.81 ± 0.15	0.00 ± 0.00
Fitted ttW events	0.34 ± 0.01	1.82 ± 0.03
Fitted diboson events	0.47 ± 0.01	11.49 ± 0.19
Fitted ttbar events	11.65 ± 0.20	9.89 ± 0.17
Fitted st events	18.52 ± 6.46	0.00 ± 0.00
Fitted ttZ events	1.75 ± 0.23	96.04 ± 12.68
Fitted other events	0.43 ± 0.01	40.74 ± 0.69
MC exp. SM events	44.49	145.29

Table 5.8: Fit results for the background only-fit in the A-type control regions, for an integrated luminosity of $140\,\mathrm{fb}^{-1}$. The total nominal MC expectations is given for comparison. The errors shown are statistical only. Uncertainties on the fitted yields are symmetric by construction, where the negative error is truncated when reaching to zero event yield.

tb+$E_{\mathrm{T}}^{\mathrm{miss}}$ CRB	CRBtt	CRttZ
Observed events	139	160
Fitted bkg events	139.07 ± 11.79	159.97 ± 12.64
Fitted W events	12.45 ± 0.21	0.00 ± 0.00
Fitted ttW events	1.26 ± 0.02	1.82 ± 0.03
Fitted diboson events	1.01 ± 0.02	11.49 ± 0.19
Fitted ttbar events	107.87 ± 11.83	7.46 ± 0.82
Fitted st events	12.60 ± 0.21	0.00 ± 0.00
Fitted ttZ events	3.13 ± 0.41	98.43 ± 12.72
Fitted other events	0.74 ± 0.01	40.76 ± 0.69
MC exp. SM events	173.57	145.29

Table 5.9: Fit results for the background only-fit in the B-type control regions, for an integrated luminosity of $140\,\mathrm{fb}^{-1}$. The total nominal MC expectations is given for comparison. The errors shown are statistical only. Uncertainties on the fitted yields are symmetric by construction, where the negative error is truncated when reaching to zero event yield.

5.4.3 Validation

In order to validate the normalisation factors obtained from the background-only fit listed in Table 5.7, we defined VRs. Per CR, summarised in Section 5.4.1, we defined one VR, located kinematically closer to the SR than the CR. We expect higher signal contamination but set the requirement that the contamination should be below 20%. In the following, the VRs are described, as well as their data-MC agreement with ("post-fit") and without ("pre-fit") the normalisation factor applied.

$t\bar{t}Z$ Validation Region

To validate the normalisation factor from the background-only fit to data in the 3L $t\bar{t}Z$ CR, a two-lepton (2L) $t\bar{t}Z$ VR is designed, with selections listed in Table 5.10. This VR was heavily inspired by a 2L $t\bar{t}Z$ enriched SR from the $tt + E_{\mathrm{T}}^{\mathrm{miss}}$(2L) analysis [178], including the definition of an additional variable:

$\Delta\phi_{\mathrm{boost}}$: the angle between $E_{\mathrm{T}}^{\mathrm{miss}}$ and $E_{\mathrm{T}}^{\mathrm{miss}+\ell}$, which describes the azimuthal angle between the $\vec{p}_{\mathrm{T}}^{\,\mathrm{miss}}$ vector and the $\vec{p}_{\mathrm{T}}^{\,\mathrm{miss}+\ell}$ vector. $\vec{p}_{\mathrm{T}}^{\,\mathrm{miss}+\ell}$ is the vectorial sum of $\vec{p}_{\mathrm{T}}^{\,\mathrm{miss}}$ and the transverse momenta vectors of the two leptons, $\vec{p}_{\mathrm{T}}(\ell_1)$ and $\vec{p}_{\mathrm{T}}(\ell_2)$, thus the lepton-corrected $p_{\mathrm{T}}^{\mathrm{miss}}$.

Selection	ttZ-VR	
n_{lep} baseline	$= 2$	
n_{lep} signal	$= 2$	
leptons flavour	DF	SF
$m_{\ell\ell}$ [GeV]	-	$< 70, > 110$
p_{T} (ℓ_1) [GeV]	> 25	
p_{T} (ℓ_2) [GeV]	> 20	
$n_{b\text{-jets}}$	≥ 1	
$\lvert\Delta\phi_{\mathrm{boost}}\rvert$ [rad]	< 1.5	
$E_{\mathrm{T}}^{\mathrm{miss}}$ significance	> 12	
$m_{\mathrm{T2}}^{\ell\ell}$ [GeV]	> 110	
$E_{\mathrm{T}}^{\mathrm{miss}}$ [GeV]	> 200	

Table 5.10: Selections for $t\bar{t}Z$ validation region.

This region definition is dominantly based on the lepton-based transverse mass, $m_{\mathrm{T2}}^{\ell\ell}$, and the angle between the original and lepton-correct met, $\Delta\phi_{\mathrm{boost}}$.
The 3L $t\bar{t}Z$ background enters the SRs in cases where the Z boson decays invisibly into neutrinos contributing to $E_{\mathrm{T}}^{\mathrm{miss}}$ and the two tops decay semi-leptonically. Therefore, the 2L $t\bar{t}Z$ VR should have a high contribution from $t\bar{t}Z$ events, where the Z decays invisible and both tops decay leptonically. To ensure this, the $t\bar{t}Z$ VR is requiring the two leptons - if they have the same flavour (SF) - to have an invariant mass which does not correspond to the Z mass, thus $m_{\ell\ell} < 70\,\mathrm{GeV}$ or $m_{\ell\ell} > 110\,\mathrm{GeV}$. Because the $E_{\mathrm{T}}^{\mathrm{miss}}$ is expected to come from Z decays to neutrinos, the direction of $E_{\mathrm{T}}^{\mathrm{miss}+\ell}$ should not differ too much from the direction of $E_{\mathrm{T}}^{\mathrm{miss}}$, thus the angle between those two is defined to be small, <1.5 rad. Similarly to the 3L CR, single-lepton triggers are used instead of the $E_{\mathrm{T}}^{\mathrm{miss}}$ trigger. The yields before the fit are summarised in Table 5.11 A good purity of 30% for the $t\bar{t}Z$ process with invisibly decaying Z is obtained. At the same time, the

signal contamination is below 20% for the highest cross-section mass point listed and therefore acceptable.

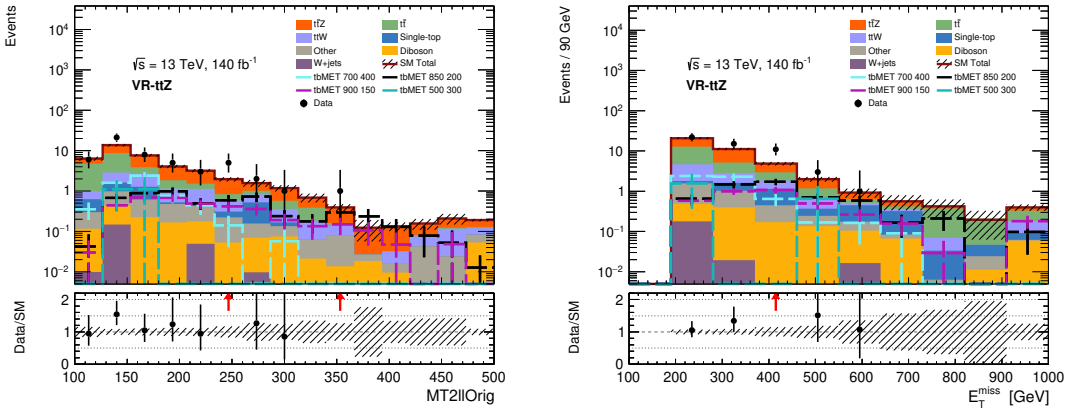

(a) $m_{\mathrm{T2}}^{\ell\ell}$ (b) $E_{\mathrm{T}}^{\mathrm{miss}}$

Figure 5.17: Distributions in 2L $t\bar{t}Z$ VR for the lepton based transverse mass (a) and $E_{\mathrm{T}}^{\mathrm{miss}}$ (b). In each subfigure the coloured, solid histograms show the SM backgrounds scaled to 140 fb^{-1}. The hatched area represents the statistical error on the prediction. The black points show the data with statistical error bars. Overlaid are dashed lines of representative signal points. The lower panel contains the ratio of data over SM prediction.

		Yield VRA-st	Yield VRB-ttbar	Yield VR-ttZ
$m(\tilde{t}/\tilde{b}, \tilde{\chi}_1^0)$:	(850, 200)	12.27 ± 0.83		5.60 ± 0.55
	(900, 250)	7.63 ± 0.53		3.05 ± 0.34
	(950, 300)	5.30 ± 0.30		2.87 ± 0.22
$m(\tilde{t}/\tilde{b}, \tilde{\chi}_1^0)$:	(500, 300)		14.14 ± 3.91	2.22 ± 1.36
	(600, 300)		5.00 ± 1.37	15.89 ± 2.33
	(700, 400)		3.99 ± 0.71	5.72 ± 0.73
	Single-top	28.44 ± 1.79	6.63 ± 0.74	2.23 ± 0.52
	$t\bar{t}Z$	15.12 ± 0.64	4.90 ± 0.47	17.35 ± 0.63
	W+jets	3.42 ± 0.60	3.29 ± 0.67	0.22 ± 0.11
	Diboson	0.65 ± 0.12	0.64 ± 0.09	1.22 ± 0.12
	$t\bar{t}$	17.69 ± 0.92	150.48 ± 2.48	12.85 ± 1.07
	$t\bar{t}W$	1.88 ± 0.26	1.21 ± 0.22	5.30 ± 0.42
	Other	1.50 ± 0.12	1.04 ± 0.07	2.20 ± 0.13
	SM	68.70 ± 2.22	168.20 ± 2.73	41.36 ± 1.42
	Data	65.00 ± 8.06	146.00 ± 12.08	52.00 ± 7.21

Table 5.11: Composition of Validation Regions with expected and observed SM background and three representative signal point predictions. The observed and expected yields are given including statistical uncertainties only.

Single-top Validation Regions

A single-top VR is defined in order to validate the background estimation obtained from the CR. The selections are listed in Table 5.12. Compared to the single-top CR, the VR has only a lower limit on the $E_{\mathrm{T}}^{\mathrm{miss}}$ significance and the am_{T2} variable is inverted. Table 5.11 lists the yields in the single-top VR, showing a good portion of signal, which is below our limit of 20% of the total expected SM background processes. The purity in single-top is $\sim 40\%$ of the total SM prediction and the ratio between data to MC prediction is 0.95 in the VR. Figure 5.18 shows the background compositions in the VR for the two variables, am_{T2} and the $E_{\mathrm{T}}^{\mathrm{miss}}$ significance.

Selection	VRA-st	VRB-ttbar
$E_{\mathrm{T}}^{\mathrm{miss}}$ [GeV]	> 250	> 250
n_{lep} baseline	$= 1$	$= 1$
n_{lep} signal	$= 1$	$= 1$
$n_{b\text{-jets}}$	$= 2$	$= 2$
n_{jets} signal	≥ 2	≥ 3
leading-p_{T} jet	is b-tagged	not b-tagged
p_{T} (j_1) [GeV]	> 50	> 200
p_{T} (j_2) [GeV]	-	> 100
p_{T} (ℓ_1) [GeV]	> 27	> 10
$\min[\Delta\phi(\mathrm{jet}_{1-4}, E_{\mathrm{T}}^{\mathrm{miss}})]$	> 0.4	> 0.4
am_{T2} [GeV]	< 350	> 280
$E_{\mathrm{T}}^{\mathrm{miss}}$ significance	-	$[8, 15]$
m_{eff} [GeV]	-	> 800
m_{T} [GeV]	> 200	> 150
m_{bl}^{min} [GeV]	< 170	< 170
$m_{\mathrm{T}_b}^{\mathrm{min}}$ [GeV]	> 270	> 120

Table 5.12: Summary of the selections that define the 1L VRs.

$t\bar{t}$ Validation Region

To validate the $t\bar{t}$ background modelling when extrapolating towards the SR, the $t\bar{t}$ VR is defined, close to the $t\bar{t}$ CR. All selections are summarised in Table 5.12. The inverted m_{T} selection being greater than 150.0 GeV places it kinematically closer to the SRB. The choice of the inverted $E_{\mathrm{T}}^{\mathrm{miss}}$ significance selection remains to ensure orthogonality. Table 5.11 summarises the yields and Figure 5.19 shows distributions of the $t\bar{t}$ validation region, before applying the normalisation factor. Slightly higher signal contamination in the VR compared to the CR is desirable, because we want to probe the background estimate in a region kinematically closer to the SR. This is shown by the expected signal contamination of 8% in the region. The agreement between data and MC prediction is within 15% and therefore slightly worse compared to the $t\bar{t}$ CR.

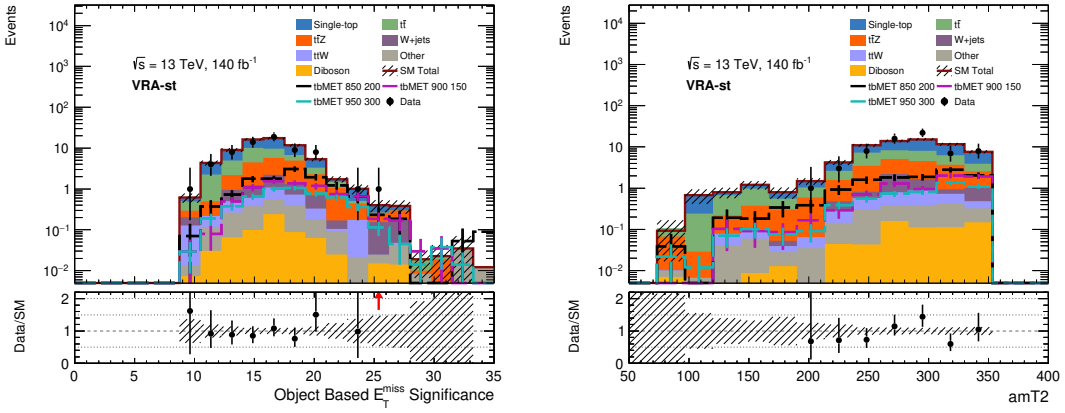

(a) $E_{\mathrm{T}}^{\mathrm{miss}}$ significance (b) am_{T2}

Figure 5.18: Distributions in single-top VR, VRA-st, for the $E_{\mathrm{T}}^{\mathrm{miss}}$ significance (a) and am_{T2} (b). In each subfigure the coloured, solid histograms show the SM backgrounds scaled to 140 fb^{-1}. The hatched area represents the statistical error on the prediction. The black points show the data with statistical error bars. Overlaid are dashed lines of representative signal points. The lower panel contains the ratio of data over SM prediction.

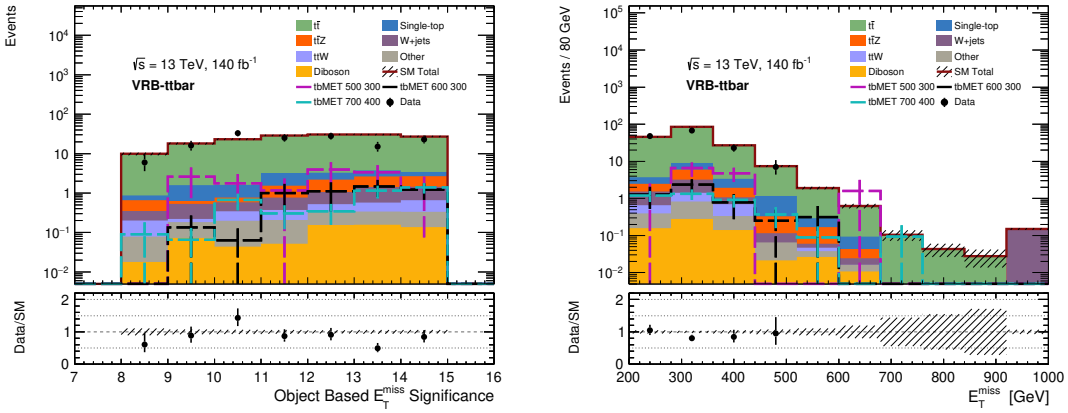

(a) $E_{\mathrm{T}}^{\mathrm{miss}}$ significance (b) $E_{\mathrm{T}}^{\mathrm{miss}}$

Figure 5.19: Distributions in VRB-ttbar for the $E_{\mathrm{T}}^{\mathrm{miss}}$ significance (a) and $E_{\mathrm{T}}^{\mathrm{miss}}$ (b). In each subfigure the coloured, solid histograms show the SM backgrounds scaled to 140 fb^{-1}. The hatched area represents the statistical error on the prediction. The black points show the data with statistical error bars. Overlaid are dashed lines of representative signal points. The lower panel contains the ratio of data over SM prediction.

To all three validation regions, the results from the background-only fits, listed in Table 5.7 have been applied. The results are summarised in Table 5.13 for the A-region fit, and in Table 5.14 for the B-region fit. An overall very good post-fit agreement between data and the MC prediction is observed. For the A-type regions, the agreement is above 95%, for the b-type regions above 85%. Table 5.15 shows how the normalisation factors apply to the SRs and the predicted SM background events. Only MC events are shown, as the regions are still blinded. We observed that in the A- and B-type region, the fitted SM background events are within 1% of the expected numbers. Therefore, the high significances above 3σ, reported in Section 5.3 remain. Based on the results from the background-only fit, and following this successful validation, a model-dependent fit is performed as described in the next section.

tb+$E_{\mathrm{T}}^{\mathrm{miss}}$ VRA	VRAst	VRttZ
Observed events	65	52
Fitted bkg events	67.69 ± 8.85	50.57 ± 3.18
Fitted W events	3.42 ± 0.06	0.22 ± 0.00
Fitted ttW events	1.88 ± 0.03	6.17 ± 0.10
Fitted diboson events	0.65 ± 0.01	1.36 ± 0.02
Fitted ttbar events	17.69 ± 0.30	14.47 ± 0.24
Fitted st events	24.72 ± 8.63	2.01 ± 0.70
Fitted ttZ events	17.85 ± 2.36	23.75 ± 3.14
Fitted other events	1.49 ± 0.03	2.58 ± 0.04
MC exp. SM events	68.69	47.24

Table 5.13: Fit results for the background only-fit in the A-type validation regions, for an integrated luminosity of $140\,\mathrm{fb}^{-1}$. Nominal MC expectations (normalised to MC cross-sections) are given for comparison. The errors shown are statistical only. Uncertainties on the fitted yields are symmetric by construction, where the negative error is truncated when reaching to zero event yield.

tb+$E_{\mathrm{T}}^{\mathrm{miss}}$ VRB	VRBtt	VRttZ
Observed events	146	52
Fitted bkg events	132.33 ± 12.40	47.92 ± 3.25
Fitted W events	3.30 ± 0.06	0.22 ± 0.00
Fitted ttW events	1.21 ± 0.02	6.18 ± 0.10
Fitted diboson events	0.64 ± 0.01	1.36 ± 0.02
Fitted ttbar events	113.57 ± 12.46	10.92 ± 1.20
Fitted st events	6.63 ± 0.11	2.31 ± 0.04
Fitted ttZ events	5.93 ± 0.77	24.34 ± 3.15
Fitted other events	1.04 ± 0.02	2.58 ± 0.04
MC exp. SM events	168.20	47.24

Table 5.14: Fit results for the background only-fit in the B-type validation regions, for an integrated luminosity of $140\,\mathrm{fb}^{-1}$. Nominal MC expectations are given for comparison. The errors shown are statistical only. Uncertainties on the fitted yields are symmetric by construction, where the negative error is truncated when reaching to zero event yield.

Signal Regions	SRA	SRB
Observed events	-	-
Fitted bkg events	6.07 ± 1.18	16.57 ± 1.27
Fitted W events	0.95 ± 0.13	2.29 ± 0.13
Fitted ttW events	0.08 ± 0.01	0.61 ± 0.04
Fitted diboson events	0.15 ± 0.02	0.82 ± 0.05
Fitted ttbar events	0.11 ± 0.01	3.73 ± 0.46
Fitted st events	2.32 ± 0.87	2.51 ± 0.15
Fitted ttZ events	2.38 ± 0.45	6.26 ± 0.88
Fitted other events	0.07 ± 0.01	0.36 ± 0.02
MC exp. SM events	6.06	16.70
$m(\tilde{t}/\tilde{b}, \tilde{\chi}_1^0) = (900,150)$	10.58 ± 0.63	-
$m(\tilde{t}/\tilde{b}, \tilde{\chi}_1^0) = (500,300)$	-	15.80 ± 3.86

Table 5.15: Fit results for the background only-fit in the blinded signal regions, for an integrated luminosity of 140 fb^{-1}. The MC is fitted with the normalisation factors from the background-only fir to data in the control regions. Nominal MC expectations are given, as well as one example signal point for both of the regions. The errors shown are statistical only. Uncertainties on the fitted yields are symmetric by construction, where the negative error is truncated when reaching to zero event yield.

5.5 Results

This section documents a first set of results when running the SRA and SRB model-dependent fits independently without applying systematic uncertainties. A combined statistical combination of both regions is foreseen, as well as including the full set of systematics. Figure 5.20 shows the expected exclusion contours for SRA (a) and SRB (b) with statistical uncertainties applied. Additionally, the observed and expected contours from the previous $tb+E_{\text{T}}^{\text{miss}}$ analysis for the 1L channel only, as well as for the combination with the 0L channel are shown for comparison. Comparing the expected exclusion for the bulk region to the expected result from the previous 1L search, we achieve an increase in exclusion of 220 GeV in excluded top-/bottom-squark masses for a 200 GeV neutralino. In the compressed region, our result closes the un-excluded corridor from the previous 1L analysis for a mass difference between the top/squark lower than 300 GeV and extends excluded neutralino masses up until 450 GeV for 750 GeV top-/bottom-quarks.

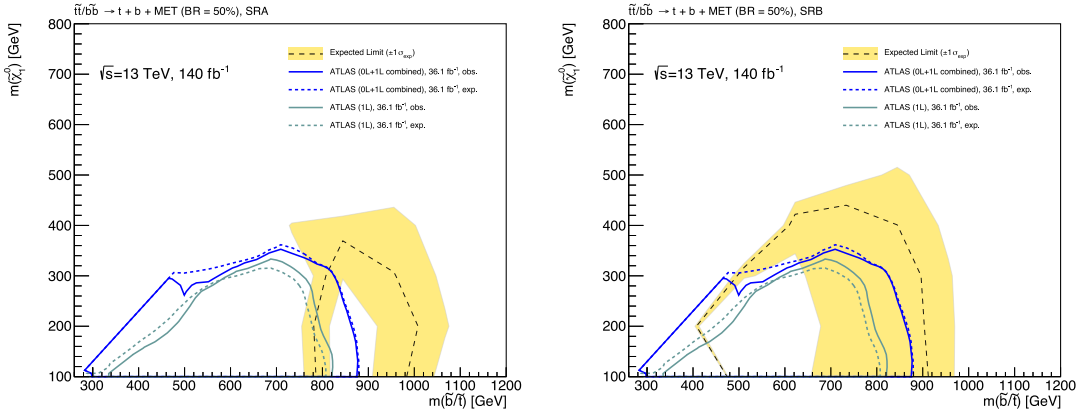

(a) SRA exclusion contour

(b) SRB exclusion contour

Figure 5.20: Expected model-dependent exclusion limits for SRA (a) and SRB (b) scaled to 140 fb^{-1}, no systematic uncertainties are included. The limit exclusion contours are shown in the sbottom mass (x-axis) and neutralino mass (y-axis) plane. The model-dependent fits use the background normalisation factors obtained from background-only fits in single-top and $t\bar{t}Z$ CRs (for SRA) and $t\bar{t}$ and $t\bar{t}Z$ CRs (for SRB). Additionally shown are the observed and expected results from the early Run 2 analysis in the 0L channel and the combination with the 1L channel.

5.6 Summary and Conclusion

In this section I presented the search for a top-/bottom-squark pair, decaying asymmetrically into the 1L $tb + E_{\text{T}}^{\text{miss}}$ final state. We defined two dedicated SRs for which I showed expected exclusion contours obtained with a background-only. By the time of the submission of this thesis, the statistical combination of the two regions is still outstanding, as well as the application of the full set of systematic uncertainties. After these steps, the analysis can be unblinded, which means the finalised region definitions are applied to the full Run 2 data set with 140 fb^{-1}. From the expected exclusion contours, displayed in Figure 5.20, I can conclude that the combination of the two signal regions will result in a total exclusion contour which exceeds the previous result from the ATLAS collaboration by at least 220 GeV, depending on the region. A combination with the 0L channel, published by the ATLAS collaboration in 2021 [29], will improve the sensitivity further, as already shown for the difference between the observed contours from the 1L only search and the combination with the 0L search in the previous analysis using 36.1 fb^{-1}.
While the search I described in this chapter assumes a R-Parity-conserving model, the following chapter summarises a contrary SUSY search, targeting a MSSM in which R-Parity violation is assumed.

Chapter 6

Search for R-parity-violating Supersymmetry

This chapter describes the full Run 2 R-parity-violating multijet (RPV multijet) analysis, searching for pair-produced gluinos decaying into an all-hadronic final state.
Massive gluinos decay either directly via the RPV coupling λ'' into three SM quarks, or into five quarks via a cascade decay through an intermediate neutralino. The quarks hadronise into jets, as discussed in Section 2.1.1. Both processes are shown in Figure 6.1.

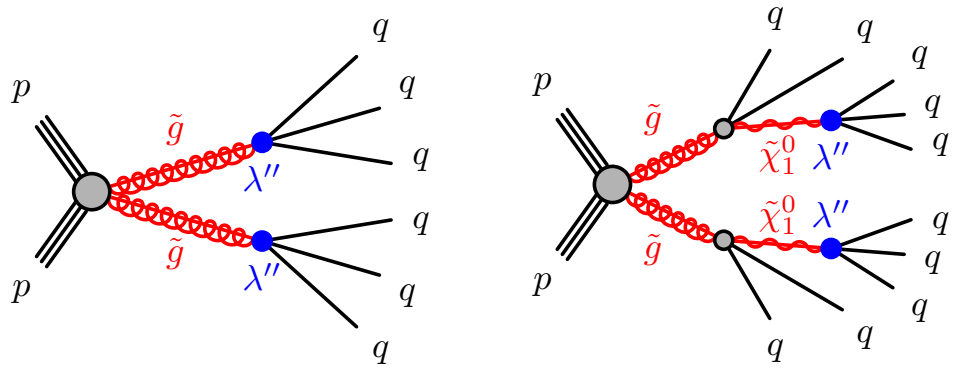

(a) 2×3 scenario

(b) 2×5 scenario

Figure 6.1: Direct gluino decay into $2{\times}3$ jets (a) and gluino cascade decay into $2{\times}5$ jets via $\tilde{\chi}_1^0$. Both decays are enabled by the R-parity-violating coupling λ''.

My work includes the following part of this analysis:

- the studies on signal/background kinematics
- the truth matching studies for ML inputs
- the early ntuple productions, implementing new truth matching procedure
- the preliminary cut-and-count analysis, including studies with b-jets
- the setup of the statistical framework

The results have been published by the ATLAS collaboration in August 2023 [179]. The following description follows closely the description in the ATLAS publication.

The RPV multijet all-hadronic final state has been studied previously by the ATLAS [35–37] and CMS [38–40, 180] collaborations. Results from the early Run 2 ATLAS analysis

are shown in Figure 6.2. The direct gluino decay model search applied to data showed no excess, but also no new exclusion, preserving the existing limit of 917 GeV at a CL of 95% from Run 1 [36]. Also for the 2×5 scenario, the search in data showed no excess and therefore limits in the gluino-neutralino mass plane were set to exclude gluino masses below 1.85 TeV for a neutralino mass of 1 TeV [37].
These results leave an unexplored region for gluino masses of ~ 1.1 TeV. In the context of the hierarchy problem, a small gluino mass in this region is considered more "natural" and therefore preferred, as discussed in Section 2.2.2. It would help to minimise the fine-tuning required to stabilise the mass of the Higgs boson, while keeping it well below the Planck scale.
While in R-parity-conserving models the gluino mass has been excluded up to 2.45 TeV in certain model scenarios [41], a low-mass RPV-decaying gluino still leaves unexplored regions. Therefore, the gaps from the early Run 2 search have a strong theoretical motivation, highlighting the need for a full Run 2 search.

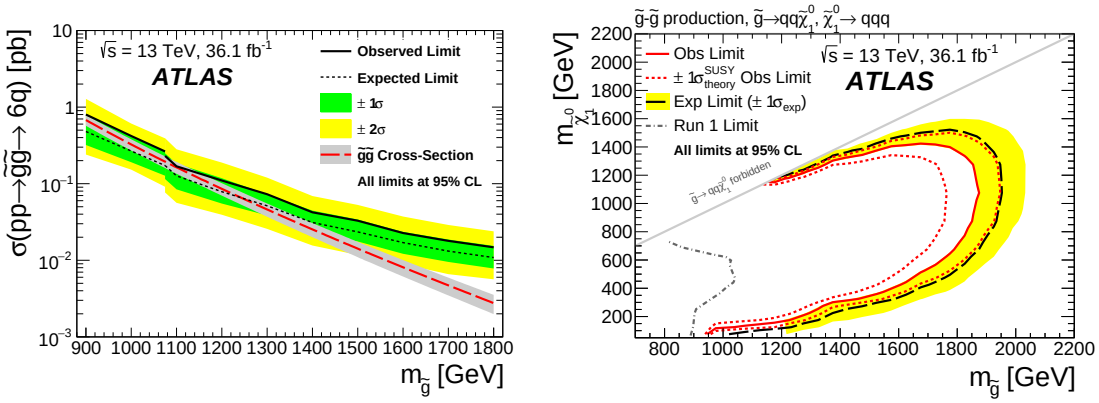

(a) Observed exclusion for 2×3 model

(b) Observed exclusion for 2×5 model

Figure 6.2: Results from the most recent ATLAS analysis targeting R-parity-violating gluino pairs decaying in multi-jet final states [37]. Figure (a) shows the observed exclusion curve for gluino masses in the 2×3 model. Figure (b) displays the exclusion for gluino and neutralino masses in the 2×5 model.

6.1 Signal Phenomenology

Gluino pairs ($\tilde{g}\tilde{g}$) are mainly produced through two mechanisms:

$$\text{gluon} - \text{gluon fusion} : gg \to \tilde{g}\tilde{g}$$
$$\text{quark} - \text{antiquark annihilation} : q\bar{q} \to \tilde{g}\tilde{g}.$$

From the PDF distributions shown in Figure 4.2, one can infer that gluon-gluon fusion, where the two gluons from the initial state protons interact and produce a pair of gluinos, is the dominant production mechanism for gluino pairs. While the quarks' PDF predict a smaller interaction probability than the gluon's PDF at high energies, this process still contributes to gluino pair production. The leading order production processes for gluino pairs are shown in Figure 6.3.

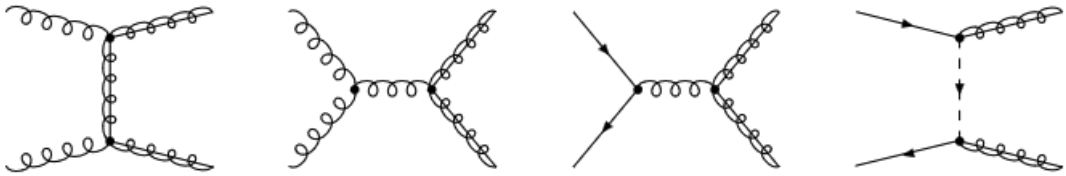

Figure 6.3: Main production processes for a gluino pair at the LHC. The mediator in the diagram on the right can be a usual quark or squark. The image is taken from [181].

For the gluino decay, two scenarios are studied. Both involve an R-parity-violating vertex with the λ''_{ijk} coupling. As discussed in Eq. (2.11) in Section 2.2, the coupling describes an interaction between one down-type and two up-type quarks, therefore also called UDD-coupling. The vertex marked with a blue dot in Figure 6.1(a) is an effective representation of the interaction

$$\tilde{g} \to q + \tilde{q}', \tag{6.1}$$

with $\tilde{q}'$, a supersymmetric off-shell quark, decaying immediately via λ'' into

$$\tilde{q}' \to q' + q''. \tag{6.2}$$

The same holds for the decay of the neutralino in Figure 6.1(b), with

$$\tilde{\chi}_1^0 \to q + \tilde{q}' \tag{6.3}$$

and the off-shell squark $\tilde{q}'$ decaying via Eq. (6.2) into two quarks.
Obeying flavour and charge conservation, λ''_{ijk} represents 18 combinations of R-parity-violating up- and down-type (anti-)quark interactions, namely

$$\begin{array}{lll} \lambda''_{112} : \ uds & \lambda''_{113} : \ udb & \lambda''_{123} : \ usb \\ \lambda''_{212} : \ cds & \lambda''_{213} : \ cdb & \lambda''_{223} : \ csb \\ \lambda''_{312} : \ tds & \lambda''_{313} : \ tdb & \lambda''_{323} : \ tsb \end{array}$$

and the same nine combinations for antiquarks.

In this analysis, two couplings are studied in particular:
the λ''_{112} and λ''_{113}, which define decays into *uds* and *udb* final states, respectively. These are, among all 18 combinations, the ones with the two lightest quarks from the first generation.

For the direct decay, the 6-jet model, we generated signal samples with gluino masses from 900 to 1800 GeV in steps of 100 GeV with the MC generators listed in Table 4.1 of Section 4.3. For each mass point two different samples for the *uds* and *udb* final states were produced (UDS and UDB), where the branching ratio into the corresponding final states is assumed to be 100%. For the cascade decay, the 10-jet model, we also produced UDB and UDS samples. In each set of samples, the gluino masses range from 1000 GeV to 2400 GeV, while the intermediate neutralino masses vary between 50 and 1900 GeV.

The main background in the RPV multijet search is dijet production, which is by far the most produced process at the LHC, as shown in Figure 2.4. By scattering or annihilating two partons of the initial proton, a quark or gluon pair with high transverse momentum is produced. Through additional initial and final radiation, more than two jets can be observed, mimicking the signal model from which at least 6 jets are expected.
The production cross-section of dijet events at the LHC is on the order of 10^6 pb. In contrast, the gluino pair production cross-section for gluinos with a mass of ~ 1 TeV is on the order of 1 pb and even lower for gluinos with higher masses, as shown in Figure 2.8. Despite additional QCD vertices suppressing the dijet processes with large jet multiplicities, the amount of background events is many orders of magnitude larger than the studied signal processes. At the same time, the final states of dijet events with high jet-multiplicities and the RPV multijet signal model are basically indistinguishable in terms of particle content.

Another SM background process is all-hadronic $t\bar{t}$ decays. While considered negligible for most of the analysis, $t\bar{t}$ becomes more significant in cases where the UDB model is studied and selection requirements on *b*-tagged jets are implied. This is discussed in Section 6.3.1.

We developed two dedicated analysis strategies in parallel, each using a different method to overcome the enormous challenges of this search. One, a cut-and-count analysis, can be considered to be a more "classical" SUSY analysis, while the other uses state of the art machine learning techniques to reconstruct the mass of the gluinos.

6.2 Analysis Strategies

The analysis is split into two approaches: a "standard" cut-and-count analysis (CCA, Section 6.3), and a machine learning based analysis (ML, Section 6.4), attempting to reconstruct the gluino mass.
While the CCA allows for easier re-interpretation of the results from a theoretical point of view, it also provides a solid comparison to the ML based approach.

6.2.1 Trigger Strategy

A variable we use, and which is commonly used for all-hadronic signatures, is the sum of all transverse momenta of jets in the event, H_{T}, see Eq. (5.5) of Section 5.2.3.
The analysis requires events to pass a trigger based on H_{T}, which sets a threshold of 850-1000 GeV on H_{T}, depending on the data-taking period.
As discussed in Section 3.2.5, the first level (L1) of the selection is provided by hardware triggers. At this stage, events are required to contain at least one jet with transverse momentum greater than 100 GeV (`L1J100`).
In the following software-based HLT stage, all jets within the event are used to calculate H_T, which is required to be $H_{\mathrm{T}} > 1000$ GeV for data recorded in 2018, 2017, and 2016 (`HLT_ht1000_L1J100`) and $H_{\mathrm{T}} > 850$ GeV for 2015 data (`HLT_ht850_L1J75`) [166].
In order to ensure full trigger efficiency, an offline selection of $H_{\mathrm{T}} > 1100$ GeV and $p_{\mathrm{T}} > 200$ GeV for the leading-p_{T} jet is applied. These two thresholds are found from the trigger turn-on curves for the HLT and L1 triggers, shown in Figure 6.4 [166]. Studies with MC signal events showed that the `HLT_ht1000_L1J100` trigger is more than 95% efficient across the different mass points generated. Therefore, no alternative trigger has been investigated.

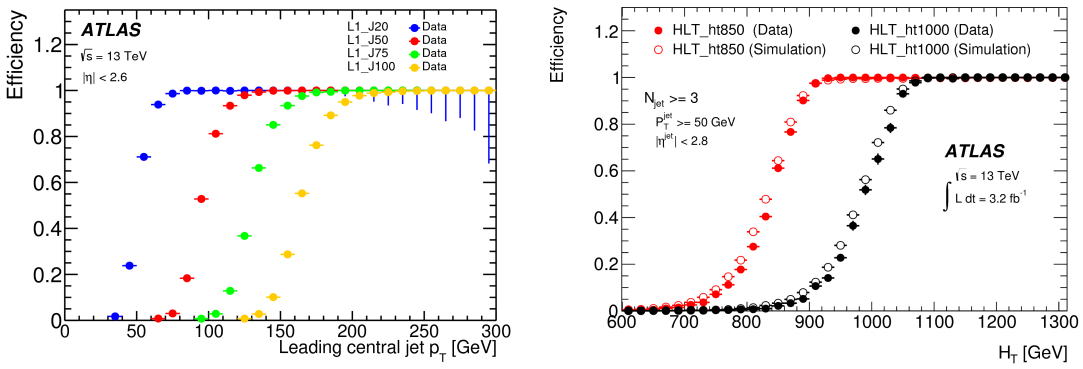

(a) L1 turn-on curve

(b) HLT turn-on curve

Figure 6.4: Turn-on curves for L1 jet trigger (a) and HLT_ht trigger (b), which combine to the trigger used in this analysis, `HLT_ht1000_L1J100` [166].

6.2.2 Pre-selection

To study the kinematics of signal and background processes, events passing pre-selection criteria have been selected. The selections require the events to pass the H_{T} trigger and requirements to ensure the trigger plateau, discussed previously. The pre-selection criteria are summarised in Table 6.1.

Selection Criteria	Value
Trigger selection	Passed `HLT_ht1000_L1J100`
p_{T} (j_1) [GeV]	≥ 200
H_{T} [GeV]	≥ 1100

Table 6.1: Pre-selection requirements

Figure 6.5 shows distributions at pre-selection level for signal and background processes for low level kinematic variables. The variable "HT" in Figure 6.5(a) is the sum of the transverse momenta of all jets in the event with a transverse momentum more than 50 GeV, corresponding to signal jets as defined in Section 3.3.2.
The p_{T} of the p_{T}-leading jet, shown in Figure 6.5(b) shows a small peak for the dijet background distribution at low p_{T} values of ~ 600 GeV, which is an artefact from the H_{T} selection and the trigger.
The distribution of the jet-multiplicities in Figure 6.5(c) peaks at lower values for dijet events than for the considered signal events, as expected. We see an "excess" for high jet multiplicities which is explained by the poor modelling of dijet MC at high numbers of jets. One sees further in Figure 6.5(d), that the dijet and $t\bar{t}$ background events have a wider span in $\Delta\eta_{12}$ than signal events. The variable $\Delta\eta_{12}$ describes the distance in η between the two leading p_{T} jets of an event.
The Figures 6.5 also show the agreement between data and the MC modelling of the SM background and signal processes. The ratio between data and MC simulations for H_{T} and $p_{\mathrm{T}}(j_1)$ exhibits a consistent flat distribution at around 0.95, with exceptions appearing in the high-value tails within the bounds of statistical uncertainty. This suggests a slight overestimation of data by the MC simulation, despite the overall flat distribution.
The agreement between data and MC for the number of jets reveals a distinct trend beginning from around 7 jets per event. This trend strongly indicates that the dijet MC samples do not adequately model the data at higher jet multiplicities, which are precisely the multiplicities this analysis is targeting. As a result, specialised background estimation methods are required, which are explained in detail in Section 6.3.2 and Section 6.4.2.

6.2.3 Discriminating Variables

Discriminating variables are defined which help differentiating between signal and background events. Event shape variables are a useful tool to study the topology of events with high jet multiplicities, describing the isotropy of the energy flow in an hadronic event [182]. The variables considered here can all be derived from the linearised sphericity tensor [183, 184],

$$M_{xyz} = \frac{1}{\sum_i |\vec{p_i}|} \sum_i \frac{1}{|\vec{p_i}|} \begin{pmatrix} p_{x,i}^2 & p_{x,i}p_{y,i} & p_{x,i}p_{z,i} \\ p_{y,i}p_{x,i} & p_{y,i}^2 & p_{y,i}p_{z,i} \\ p_{z,i}p_{x,i} & p_{z,i}p_{y,i} & p_{z,i}^2 \end{pmatrix}, \tag{6.4}$$

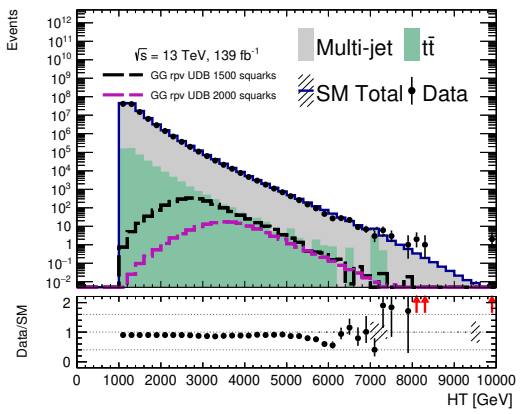

(a) H_T

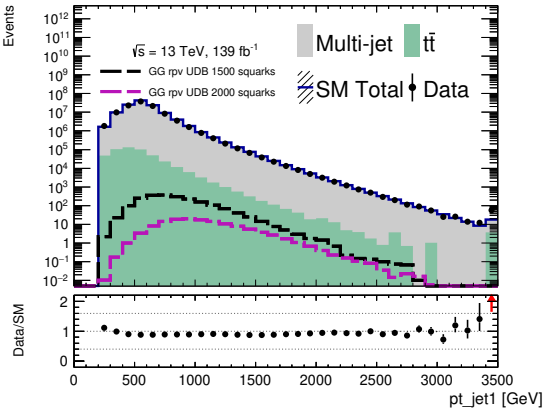

(b) $p_{\mathrm{T}}(j_1)$

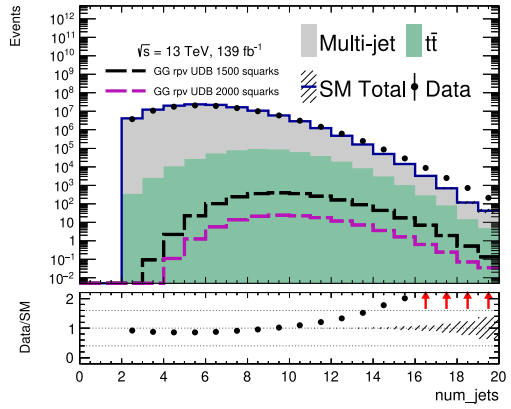

(c) Number of jets

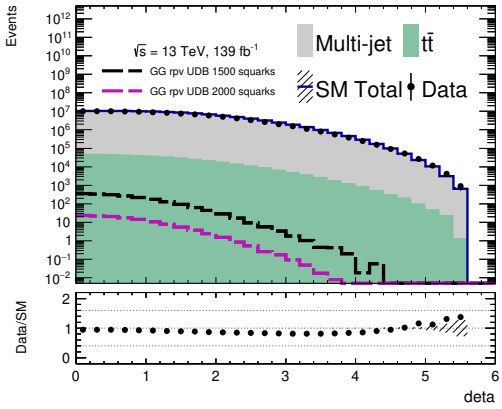

(d) $\Delta\eta_{12}$

Figure 6.5: Data-MC comparison distributions variables used in this analysis: the sum of transverse momenta of all jets, H_{T} (a), the leading jet's p_{T} (b), the number of jets (c), and the $\Delta\eta_{12}$ between the two leading jets per event. The number of events is scaled to 139fb^{-1}. Statistical uncertainties are shown. Pre-selection requirements are applied to the distributions, with signals overlaid for comparison.

where $p_{x,i}, p_{y,i}$, and $p_{z,i}$ are the x-,y-, and z-components of the jet axis vectors $\vec{p_i}$ in the event. The sum of three eigenvalues of the normalised tensor with $\lambda_1 \geq \lambda_2 \geq \lambda_3$ fulfil $\sum_i \lambda_i = 1$.
From these eigenvalues four variables are derived which can be used to interpret the isotropy of an hadronic event:

- Sphericity S, which is defined as

$$S = \frac{3}{2}(\lambda_2 + \lambda_3), \tag{6.5}$$

interprets the sphericity of an event. For *pencil-like* events, thus two jets back-to-back, it has larger values close to 1, while for isotropic events it has smaller values towards 0.

- Aplanarity A, defined as

$$A = \frac{3}{2}\lambda_3, \tag{6.6}$$

quantifies the degree to which an event deviates from a perfect plane. In other words, it is a measure of the three-dimensionality of an event. It ranges from 0 to 0.5, where small values indicate planar events, while larger values point towards higher isotropy of the event.

- C-parameter C, which is a linear combination of the eigenvalues λ_i,

$$C = 3(\lambda_1\lambda_2 + \lambda_1\lambda_3 + \lambda_2\lambda_3). \tag{6.7}$$

It involves the products of pairs of eigenvalues. In the case of a two-jet event, where all momenta lie in a plane, one of the eigenvalues becomes approximately zero, leading to a significant reduction of the C-parameter and thus small values. Higher values indicate events more likely to consist of more jets.

- D-parameter D,

$$D = 27(\lambda_1\lambda_2\lambda_3), \tag{6.8}$$

is the cubic product of all three eigenvalues. If all jet momenta lie in the same plane, one of the eigenvalues of the momentum tensor becomes approximately zero, making the D-parameter also zero. Therefore, the D-parameter also provides sensitivity to the planarity of the event, vanishing for planar events and becoming non-zero when the event involves a distribution of momenta in three dimensions.

While we studied all four event shape variables, we found the C variable to be the most useful in terms of discrimination between background and signal distributions. Figure 6.6 shows the C variable at pre-selection level for data and MC. We observe that the signal distributions peak more distinct towards higher values of C than the dijet and $t\bar{t}$ backgrounds.

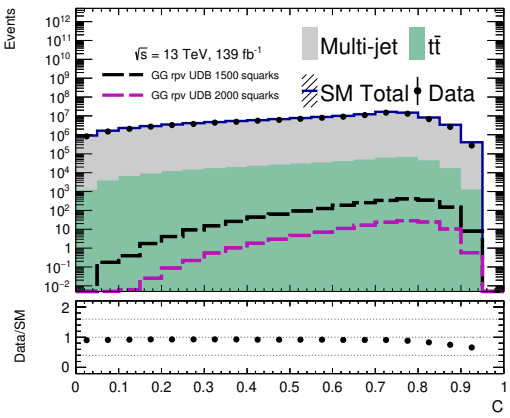

Figure 6.6: Data-MC comparison distribution for the event shape variable C used in this analysis, scaled to 139fb^{-1}. Pre-selection requirements are applied to the distributions, with signal overlaid for comparison. Statistical uncertainties are included but too small to be seen by eye.

6.3 Cut and Count Analysis

I performed a preliminary CCA, based on the principles of Control, Validation, and Signal Regions, as explained in Section 4.4, to test the workflow of the analysis and to get a first estimate for the potential sensitivity of the full Run 2 analysis.

The selections to define the CR,VR, and SR are listed in Table 6.2. For all the regions, I applied the pre-selections listed in Table 6.1 prior to the region specific selections.
The SR is defined with a high jet-multiplicity of more than seven jets, while the VR and CR are requiring lower jet-multiplicities. Additionally, the SR uses a larger selection on H_{T} to increase signal efficiency and $|\Delta\eta_{12}| < 1.0$, which is inverted for the CR and VR to suppress signal contamination.

Selection	CR	VR	SR
n_{jets}	≤ 4	$= 5$	≥ 7
H_{T} [GeV]	> 1100	> 1100.0	> 2000
$p_{\mathrm{T}}(j_1)$ [GeV]	> 140	> 140	-
$p_{\mathrm{T}}(j_3)$ [GeV]	-	-	> 470
$p_{\mathrm{T}}(j_7)$ [GeV]	-	-	> 170
$\lvert\Delta\eta_{12}\rvert$	> 1.5	> 1.5	< 1.0

Table 6.2: Region definitions for CR,VR, and SR for preliminary sensitivity studies.

Using these region definitions, I performed data to MC comparison studies. Figure 6.7 shows this comparison in one-bin plots for the CR and VRs. Good agreement between the full Run 2 data and MC generated multijet background scaled to 139 $\mathrm{fb}^{-1}$is observed in both regions. The 1.5 TeV test signal point revealed no significant signal contamination in neither of the two regions.

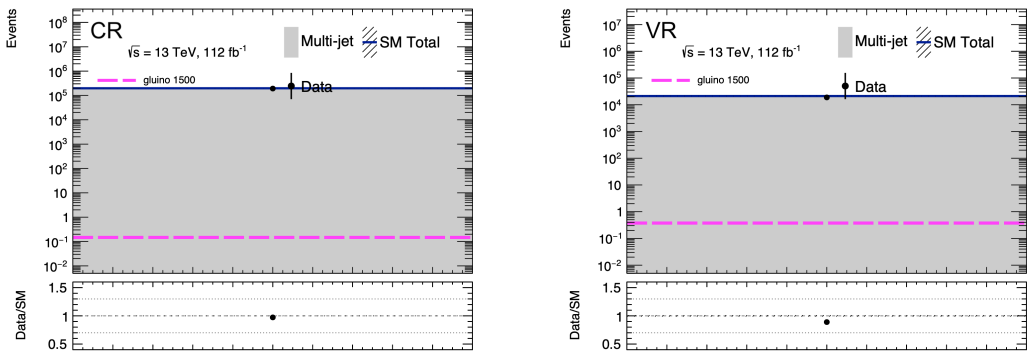

(a) Control Region

(b) Validation Region

Figure 6.7: One-bin yield plot for the CR and VR showing the data-MC agreement in both regions being close to one. Statistical uncertainties are included but too small to be seen by eye. The lower panels show the ratio of data to the MC background prediction.

Using the SR selections from Table 6.2, I studied the expected significance for specific signal points in Figure 6.8. The significance is calculated using the standard ATLAS recommendation with an uncertainty of 30% [158].

Compared to the one-bin plots in Figure 6.7, I included the $t\bar{t}$ background. As one can see, the contribution is in the order of a few single events, compared to dijets events in the order of 10^2, and are therefore negligible.

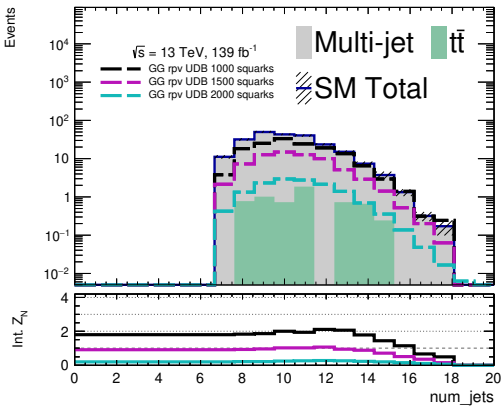

(a) Number of jets, UDB

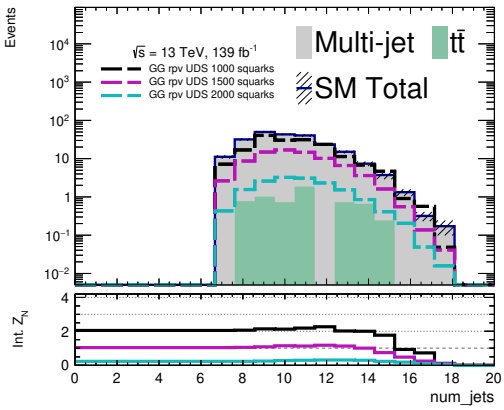

(b) Number of jets, UDS

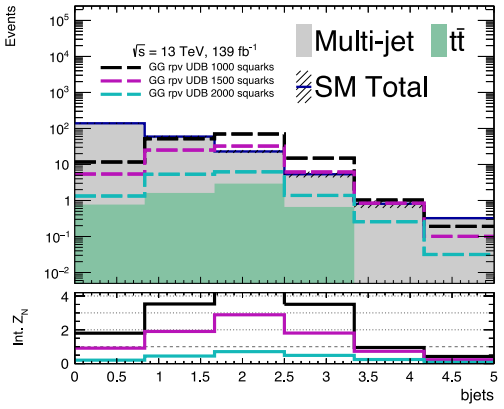

(c) Number of b-jets, UDB

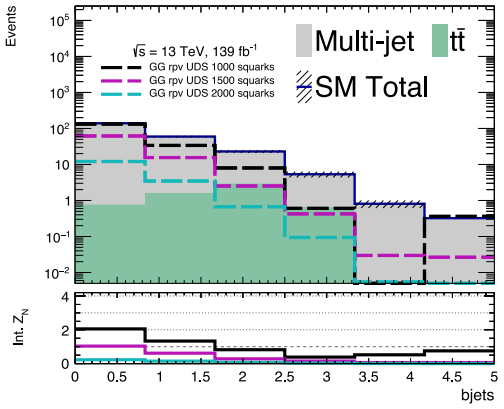

(d) Number of b-jets, UDS

Figure 6.8: Distributions of data, SM background MC and UDB (a,c) and UDS (b,d) signal points in the preliminary signal region, scaled to the full Run 2 dataset with 139 fb^{-1}. Statistical uncertainties are shown as hatched areas.The lower panels shows the integrated significance with 20% uncertainty as a function of potential additional selections in the shown variable

A background-only fit returns a background normalisation factor for the dijet background of 0.873 ± 0.003. For this fit, I only applied statistical systematics. Comparing this value to the ratio of data to MC background yields in Figure 6.7(b) shows that the normalisation factor reasonably reduces the MC prediction to match the data. Following this, I performed a model-dependent fit in the defined SR for all available signal mass points. The expected exclusion limits resulting from this fit can be seen in Figure 6.9 for the UDS and UDB samples respectively. I applied no systematic uncertainties for these studies.
One observes that compared to the early Run 2 analysis shown in Figure 6.2(a), a large increase in sensitivity is to be expected, even without further optimisation of the simple CCA regions defined in Table 6.2. These studies show that the possible sensitivity reach in an idealised scenario could be up to 1.8 TeV as seen in Figure 6.9.

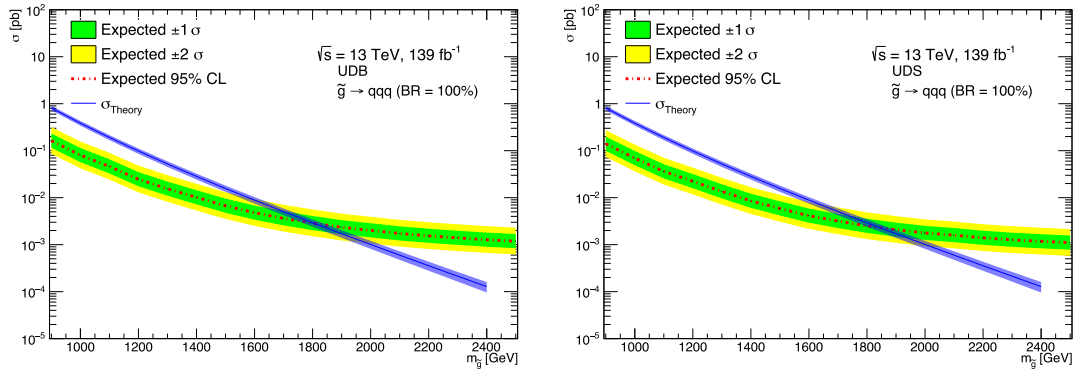

(a) UDB Exclusion

(b) UDS Exclusion

Figure 6.9: Exclusion limits for the UDB (a) and UDS (b) models based on the preliminary region definitions. No systematic uncertainties are applied, only statistical, which are shown as the yellow and green band around the expected contours.

6.3.1 B-jet requirements

Figures 6.8(c) and (d) show the distributions of the number of b-tagged jets in the SR and the related significance for the UDB and UDS mass points. As can be seen, the significance for the UDB mass points could improve by requiring two or more b-jets in the SR. To study the effect of this additional requirement in the preliminary region definitions for UDB, and vice-versa a b-jet veto for the UDS mass points, I defined two additional sets of preliminary CR, VR, and SR regions.
The regions CR-2b,VR-2b, and SR-2b require, additionally to the selections summarised in Table 6.2, at least two b-jets, and are only applied to the UDB mass points. For the UDS points, the other set of regions, CR-0b,VR-0b and SR-0b are setting a veto on b-tagged jets in the events, as they are not expected from the decay of the gluinos into the UDS final states.

Figure 6.10 shows two significance plots for the SR-0b and SR-2b regions. The distributions of the integrated significance Z_N is shown and how additional selections on the shown variable would affect the integrated significance in the region. Great enhancement of the signal significance by almost a factor of 2 can be observed for the UDB model when including the b-tagged jet requirement. Following the same procedure with a background-only fit and a fully blinded exclusion fit, I obtained the limit curves in Figure 6.11.

This study shows that an additional requirement of at least two b-tagged jets in a signal region targeting the UDB mass grid improves the exclusion by around 100 GeV compared to a signal region without this requirement (shown in Figure 6.9(a)). The veto on b-jets for the UDS mass grid has no significant effect on the exclusion, as shown in Figure 6.11(b) compared to Figure 6.9(b).
The results of this study are transferred to the final CCA and ML based analysis strategies, where additional strategies for the UDB model including requirements on b-tagged jets are outlined.

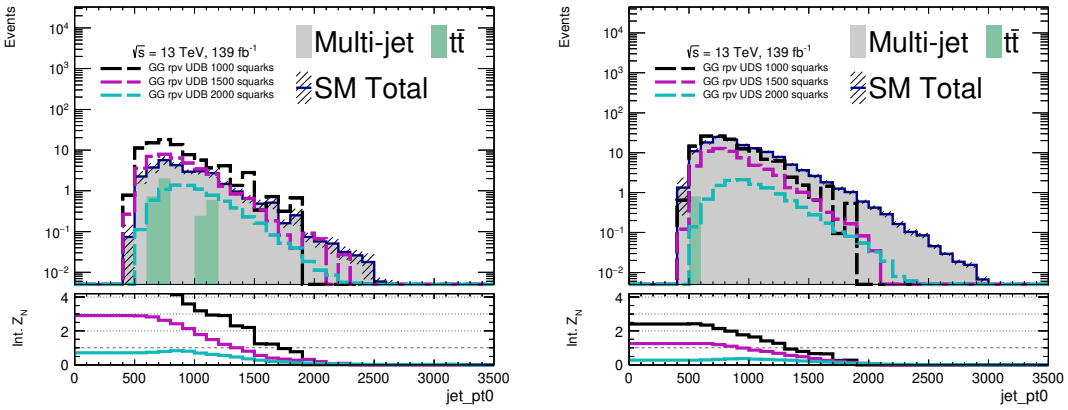

(a) SR-2b for UDB

(b) SR-0b for UDS

Figure 6.10: Leading-jet p_T distribution for the SM backgrounds and signal-mass points of the UDB (a) and UDS (b) grids in two SR with at least two b-jets (a) or a b-jet veto (b). The lower panels shows the integrated significance with 20% uncertainty as a function of potential additional selections in the shown variable.

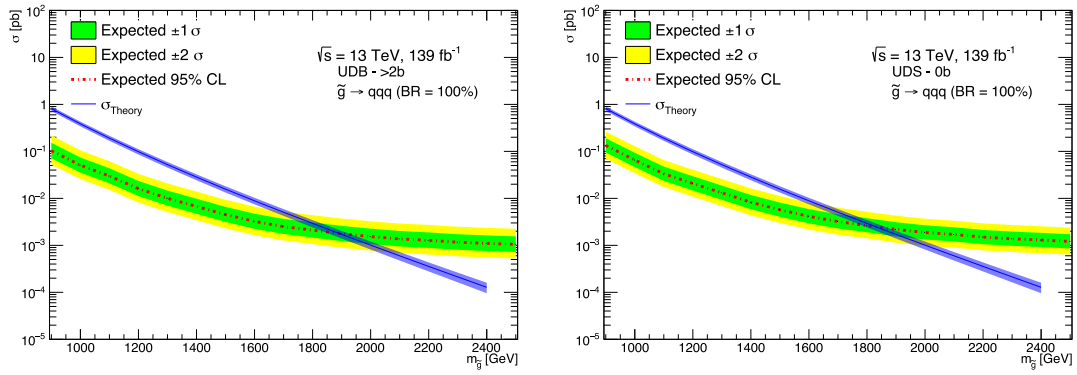

(a) SR-2b for UDB

(b) SR-0b for UDS

Figure 6.11: Exclusion limits for the UDB (a) and UDS (b) models based on regions which require at least 2 b-jets (for UDB) and a b-jet veto (for UDS).

6.3.2 Final CCA Strategy

The jets from the heavy gluino decay are likely to have large transverse momenta. The combined information of jet multiplicity and the p_{T} of these jets has high discrimination power to distinguish signal from background in all-hadronic final states. Counting the jets above a given transverse momentum threshold, referred as "jet-counting method", has been used in previous ATLAS searches [36] and it is adopted as final strategy for the CCA presented in this thesis. My preliminary studies showed the potential of a CCA. The final method was further developed and finalised by the analysis team, which I outline here for completeness. The following section is a summary of the CCA strategy as outlined in [179].

In this method, the number of events with at least n jets above a certain p_{T} threshold are counted. Figure 6.12 displays two distributions as a function of the p_{T} threshold, where the number of events with more than 6 (7) jets above the threshold are shown for signal and SM background. One observes that for high jet p_{T} requirements and increased jet multiplicity, the sensitivity to the signal points increases.

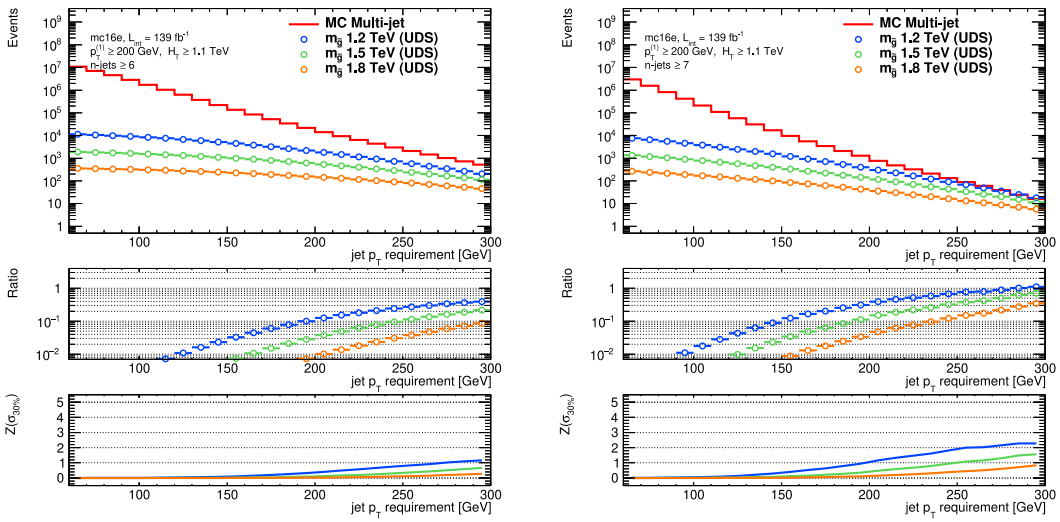

(a) ≥ 6 jets (b) ≥ 7 jets

Figure 6.12: Distributions showing the number of events for more than 6 (a) and more than 7 (b) jets above the shown p_{T} threshold at pre-selection level. The MC signal and SM background predictions are scaled to 139 fb^{-1}. The middle panels show the ratio between the expected data and MC events per bin, the lower panels give the significance per bin including a 30% uncertainty applied.

Signal Regions

This analysis targets a wide range of gluino masses for the 2×3 model, and a large variety of masses and mass differences for the 2×5 model. We, the analysis team, conducted extensive studies to isolate optimal SRs for the different mass ranges according to their signatures and kinematics. It was found that adding additional selections on the C-parameter, introduced in Eq. (6.7) of Section 6.2, and on the number of b-tagged jets for the UDB samples, improves the significance further as shown in Section 6.3.1.

Table 6.3 summarises all SRs, which we optimised for different mass regions of the signal models.

	n_{jets}	$p_{\text{T}}(j)$ [GeV]	C	$n_{b-\text{tags}}$	Target model
SR1	≥ 7	180	≥ 0.90	-	(2×3) low
SR2	≥ 7	220	≥ 0.90	-	(2×3) medium
SR3	≥ 7	240	≥ 0.90	-	(2×3) high
SR4	≥ 8	180	≥ 0.85	-	(2×5) medium
SR5	≥ 8	210	≥ 0.85	-	(2×5) high
SR1bj	≥ 7	180	≥ 0.85	≥ 2	(2×3) UDB high
SR2bj	≥ 8	180	≥ 0.85	≥ 2	(2×5) UDB high

Table 6.3: Selection criteria for all SRs used for the 2×3 and 2×5 models. The number of jets indicates the amount of jets above the given p_{T} threshold, $p_{\text{T}}(j)$. The targeted mass range of the individual signal regions is stated.

For the 2×3 model we found that requiring at least 7 jets in the final state suppresses the SM background more efficiently, while still enough signal events remain. For the low gluino masses (900-1000 GeV), a lower p_{T} threshold of 180 GeV is set, while for the high masses (1600-2400 GeV) the p_{T} threshold is increased to 240 GeV.

For the 2×5 model, the final state kinematics depend on the masses of both SUSY particles, the gluino and the neutralino. In cases where the mass of the $\tilde{\chi}_1^0$ is very low, it is highly boosted. This means that quarks from the $\tilde{\chi}_1^0$ decay are very collimated and thus may not be reconstructed as individual jets.
For $\tilde{\chi}_1^0$ masses close to the gluino mass, the three jets from the $\tilde{\chi}_1^0$ decay carry most of the gluinos momentum. This means the final state would look more similar to the 2×3 model. We defined separate SRs for low gluino masses, up until 1.6 TeV and for high gluino masses, from 1.8 TeV onward, differing in the jet p_{T} threshold. As shown previously in Section 6.3.1, requiring at least two b-jets has a large impact on the sensitivity to the UDB models. In order to study the effect of a b-jet requirement in the CCA strategy, we tested the jet-counting spectrum including b-jet requirements for the UDB signal models. Based on the preliminary results from a veto in the UDS mass grid, no further studies are performed with a b-jet veto for the UDS signal mass grid. Figure 6.13(a) shows the p_T spectrum for 2×3 UDB signals with an extra selection requiring at least two b-tagged jets. One can see great enhancement of the sensitivity compared to the definition without b-jets shown in Figure 6.13(b). Therefore, we defined for both models one additional SR each with a selection on b-tagged jets, which are also listed in Table 6.3. Additionally to those selections. we applied the standard pre-selection listed in Table 6.1.

Background Estimation

The main background process is the production of dijets with additional initial and final state radiation. Its modelling depends on many parameters modelling QCD background, and is therefore known to be not as accurate as for other, theoretically better described SM processes. A background extrapolation method based on MC and data is used to reduce the effect of poorly modelled background processes, which also uses the p_{T} spectra from the jet-counting method introduced previously.

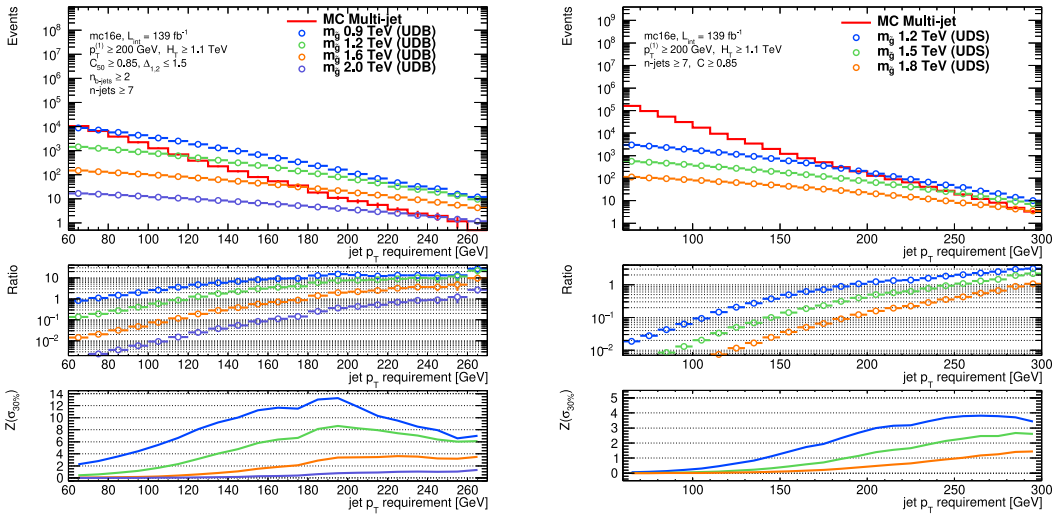

(a) ≥ 2 b-tagged jets

(b) no b-tags required

Figure 6.13: Jet counting p_{T} spectrum for SR-like definitions, requiring at least 7 jets, $\Delta\eta_{1,2} \leq 1.5$, and $C \geq 0.85$. Figure (a) shows the spectrum with an additional selection of the number of b-tagged jets. Figure (b) has no selection on b-jets. The selection on the C-parameter is slightly lowered, compared to the SR defined in Table 6.3, in order to reduce the signal contamination. The selection on $\Delta\eta_{1,2} \leq 1.5$ shown in (a) is removed after studies revealed no significant impact.

The expected number of background events in the SR is extrapolated from a low jet multiplicity region and normalised to data. The number of predicted events from an extrapolation starting in a region with m=4 jets into in a region with $n \geq 7$ jets is given by

$$N^{\mathrm{Extr.}}_{\geq 7\mathrm{jets}} = \sum_{i=7}^{9} w_{4i} \cdot N^{\mathrm{Data}}_{4-\mathrm{jets}} \cdot \frac{N^{\mathrm{MC}}_{i-\mathrm{jets}}}{N^{\mathrm{MC}}_{4-\mathrm{jets}}}, \tag{6.9}$$

with $N^{\mathrm{MC}}_{i-\mathrm{jets}}$ ($N^{\mathrm{MC}}_{4-\mathrm{jets}}$) being the number of events with i (4) jets in MC samples and $N^{\mathrm{Data}}_{4-\mathrm{jets}}$ the number of events in the region with 4 jets in data. The factor w_{4i} is defined as

$$w_{4i} = \frac{s_i}{s_4} \text{ with } s_i = \left.\frac{N^{\mathrm{Data}}_{i-\mathrm{jets}}}{N^{\mathrm{MC}}_{i-\mathrm{jets}}}\right|_{p_{\mathrm{T}} \geq 60\,\mathrm{GeV}}, \tag{6.10}$$

where the scaling factors s_i are correcting the data to MC ratio in a low p_{T} threshold ($\geq 60\,\mathrm{GeV}$) region.

Figure 6.14 shows the prediction with and without the scaling factors applied for an extrapolation from a region with 4 jets into a region with more than 7 jets. In order to avoid signal contamination, we added an inverted and lowered selection on the C-parameter. It becomes clear that applying the correction factor results in a better data MC agreement for the extrapolated distribution.

To validate the extrapolation method, we defined a series of validation regions. Table 6.4 summarises all of them. Listed are the requirements in number of jets above the given p_{T} threshold, the C-selection, as well as the expected number of background events, the maximal signal contamination expected and the observed data events including the

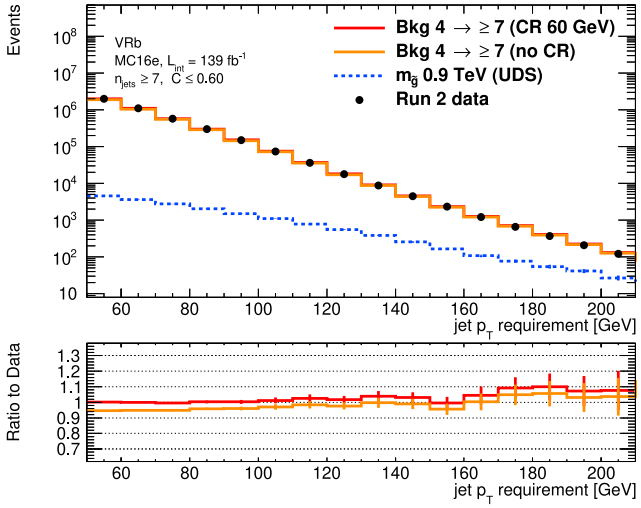

Figure 6.14: Validation of background estimation for extrapolation from a region with 4 jets to a region with more than 7 jets. The background estimation includes an additional correction factor, which is the ratio between data and MC in the 4 jets region at a p_{T} threshold of 60 GeV. The orange histogram of the lower panel shows the data-MC agreement after extrapolation without that correction factor, while the red line includes the correction factor, yielding better results.

statistical and systematic uncertainties. Additionally to those selections, we applied the standard pre-selection listed in Table 6.1.

Two types of VRs for extrapolation are defined: testing the method for high values of C, but extrapolating to lower jet-multiplicities than in the SRs (VRA and VRB), and testing the method for extrapolation to SR like jet multiplicities, but inverting the selection on VRC.

Figure 6.15 shows the two VRs with the additional b-jet requirements. One can see that the signal contamination at high jet p_{T} requirements above 200 GeV is higher than 10% for mass points below 1.6 TeV. Therefore, we decided to include the b-jet requirement as a final step in the un-blinding strategy, where the SR without b-jets are un-blinded first. Only if no excess above 2σ is observed in the regions targeting the gluino mass points of 1.6 TeV and beyond, the b-jet requirement is added on top.

The results from the background extrapolation validation is shown in Figure 6.16. For all validations, we tested the extrapolation from a region with 4 jets. A CR to correct the data-MC ratio in that region with a p_{T} threshold of 60 GeV was applied. All regions show a good data-MC agreement within the uncertainties, suggesting that the method should be applied to extrapolate into the SRs.

	n_{jets}	$p_{\text{T}}(j)$ [GeV]	C	Background Expectation	Data
VR-A1	$= 5$	180	≥ 0.80	73000^{+1800}_{-2400}	70184
VR-A2	$= 5$	160	≥ 0.85	65000^{+1800}_{-2200}	64985
VR-A3	$= 5$	150	≥ 0.90	30000^{+2100}_{-1000}	30360
VR-A-bj	$= 5$	180	≥ 0.85	2100^{+600}_{-100}	1973
VR-B1	$= 6$	120	≥ 0.80	80000^{+2100}_{-2800}	80271
VR-B2	$= 6$	110	≥ 0.85	58000^{+3900}_{-1800}	59997
VR-B3	$= 6$	100	≥ 0.90	28000^{+1000}_{-2000}	30212
VR-B-bj	$= 6$	120	≥ 0.85	3700^{+500}_{-300}	3425
VR-C1	≥ 7	180	≤ 0.60	350^{+37}_{-72}	372
VR-C2	≥ 7	220	≤ 0.60	47^{+6}_{-10}	35
VR-C3	≥ 7	240	≤ 0.60	18^{+4}_{-3}	14
VR-C-bj	≥ 7	180	≤ 0.60	34^{+13}_{-6}	39
VR-D1	≥ 8	180	≤ 0.60	23^{+5}_{-6}	16
VR-D-bj	≥ 8	160	≤ 0.60	8^{+6}_{-5}	6

Table 6.4: Selection criteria for all VRs. VRs with an additional requirement for at least two b-tagged jets are denoted with "-bj". The number of expected and observed SM background events are given with statistical and systematic uncertainties.

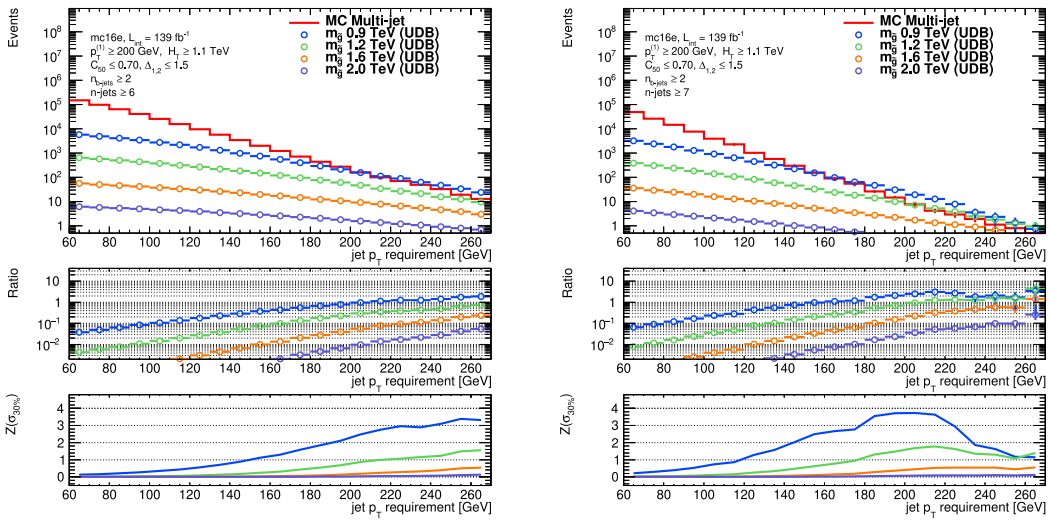

(a) VRB-like with ≥2 b-jets

(b) VRC-like with ≥ 2 b-jets

Figure 6.15: Validation regions with additional requirements on at least two b-tagged jets. Figure (a) is similar to the VRB regions, but has an inverted C-selection applied. Figure (b) is VRC-like with a less tight selection on C. The middle panels show the ratio of the number of events between signal and background predictions, while the lower panels show the expected significance computed with the MC yields and assuming 30% systematic uncertainty on the background events. Both regions show very high signal contamination caused by the increased sensitivity of UDB models when setting selections on b-jets.

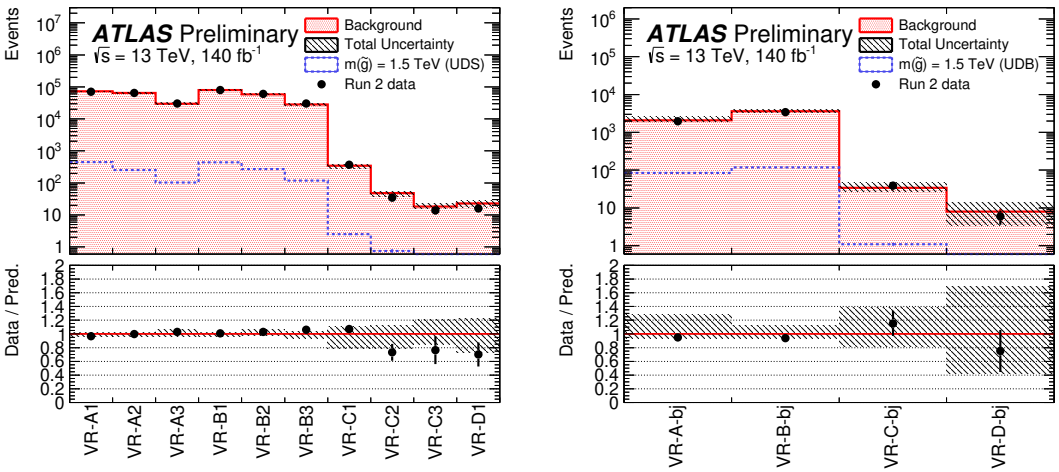

(a) VRs without b-tag requirement

(b) VRs with $\geq 2b$-tags required

Figure 6.16: Validation of the background estimation method in all the VRs without (a) and with b-jet requirements (b), defined in Table 6.4. The background was extrapolated from a region with 4 jets above a p_{T} threshold of 60 GeV. The bottom panels show the ratio of data over the predicted number of background events. The hatched region represents all uncertainties including systematic and statistical.

Results

Figure 6.17 shows the observed yields in all SRs from Table 6.3 compared to the expected background yields. We observe no excess in any of the regions. However, the results are used to set upper limits on the gluino masses, summarised in Section 6.5.

The results from the model-independent fit are listed in Table 6.5. Upper limits on the product of cross-section, acceptance, and efficiency are given. The upper limits on that product range from 0.32 to 0.03 fb for the different regions.

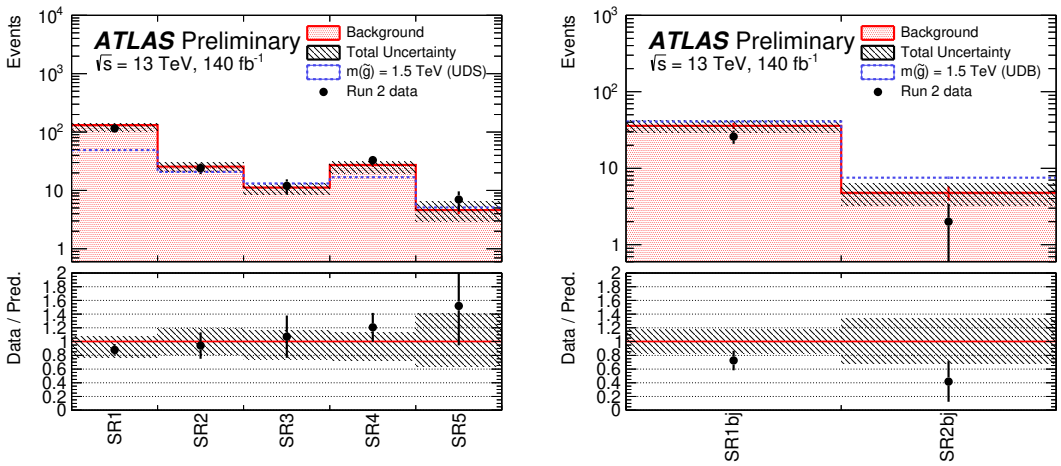

(a) SRs without b-tag requirements

(b) SRs with $\geq 2b$-tagged jets

Figure 6.17: Expected and observed yields in the SRs of the CCA analysis strategy. The SR definitions are given in Table 6.3 for regions without b-jet requirements (a) and with requiring at least two b-jets (b). No significant excess above the SM predictions is observed. The grey uncertainty band includes systematic and statistical uncertainties.

Signal region	$\langle\epsilon\sigma\rangle^{95}_{\text{obs}}$ [fb]	S^{95}_{obs}	S^{95}_{exp}	CL_B	$p(s=0)$ (Z)
SR1	0.32	45	57^{+18}_{-14}	0.51	0.50 (0.00)
SR2	0.09	13	$14.1^{+5.7}_{-4.1}$	0.56	0.50 (0.00)
SR3	0.07	10	$9.5^{+4.1}_{-2.7}$	0.52	0.42 (0.20)
SR4	0.16	22	$17.4^{+6.5}_{-4.7}$	0.26	0.21 (0.79)
SR5	0.07	9.4	$7.4^{+3.6}_{-2.4}$	0.42	0.32 (0.46)
SR1bj	0.08	11	$17.0^{+6.9}_{-4.8}$	0.55	0.50 (0.00)
SR2bj	0.03	4.4	$6.6^{+2.9}_{-1.9}$	0.66	0.50 (0.00)

Table 6.5: Results for the upper limits in the jet-counting analysis signal regions. $\langle\epsilon\sigma\rangle^{95}_{obs}$ describes the 95% CL upper limits on the visible cross-section in fb, S^{95}_{obs} the 95% CL upper limits on the number of signal events, S^{95}_{exp} is the 95% CL upper limit on the number of signal events, given the expected number and the last two columns are the CL_B value, i.e. the confidence level observed for the background-only hypothesis, and the discovery p-value ($p(s=0)$).

6.4 ML Analysis

The ML approach in the analysis tries to reconstruct the gluino masses from the jet kinematics using a neural network (NN). The resulting gluino mass distribution is used for a bump-hunt search for signal excess.
The 2×3 jet model has

$$\binom{6}{3} = 20 \tag{6.11}$$

possible combinations to group three jets into pairs. For the 2×5 model this becomes an even bigger combinatorial challenge with

$$\binom{10}{5} = 252 \tag{6.12}$$

possibilities to find the correct group of five jets coming from the same gluino. To address this challenge, by making use of the entire set of available kinematic information present in the jet four-momenta, a NN is trained only on signal events and later applied to data. The ML approach presented here is only carried out for the 2×3 model. The network architecture follows closely the one described in [185]. A brief description is given in the following.

The NN uses up to eight jet four-momenta as input and returns three output scores per jet. The three scores are indicating, how likely the jet is coming from $\tilde{g}_1$, $\tilde{g}_2$, or if it is not associated with an gluino and therefore identified as an ISR jet. The three jets which are assigned to the same parent gluino are combined, and their invariant mass is calculated. The average of both gluino masses $m_{\tilde{g}_1}$ and $m_{\tilde{g}_2}$ per event is determined via

$$m_{\text{avg}} = \frac{1}{2}\left(m_{\tilde{g}_1} + m_{\tilde{g}_2}\right), \tag{6.13}$$

and the resulting spectrum is used for a bump-hunt search. Figure 6.18 shows the ML analysis workflow.

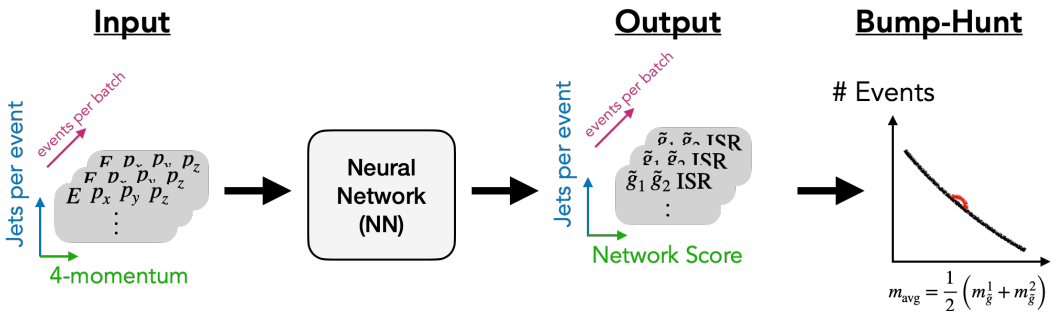

Figure 6.18: Steps of the RPV multijet analysis utilising the ML approach: jet 4-momenta are fed into a NN, which returns three output scores per jet. Based on the output scores, the gluino masses are reconstructed. The spectrum of averaged gluino masses per event are used for a bump-hunt search. Image by A.Badea [186].

6.4.1 Truth Matching

The developed supervised ML algorithm for the gluino mass-reconstruction requires the four-momenta of the jets as inputs. For the NN training, the jets from gluino decays are assigned an additional truth-label, indicating from which of the two gluinos they are coming from or if the jet is not from a gluino, thus an ISR jet.
In the generated MC signal samples, the "truth" information describing the exact gluino decay in three quarks is stored. For these truth quarks, the transverse momentum, the energy, the ϕ and η coordinates, as well the particle identity (ID) and the information from which of the two gluinos the quark came from is saved. While for the reconstructed jets, only the transverse momentum, the energy, and the ϕ and η coordinates are stored. Therefore, the reconstructed jets are matched to their corresponding truth-quarks in the generated MC signal samples via the ΔR matching. Figure 6.19 shows an illustration of the two different pieces of information which need to be matched together.

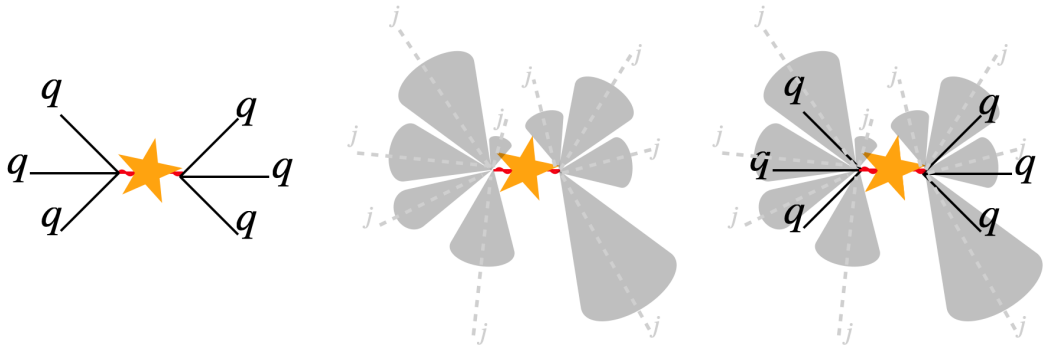

(a) (b) (c)

Figure 6.19: Truth matching between the "true" quarks from the gluino decay (a) and the reconstructed jets (b), which were initiated by these quarks and additional ISR/FSR radiation. Figure (c) shows that in this illustrative example five out of six quarks were successfully matched to a reconstructed jet within $\Delta R = 0.4$.

Every final state truth-quark originating from one of the two signal gluinos is associated with its nearest reconstructed jet in the η-ϕ plane. For every truth-quark q, the distance ΔR to all reconstructed jets, j, is calculated as shown in Eq. (3.7) and the nearest matching-candidate within $\Delta R \leq 0.4$ is stored as a matched jet, including the information to which of the two gluinos the jet is assigned to. As soon as a jet is matched to a truth-quark, it is removed from the list of matching-candidates and the next truth-quark is considered. The truth-quarks are sorted by their generation time stamp. Figure 6.20 shows two events from a generated signal sample, where all six truth-quarks from the two gluinos are successfully matched to reconstructed jets.

The performance of the ML algorithm, and thus the mass reconstruction, is highly dependent on the ingoing training and validation sample. In order to have as many fully matched events to train on as possible, I conducted multiple studies to improve the truth-matching efficiency. The truth-matching efficiency is defined as the fraction of events for which all signal truth-quarks are matched to reconstructed jets.

The jets going into the matching are sorted by their p_{T}. In order to avoid the matching failing due to this p_{T} ordering of potential matching candidates, I investigated a p_{T}-agnostic matching procedure. In this approach, the ΔR between all n truth-quarks and

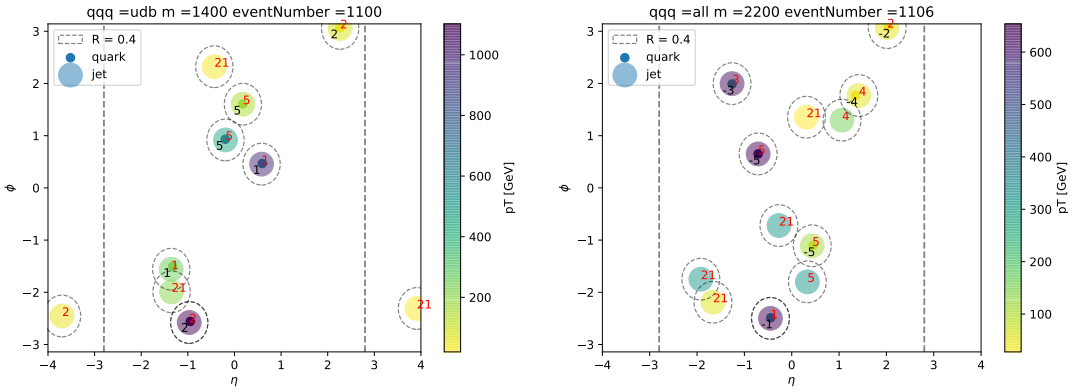

(a) (b)

Figure 6.20: Two events where all six truth-quarks are matched to reconstructed jets within $\Delta R = 0.4$ in the $\eta - \phi$-plane. The black numbers identify the particle ID of the quarks coming from the gluino decays. The red numbers are the IDs of the particles initiating reconstructed jets.

all m reconstructed jets is calculated and stored as a $n \times m$ matrix. Among all $n \times m$ values, the minimal ΔR of all of the quark-jet pairs is considered first, which means all reconstructed jets are considered in the order of their distance to a truth-quark, rather than their p_{T}. As shown in Figure 6.21 for all available mass points on the UDS and UDB sample sets, the matching efficiency is not improving by this attempt. Therefore, we kept the default matching procedure to avoid unnecessary extra computing time.

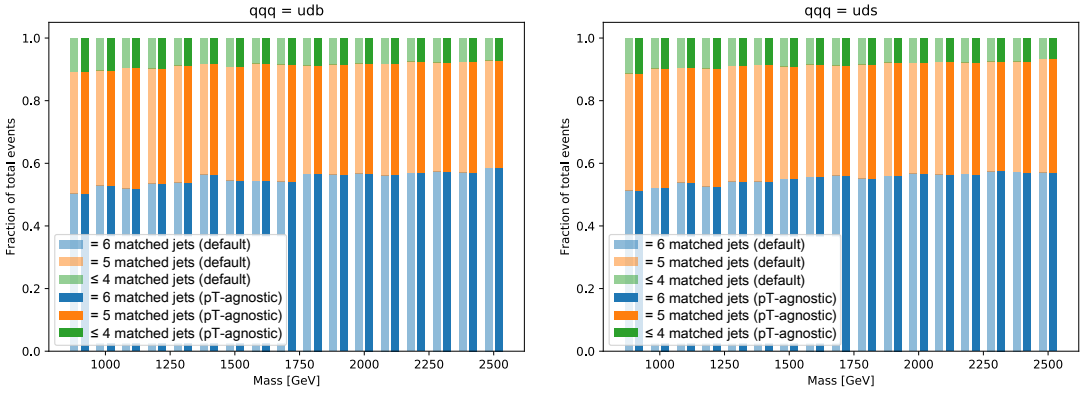

(a) (b)

Figure 6.21: Matching efficiency for the default (a) and p_{T}-agnostic (b) matching approach. No significant improvement is observed.

Figure 6.22 displays two examples of events where the matching fails. These two events are examples for two possible reasons that result in a wrong truth-matching: the requirement of $\Delta R \leq 0.4$ for a jet-quark pair to be matched is too low, as seen in Figure 6.22(a)($\eta = -1.2, \phi = -1.6$), or two quarks are within the 0.4 radius of the same reconstructed jet, shown in Figure 6.22(b) ($\eta = 1.3, \phi = 0$).

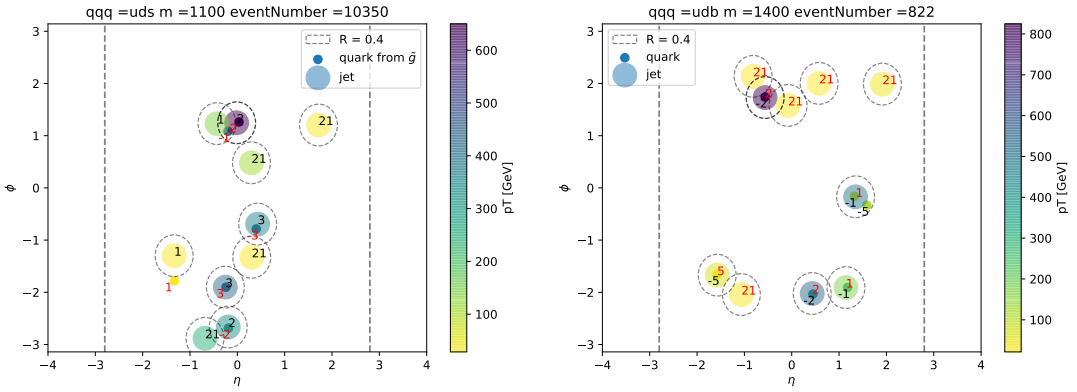

(a) (b)

Figure 6.22: Two events which are not fully matched, either because the jet-quark pair is too far apart to be matched (a) or two quarks are within the same jet (b).

In order to investigate how large the fraction of events with two quarks being assigned to the same reconstructed jet is, I performed a baseline study on boosted gluinos.
If a gluino is highly boosted, its decay products are likely to be collimated and therefore within $\Delta R = 0.4$ of the same jet. The study I present here considers three mass points: 900, 1600, and 2000 GeV. The fraction of events, in which the minimal ΔR between two truth-quarks from the same gluino is $\Delta R \leq 0.4$ is evaluated and interpreted as events in which two quarks are merged into the same jet with $R = 0.4$.
Similarly, events in which the maximal ΔR between two truth-quarks from the same gluino is $\Delta R \leq 1.0$ give an estimation how likely it is that the whole gluino is contained in a single large-R jet ($R = 1.0$).
The results from this study are listed in Table 6.6 and show that between 8 and 10% of the events, depending on the mass point, can not be matched fully because at least for one of the two gluinos, two quarks are merged into the same jet. Events for which all three quarks from the same gluino are boosted into one single large-R jet are almost not present (corresponds to the fraction of events for which the maximum $\Delta R < 1.0$).
Additionally, I studied if all six truth-quarks from the gluino-pair are fulfilling the requirements which qualify a reconstructed jet as a signal jet as defined in Section 3.3.2. I found that for the low-mass point at 900 GeV, the fraction of events with one or more truth-quarks not fulfilling the requirements are as high as 20%, while it decreases to 9.3% for the high mass point at 2200 GeV.

This study reveals that there is a significant fraction of events of up to 30%, depending on the mass of the gluino, which can not be fully truth-matched. This is because at least two quarks are too close to be matched separately, or because the quark itself is not within the requirements to be categorised as a signal jet because it is out of the sensitivity area or has too low p_{T}.

To study the effect of the ΔR requirement on the matching being defined as $\Delta R = 0.4$ and therefore being too low, as seen in Figure 6.22(a), I performed another study on the truth signals. Figure 6.23 shows the result of a study in which I varied the requirement on ΔR between 0.2 and 1.6. The same figure shows the "correctness" of the matching as a function of ΔR requirement for matching. This correctness is obtained by comparing

Gluino mass ($m_{\tilde{g}}$)	900 GeV	1600 GeV	2200 GeV
Events with min. $\Delta R < 0.4$	10.6%	9.0%	8.4%
Events with max. $\Delta R < 1.0$	0.2%	0.1%	0.1%
Events with truth quark with $p_{\mathrm{T}} < 50\,\mathrm{GeV}$ or $\eta > 2.7$	20.1%	12.2%	9.3%

Table 6.6: Fraction of events for three gluino mass points in which the minimal (maximal) ΔR between two quarks from at least one gluino is smaller than 0.4 (1.0), or where of the quarks from a gluino has a p_{T} lower than 50 GeV and is outside of the sensitive η range of ATLAS.

the particle ID of the truth quark from the gluino with the particle ID of the quark initiating the reconstructed jet.
If all 6 IDs correspond to each other, the event is categorised as correct, otherwise as not correct. The particle ID for the reconstructed jets comes from a ghost-association algorithm and introduces by itself an uncertainty, which was not considered in this study. Figure 6.23 shows that the ΔR cut of 0.4 gives the best compromise between matching efficiency and correctness of the matching and is therefore kept at this value.

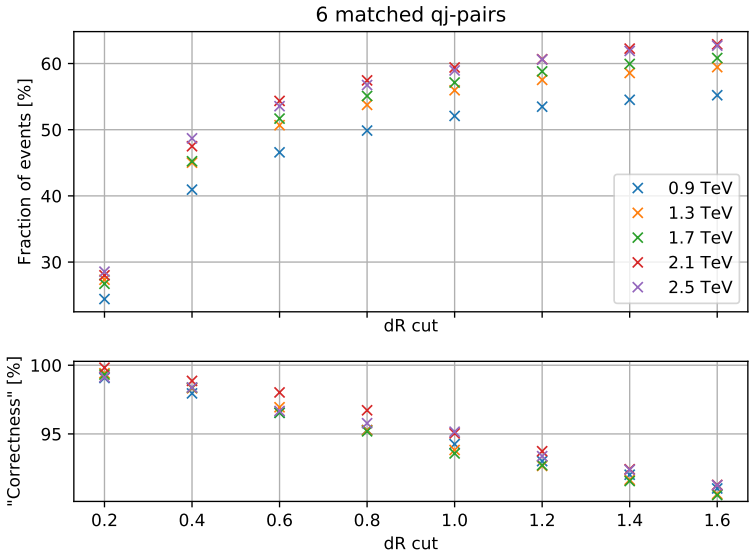

Figure 6.23: Matching efficiency and "correctness" as a function of the ΔR requirement for matching for various signal points. The looser the requirements becomes (thus, the larger ΔR), the less likely it is that all six quarks are matched to their correct reconstructed jets.

The high momentum quarks from the massive gluino decay are very likely to radiate gluons as final state radiation (FSR) before they hadronise. This may result in a slight change of direction of the jet axis compared to the initial quark's direction and therefore to a non-matching with a reconstructed jet.
Therefore, I performed a truth study with the generated quarks from gluinos. The MC generated signal samples contain all information on various FSR gluons along the "path" of the quark before it decays.

Figure 6.24 shows an illustration of this path, where one can see the difference in direction between the quark before FSR and and after FSR, caused by the FSR gluon radiation. The hadronisation of the quark is happening immediately, thus there is no displaced vertex between the "before" and "after" FSR quark, meaning Figure 6.24 is just for explaining the change in direction of the quark from a gluino.

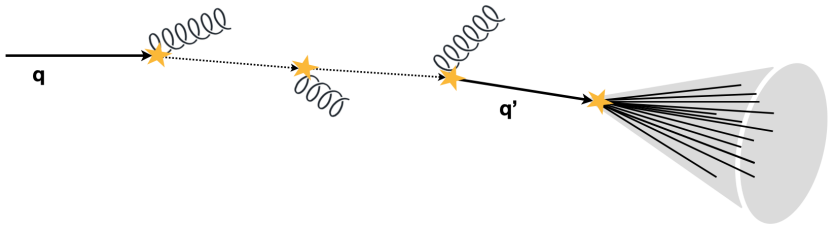

Figure 6.24: The quark from the gluino (q) radiates off three gluons as final state radiation. Because these gluons take away a certain fraction of the momentum, the direction of the quark after FSR (q') may slightly change, affecting the ability to match the reconstructed jet with the quark before the FSR process. The image is not presenting a displaced vertex, as the hadronisation of the quark q' happens immediately.

Figure 6.25 shows the differences in transverse momentum and ΔR between the quark before and after FSR. It becomes clear that for a good fraction of events, the directions might slightly change, affecting the matching efficiency.
By default, the reconstructed quarks are matched to the initial quarks from gluinos in the MC samples we used. By changing the matching to the final, rather than the first "quark in the chain" the matching efficiency can be improved by almost 15%, depending on the mass point, in both sets of sample, UDS and UDB.
The ML algorithm is only trained and evaluated on MC signal samples. Only events which are fully truth matched, meaning exactly three jets per gluino are matched, are used. Therefore, a high matching efficiency increases the training set and thus the ML algorithm. Compared to the matching efficiency of $\sim 55\%$ showed in Figure 6.21, the matching efficiency is increased to $\sim 70\%$. This result also aligns well with the results from Table 6.6, stating that in roughly 30% of the events, the event can not be reconstructed because either at least one jet is outside the requirements for signal jets or because two gluinos are within $\Delta R < 0.4$ of each other. Therefore, I implemented the matching based on the "last-quark-in-the-chain" as standard procedure for the truth matching of this analysis.

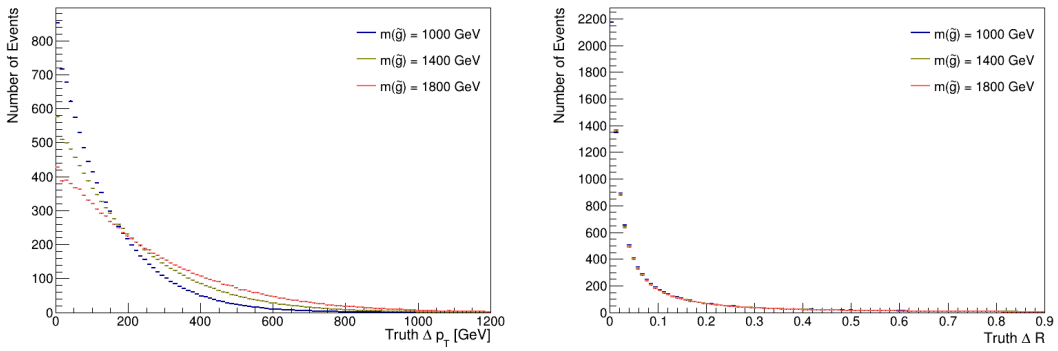

(a) (b)

Figure 6.25: Absolute differences in transverse momentum (a) and ΔR (b) between the quark before and after FSR processes for three representative mass points. The event numbers are normalised to the same number of events per mass point. Clear differences can be seen which has an effect on the matching efficiency.

6.4.2 Final Strategy

The final ML strategy is based on the mass reconstruction with a dedicated NN. My preliminary studies showed the potential of an improved matching procedure. The final method was developed and finalised by the analysis team, which I summarise here for completeness. The following section is a summary of the ML strategy as outlined in [179]. A NN is used to reconstruct the invariant masses of the two gluinos, $m^i_{\tilde{g}}$. The two reconstructed invariant masses are used to calculate the average mass of the gluino pair, m_{avg}. Events entering the network are pre-selected, requiring at least six jets with transverse momentum greater than 100 GeV. An additional selection on the C-parameter is applied, $C \geq 0.9$, to suppress background contamination. For the UDB model, one b-tagged jet is required to enhance the sensitivity.

Event Reconstruction

The four-momenta of up to eight jets are used as inputs. For events with less than eight jets, the entries are zero-padded, meaning they are filled with zeros. For events with more than eight jets, the eight highest p_{T} jets are used. The data-set for training and validation consists of all available mass points from both sample sets, UDS and UDB. Only events with three truth partons matched to reconstructed jets per gluino, as described previously, are considered. To avoid background sculpting, the NN is trained on all masses simultaneously.The total number of events considered for training and validation of the network is 1.73 million events, of which 90% are used for training and 10% for validation.

Every jet gets assigned three NN output scores: two for the probabilities to come from either of the two gluinos and one for the probability to come from an ISR jet instead. The highest score determines the predicted label of the jet. Figure 6.26 shows the performance of the NN in terms of the averaged gluino mass from the NN output. A comparison between the reconstruction with the NN and the truth mass distributions, normalised, is shown. As discussed earlier, I changed the truth-matching to match the

truth-quark after final state radiation. Through FSR, additional jets are produced, which are carrying non-negligible fractions of the initial momentum away. Therefore, the mass distributions have tails towards lower masses. This effect becomes especially important for high-mass gluinos. Besides this effect, the reconstructed averaged gluino masses are in good agreement with the truth-targets.

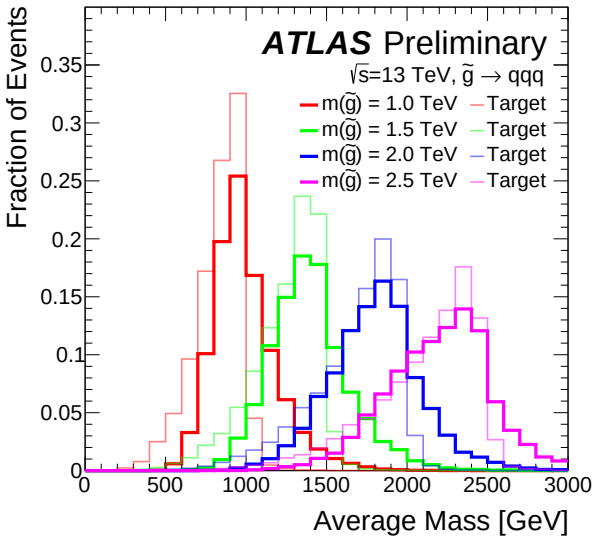

Figure 6.26: Normalised average mass distribution for various signal mass points. Shown are the reconstructed distributions, which is based on the output from the NN (solid), and the target distributions, defined by the truth label of the jets.

Background Estimation

The background estimation for the mass reconstruction analysis is fully data-driven. The SM background MC samples are used for cross check of the method but are not used in the final result.

Many previous analyses from ATLAS [187–191] and CMS [192–194], which performed searches in multijet or dijet resonances, showed that the mass spectrum of multijet events follows a smoothly falling distribution. We used a parametric fit function,

$$f(x) = p_1 \, (1 - x)^{p_2} \, x^{p_3 + p_4 \ln x}, \tag{6.14}$$

with $x = m_{\text{avg}}/\sqrt{s}$ and fitting parameters p_{1-4} to perform a fit of the background distribution.
To validate the background estimation method, the fit was applied to the dijet MC scaled to 140 fb^{-1}. Additionally, we validated the method with 3.2 $\text{fb}^{-1}$of 2015 data with loser selections ($C \leq 0.7$, six jets with transverse momentum $p_{\text{T}} \geq 70\,\text{GeV}$), containing roughly the same number of events as expected for the full Run 2 dataset.

The validation is shown in Figure 6.27. For both validations, on MC and on the 2015 data, the fit shows good agreement. Our studies showed that the mass distribution for dijets is smoothly falling for averaged masses above 650 GeV. Therefore the region

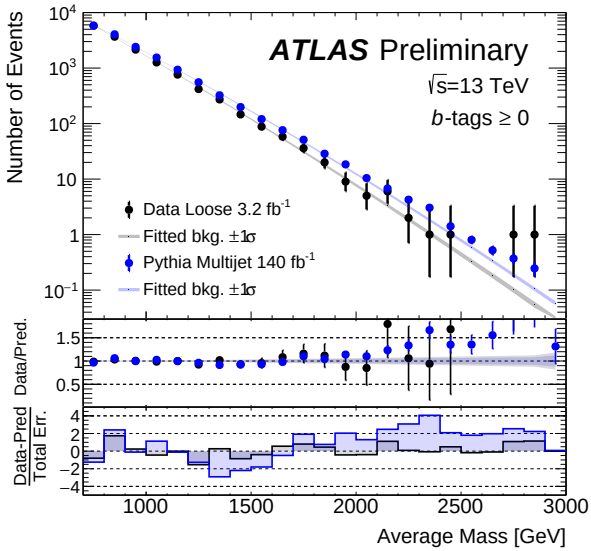

Figure 6.27: Validation of the background estimation method. The observed and fitted background model show good agreement. The dijet MC is scaled to 140 fb^{-1} the 3.2fb^{-1} of 2015 data uses loser selections in order to have comparable numbers of events with the full Run 2 expectation. The statistical and systematic uncertainties are shown in the grey and blue band respectively.

between 700 and 3000 GeV was used for the fit. The same study including a requirement on one b-tagged jet for the UDB model showed comparable results.

For the ML based analysis, the systematic uncertainties described in Section 4.6 have been used. Additionally, uncertainties from the background fitting function and the statistical uncertainty on the fit results have been added. No systematics related to the NN have been applied, because the network assigns jets together in an arbitrary way, which may result in worse results but does not lead to systematic uncertainties to be included.

Results

Figure 6.28 shows the fit of the nominal background-only fitting function to the full Run 2 data set with no requirements on b-tagged jets (a) and the with an requirement on b-tagged jets (b). As can be seen in the lower panel, no significant excess above the SM prediction was observed. Therefore, the results are re-interpreted as upper limits on the excluded gluino masses in the next Section.

The results from the model-independent fit are listed in Table 6.7 and Table 6.8. For these results, model-independent SRs are defined using single bins in the invariant mass distribution. Every SR uses a window in the distribution of 300 GeV and assumes there is no signal contribution outside the SR. While in the model-dependent case, the background-fit considered the full averaged mass distribution, the background is fitted to the averaged mass distribution function without the considered signal region bin for the model-independent signal regions. The upper limits on the product of cross-section, acceptance, and efficiency range from 7.3 to 0.02 fb for the different regions.

Signal region	$\langle\epsilon\sigma\rangle^{95}_{\text{obs}}$ [fb]	S^{95}_{obs}	S^{95}_{exp}	CL_B	$p(s=0)$ (Z)
700 - 1000	7.3	1000	1300^{+460}_{-300}	0.22	0.50 (0.00)
800 - 1100	5.7	800	360^{+150}_{-49}	0.99	0.01 (2.5)
900 - 1200	2.1	290	210^{+88}_{-25}	0.81	0.18 (0.91)
1000 - 1300	1.5	210	160^{+50}_{-34}	0.80	0.18 (0.90)
1100 - 1400	0.54	76	120^{+45}_{-30}	0.09	0.50 (0.00)
1200 - 1500	0.27	37	85^{+33}_{-24}	0.00	0.50 (0.00)
1300 - 1600	0.16	23	63^{+37}_{-18}	0.00	0.50 (0.00)
1400 - 1700	0.16	22	47^{+19}_{-13}	0.00	0.50 (0.00)
1500 - 1800	0.24	33	$38.8^{+16}_{-9.9}$	0.25	0.50 (0.00)
1600 - 1900	0.26	37	$37.9^{+15}_{-9.7}$	0.47	0.50 (0.00)
1700 - 2000	0.30	42	$34.1^{+12}_{-6.8}$	0.71	0.29 (0.55)
1800 - 2100	0.25	35	$28.2^{+12}_{-7.6}$	0.72	0.28 (0.57)
1900 - 2200	0.29	41	$24.5^{+11}_{-3.8}$	0.93	0.06 (1.5)
2000 - 2300	0.19	27	$21.5^{+7.6}_{-4.4}$	0.78	0.19 (0.89)
2100 - 2400	0.15	21	$15.5^{+6.2}_{-2.3}$	0.74	0.20 (0.84)
2200 - 2500	0.08	11	$10.5^{+3.2}_{-1.9}$	0.57	0.40 (0.26)
2300 - 2600	0.08	11	$9.2^{+3.9}_{-1.2}$	0.66	0.27 (0.61)
2400 - 2700	0.05	6.9	$6.8^{+2.1}_{-1.4}$	0.51	0.48 (0.05)
2500 - 2800	0.02	2.3	$3.1^{+2.1}_{-1.2}$	0.26	0.50 (0.01)
2600 - 2900	0.04	5.3	$5.2^{+2.2}_{-1.3}$	0.52	0.46 (0.10)
2700 - 3000	0.06	8.3	$8.2^{+0.4}_{-0.7}$	0.53	0.44 (0.16)

Table 6.7: Results for the upper limits in the ML analysis signal regions for the UDS model. $\langle\epsilon\sigma\rangle^{95}_{obs}$ describes the 95% CL upper limits on the visible cross-section, S^{95}_{obs} the 95% CL upper limits on the number of signal events, S^{95}_{exp} is the 95% CL upper limit on the number of signal events, given the expected number and the last two columns are the CL_B value, i.e. the confidence level observed for the background-only hypothesis, and the discovery p-value ($p(s=0)$).

Signal region	$\langle\epsilon\sigma\rangle^{95}_{\text{obs}}$ [fb]	S^{95}_{obs}	S^{95}_{exp}	CL_B	$p(s=0)$ (Z)
700 - 1000	5.7	800	960^{+330}_{-240}	0.31	0.50 (0.00)
800 - 1100	3.3	460	320^{+100}_{-65}	0.89	0.11 (1.2)
900 - 1200	1.1	150	130^{+38}_{-31}	0.74	0.24 (0.71)
1000 - 1300	0.92	130	92^{+40}_{-13}	0.81	0.18 (0.91)
1100 - 1400	0.36	51	70^{+27}_{-20}	0.17	0.50 (0.00)
1200 - 1500	0.16	23	52^{+21}_{-15}	0.00	0.50 (0.00)
1300 - 1600	0.11	16	39^{+15}_{-11}	0.00	0.50 (0.00)
1400 - 1700	0.12	17	$28.9^{+12}_{-8.1}$	0.04	0.50 (0.00)
1500 - 1800	0.20	27	$24.9^{+25}_{-7.1}$	0.61	0.38 (0.29)
1600 - 1900	0.25	35	$30.0^{+10}_{-7.1}$	0.68	0.45 (0.13)
1700 - 2000	0.21	30	$27.7^{+10}_{-7.7}$	0.58	0.42 (0.20)
1800 - 2100	0.17	24	$24.0^{+5.9}_{-6.2}$	0.51	0.49 (0.03)
1900 - 2200	0.18	25	$21.6^{+5.9}_{-5.8}$	0.71	0.26 (0.65)
2000 - 2300	0.13	18	$17.1^{+5.3}_{-2.1}$	0.63	0.32 (0.47)
2100 - 2400	0.10	13	$12.4^{+3.3}_{-2.6}$	0.63	0.30 (0.51)
2200 - 2500	0.05	6.4	$6.4^{+2.5}_{-1.5}$	0.50	0.50 (0.00)
2300 - 2600	0.05	6.8	$6.7^{+2.6}_{-0.8}$	0.54	0.42 (0.20)
2400 - 2700	0.03	4.0	$3.9^{+2.2}_{-1.2}$	0.52	0.45 (0.14)
2500 - 2800	0.01	2.0	$2.1^{+1.8}_{-0.9}$	0.47	0.49 (0.02)
2600 - 2900	0.04	5.4	$5.3^{+2.2}_{-1.3}$	0.53	0.43 (0.19)
2700 - 3000	0.04	6.1	$6.0^{+2.3}_{-0.6}$	0.53	0.42 (0.20)

Table 6.8: Results for the upper limits in the ML analysis signal regions for the UDB model. $\langle\epsilon\sigma\rangle^{95}_{obs}$ describes the 95% CL upper limits on the visible cross-section, S^{95}_{obs} the 95% CL upper limits on the number of signal events, S^{95}_{exp} is the 95% CL upper limit on the number of signal events, given the expected number and the last two columns are the CL_B value, i.e. the confidence level observed for the background-only hypothesis, and the discovery p-value ($p(s=0)$).

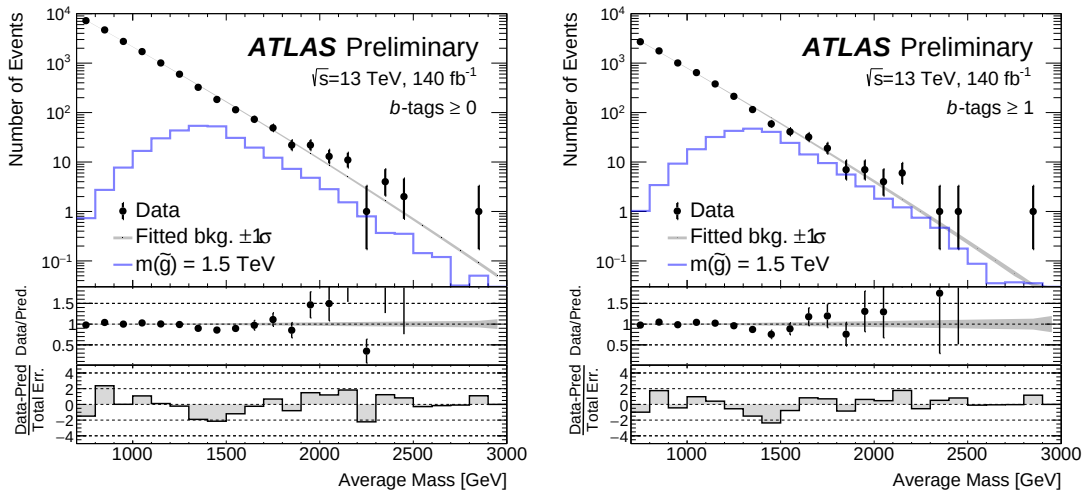

(a) (b)

Figure 6.28: Unblinded fit results of the nominal background function to the full Run 2 data. Figure (a) shows the result without the b-tagged jet requirements, Figure (b) shows the result with the requirement of at least one b-tagged jet. No excess with a significance 2σ above the expected background prediction is observed. The lower panel shows the significance over the mass range of considered gluino masses. Statistical and systematic uncertainties are included in the grey band.

6.5 Summary and Conclusion

This section summarises the model-dependent interpretation of the results from both, the CCA and the ML based analysis.

Figures 6.29 and 6.30 show the results from model-dependent fits of the CCA and the ML approach, interpreted as exclusion limits for the gluino mass in the 2×3 model. For both analyses, a result with and without additional b-jet requirements in the selections are presented. We observed no excess over the SM background in both analyses, but they result in a significant improvement of exclusion power for pair-produced gluinos decaying into all-hadronic final states. For the 2×3 model, the current ATLAS limit was 917 GeV, as presented in Figure 6.2. The analysis summarised here, using the full Run 2 data, increases this up until 1.6 TeV with the CCA analysis and 1.73 TeV with the mass reconstruction ML approach at 95% CL for the UDS model. For the UDB model, both strategies result in an exclusion of gluino masses until 1.8 TeV at 95% CL.

By design, this analysis allows a direct comparison between a CCA and a ML based analysis strategy. We observed that both analyses reach similar exclusion power. The ML analysis exceeds the CCA with its expected exclusion in all shown regions. Due to deviations between expectations and observations, such as the under-fluctuation shown in the UDB exclusion contour for the CCA analysis, the CCA approach has better sensitivity in that region, which is shown in slightly better observed limits.

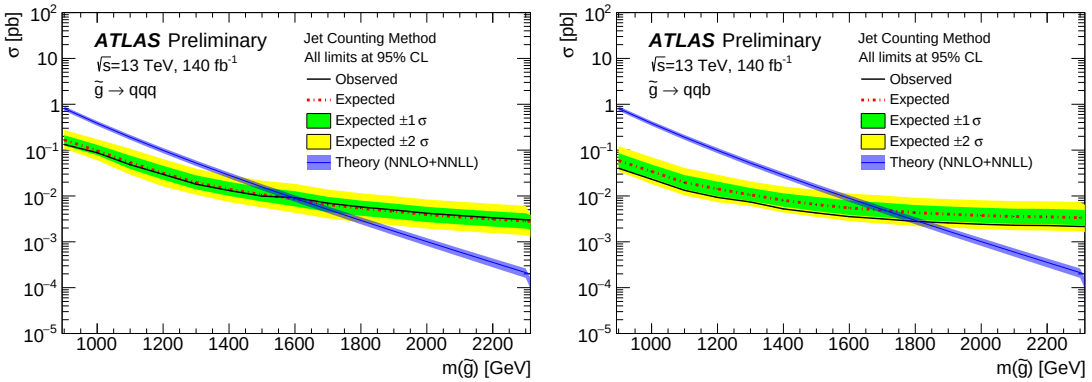

(a) UDS - CCA (no b)

(b) UDB - CCA ($\geq 2b$)

Figure 6.29: Observed and expected exclusion limits from the jet-counting analysis strategy. Figure (a) shows the result for the UDS samples for the most sensitive SR (SR3). Figure (b) shows the results for the UDB samples with the additional requirement on at least two b-jets in the event selection. All systematic and statistical uncertainties are included in the green and yellow bands.

Figure 6.31 shows the results from model-dependent fits of the CCA approach, interpreted as exclusion limits for the gluino and neutralino masses in the 2×5 model. Early on in this chapter, the analysis was motivated due to an unexplored corridor for the 2×5 model at a gluino mass of ~ 1 TeV, shown in Figure 6.2.
With this analysis, we excluded this corridor up until 1.6 TeV (1.7 TeV) for light neutralinos in the UDS (UDB) model at 95%CL. Compared to the previous search, this analysis shows a great improvement in its sensitivity and improved the excluded limits by several hundred GeV. With the planned LHC and detector upgrades summarised in

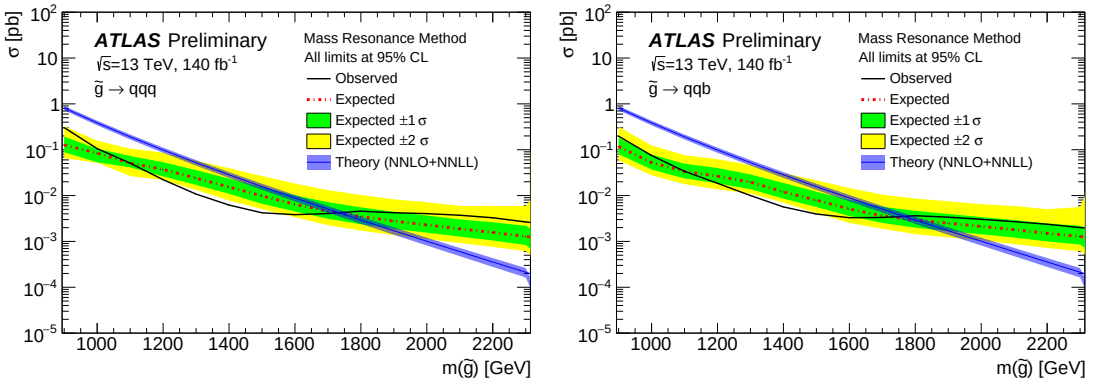

(a) UDS - ML (no b) (b) UDB - ML ($\geq 1b$)

Figure 6.30: Observed and expected exclusion limits from the ML based bump-hunt. Figure (a) shows the result for UDS samples, Figure (b) shows a slightly higher exclusion due to the additional b-jet requirement in the event selection for the UDB samples. All systematic and statistical uncertainties are included in the green and yellow bands.

the following chapter, the sensitivity to gluino masses will be expanded further. This s allow searches for higher mass gluinos than the ones excluded with this analysis.

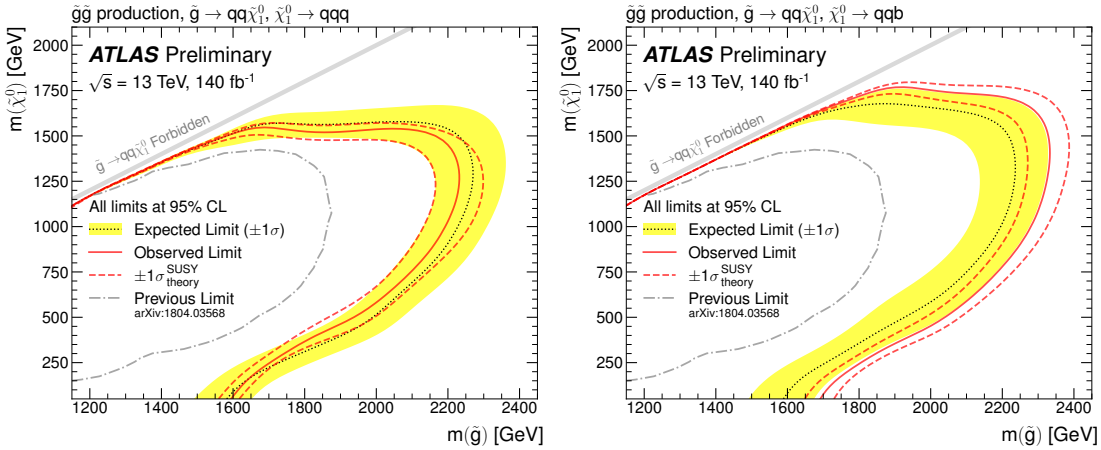

(a) UDS - CCA (no b) (b) UDB - CCA ($\geq 2b$)

Figure 6.31: Observed and expected exclusion limits from the jet-counting search for pair-produced gluinos decaying via a cascade into 10 jets. Figure (a) shows the result for the UDS sample set without requirements on the number of b-tagged jets. Figure (b) shows the results for the UDB sample set, including the additional b-jet requirement. All systematic uncertainties are included in the band around the expected contour. The band around the observed limit shows how the exclusion changes when the signal cross-section is varied up and down by the theoretical uncertainty.

Chapter 7

Irradiation Studies of ATLAS ITk Pixel Services Components

BSM physics and precision measurements, as well as the study of rare SM processes benefit from more statistics. To maximise the scientific output of the LHC, the accelerator will therefore be upgraded to the High-Luminosity LHC (HL-LHC). The 10-year data collection period of the HL-LHC is expected to start in 2029 and will provide up to $4\,000\,\text{fb}^{-1}$of pp collision data (Figure 3.6), requiring an increase of the instantaneous luminosity by a factor 5-7.5.

To reach such high luminosities, more collisions per bunch crossing are needed. According to Eq. (3.2), this requires strong collimation and a high number of particles per bunch. To deliver such dense, high pile-up collision regions, the LHC will undergo major upgrades, including changes to the pre-accelerator complex, stronger focusing magnets, and upgrades to the LHC accelerator units [195, 196]. Figure 7.1 gives an impression how the pile-up, the average number of collisions per bunch crossing as discussed in Section 4.2, in the ATLAS detector will change compared to the current collisions. Whereas in Run 2 the average number of proton interactions was around 33, there will be in the order of 200 interactions per beam crossing in the HL-LHC era.

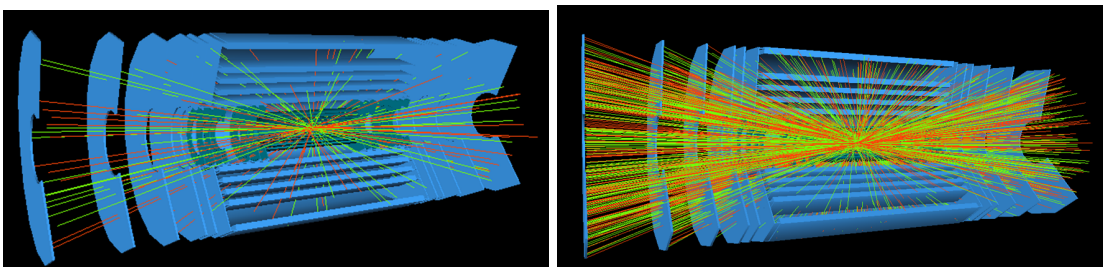

(a) (b)

Figure 7.1: Simulation of particle environment in ATLAS during a bunch crossing [197]. Figure (a) shows 23 pp collisions per bunch crossing, while (b) shows a factor 100 more collisions. These simulations give an impression of the increase in particle density when going from low to high luminosities.

This increased pile-up environment will require a more granular tracking detector to resolve the dense particle environment and separate the vertices. Because more channels will need to be read-out at the same time, the read out of the detector also needs to be upgraded. Therefore, the current ID and its readout will be replaced with the completely new Inner Tracker (ITk) detector, one of several major upgrades of ATLAS for the HL-LHC phase.

An additional challenge that comes with the increasing particle density is the much harsher radiation environment for all LHC experiments than what is currently observed. Therefore, all detector upgrades need to be radiation tolerant and will require the used components and materials to be qualified for these unprecedented radiation levels. Therefore, radiation tests at the 18-MeV Bern medical cyclotron are performed and potential radiation damage is quantified, as described in this chapter.

This chapter motivates and introduces the ATLAS ITk in Section 7.1. Especially the main component of the ATLAS ITk Pixel readout chain, the Optosystem developed in Bern, introduced and its expected radiation levels discussed. Section 7.2 describes the Bern cyclotron as an irradiation facility including the used irradiation setup, dose measurement, and beam profiling. The specific irradiation campaigns of components of the Optosystem, performed at the Bern cyclotron, are explained in detail in Section 7.3. Finally, Section 7.4 summarises the findings and their implications for the ATLAS ITk Pixel upgrade.

7.1 ATLAS ITk Upgrade for the HL-LHC Phase

The current ID of the ATLAS detector, described in Section 3.2.1, was designed to operate for 10 years at a peak luminosity of $10^{34}\text{cm}^{-1}\text{s}^{-1}$, with an average of 23 pile-up events per 25 ns bunch crossing, and a L1 trigger rate of 100 kHz. The HL-LHC conditions will exceed these design parameters by far.
The instantaneous luminosity, and thus the pile-up, will increase by a factor of up to ~ 7.5 [198].
These large particle fluxes will cause radiation levels to increase by an order of magnitude or more, depending on the total run time of HL-LHC. This means that the damage due to radiation and the detector occupancy would increase immensely for the current technology. Therefore, the ID will be completely replaced by a new all-silicon tracking detector, the ATLAS Inner Tracker (ITk) [199, 200], designed to meet the new, challenging requirements.

7.1.1 The ATLAS ITk Upgrade

The ATLAS ITk detector is designed to overcome several upcoming challenges, including [198, 201]:

- Radiation hardness of all components: the ITk will be exposed to a higher particle flux than the current ID. Therefore it is subject to a much higher radiation environment. The average dose in the area where the ID and ITk are located is expected to increase by one order of magnitude when optimistically expecting an improvement in luminosity from $400\,\text{fb}^{-1}$ (end of Run 3) to $4000\,\text{fb}^{-1}$ (HL-LHC). Thus, the materials and electronics used must be more radiation-hard than current technologies to ensure the longevity and reliability of the detector under these harsh conditions.
- Higher granularity: the pixel segmentation is finer than for the current ID detector to provide a better resolution of particle tracks, but also to keep the occupancy, which scales linearly with luminosity, in the detector below 0.1% (1%) in the ITk Pixel (Strip) detector.

- Higher data rate: the finer granularity means also more read-out channels and thus increased amount of data, which presents a challenge in terms of data acquisition, storage, and analysis.
- Material budget: While adding more active detector material into the same volume, the materials used to build the ITk should not increase the interference with the measurements being. Therefore, materials with low material budget (low densities) are selected.

While the current ID is composed of three subsystems, relying on different detector technologies, as discussed in 3.2.1, the ATLAS ITk will only rely on the semiconductor technology, including a Pixel and a Strip detector. The Pixel detector covers the innermost region from 3.4 cm (3.3 cm) away from the beam-pipe in the barrel (endcap) part. The Strip detector surrounds the Pixel, with its innermost layer at a radius of ~ 40 cm to the collision point, shown in Figure 7.2(a).
The ITk detector will cover a range in pseudorapidity up to $|\eta| < 4.0$, extending the sensitivity of the tracking detector towards the forward region by a factor of 1.6.
As shown in Figure 7.2(b), the ITk Pixel detector is made of a five-layer barrel region in the central barrel part of the detector and ring-shaped end-caps (EC) on either side with discs of sensors. The pixel sizes have been reduced down to $50 \times 50\,\mu\text{m}^2$ and $25 \times 100\,\mu\text{m}^2$ respectively.

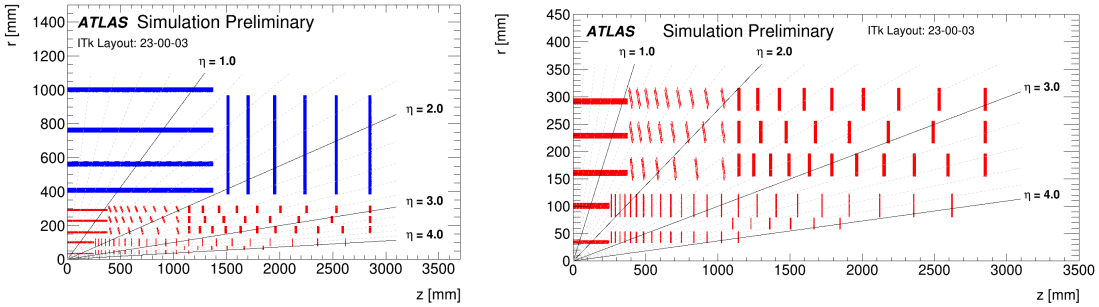

(a) ITk layout

(b) ITk Pixel layout

Figure 7.2: Schematics of the full ITk detector (a) and the ITk Pixel detector (b) for one quarter of the detector in z- and r-directions. Shown are the locations of all layers within the detector volume. Both images are taken from [202].

The design of the ITk pixel detector is a hybrid module design, where the sensor and readout electronics are separate components that are bonded together [199].
To cope with the expected high-radiation environment, the pixel detector is designed to use advanced 3D silicon pixel sensors for the innermost layer [203]. In 3D pixel sensors, the electrodes are implanted into the silicon perpendicularly to the surface, not laid on top, leading to shorter charge collection distances and higher radiation hardness. Nevertheless, the two innermost layers of the ITk Pixel detector will be replaced after exposure to a luminosity of 2000 $\text{fb}^{-1}$of pp collisions, marking half of the HL-LHC phase. For the outer layers of the pixel detector, the design includes thin planar sensors. These sensors use a more traditional design with electrodes on top of the silicon wafer and offer good performance while being less costly and complex to produce than 3D sensors.

The ATLAS ITk Strip detector is surrounding the Pixel detector. It comprises four layers in the barrel region and six discs in each end-cap. The Strip detector utilises single-sided

silicon microstrip sensors, which are more cost-effective and easier to produce in large quantities than pixel sensors [200]. In the following, only the ITk Pixel detector will be further discussed.

7.1.2 The ITk Pixel Optosystem

The $\sim 10\,000$ modules of the ITk Pixel detector generate a data output of up to 11 Tb/s, which is transmitted to the off-detector readout cards located ~ 80 m away from the detector site [204, 205]. To ensure error-free data transmission, the electrical signals are converted into optical signals, which are less sensitive to interference and signal degradation over long distances. Although the optical-to-electrical conversion should be as close as possible to the actual signal generation, space limitations, material budget, and radiation hardness considerations determined the location of the conversion system, relatively far from the actual front-end chips, namely 1450 mm in r direction and 3500 mm in z direction. Electrical cables (Twinax cables) are used for the few metres between the modules and the conversion system.
The conversion is carried out by a high-speed data transmission chain developed in Bern: the Optosystem. The Optosystem is the electrical-to-optical conversion and multiplexing system for the signal and command lines coming from the detector (uplinks) and going down towards the detector (downlinks). The 1.28 Gb/s electrical uplink signals from the front-end chips are serialised into a 10.24 Gb/s stream before being converted into optical signals. Downlink command lines at 2.56 Gb/s are first converted to electrical signals and then parallelised into eight 160 Mb/s lines.

The ITk front-end chips, bump-bonded to the silicon sensor, are connected to the patch panels 0 (PP0) [198]. The PP0s are printed circuit boards (PCBs), through which the data transmission lines, powering, and monitoring of the modules are distributed. Differential electrical cables, the already mentioned Twinax cables, are attached to the PP0 and from here, they transmit the signals to the heart of the Optosystem, the Optoboard.
Depending on the location of the modules, the length of the Twinax cables is between 3 and 6 m. They are connected to the Optoboard via an interface PCB called termination board. The Optoboard itself is a PCB on which a number of dedicated application-specific integrated circuit (ASIC) chips are mounted: up to four GigaBit Cable Receiver (GBCR) chips [206] to recover incoming signals, up to four Low-Power GigaBit Transceiver (lpGBT) chips [207] to aggregate six incoming signal links into one, a Versatile Link Transceiver Plus (VTRx+) module [208] for optical-to-electrical conversion, and a bPOL2V5 DC/DC converter [209] to provide the chips with power. From here, serialised signals are routed out of the detector to the readout cards in the ATLAS counting room via optical fibres. Commands are transmitted the same way in the opposite direction. Figure 7.3 gives an overview of the Optosystem's data and command lines, highlighting the main components of the Optoboard.

Up to eight Optoboards are housed in a mechanical structure called the Optobox. Figure 7.4 shows the design of an open Optobox along with an image of the latest version produced and assembled in Bern. The Optobox is the smallest unit of the Optosystem that can be replaced, thus ensuring the modularity of the ITk Pixel readout chain. In addition to the eight Optoboards, it contains the services to the Optoboards, including the connector board, the power board and various connectors for signal lines, Controller Area Network (CAN) bus lines, and power lines.

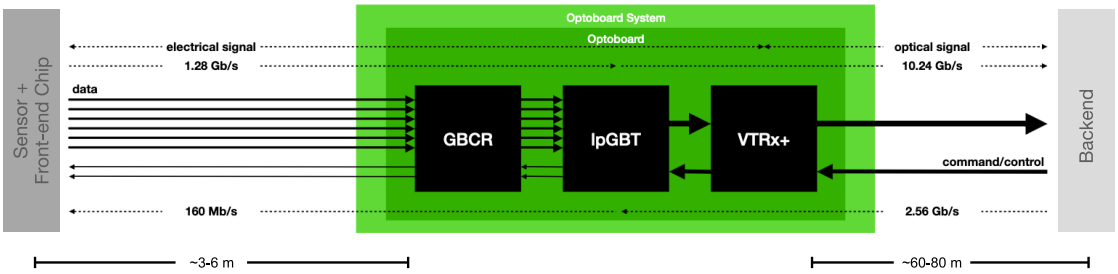

Figure 7.3: Schematics of the Optosystem, figure provided by R. Müller. Electrical signals coming from the ITk Pixel front-end chips at 1.28 Gb/s are recovered (GBCR), serialised (lpGBT), and converted into optical signals (VTRx+) before they are sent at a frequency of 10.24 Gb/s to the off-detector readout cards at the backend. Command lines run from the backend with a speed of 2.56 Gb/s to the Optoboard, where the process is inverted, and the multiplexed downlink signals are transmitted at 160 Mb/s to the front-ends.

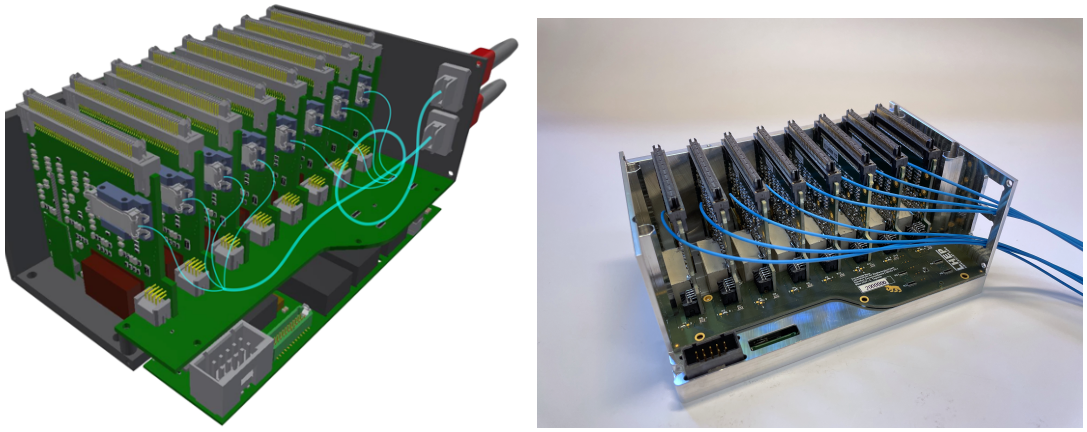

(a) (b)

Figure 7.4: The design of the Optobox (a) fully populated with eight Optoboards and all connectors. The connected optical fibres are also shown. Figure (b) shows a picture of the latest version of a fully populated Optobox produced in Bern.

The Optoboxes are further arranged on Optopanels. The Optopanels are mechanical structures for 28 Optoboxes, cable routing, its cooling system and protection against electromagnetic interference (EMI). The top view layout of an Optopanel is shown in Figure 7.5 with the Optoboxes and corridors for Twinax cables and power/sensing line cables. The bottom plate of the Optopanel is the cooling plate, which keeps the Optoboxes at a Temperature of 15-20 °C. The cooling system uses a Perfluorohexane cooling fluid which is routed through cooling pipes inside the bottom panel.

All powering, sensing, and optical lines are leaving the Optopanel at the wide end through the Optopanel patch panel. Despite being located outside of the ITk Pixel detector volume, the Optopanels are still a part of the ITk Pixel Faraday cage, which encloses the actual detector volume up to the patch panel 1 (PP1), through which the Twinax cables are guided. Figure 7.6 shows the Optopanel locations on one side of the detector. To ensure that the Faraday cage of the ITk detector is shielded, including to the Optopanels,

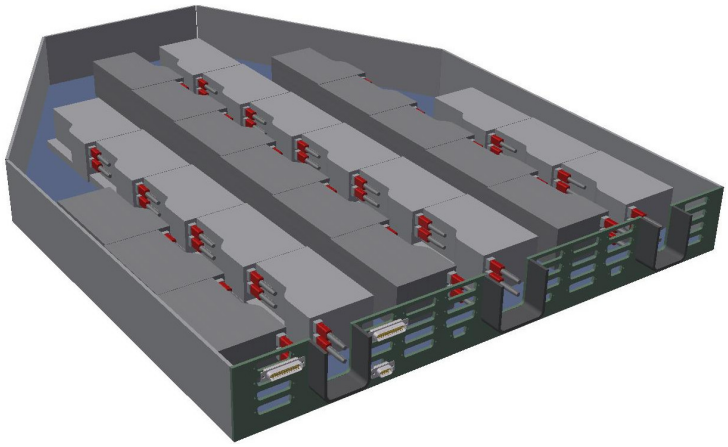

Figure 7.5: Top view of the Optopanel design (without lid), housing 28 Optoboards and corridors for cable routing. The bottom panel is also the cooling plate for the Optopanel.

bundles of $\sim$ 3500 Twinax cables are enclosed in a shielding layer, the Z-shield, between PP1 and the Optopanel. On each side of the detector, four Optopanels are attached to the sealing endcap. This gives a total of 220 Optoboxes and 1562 Optoboards to readout and control the ITk pixel detector.

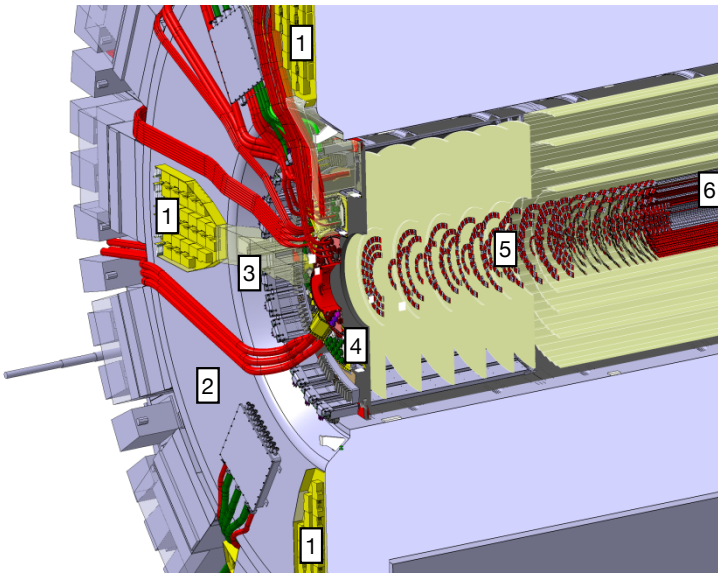

Figure 7.6: Location of the Optopanels (1) on the sealing endcap (2). Shown are only three out of four Optopanels, which are located at both ends of the detector. The light yellow volumes (3) mark the region where the Z-shield is used to wrap the Twinax cable bundles between the PP1 (4) and the Optopanel. The ITk Pixel endcaps (5) and barrel structures (6) are also shown. Image provided by M. Janda, adapted.

7.1.3 Radiation Levels

The components of the Optosystem are placed at different distances to the collision point, and thus are subject to different levels of radiation over the lifespan of the HL-LHC. It is important to quantify the materials against the expected radiation fluences to ensure the efficient functionality of the detector. In this work, the irradiation of four different types of components, which are located at different parts of the data transmission chain, is discussed.

Figure 7.7 shows the simulated distributions of Total Ionising Dose (TID) and Non-Ionising Energy Loss (NIEL) at the end of the HL-LHC lifetime. This corresponds to an integrated luminosity of 4000 fb^{-1} within 10 years. One can see that with increasing distance to the collision point and beam pipe, the dose decreases. The peak towards higher z values is a result of most particles undergoing inelastic scattering into the forward region, which coincides with the regions of highest material budget and therefore highest interaction probabilities.

The components in the innermost regions, such as the modules of the ATLAS ITk Pixel detector, are located between 3.4 cm and 33 cm in r- and 0 cm and 285 cm in z-direction. They will be exposed to the highest doses in TID up to 10 MGy or up to $2\times10^{16}\,n_{\text{eq}}/\text{cm}^2$ in NIEL [210]. For all components the maximal dose is obtained by identifying their locations and obtaining the maximal dose at this point from the simulations.

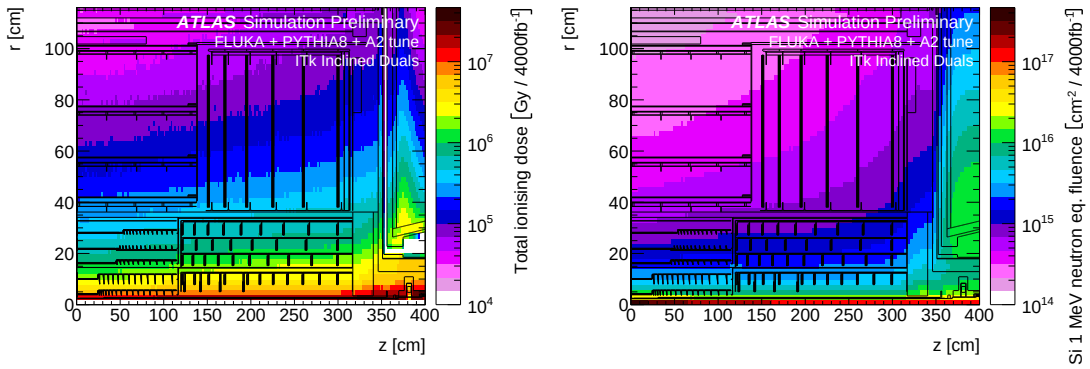

(a) (b)

Figure 7.7: Distribution of total ionising dose (a) and 1 MeV neutron equivalent fluence in silicon, (b) normalised to the total integrated luminosity of 4000 fb^{-1}at the end of the HL-LHC phase in one quarter of the ITk layout. Public radiation plots [210].

The irradiation campaigns of the Twinax cables, the Z-shield, connectors within the Optobox and filtered D-sub connectors on the Optopanel patch panel are discussed. Table 7.1 summarises the locations in z- and r- direction and the maximum TID and NIEL for all these components based on the simulations in Figure 7.7. To extract the expected doses at specific locations, an ATLAS internal tool is available based on FLUKA [211] and GEANT4 [212] simulations. It takes into account the geometry of the upgraded ATLAS detector and the different materials and can be normalised to different luminosities.
It is not foreseen to replace any of the Optosystem service components during the 10 years of HL-LHC, except the Twinax cables. As mentioned before, the first two layers (L0, L1) of silicon sensors of the ITk Pixel detector will be replaced after 2000 $\text{fb}^{-1}$of pp

collisions, because the dose after 4000 fb^{-1}would be well beyond what these electronic components can withstand. As the Twinax cables are soldered at the PP0 connected to the modules, the L0 and L1 ones will be replaced. The "half-dose" on those two layers is still higher than the dose expected at L2 and following, and is therefore taken as reference dose for irradiation.

Component	Location	z_{min}	r_{min}	TID	NIEL
Connectors	Optobox	3405	1450	$(43.6 \pm 0.5) \cdot 10^3$	$(60.7 \pm 0.2) \cdot 10^{13}$
D-sub Filters	Optopanel	3405	1450	$(43.6 \pm 0.5) \cdot 10^3$	$(60.7 \pm 0.2) \cdot 10^{13}$
Z-shield	Feedthrough PP1	3185	430	$(56.8 \pm 0.8) \cdot 10^4$	$(13.3 \pm 0.5) \cdot 10^{14}$
Twinax Cables	ITk Pixel L0	43	50	$(23.4 \pm 0.2) \cdot 10^5$	$(59.4 \pm 0.3) \cdot 10^{14}$

Table 7.1: Locations of components z_{min} [mm] and r_{min} [mm], expected TID [Gy], as well as NIEL in Si 1 MeV n_{eq} [cm^2] after 4000 fb^{-1}(2000 $\text{fb}^{-1}$for Twinax cables) of pp collisions.

7.2 The Bern Cyclotron as an Irradiation Facility

All irradiation campaigns described in this thesis were performed at the Bern cyclotron [213]. The Bern cyclotron is an 18 MeV proton cyclotron with a unique infrastructure and versatile setup possibilities allowing multidisciplinary research. Initially, H^- ions are accelerated up until 18 MeV. The protons are extracted at the exit ports, where stripper foils can be moved inside the beam's trajectory. These are thin pyrolytic carbon foils, where all electrons of the negative H^- are removed. By removing the electrons, the remaining proton is extracted through a change of direction by the change of the particle's charge. While during the night the production of ^{18}F and other radioisotopes for cancer diagnostics is prioritised, during daytime the protons can be extracted into a separate experimental bunker for scientific research. Figure 7.8 shows the two separate bunkers connected by the Beam Transfer Line (BTL). The ion source current can be adjusted to vary the proton flux on the Device Under Test (DUT). The standard setup used for irradiations has been calibrated in the range from $5 \times 10^9\,\text{cm}^{-2}\text{s}^{-1}$ to $4 \times 10^{11}\,\text{cm}^{-2}\text{s}^{-1}$ [214]. Two quadrupole magnets on both sides of the bunker-separating concrete wall can be used to adjust the beam profile.
The facility is well equipped with an extra physics laboratory, which is still inside the controlled radiation area and allows to conduct post-irradiation tests of irradiated samples.

7.2.1 Irradiation Setup

The setup for radiation hardness studies is mounted at the end of the BTL, as shown in Figure 7.9. All components can be mounted individually, allowing very versatile component combinations. For the irradiations presented here, I used the standard setup including the collimator for real time dose measurement, a beam profile monitor and the extraction window, made out of aluminium. The 300 µm thin aluminium layer of the extraction window reduces the proton beam energy to 16.7 MeV [214]. I mounted most of the irradiated samples on a 2D stage, which was then laser-aligned with the centre of the beam. The stage can be programmed and remotely controlled, allowing several different samples to be irradiated without opening the bunker and therefore minimising the exposure of humans to induced radioactivity. Remote control of the 2D stage saves time and allows multiple samples to be irradiated in one go.

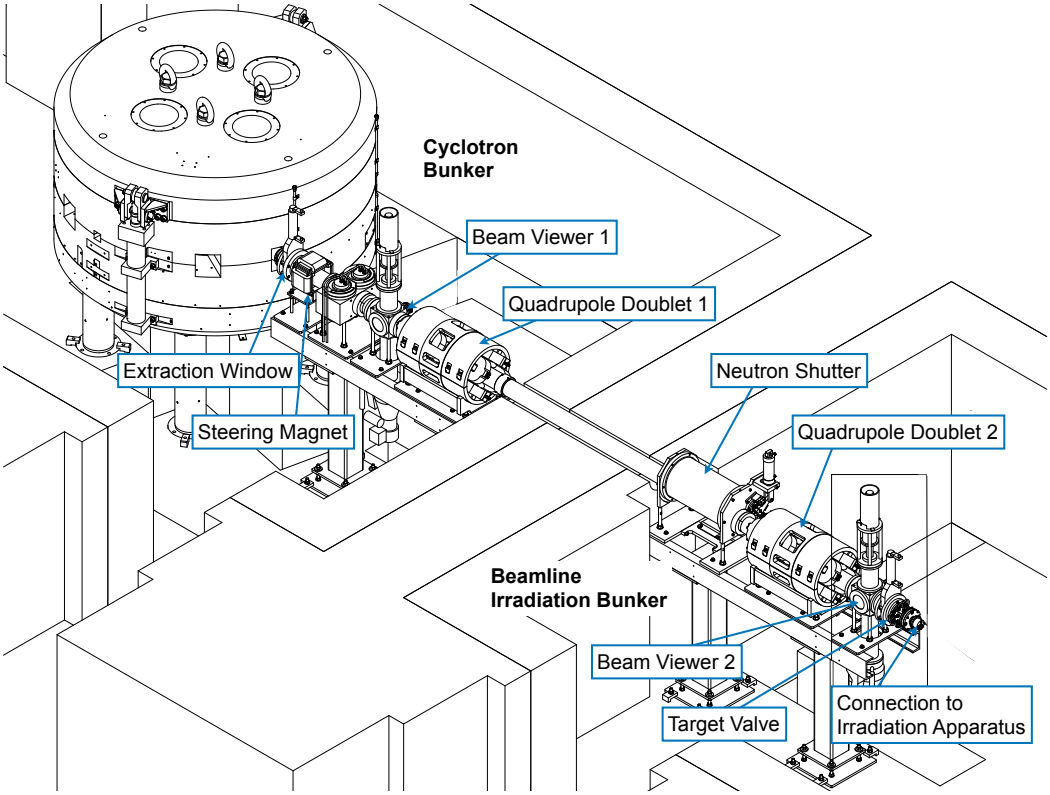

Figure 7.8: 3D schematic of the cyclotron facility in Bern. The cyclotron is located in the cyclotron bunker. Once the H^- ions are accelerated up to 18 MeV, protons are extracted through the extraction window into the Beam Transfer Line, which allows transporting the protons into the Beamline Irradiation Bunker through a 2 m thick concrete wall. Along the BTL are magnets for steering and focusing and beam viewers. The campaign-specific setup for radiation hardness studies is attached to the target valve, which is closed when there is no beam to preserve the vacuum in the BTL [214].

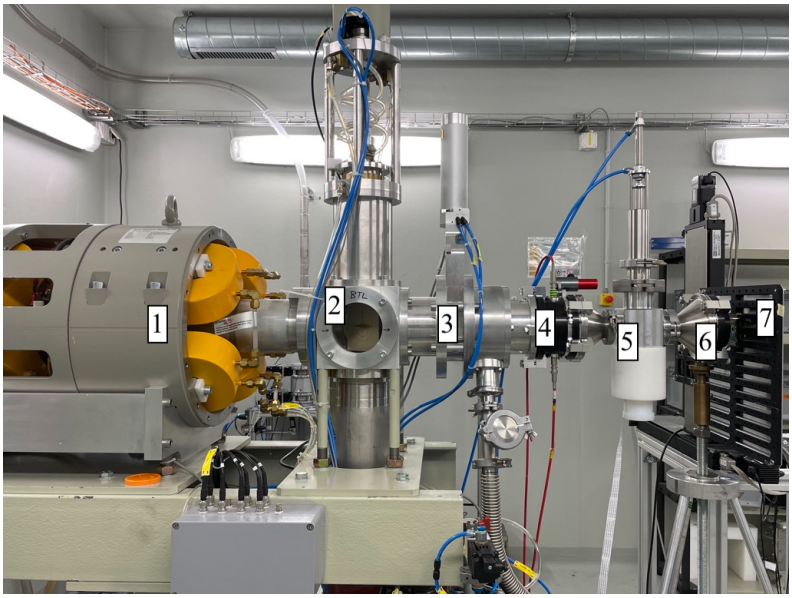

Figure 7.9: Setup for radiation hardness studies attached to the Beam Transfer Line at the Bern cyclotron. The proton beam is steered with the quadrupole magnet (1), guided through a beam viewer (2), a shutter (3), the collimator for dose measurement (4), the π^2 detector for beam monitoring (5) through the aluminium extraction window (6) onto the sample mounted on the 2D stage (7) [214].

For beam monitoring several different devices are available at the Bern cyclotron. The UniBEam [215], a commercial product developed in Bern, makes use of scintillating fibres traversing the beam in x- and y-direction.s Another beam monitoring device developed in Bern is the π^2 detector [216]. A 15 µm thin scintillating foil is placed with 45° towards the beam direction. The scintillating light, induced by the protons, is caught by a camera, placed above the foil. Both devices are explained in great detail in reference [214].

7.2.2 Determination of TID/NIEL

When high-energy particles interact with a material, they can deposit energy (and cause damage) through two main mechanisms: ionising energy loss and non-ionising energy loss.

NIEL is the energy lost through non-ionising processes, such as atomic displacement damage or lattice defects, without ionising the atoms or producing large amounts of free charge carriers. It is particularly relevant for evaluating the radiation response of semiconductor-based detectors and electronics, where lattice defects and displacement damage within the material can cause significant additional noise through increased leakage current. Typically it is quantified in units of 1 MeV neutron equivalent fluence in Silicon. That is the fluence of 1 MeV neutrons that would be required to induce the same amount of displacement damage in Silicon.

The total ionising dose refers to the cumulative ionising radiation dose that a material or electronic device is exposed to over time. It is a measure of the amount of energy absorbed in form of ionisation processes per unit mass of the material or device and depends on the properties of the material and the energy of the ionising particle. It is

calculated via

$$\mathrm{TID} = \phi \frac{1}{\rho} \frac{\mathrm{d}E}{\mathrm{d}x}, \tag{7.1}$$

with ϕ the integrated flux of charged particles, ρ the density of the irradiated material and $\mathrm{d}E/\mathrm{d}x$ the electronic stopping power of charged particles in the material. Typically it is expressed in units of Gray (Gy) or rad, where 1 Gy = 0.01 rad. The unit of 1 Gy is defined as 1 J/kg. The TID can cause permanent charge trapping in the dielectrics present in cables and capacitors, altering its electrical properties, and is therefore relevant for all components discussed here [217].

For radiation hardness studies, usually both, NIEL and TID, are relevant. For 16.7 MeV protons, the energy loss through ionising processes is a factor 3.7 higher than for non-ionising processes [218]. Therefore, one would need to irradiate all samples by almost a factor 4 longer to test also for NIEL. While studies on semiconductors have shown that the non-ionising energy loss causes much more harm than the ionising loss, it is the opposite for the passive materials I studied in this work. Therefore, I decided to test only for TID to also reasonably limit the already long irradiation time down to comply with the availability of the Bern cyclotron.

Equation (7.1) is used to measure dose in real-time at the cyclotron. With the SRIM software [219], the energy loss through ionising effects for 16.7 MeV protons in the irradiated material is estimated. Typical values for common materials are summarised in Table 7.2. Together with the density and the flux of protons, the TID can be determined.

Material	$\mathrm{dE/dx_{elec}}$ [MeV cm^2/g]	Projected Range [µm]
Lead	12.2	46.0
Copper	18.7	630
Aluminium	23.4	1.50
Silicon	22.5	2.10
Liquid Crystal Polymer	30.08	3.32
Polypropylene	33.12	3.44

Table 7.2: Stopping power via ionising losses of 16.7 MeV protons in various materials. Given are the material, the energy loss and the projected range of the protons into the material. All values are simulated with SRIM [219].

To measure the flux of protons, the collimator is used. Figure 7.10(a) shows a cross-section of the collimator design and how it looks mounted on the BTL (b). As shown, the proton beam is first guided through the shaping ring to confine it to a 7 cm-diameter circular area. After the shaping ring, the dump ring gives the beam its final, extracted shape. The beam ring is an exchangeable piece: rings with quadratic windows between $0.5\times0.5\,\mathrm{cm}^2$ and $2.5\times2.5\,\mathrm{cm}^2$ are available. The dump ring is connected to a high-frequency module to measure the proton current which is stopped by the ring. Secondary electrons, which are produced when the protons hit the dumping ring, are forced back onto the dump ring by an applied voltage on the bias ring. Without the bias ring, the measured current is overestimated [214]. Depending on the size of the opening window, as seen in Figure 7.10(b), the current measurement needs to be scaled by a different factor to account for the amount of protons "dumped" to measure the beam current.

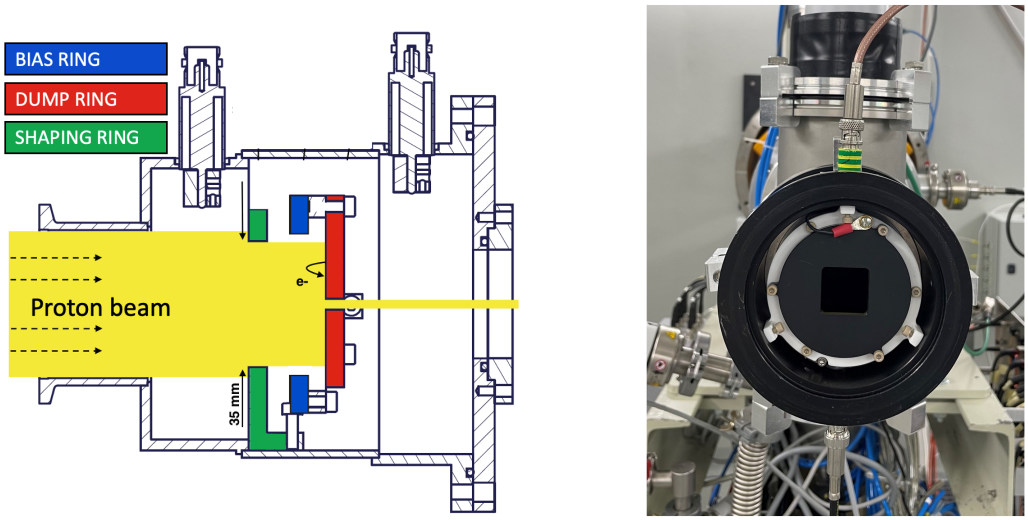

(a) (b)

Figure 7.10: Cross-section of the collimator used for dose measurement at the Bern cyclotron (a) and the opening window of the dump ring attached to the BTL (b). Image from [214].

Dose Calibration

A collimator is used to obtain the real-time dose to the sample being irradiated. The beam profile has a Gaussian shape, but the current (and therefore the dose) is measured at the outer edges of the beam spot. Therefore, for any choice of opening window size, the measured current must be scaled to the actual dose at the centre of the beam. To determine the scaling factor for the largest aperture window, the $2.5 \times 2.5\,\mathrm{cm}^2$ window, we performed a Faraday cup calibration. A Faraday cup is a conducting cup or a metallic enclosure that captures the entire beam spot compared to the dump ring of the collimator. The charged particles, protons in our case, enter the cup, which is connected to a multimeter. The protons create an electric current that can then be measured. Since the current is proportional to the charge of the incident particles and the area is defined by the collimator, the measured current can be converted to the number of charges per unit area, the flux, and from this the dose rate on the target.
For the calibration, we mounted the collimator on the BTL, followed by the Faraday cup, which allowed a measurement of the beam current with the collimator and the Faraday cup simultaneously. Figure 7.11(a) shows the measured current with the collimator and the Faraday cup as a function of time. During 10 minutes, we gradually increased the current setting at the cyclotron ion source from 1 to 8 mA in order to vary the dose rare at the target. Averaging the data points per ion source current setting gives the results shown in Figure 7.11(b). The slope corresponds to the scaling factor to be applied when using the $2.5 \times 2.5\,\mathrm{cm}^2$ extraction window, which we found to be 2.12 ± 0.02.
The accelerator settings affect the beam profile and thus the scaling factor. For this reason, similar settings were used for all irradiation campaigns, and the beam profile was frequently checked with the available beam monitoring devices.

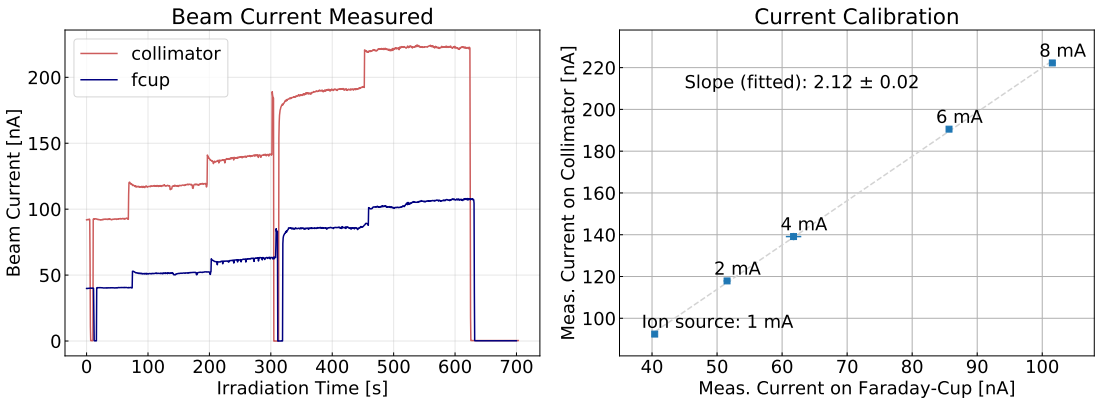

(a) (b)

Figure 7.11: Results from the dose calibration campaign performed with a Faraday cup and the collimator. For different ion source values, the current was measured for small time windows in the order of one minute each, shown in (a). Once the current of the ion source is increased, a short spike in the measured beam current is seen. Excluding this initial spike, the measured values per interval were averaged and are shown for the Faraday-cup against the collimator values in (b).

7.3 Irradiation Campaigns

In order to ensure their functionality during the entire lifespan of the HL-LHC era, I irradiated various Optosystem components, including all the connectors on the Optoboard, the filtered connector used on the Optopanel patch panel, the shielding material for the Twinax cables (Z-shield) and the Twinax cables. For all these components, I defined individual test procedures, taking into account their usage in the Optosystem. These tests are performed before and after irradiation to their total expected dose to ensure their functionality throughout the lifetime of the HL-LHC. In addition, the different shapes, sizes and mounting options require different irradiation setups for all components. The following sections describe my irradiation campaigns for all four types of components, including their specific pre- and post-irradiation tests, the irradiation setups and the results of these campaigns. Conclusions and implications of all campaigns are summarised and interpreted in Section 7.4.

I presented the results discussed in this section in a reduced version at the TIPP-21 online conference, which is summarised in [220] and follows closely this description.

7.3.1 Optobox Connectors

Five different connectors are used inside the Optobox. They vary in shape and number of pins from the smallest connector with 8 pins (SFM/TFM) for power to the largest connector with 100 pins (Edgerate 8) for the connection between the termination board and the Optoboard. Figure 7.12(a) shows all five connectors, including their names and purpose, while Figure 7.12(b) describes their locations in the Optobox.

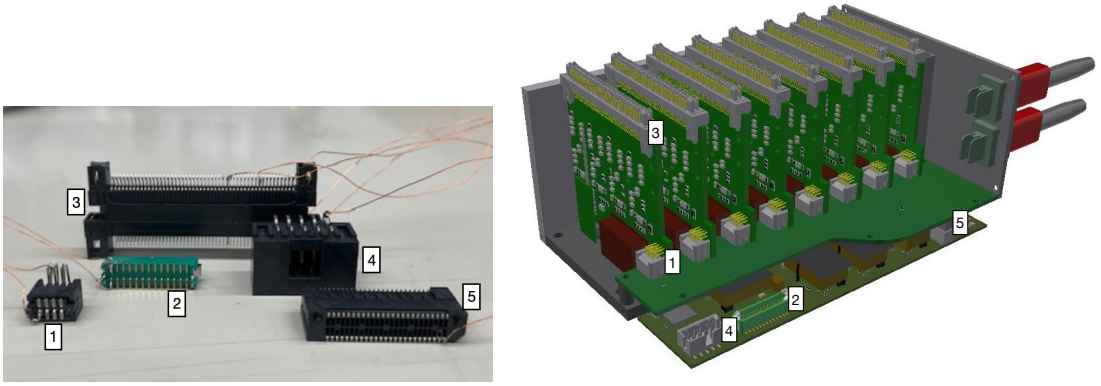

Figure 7.12: Irradiated connectors and their location within the Optobox: (1) the SFM/TFM connector, which provides power to the Optoboard, (2) the G125 connector for power sensing and interlock lines, (3) the Edgerate 8 Elink connector to the termination board, (4) the 2.54 mm Pitch Header SMD for the Vcan and CAN bus lines, and (5) the ERF/ERM8 connector for power.

Radiation Setup

As the connectors are lightweight and have no special mounting feature, I simply placed them on the 2D stage and secured them with Kapton tape. All five connectors were irradiated individually to the maximum TID expected during the HL-LHC of 0.15 MGy, including a generous safety factor compared to the value given in Table 7.1. For the dose measurement, the stopping power and density for the casing material, liquid crystal polymer, was used, as listed in Table 7.2.

Definition of pre-/post-irradiation tests

The connectors are simple plastic-shielded pin-to-pin connectors without any active components. I defined two tests to compare their functionality before and after irradiation: a visual inspection with and without a microscope and a resistance measurement of the connector pins.

For the resistance, I applied a current of 500 mA to individual pins of the connectors using an Agilent E3649A, and measured the voltage using a Keysight 34461A $6_{1/2}$ digit multimeter. The resistance was calculated from the voltage and current. I applied an uncertainty of 0.75 mV to all voltage measurements to account for the experimental uncertainties, which propagates into $\pm 1.5\,\mathrm{m\Omega}$ applied to resistance values.

Results

Figure 7.13 shows the results of the resistance measurements for all five components before and after irradiation, including their uncertainty. While all connectors show different values before and after irradiation, the deviations can be considered to be negligible within the uncertainties. No strong evidence for effects of radiation damage is observed. All connectors are still working after irradiation. Following these measurements, I dis- and re-connected the connectors 20 times. Afterwards, I measured the resistances again. Their functionality was still unchanged.

The inspection with the microscope did not reveal any microscopic damage to the shielding materials of the connectors.

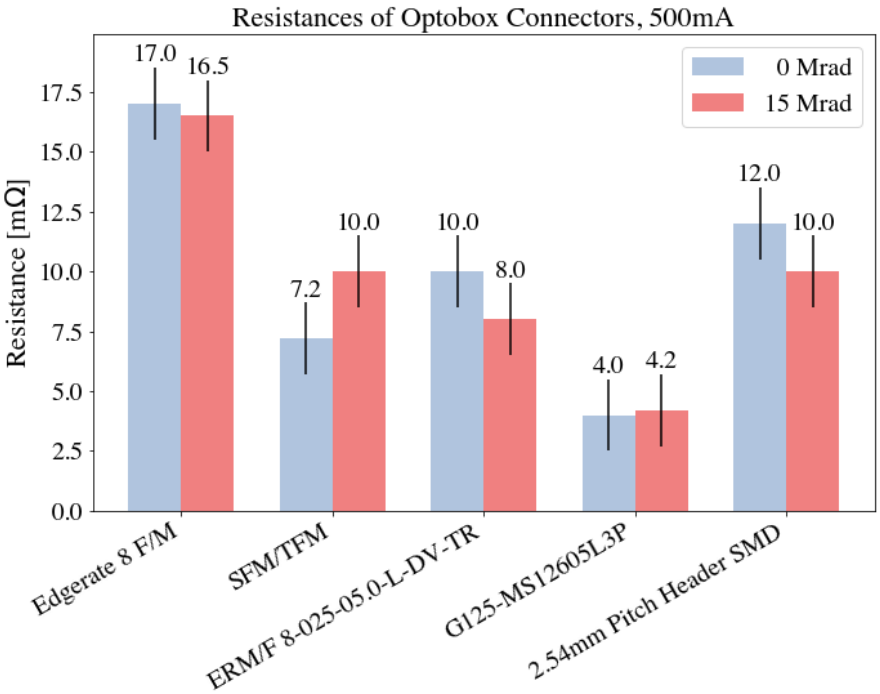

Figure 7.13: Measured resistance before and after irradiation of the five different Optobox connectors. The resistance was obtained as the ratio between the measured voltage at an applied current of 500 mA. For each connector, three pins were used for measurements. The averaged value, including the uncertainty, is shown. Each value is assigned an uncertainty of 1.5 mΩ to account for systematic uncertainties related to the measurement setup.

7.3.2 D-sub filtered Optopanel Patch Panel Connectors

The Optopanel patch panel incorporates connectors with integrated capacitors, known as filtered D-Sub connectors. These low-pass filters play a crucial role in filtering out noise and electromagnetic interference from the power and monitoring lines before they enter the Faraday cage of the ITk at the Optopanel. These lines, spanning 60-80 metres and passing through various components of the ATLAS detector, are susceptible to noise. The DC lines, such as power and interlock lines, require capacitors with a capacitance of 1-10 nF, while AC signals like CAN should have capacitances in the range of 0.1-1 nF, according to the ATLAS ITk Grounding and Shielding guidelines.

The Optopanel patch panel includes two types of D-Sub filters: a 9-pin filter with 330 pF for the CAN bus system, including its power supply, and a 25-pin filter with 6800 pF for the power of the Optosystem (Vopto), power of the sensing lines (Vopto sense), and the interlock system. The location of these filters on the Optopanel patch panel is illustrated in Figure 7.14. For each Optopbox one 25-pin filter is foreseen, while per Optopanel only four 9-pin filters are needed.

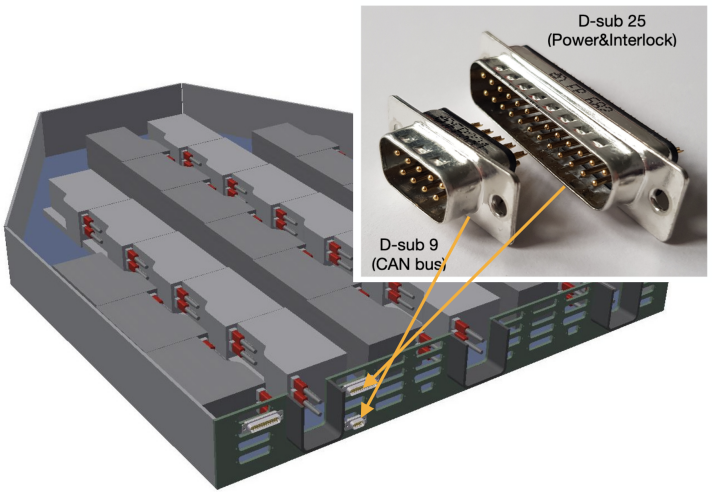

Figure 7.14: Location of the two D-sub filters on the Optopanel. The 9-pin filter is filtering the CAN bus lines, while the 25-pin filter is for the power and interlock lines.

Irradiation Setup

The irradiation setup is identical as for the Optosystem connectors described in the previous section. For irradiation, I removed the aluminium shielding to ensure that the critical components, namely the ceramic capacitors inside the filters, are irradiated.

Definition of Pre-/Post-Irradiation Tests

To ensure the durability of the connectors under a TID of 0.15 MGy, I conducted a series of tests both before and after irradiation. These tests included optical inspection, leakage current measurements at different voltage levels between individual pins and the casing, stability of current at a constant voltage over more than 10 hours, and measurements of the cutoff frequency.

I measured the leakage current between individual pins and the shielding of the connector with an M-pod HV module between 0 and 40 V in automated steps of 1 V. At each step, I took 12 measurements during 60 seconds. For each filter, the series of measurements was repeated with three different pins and averaged. This was done before and after irradiation. The leakage current is required to be very small, in order to ensure that the passing lines are well grounded and none of the voltage is conducted via the surface of the connector.

For the study of the leakage current stability, I measured the leakage current at a constant voltage over a period of more than 10 hours. Stability of the leakage current is important to ensure that the filters can be used over a long period of time without any effects on the conductivity properties. During the detector operation, the lines connected to the filters will transmit 2 V for the 9-pin filter and 9 V for the 25-pin filter, therefore these voltages were chosen for the stability tests.

The D-sub filters are acting as low-pass filters, therefore only frequencies below a certain threshold should be transmitted. This cutoff frequency is typically defined as the frequency at which the voltage (power) has dropped by $1/\sqrt{2} = 0.7$ (1/2), corresponding to a loss of -3 dB. The cutoff frequency for a low-pass filter can be calculated as

$$f_C = \frac{1}{2\pi RC}, \tag{7.2}$$

with the resistance R and the capacitance C of the filter.

I measured the cutoff frequencies by using a signal generator (Agilent 80 MHz Pulse Generator) and an oscilloscope (SDA 816Zi-B 16 GHz Serial Data Analyzer), comparing the amplitude that was generated with the amplitude that was observed after the filters. To eliminate the effects of the cables being used, the measured values were normalised with a reference measurement in parallel where no filter was connected. While the effect of used cables is not fully eliminated by doing so, it is still reduced to a minimal contribution within the scope of this study. With this setup and Eq. (7.2), the theoretically expected cutoff frequencies are $f_{C,25} \approx 1.02$ MHz for the 25-pin filter and $f_{C,9} \approx 20.96$ MHz for the 9-pin filter.

Results

The results of the leakage current and leakage current stability measurements for the 9-pin and 25-pin filters are presented in Figure 7.15 and 7.16. The leakage current, measured between the pins and casing of the connector, showed minimal deviation between the pre- and post-irradiation tests, as visible from the slopes of Figure 7.15. The trend differs between the two filters. While the 9-pin filter shows a slight increase in resistance, the 25-pin filter shows a small decrease. In both cases the resistances are in the order of GΩ, which is sufficient high to keep the leakage current low enough in the nA range. Figure 7.16 demonstrates the stability of the leakage current over a period of more than 10 hours at a constant voltage, both before and after irradiation. I measured the mean leakage currents to be slightly higher after irradiation for both filters. The distributions of the currents showed similar widths, indicating no significant change in fluctuations around the mean values. Lastly, the results of the cutoff frequency measurements for both filters are shown in Figure 7.17. A slight effect for both filters towards a slightly lower cutoff frequency after irradiation is observed. Comparing the measured values with the expected cutoff frequencies for the given setup, good agreement can be seen.

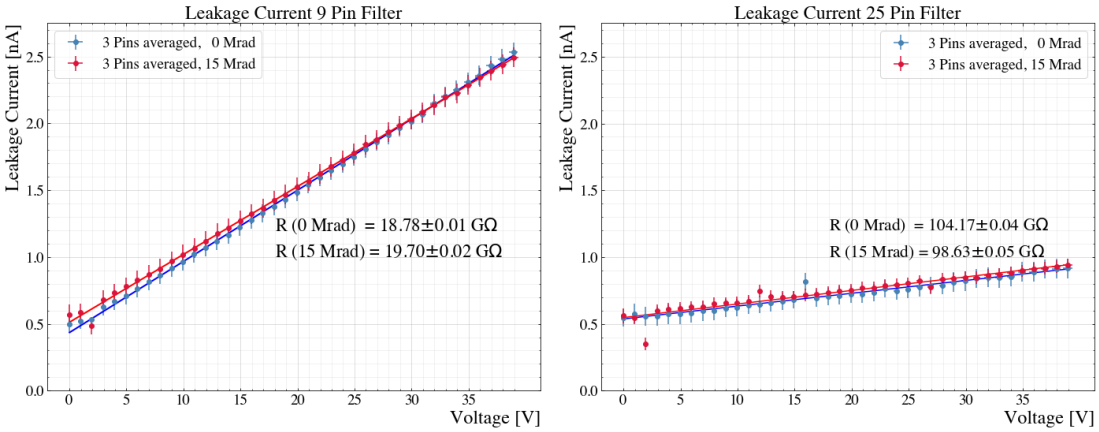

(a) 9-pin D-sub (b) 25-pin D-sub

Figure 7.15: Leakage current measurements of D-sub filters before and after irradiation to 15 Mrad as a function of voltage. At each voltage step, the measurement time was 60 seconds. The data points are averaged over results from three different measurements with different pins. For both filters, a small deviation in the resistance is observed after irradiation.

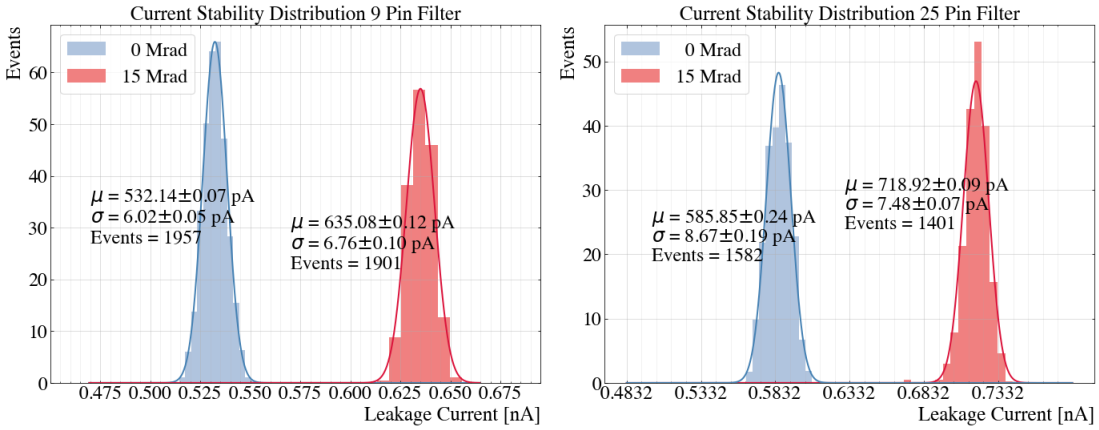

(a) 9-pin D-sub (b) 25-pin D-sub

Figure 7.16: Distributions of measured leakage currents during leakage current stability tests lasting 15 hours (a) or 10 hours (b). Over that period of time, two measurements per minute were taken. The varying number of events per histogram are a result of slightly differing measurements times between 15 hours for the 9-pin filter and 10 hours for the 25-pin filter. After irradiation, the leakage current is slightly higher but still stable.

7.3.3 Z-shield

The Z-shield is introduced to be wrapped around the Twinax cables between the mechanical structure PP1 and the opening of the Optopanel where they are routed to. This shielding has the purpose to extend the Faraday cage from PP1 to the Optopanel and additionally shield the cables from radiation and electromagnetic interference as shown in Figure 7.6. It is a foil, which has an aluminium layer on the inside, and a polyurethane film on the outside. It is $\sim$ 6-metres-long and wrapped around bundles of $\sim$ 3500 Twinax

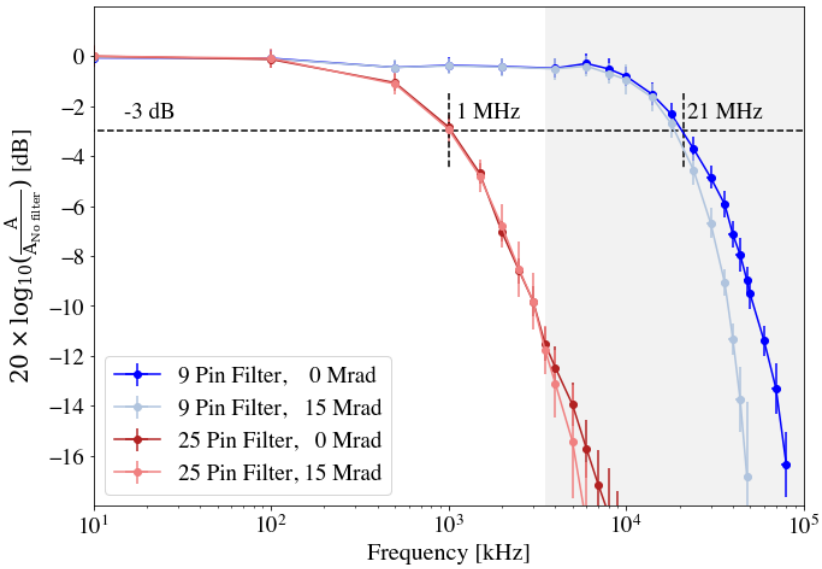

Figure 7.17: Measurements of the loss in dB as a function of frequency. In voltage, a loss of -3 dB marks the cutoff frequency at which the amplitude is reduced to 70%. Shown are the results for the 9-pin and 25-pin filters before and after irradiation. Slight changes can be seen towards high frequencies.

cables. It can be closed with an adhesive strip, which is attached in a way that the grounding wire, which is at the edge of the foil, has good contact with the aluminium layer. Figure 7.18(a) shows how the foil looks on both sides, with the ground wire on the bottom right corner and the adhesive strip under its white cover on the aluminium side.

Irradiation Setup

For irradiation, I cut the Z-shield into a 2 cm wide strip, glued it together with its adhesive strip to form a ring, and attached it to the 2D stage so that the area where the adhesive and the ground wire are located is in the beam window. Figure 7.18(b) shows the Z-shield after irradiation. It was irradiated in two close but non-overlapping areas to ensure that the adhesive and the ground wire were irradiated. Hereby, I controlled the movement with the remote controllable 2D stage. Both areas were irradiated up to 1.2 MGy, applying a safety factor of ~ 2 to the value given in Table 7.1. The shielding foil was facing the proton beam, therefore a material with properties similar to the shielding material, Polypropylene, was used to estimate the stopping power, which is listed in Table 7.2.

Definition of Pre-/Post-Irradiation Tests

For the Z-shield, I defined tests including an optical inspection, a pull test over the adhesive and a check that the electrical conductivity over the ground wire is still ensured after irradiation. The pull test was performed using a Newton meter as shown in Figure 7.18(c). I used different samples for the pre- and post-irradiation test, to ensure a previous pull-test has no effect on a pull-test after irradiation. The pre-irradiation pull-test was conducted with a 1 cm and a 2 cm wide ring to also compare the effect of the thickness. For the conductivity test, I cut the ring into two pieces. A multimeter was

(a) Z-shield (b) Irradiated ring (c) Pull test

Figure 7.18: Images of the Z-shield. Image (a) shows both sides of the shielding foil with the aluminium layer inside and the shielding layer outside. Visible is also the adhesive strip on the aluminium layer and the grounding wire on top of the black foil. Image (b) shows the irradiated area, and the adhesive after the pull-test, which is shown in (c).

applied on both ends, which were still in contact via the grounding wire. This way I was able to quantify if the grounding wire remains conductive after irradiation.

Results

Optical inspection showed that the black film had a slight colour change, as shown in Figure 7.18(b). The pull test showed that the adhesive did not have the same strength as before irradiation. Once the ring opened due to the applied force, it was "re-glued" once again and the pull-test was performed again. Before irradiation, the adhesive strip on the ring was sticky enough to be re-glued and a second pull test was carried out for two rings with different thicknesses. The ring with 2 cm width showed approximately twice as much adhesive strength compared to the 1 cm ring. After the first pull test of the irradiated ring, the film could no longer be stuck together due to the lack of adhesive power. The results of the pull test tests with the Newton meter are summarised in Table 7.3. Once the pull-test was performed, the ring was cut into two pieces, and I evaluated the electrical conductivity, which was still present after irradiation.

Sample	Width	Dose	Test 1	Test 2
1	1 cm	0 Mrad	24 N	22 N
2	2 cm	0 Mrad	55 N	48 N
3	2 cm	120 Mrad	46 N	–

Table 7.3: Results of the Z-shield pull tests before and after irradiation. Sample 1 (1 cm wide) and sample 2 (2 cm wide) were not irradiated, while the pull test for sample 3 (2 cm wide) was performed after irradiation. The second test for sample 3 was not possible because the adhesive did not adhere after the first test. Sample 3 was irradiated after being glued.

7.3.4 Twinax Cables

The electrical signals produced when charged particles interact with the silicon sensors of the ITk Pixel detector are digitised on the chip. Then, they are transmitted from the PP0, to which the modules are connected, via Twinax cables out of the most central regions towards the Optopanel.

Twinax cables, also known as Twinaxial cables, are high-speed, shielded data transmission cables commonly used in electronic communication systems. They consist of two copper conductors that are twisted together in a coaxial configuration. The conductors are surrounded by insulation material and an outer shield, which provides protection against electromagnetic interference and crosstalk. Twinax cables are designed to transmit differential signals, where data is sent simultaneously on the two conductors with opposite polarities. This configuration helps in reducing signal degradation and improves noise immunity, making them suitable for high-speed and long-distance data transmission.

For the Optosystem, two cables from different manufactures, namely Samtec and Molex, are being qualified for ATLAS. Their main differences are how grounding is achieved and the material composition. For the Molex design, the grounding is a third, separate wire, running in parallel with the two signal conductors. The Samtex cable uses a layer of the cable shielding as a grounding line.

In the Optosystem, the Twinax cables have different lengths, depending on which subsystem of the Pixel ITk detector they are routed to. Their individual length spans between 3 m and 6 m. A total of about 17 800 Twinax cables for the uplinks and 8 400 for the downlinks will be used.

Irradiation Setup

The irradiation of 6 m long Twinax cables to their expected maximum TID of 5 MGy was the most challenging campaign, requiring the development of dedicated irradiation and testing setups.

The cyclotron beam extraction window covers an area of $2.5 \times 2.5\,\mathrm{cm}^2 = 6.25\,\mathrm{cm}^2$. With the maximally optimised cyclotron setting for irradiation, the irradiation of a 6 m long, and 1 mm wide cable would lead to more than 500 hours of irradiation, unrealistically assuming the cable can be packed together with a 100% efficiency.

Therefore, we developed a rotating spool, onto which a 6 m long cable can be rolled up, optimising the packing factor, while minimising the required beam time. The spool design was chosen such that one can achieve the TID within 5 irradiation days. We achieved this by a spool with a diameter of 3.18 cm which constantly rotates during irradiation. Additionally, the rotating spool is enclosed in an air-tight container, prohibiting activated air to be released into the bunker air: this allows the usage of a much higher beam current, therefore also a higher dose rate. The motor, which controls the rotation of the spool via a Raspberry Pi, is on top of the air-tight container, outside the beam and thus less subject to radiation. The cable is rolled up in two layers, starting at the top of the spool, going to the bottom and up again with a second layer. Figure 7.19(a) shows two spools with 6 m cables spooled on. The ends of the Twinax cables are attached to SMA connector boards on top of the spool, allowing various tests before-, in-between, and after irradiation. They are fixed, and do not need to be removed before irradiation, allowing easier handling for tests. Due to the design of the spool, the connector boards are outside the beam extraction window and are therefore not irradiated directly to avoid damage and activation of these boards. Figure 7.19(b) shows one of the spools attached to the motor inside its enclosed container with opened endcap, attached at the end of the BTL. The closed irradiation container is displayed in Figure 7.19(c).

The spool is larger than the extraction window and the cable rolled up in two layers, which means the irradiation profile of the cable is not homogeneous. The energy loss of

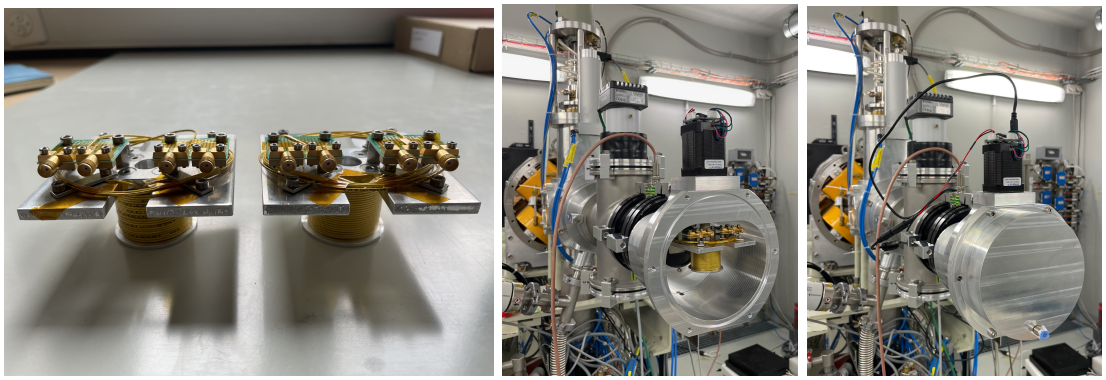

(a) (b) (c)

Figure 7.19: Irradiation setup for 6 m long Twinax cables. Figure (a) shows two of the spools for irradiation, onto which the cables are attached. The spool was designed, such that connector boards for testing at intermediate radiation steps are accessible on the top. They do not have to be removed for irradiation. Figures (b) and (c) show the irradiation container inside which the spool gets attached to the motor (on top). After closing the volume, the irradiation can start.

the incoming protons was estimated with the simulation tool SRIM, taking into account the different cable layers made of different materials. The detailed approximation can be found in Appendix A. This simulation revealed that protons penetrate through both layers of cable and will be stopped in the spool body made out of aluminium, thus will not reach the cable layers on the other side of the spool body. Based on the simulation the dose on the surface of the lower layer was also estimated. The energy loss scales inversely with the energy of the incoming protons. Because the protons already lose some energy in the first layer, the energy loss, and thus the dose, is higher in the second layer of cable. Figure 7.20 shows the delivered dose as a function of length of the cable obtained with SRIM. The cable is hereby defined into three parts of the cable lengths (each 2 m long), of which the first half of the cable, 3 m, is the lower layer on the spool. The first third, being part of the lower layer, receives a dose which is a factor 1.4 higher than the expected 500 Mrad, the middle one is outside of the irradiation window, and the last one, the outer layer, receives the required 500 Mrad. After careful consideration and discussion, it was agreed that the inhomogeneous irradiation profile models even better the real time conditions of the cable on the detector side. Only the first few cm will be subject to 500 Mrad, and there might be more inhomogeneities due to the different detector materials and the different paths the cables are routed along their way.

For the Molex cables, we prepared three spools, of which two were irradiated in steps of 100 Mrad in alternating mode. The cyclotron's availability made it possible to have one day of irradiation per week over the course of 10 weeks in autumn 2021. This meant that each of the two spools was irradiated every second week, which allowed enough time for most of the induced radioactivity to decay away to conduct measurements before they were further irradiated. We kept the third spool unirradiated as a reference cable.

For the Samtec cable, we prepared only one spool and irradiated it within two consecutive days to the full dose.

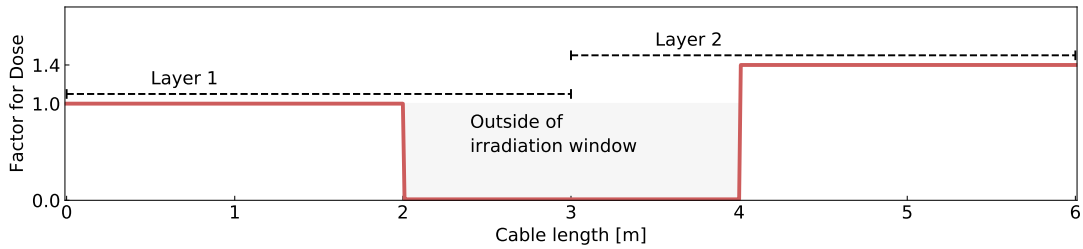

Figure 7.20: Dose profile of a 6 m long Twinax cable irradiated on the spool. Shown is the factor for dose as a function of Twinax length. The factor of 1.0 corresponds to the targeted 500 Mrad.

Definition of Pre-/Post-Irradiation Tests

The requirements on the data transmission chain combine a maximal signal attenuation of -20 dB and a bit error rate (BER) of less than 10^{-12}. I set up dedicated tests to measure the contribution of the Twinax cables with increasing radiation dose to these requirements.

I measured the signal attenuation, or insertion loss, with a 4-point Vector Network Analyser (VNA), the "Rhode & Schwarz ZVA 40 VNA 10 MHz ... 40 GHz" over a wide range of frequencies. The power loss L is one of four possible S-parameters, $Sdd21$, for differential cables via

$$L\ [\mathrm{dB}] = -20 \times \log_{10}\left(\frac{A_2}{A_1}\right), \tag{7.3}$$

with incoming amplitude A_1 and outgoing amplitude A_2, which specifies the transmission of the signal's amplitude through the cable [221, 222]. A loss of 1.5 dB corresponds to a drop in amplitude of roughly 15%.
For the measurements with the 4-port VNA, a calibration of the used cables and connectors needs to be performed. The 4-port VNA could not be transported to the Bern cyclotron facility, therefore sufficient cool-down of the cable had to be awaited before it was safe to transport it to the Physics Institute of the University of Bern where the measurement could be taken. The radiation levels for active material are required to be below 300 nSv/hour on contact and 100 nSv/hour at 10 cm distance, measured with a high-sensitive dosimeter at the irradiation facility, to be safe to leave the facility. I performed this measurement after irradiation intervals of 100 Mrad for the Molex cable, and only after the total 500 Mrad dose for the Samtec cable.

The second test uses the entire preliminary data transmission chain, following the principles introduced in Section 7.1.2. For the purpose of this study, we designed a dedicated setup, which was easy to transport to the Irradiation facility and small enough such that it could stay there, despite limited space availability. Only a few days after irradiation, I removed the cable from its irradiation container and conducted measurements in the controlled area of the physics lab at the cyclotron. With this setup, explained in the next section, I performed BER tests for the Molex cables.

Preliminary Data Transmission Chain for Cable Testing

The cyclotron setup used almost all key components of the ITk Pixel data transmission chain except that the uplink signals are generated on a clock data recovery (CDR) chip [223] and are not coming from an actual module. Therefore, the setup shown and used here, is more a preliminary testing setup than the final design. The components used for this setup were at the time the most recent versions, which may differ in certain aspects compared to the final design. The entire read-out was based on a KC705 FPGA board [224], which is replaced by the FELIX readout cards of the ATLAS ITk Pixel detector.

Figure 7.3.4 shows a top view of the setup. The CDR chip (1) generates a pseudo-random binary sequence, known as the PRBS7 pattern, which simulates a signal string from the detector. It is controlled via the BDAQ board (2) [225]. Once the signal is generated, it is sent via SMA cables to the uplink Twinax spool (3). From here, the signals are directed via the SMA connector board (6) to the Optoboard (5), where serialising and conversion into optical signals takes place. From here, the data string is transmitted through optical fibres to the FPGA (7), which is the interface to the user. Commands processed on the FPGA take the same route but opposite direction: from the FPGA, to the Optoboard and connector board to the downlink Twinax spool (4) and to the CDR. The connection of the CDR and BDAQ requires two extra display port connector boards (8). An SMA patch panel (9) was designed to easily swap components, such as the spools for irradiation.

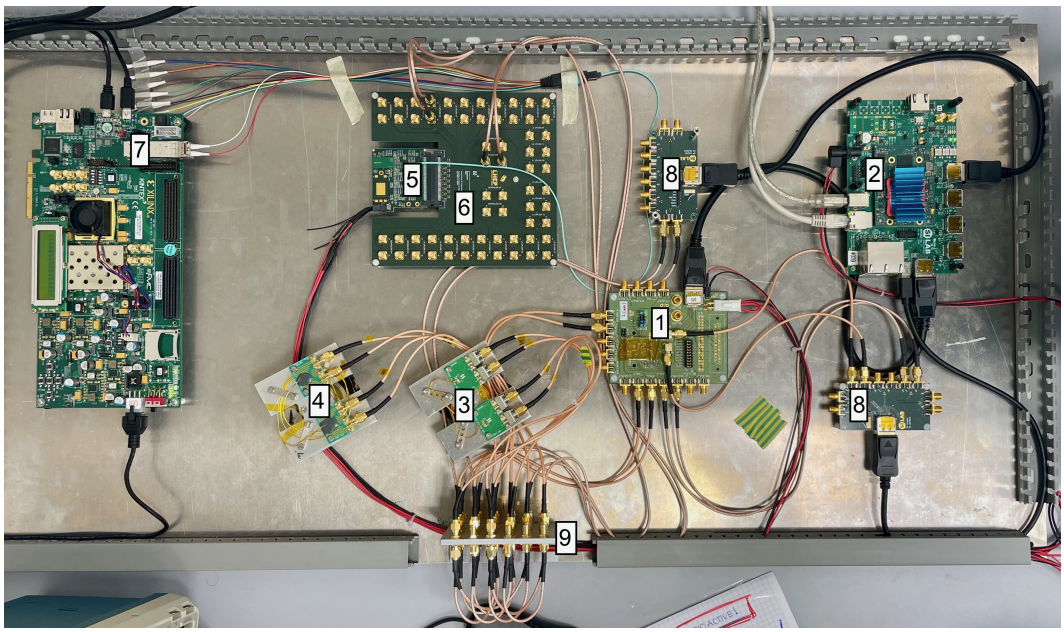

Figure 7.21: Top view of the Optosystem data-transmission setup used for cable testing during the irradiation campaign at the Bern cyclotron. The main components are the CDR chip (1), the BDAQ board (2), spools with irradiated cables for the up- and downlink (3, 4), the Optoboard (5) with its termination board (6), the FPGA (7), two display port connector boards (8) and the connector patch panel (9).

The lpGBT chip on the Optoboard has an integrated PRBS7 pattern checker, which allows for BER tests. A PRBS7 generated bit string is sent from the CDR via the uplink

at 1.28 Gb/s through the Twinax cable to the Optoboard, where the lpGBT compares the incoming pattern with the expected pattern.

In order to quantify a BER of 10^{-12} with a certain confidence level, e.g. 95% is this case, a minimum amount of bits, N_{bits} needs to be sent and registered. The BER distribution can be approximated with the Poisson distribution and an average amount of errors μ to be

$$\mu = \text{BER} \cdot \text{N}_{\text{bits}}. \tag{7.4}$$

The Poisson probability function for the number of errors, N_{err} given μ is

$$P(N_{\text{err}}, \mu) = \frac{e^{-\mu}\mu^{N_{\text{err}}}}{N_{\text{err}}!} = \frac{e^{-\text{BER}\cdot\text{N}_{\text{bits}}}(\text{BER} \cdot \text{N}_{\text{bits}})^{\text{N}_{\text{err}}}}{N_{\text{err}}!}. \tag{7.5}$$

Having more than N_{err} with a probability less than 5% (95% confidence level) results in

$$\sum_{0}^{N_{\text{err}}} P(N_{\text{err}}, \mu) = 1.0 - 0.95 = 0.05. \tag{7.6}$$

Now, assuming a BER of 10^{-12}, we can calculate the number of bits needed to be sent, with zero errors via

$$e^{-\text{BER}\cdot\text{N}_{\text{bits}}} = 0.05, \tag{7.7}$$

$$N_{\text{bits}} = -\frac{\ln(0.05)}{\text{BER}}, \tag{7.8}$$

which gives

$$N_{\text{bits}} = 2995732273554 \approx 3 \cdot 10^{12}, \tag{7.9}$$

which need to be transmitted correctly, if one wants to quantify a BER of 10^{-12} at 95% confidence level with still observing no errors. Contrary, the longest measurement time available for the lpGBT pattern checker is 2^{35} clock cycles, which corresponds to $\sim 1.09 \cdot 10^{12}$ bits. The measurement time is 14:33 minutes and is the maximum available measurement time. This reduced the BER which we can measure with a 95% confidence level by a factor 1.09/3.0, meaning we effectively measured a BER $< 3 \cdot 10^{-12}$ with a confidence level of 95%.

The signals have a rectangular waveform. Through a Fourier series representation, the signal can be decomposed into its various sinusoidal frequencies, which modulate the waveform. While these frequencies span over a wide range, the most dominant is the carrier frequency. For a 1.28 Gbps periodic clock signal, corresponding to a subsequent series of 0-1-0-1-0... bits with 2 bits per clock cycle, the carrier frequency is 640 MHz. On the Optoboard, the GBCR is recovering the incoming uplink signal by enhancing it, before it gets processed by the lpGBT. The GBCR has a continuous time linear equaliser (CTLE) that can boost certain frequency regions of the modulating frequencies to recover sharp edges of the rectangular waveform. For this study, the BER test was performed for 16 different settings of the CTLE for mid and high frequencies, respectively, which results in 256 combinations for which a BER was performed.

Results

Figure 7.22 shows the results of the signal attenuation measurements for both cable types, the Molex (a) and Samtec (b) cable. One can observe a similar trend for both cables, which shows higher deviation with increasing dose for higher frequencies. At 640 MHz, the carrier frequency for a periodic clock signal of 1.28 Gbps, the attenuation of the Molex cable decreased by 1.31 dB to -11.689 dB. For the Samtec cable, the increase in loss was slightly lower with 0.51 dB, resulting in a attenuation of -11.51 dB at 640 MHz. If one considered signals which are not periodic clock signals, the Fourier transformation shows a more complicated composition of the frequencies modulating the waveform. We observed that the most dominant frequencies are below 640 MHz, which makes the comparison made in Figure 7.22 at 640 MHz, still a valid representation to quantify the change in power loss for non-periodic signals.

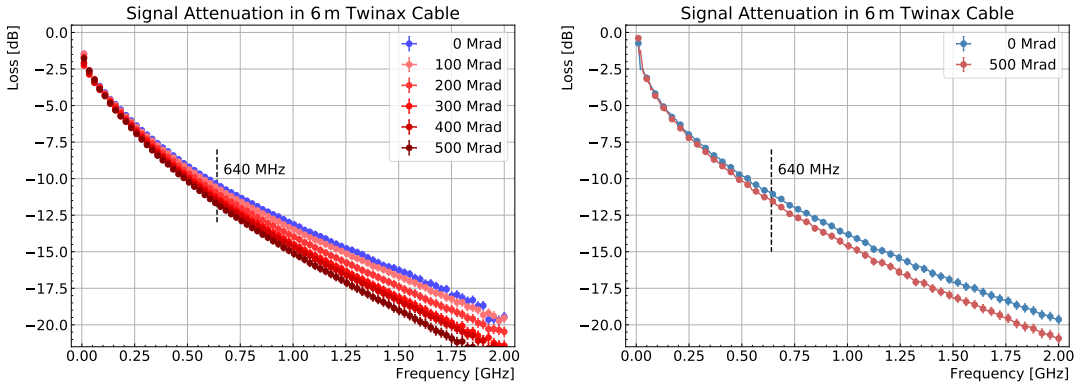

(a) Molex

(b) Samtec

Figure 7.22: Loss curves for the Molex (a) and Samtec (b) cables at different dose levels between 0 and 500 Mrad. The signal attenuation was measured between 10 MHz and 2 GHz with a 4-port VNA. The 640 MHz line marks the frequency at which the uplinks will be transmitted through the Twinax cables, corresponding to a data rate of 1.28 Gb/s.

Figure 7.23 shows the results of the 2D BER scan for the unirradiated Molex cable (a) and after the full dose of 500 Mrad. The 2D scan was performed in the parameter space for high and mid frequency CTLE parameters. One can see that, for the central area of both parameters, the BER is below the limit of $3 \cdot 10^{-12}$ at 95% confidence level, meaning that no bit errors were observed during the BER test with $1.09 \cdot 10^{12}$ bits sent. For the corner regions, especially for low enhancement in the mid frequency range, the BER is not sufficient. Same holds for very low or very high enhancement of the high frequency ranges. Comparing the scan before and after irradiation, one can see that the central bulk region gets smaller, but the majority of the central area remains in good condition for the BER.

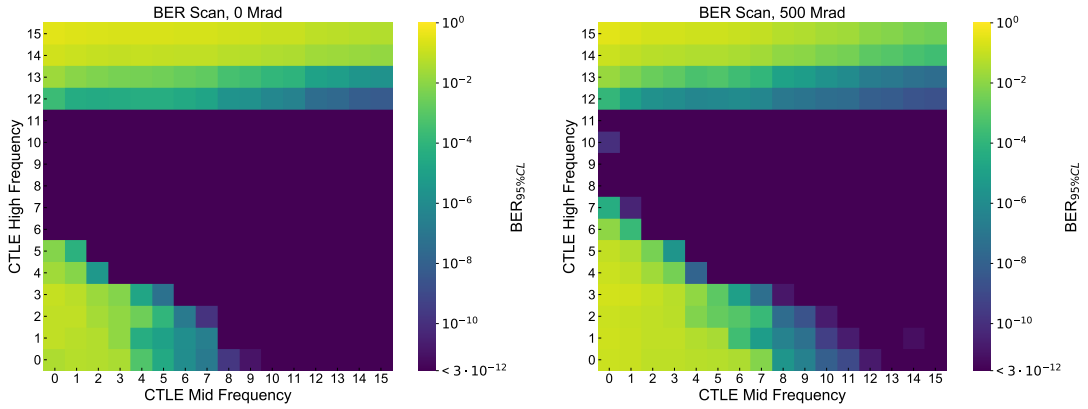

(a) BER Scan before irradiation

(b) BER Scan after irradiation to 500 Mrad

Figure 7.23: BER scans for the Molex cable before (a) and after (b) irradiation in the CTLE plane for mid and high frequencies. Small changes towards the corner regions can be observed, the bulk central region remains at a BER of less than $3 \cdot 10^{-12}$ at 95% confidence level.

7.4 Conclusion and Implications

In Section 7.3, I describe four different irradiation campaigns that I conducted at the Bern cyclotron for the ITk Pixel Optosystem service components. For all four types of components, I extracted the expected TID from simulations, and defined specific tests to validate their performance after irradiation to full dose.

The Optobox connectors were affected by radiation such that their resistance changed, described in Section 7.3.1. No general trend for all connectors was observed. The changes of the measured resistances before and after irradiation are all - within their uncertainties - negligible, the connectors work well after irradiation to their TID of 0.15 MGy. I would recommend using the Optobox connectors for the ATLAS ITk, as they showed no hints for degradation after exposure to the full HL-LHC TID.

Similar results are seen from the irradiation campaign of the Optopanel patch panel filters, described in Section 7.3.2. The performed tests on the leakage current showed an effect of radiation resulting in higher leakage currents, but were still in the order of nA and therefore negligible. The same result was found for the measurements of the cutoff frequency, where an effect was observed, but no signs of failure. The tendency to slightly worse performance of the filters towards an increased cutoff frequency after irradiation can be explained with the effect of ionising radiation on the capacitors. The ionisation could cause an increase in capacitance, which is measured by a lower voltage. I found the cut-off frequencies after irradiation still below the theoretically measured limits. The deviations are well within one order of magnitude and do not exceed the specifications for the filters. Therefore, I would recommend using the D-sub filtered connectors for the Optopanel.

The irradiation campaign of the Z-shield was summarised in Section 7.3.3 and included pull-tests. These showed significant reduction of the adhesive strength compared to pre-irradiation tests. The non-negligible effect of high temperatures through irradiation could - together with the ionising radiation - cause changes of the atomic structure of

the adhesive. Therefore, I would strongly suggest to either find an alternative with a different closing mechanism or to support the Z-shield surrounding the Twinax cable bundles with additional cable ties or similar tools.

Lastly, the Twinax cable irradiation campaign was discussed in Section 7.3.4. The requirements in terms of dimension and high dose required the design of a novel irradiation setup and a readout chain. The cables showed slightly worse performance in their signal attenuation after irradiation. This could result, similar to the D-sub filters, from atomic changes in the insulator material, causing increased capacitances and thus a stronger signal attenuation. We also tested the BER up to $3 \cdot 10^{-12}$ with a confidence level of 95%. Unfortunately the available measurement time was by a factor 1/3 too short to measure the required limit of $< \cdot 10^{-12}$ with a confidence level of 95%. While we observed good results, I would recommend repeating the BER with a longer measurement time for a few CTLE Mid and High frequency settings in the central parts of the plots in Figure 7.23 to confirm the results I observed.

Chapter 8
Conclusion and Outlook

In this doctoral thesis, I described three major achievements in the field of experimental particle physics: first, the extension of the expected limits for the existence of third-generation supersymmetric quarks in final states with a top-quark, a bottom-quark, and missing transverse energy ($tb + E_{\mathrm{T}}^{\mathrm{miss}}$); second, the extension of the observed limits for the existence of R-parity-violating supersymmetry in final states with at least 6 quarks (RPV multijet); and third, the demonstration of radiation tolerance of ITk Pixel service components up until the expected total ionising dose for the full HL-LHC lifespan.

The results from the $tb + E_{\mathrm{T}}^{\mathrm{miss}}$ analysis in this thesis have been summarised in an internal ATLAS documentation. By the time of the submission of this thesis, the analysis was still blinded, meaning the finalised region definitions have not yet been applied to the full Run 2 data as planned in the introduction. The unblinding is foreseen for autumn 2023 with a subsequent publication.
From the two expected exclusion contours in the 2D mass grid, I can already draw promising conclusions about its potential combined sensitivity. The aim of my work was to improve the sensitivity in the compressed region, where the mass difference between the third-generation squarks and the neutralinos is low ($\leq$ 400 GeV), therefore extending the reach of the SUSY search for $tb + E_{\mathrm{T}}^{\mathrm{miss}}$ final states including one lepton with 36.1 fb^{-1} of data [34]. I demonstrated that we can achieve an improvement in this region, closing un-discovered corridors from the the previous analysis. The unblinding will show whether we observe an excess in this region or if the probed $tb + E_{\mathrm{T}}^{\mathrm{miss}}$ signature will be excluded for higher SUSY particle masses.
The immediate next step of the analysis is to combine the two individual signal regions SRA (bulk) and SRB (compressed) to enhance the sensitivity to higher masses. From the individual exclusion contours, I expect an increase of exclusion by at least 220 GeV in the bulk region and 100 GeV in the compressed region compared to the previous analysis. As expected, the improvement of sensitivity is lower in the compressed region due to its difficult kinematics.
The further continuation of the here presented Run 2 analysis is the combination with the $bb + E_{\mathrm{T}}^{\mathrm{miss}}$ zero-lepton analysis, published in [29]. It will increase the sensitivity further, as already demonstrated in the 36.1 fb^{-1}search.
In a next iteration of the analysis including Run 3 data, I would investigate the potential of a dedicated ML classifier, as used in the $tc + E_{\mathrm{T}}^{\mathrm{miss}}$ analysis [226], to improve the sensitivity in the compressed region further.
If no excess is observed, I would additionally re-interpret the $tb + E_{\mathrm{T}}^{\mathrm{miss}}$ analysis in different theoretical frameworks predicting other new particles, such as leptoquarks [227] or weakly interacting massive particles (WIMPs) [228]. Overall, the expected exclusion contours presented in this work fulfil the analysis goals to improve sensitivity in the compressed region.

The RPV multijet analysis is fully completed and published in [179]. The results improve the sensitivity to pair-produced gluinos decaying via an R-parity-violating coupling into many jets by several hundred GeV compared to the early Run 2 ATLAS analysis.
No excess was found by either analysis strategy I presented in this thesis. In the 10-jet scenario, the low-mass gluino corridor, which had left undiscovered regions for a light RPV gluino with a mass of ~ 1 TeV, was closed up until 1.6 TeV for a light intermediate neutralino of 50 GeV. In the 6-jet scenario, gluino masses up to 1.8 TeV were excluded. The CMS collaboration updated in parallel their results on the 6-jet scenario with an exclusion of RPV gluino masses up to 1.7 TeV [229]. Therefore, the highest limits on RPV gluinos pair-produced at the LHC to-date are defined by our analysis presented in this thesis.
The analysis provides a unique direct comparison between a traditional cut-and-count strategy and a novel machine learning approach for the 6-jet model. Initially, I expected, that the ML approach will outperform the cut-and-count strategy significantly. However, the results I presented here show that both approaches result in a similar exclusion. In the achieved exclusion contours for the UDS (UDB) 6-jet model, the ML analysis achieved a 130 GeV (60 GeV) better expected exclusion than the jet-counting analysis. Deviations from the expectations in form of a underfluctuation improved the observed exclusion for the UDB jet-counting analysis, outperforming the ML analysis.
This result is, in my opinion, very interesting and shows that traditional methods are not always to be replaced by ML algorithms to achieve better sensitivity. A further aspect I would like to mention here is that the results obtained from cut-and-count based analyses are generally easier to be used for re-interpretations and combinations and the entire strategy is simpler to adopt to target different final state models (UDB), or gluino decay modes (from direct 6-jet to cascade 10-jet model). The ML approach requires dedicated architectures, training, and optimisation for each of the different signatures, which makes it less flexible than the jet-counting analysis. Nevertheless, I would like to point out that the mass reconstruction application of a ML algorithm is a novel technique and its potential for combinatorial challenges was demonstrated in our analysis.
In a follow up of this analysis, I would adapt the ML algorithm to the 10-jet model. This requires significant changes in the network architecture and was therefore not done for the analysis presented in this thesis. Reinterpretations can include many possible pair-produced BSM particles, which decay into all-hadronic final states. Because we used very generic selection criteria on the multijet final states, models with 2×4 or 2×2 jets from SUSY decays or other BSM predictions could also be interpreted.

The results of the irradiation campaigns for filters, connectors, cables, and shielding materials, all to be used as part of the ATLAS ITk Pixel read-out chain, led to the approval of the final design review (FDR) of the data transmission of the ATLAS ITk Pixel detector.
The studies I presented here showed overall that the components to be used were still functional after irradiation up to their expected total ionising doses after 10 years of HL-LHC. The irradiation of the Twinax cable required the development of a dedicated setup to reduce the irradiation time of several hundred hours down to a few working days. All irradiations, as well as the pre- and post-irradiation tests, went as planned.
To test the entire ITk Pixel data-transmission chain for radiation tolerance, the immediate continuation is the irradiation of the Optoboards. This was done in 2022 by Samuel Juillerat who summarised his results in his Bachelor thesis [230]. Based on the results Samuel and I observed, all materials and components are qualified in terms of radiation

hardness for the radiation exposure expected during the HL-LHC phase. I would like to mention that, despite showing radiation tolerance, the Z-shield will need to be handled with care during its installation. My tests showed that the glueing component will degrade with increased radiation, especially when it will be open and closed. I recommend additional fixtures to ensure shielding over all 10 years of HL-LHC. With the passing of the ITk Pixel services FDR, the production of the ATLAS ITk data transmission components was launched. The integration of the ITk detector will start in 2024 to meet the deadline for the detector to be installed inside the ATLAS detector in 2028. With the start of the HL-LHC phase, the ATLAS ITk Pixel detector will be a crucial component to separate the dense particle environments and to find new particles.

My data analysis studies showed no hints for new physics beyond the Standard Model, but I placed higher limits on masses of supersymmetric particles. Unfortunately, this aligns with all SUSY searches at the LHC presented by the ATLAS and CMS collaborations so far [231]. Despite the impressive number of searches, combinations, and re-interpretations, no excess has been found in the largest high-energy *pp*-collision data-set we have at hand to-date. In my opinion, this is not a sign to stop searching, but to expand the search programmes, develop new search techniques and incorporate additional detectors.

To follow up RPV searches for example, I see a very promising direction in the investigation of long-lived particles (LLPs) that decay via RPV couplings into SM particles. These could either decay at a displaced vertex within ATLAS or escape detection, depending on their lifetimes. These LLPs travelling in the forward region, where ATLAS' sensitivity is limited, can be detected with new detectors, placed several hundred metres downstream to ATLAS, like the FASER [232, 233] or SND@LHC [234, 235] experiments. These experiments, generally summarised as the Forward Physics Facility at the High-Luminosity LHC [236], offer new, complementary opportunities to expand the search for new physics and just started taking data with Run 3. Despite their complementary geometrical detection range, FASER and SND@LHC are also capable of detecting neutrinos, which adds another important particle detection to the main LHC experiments. First results have already been published, showing the potential for new physics searches [237].
Targeting more model-independent searches, thus focusing on anomalies instead of searching for distinct signatures predicted by defined model assumptions, collecting more data during the HL-LHC phase, and combining measurements from ATLAS with new detectors will allow us to further explore the limits of the Standard Model. The LHC offers the most-likely place on Earth to observe new BSM particles and to contribute to the history of particle discoveries outlined in Figure 1.1. With upgrades such as the ATLAS ITk and new additions as forward detectors, I am confident that the journey of discoveries will continue within the (HL-)LHC era.

Bibliography

[1] J. J. Thomson, *Cathode rays*, Phil. Mag. Ser. 5 **44** (1897) 293.

[2] C. D. Anderson, *The Positive Electron*, Phys. Rev. **43** (1933) 491.

[3] C. D. Anderson and S. H. Neddermeyer, *Cloud Chamber Observations of Cosmic Rays at 4300 Meters Elevation and Near Sea-Level*, Phys. Rev. **50** (1936) 263.

[4] G. Danby et al., *Observation of High-Energy Neutrino Reactions and the Existence of Two Kinds of Neutrinos*, Phys. Rev. Lett. **9** (1962) 36.

[5] J. E. Augustin et al., *Discovery of a Narrow Resonance in e^+e^- Annihilation*, Phys. Rev. Lett. **33** (1974) 1406.

[6] M. L. Perl et al., *Evidence for Anomalous Lepton Production in e+ - e- Annihilation*, Phys. Rev. Lett. **35** (1975) 1489.

[7] G. Arnison et al., *Experimental Observation of Isolated Large Transverse Energy Electrons with Associated Missing Energy at $\sqrt{s} = 540$ GeV*, Phys. Lett. B **122** (1983) 103.

[8] M. Banner et al., *Observation of Single Isolated Electrons of High Transverse Momentum in Events with Missing Transverse Energy at the CERN anti-p p Collider*, Phys. Lett. B **122** (1983) 476.

[9] G. Arnison et al., *Experimental Observation of Lepton Pairs of Invariant Mass Around 95-GeV/c**2 at the CERN SPS Collider*, Phys. Lett. B **126** (1983) 398.

[10] P. Bagnaia et al., *Evidence for $Z^0 \to e^+e^-$ at the CERN $\bar{p}p$ Collider*, Phys. Lett. B **129** (1983) 130.

[11] ATLAS Collaboration, *Observation of a new particle in the search for the Standard Model Higgs boson with the ATLAS detector at the LHC*, Physics Letters B **716** (2012) 1.

[12] CMS Collaboration, *Observation of a new boson at a mass of 125 GeV with the CMS experiment at the LHC*, Physics Letters B **716** (2012) 30.

[13] N. Aghanim et al., *Planck 2018 results. VI. Cosmological parameters*, Astron. Astrophys. **641** (2020) A6, [Erratum: Astron.Astrophys. 652, C4 (2021)], arXiv: 1807.06209 [astro-ph.CO].

[14] Y. Golfand and E. Likhtman, *Extension of the Algebra of Poincare Group Generators and Violation of P Invariance*, JETP Lett. **13** (1971) 323, [Pisma Zh. Eksp. Teor. Fiz. **13** (1971) 452].

[15] D. Volkov and V. Akulov, *Is the neutrino a goldstone particle?*, Phys. Lett. B **46** (1973) 109.

[16] J. Wess and B. Zumino, *Supergauge transformations in four dimensions*, Nucl. Phys. B **70** (1974) 39.

[17] J. Wess and B. Zumino, *Supergauge invariant extension of quantum electrodynamics*, Nucl. Phys. B **78** (1974) 1.

[18] S. Ferrara and B. Zumino, *Supergauge invariant Yang-Mills theories*, Nucl. Phys. B **79** (1974) 413.
[19] A. Salam and J. Strathdee, *Super-symmetry and non-Abelian gauges*, Phys. Lett. B **51** (1974) 353.
[20] R. Barbieri and G. Giudice, *Upper bounds on supersymmetric particle masses*, Nucl. Phys. B **306** (1988) 63.
[21] B. de Carlos and J. Casas, *One-loop analysis of the electroweak breaking in supersymmetric models and the fine-tuning problem*, Phys. Lett. B **309** (1993) 320, arXiv: hep-ph/9303291.
[22] S. P. Martin, *A Supersymmetry Primer*, Adv. Ser. Direct. High Energy Phys. **18** (1998) 1, arXiv: hep-ph/9709356.
[23] R. L. Workman and Others, *Review of Particle Physics*, PTEP **2022** (2022) 083C01.
[24] O. S. Bruening et al., *LHC Design Report. Volume 1: The LHC Main Ring.* CERN Yellow Reports: Monographs, CERN, 2004, URL: https://cds.cern.ch/record/782076.
[25] ATLAS Collaboration, *The ATLAS Experiment at the CERN Large Hadron Collider*, Journal of Instrumentation **3** (2008) S08003.
[26] ATLAS Collaboration, *Search for new phenomena with top quark pairs in final states with one lepton, jets, and missing transverse momentum in pp collisions at* $\sqrt{s} = 13$ *TeV with the ATLAS detector*, ATLAS-CONF-2020-003, 2020, URL: https://cds.cern.ch/record/2711489.
[27] ATLAS Collaboration, *Search for new phenomena in events with two opposite-charge leptons, jets and missing transverse momentum in pp collisions at* $\sqrt{s} = 13$ *TeV with the ATLAS detector*, ATLAS-CONF-2020-046, 2020, URL: https://cds.cern.ch/record/2728056.
[28] ATLAS Collaboration, *Search for a scalar partner of the top quark in the jets plus missing transverse momentum final state at* $\sqrt{s} = 13$ *TeV with the ATLAS detector*, JHEP **12** (2017) 085, arXiv: 1709.04183 [hep-ex].
[29] ATLAS Collaboration, *Search for new phenomena in final states with b-jets and missing transverse momentum in* $\sqrt{s} = 13$ *TeV pp collisions with the ATLAS detector*, JHEP **05** (2021) 093, arXiv: 2101.12527 [hep-ex].
[30] CMS Collaboration, *Search for direct top squark pair production in events with one lepton, jets, and missing transverse momentum at 13 TeV with the CMS experiment*, JHEP **05** (2020) 032, arXiv: 1912.08887 [hep-ex].
[31] CMS Collaboration, *Search for top squark pair production using dilepton final states in pp collision data collected at* $\sqrt{s} = 13$ *TeV*, Eur. Phys. J. C **81** (2021) 3, arXiv: 2008.05936 [hep-ex].
[32] CMS Collaboration, *Combined searches for the production of supersymmetric top quark partners in proton–proton collisions at* $\sqrt{s} = 13$ *TeV*, Eur. Phys. J. C **81** (2021) 970, arXiv: 2107.10892 [hep-ex].
[33] CMS Collaboration, *Search for top squark production in fully-hadronic final states in proton-proton collisions at* $\sqrt{s} = 13$ *TeV*, Phys. Rev. D **104** (2021) 052001, arXiv: 2103.01290 [hep-ex].

[34] ATLAS Collaboration,
Search for supersymmetry in events with b-tagged jets and missing transverse momentum in pp collisions at $\sqrt{s} = 13$ TeV with the ATLAS detector,
JHEP **11** (2017) 195, arXiv: 1708.09266 [hep-ex].
[35] ATLAS Collaboration,
Search for pair production of massive particles decaying into three quarks with the ATLAS detector in $\sqrt{s} = 7$ TeV pp collisions at the LHC, JHEP **12** (2012) 086,
arXiv: 1210.4813 [hep-ex].
[36] ATLAS Collaboration, *Search for massive supersymmetric particles decaying to many jets using the ATLAS detector in pp collisions at $\sqrt{s} = 8$ TeV*,
Phys. Rev. D **91** (2015) 112016, arXiv: 1502.05686 [hep-ex].
[37] ATLAS Collaboration,
Search for R-parity-violating supersymmetric particles in multi-jet final states produced in pp collisions at $\sqrt{s} = 13$ TeV using the ATLAS detector at the LHC,
Phys. Lett. B **785** (2018) 136, arXiv: 1804.03568 [hep-ex].
[38] CMS Collaboration,
Search for new phenomena in events with high jet multiplicity and low missing transverse momentum in proton–proton collisions at $\sqrt{s} = 8$ TeV,
Phys. Lett. B **770** (2017) 257, arXiv: 1608.01224 [hep-ex].
[39] CMS Collaboration, *Searches for light- and heavy-flavour three-jet resonances in pp collisions at $\sqrt{s} = 8$ TeV*, Phys. Lett. B **730** (2014) 193,
arXiv: 1311.1799 [hep-ex].
[40] CMS Collaboration, *Search for pair-produced three-jet resonances in proton–proton collisions at $\sqrt{s} = 13$ TeV*, Phys. Rev. D **99** (2019) 012010,
arXiv: 1810.10092 [hep-ex].
[41] ATLAS Collaboration, *SUSY March 2023 Summary Plot Update*, tech. rep.,
CERN, 2023, URL: https://cds.cern.ch/record/2852738.
[42] M. Thomson, *Modern Particle Physics*, Cambridge University Press, 2013.
[43] P. A. M. Dirac, *On the theory of quantum mechanics*,
Proceedings of the Royal Society of London. Series A, Containing Papers of a Mathematical and Physical Character **112** (1926) 661.
[44] E. Fermi, *Zur Quantelung des idealen einatomigen Gases*,
Zeitschrift für Physik **36** (1926) 902.
[45] A. Purcell, *Go on a particle quest at the first CERN webfest*, URL: https://cds.cern.ch/journal/CERNBulletin/2012/35/News\%20Articles/1473657.
[46] Y. Fukuda, T. Hayakawa, E. Ichihara, K. Inoue, and K. Ishihara,
Evidence for Oscillation of Atmospheric Neutrinos,
Physical Review Letters **81** (1998) 1562.
[47] Q. R. Ahmad et al.,
Measurement of the Rate of nu_e + d –> p + p + e^- interactions produced by 8B Solar Neutrinos at the Sudbury Neutrino Observatory,
Physical Review Letters **87** (2001).
[48] M. Gell-Mann, *A schematic model of baryons and mesons*,
Physics Letters **8** (1964) 214.
[49] S. N. Bose, *Plancks Gesetz und Lichtquantenhypothese*,
Zeitschrift für Physik **26** (1924) 178.
[50] A. Einstein, *Quantum theory of the monatomic ideal gas*,
Sitzungsberichte der Preussischen Akademie der Wissenschaften,

Physikalisch-mathematische Klasse (1924) 261, URL: http://www.fisica.uns.edu.ar/albert/archivos/46/156/495246252_apuntes.pdf.

[51] E. Noether, *Invariant variation problems*, Transport Theory and Statistical Physics **1** (1971) 186.

[52] S. L. Glashow, *The renormalizability of vector meson interactions*, Nuclear Physics **10** (1959) 107.

[53] A. Salam and J. Ward, *Electromagnetic and weak interactions*, Physics Letters **13** (1964) 168.

[54] S. Weinberg, *A Model of Leptons*, Physical Review Letters **19** (1967) 1264.

[55] P. W. Higgs, *Broken Symmetries and the Masses of Gauge Bosons*, Physical Review Letters **13** (1964) 508.

[56] P. W. Higgs, *Broken symmetries, massless particles and gauge fields*, Physics Letters **12** (1964) 132.

[57] F. Englert and R. Brout, *Broken Symmetry and the Mass of Gauge Vector Mesons*, Physical Review Letters **13** (1964) 321.

[58] ATLAS Collaboration, *Combined measurement of the Higgs boson mass from the $H \to \gamma\gamma$ and $H \to ZZ^* \to 4\ell$ decay channels with the ATLAS detector using $\sqrt{s}$ = 7, 8 and 13 TeV pp collision data*, (2023), arXiv: 2308.04775 [hep-ex].

[59] ATLAS Collaboration, *Standard Model Summary Plots February 2022*, tech. rep., CERN, 2022, URL: https://cds.cern.ch/record/2804061.

[60] P. A. R. Ade et al., *Planck 2015 results. XIII. Cosmological parameters*, Astronomy & Astrophysics **594** (2016) A13.

[61] M. Dine and A. Kusenko, *Origin of the matter-antimatter asymmetry*, Reviews of Modern Physics **76** (2003) 1.

[62] S. P. Martin, "A Supersymmetry Primer", *Advanced Series on Directions in High Energy Physics*, World Scientific, 2010 1.

[63] H. Dreiner, *An introduction to explicit R-parity violation*, Pramana **51** (1998) 123.

[64] S. Ask, *A Review of the Supersymmetry Searches at LEP*, tech. rep., CERN, 2003, URL: https://cds.cern.ch/record/615357.

[65] P. Gris, *SUSY Searches at the Tevatron*, 2011, arXiv: 1106.1032 [hep-ex].

[66] The LHCb Collaboration, *The LHCb Detector at the LHC*, Journal of Instrumentation **3** (2008) S08005.

[67] T. Abe et al., *Belle II Technical Design Report*, 2010, arXiv: 1011.0352 [physics.ins-det].

[68] A. J. Bevan et al., *The Physics of the B Factories*, The European Physical Journal C **74** (2014).

[69] C. Borschensky et al., *Squark and gluino production cross sections in pp collisions at $\sqrt{s} = 13, 14, 33$ and 100 TeV*, Eur. Phys. J. C **74** (2014) 3174, arXiv: 1407.5066 [hep-ph].

[70] L. Evans and P. Bryant, *LHC Machine*, JINST **3** (2008) S08001.

[71] M. Brice, *Aerial View of the CERN taken in 2008.*, 2008, URL: https://cds.cern.ch/record/1295244.

[72] G. Bachy, A Hofmann, S Myers, E. Picasso, and G. Plass, *The LEP collider: construction, project status and outlook*, Part. Accel. **26** (1990) 19, URL: https://cds.cern.ch/record/202961.

[73] S. Bethke, *Precision Physics at LEP*, (2017), arXiv: 1712.03035 [hep-ex].

[74] CMS Collaboration, *The CMS experiment at the CERN LHC*, JINST **3** (2008) S08004.
[75] The ALICE Collaboration, *The ALICE experiment at the CERN LHC. A Large Ion Collider Experiment*, JINST **3** (2008) S08002.
[76] The CERN Courier, *LHC first beam: a day to remember*, URL: https://cerncourier.com/a/lhc-first-beam-a-day-to-remember/.
[77] M. Benedikt, P. Collier, V Mertens, J. Poole, and K. Schindl, *LHC Design Report. Volume 3: The LHC Injector Chain.* CERN Yellow Reports: Monographs, CERN, 2004, URL: https://cds.cern.ch/record/823808.
[78] E. Lopienska, *The CERN accelerator complex, layout in 2022. Complexe des accélérateurs du CERN en janvier 2022*, last accessed 29.04.2023, 2022, URL: https://cds.cern.ch/record/2800984.
[79] J. Vollaire et al., *Linac4 design report*, ed. by M. Vretenar, vol. 6/2020, CERN Yellow Reports: Monographs, CERN, 2020, ISBN: 978-92-9083-579-0, 978-92-9083-580-6.
[80] CERN, *Facts and figures about the LHC*, last accessed 29.04.2023, URL: https://home.cern/resources/faqs/facts-and-figures-about-lhc.
[81] ATLAS Collaboration, *Luminosity determination in pp collisions at* $\sqrt{s} = 13$ *TeV using the ATLAS detector at the LHC*, ATLAS-CONF-2019-021, 2019, URL: https://cds.cern.ch/record/2677054.
[82] The ATLAS Collaboration, *Public ATLAS Luminosity Results for Run-2 of the LHC*, URL: https://twiki.cern.ch/twiki/bin/view/AtlasPublic/LuminosityPublicResultsRun2#Pileup_Interactions_and_Data_Tak..
[83] K. Anthony, *Preparing ATLAS for the future*, [Accessed 29-Jan-2023], URL: https://atlas.cern/updates/news/preparing-ATLAS-for-future.
[84] ATLAS Collaboration, *ATLAS Inner Detector: Technical Design Report, Volume 1*, ATLAS-TDR-4; CERN-LHCC-97-016, 1997, URL: https://cds.cern.ch/record/331063.
[85] ATLAS Collaboration, *ATLAS Inner Detector: Technical Design Report, Volume 2*, ATLAS-TDR-5, CERN-LHCC-97-017, 1997, URL: https://cds.cern.ch/record/331064.
[86] ATLAS Collaboration, *ATLAS Insertable B-Layer: Technical Design Report*, ATLAS-TDR-19; CERN-LHCC-2010-013, 2010, URL: https://cds.cern.ch/record/1291633.
[87] ATLAS Collaboration, *Track Reconstruction Performance of the ATLAS Inner Detector at* $\sqrt{s} = 13$ *TeV*, ATL-PHYS-PUB-2015-018, 2015, URL: https://cds.cern.ch/record/2037683.
[88] ATLAS Collaboration, *Particle Identification Performance of the ATLAS Transition Radiation Tracker*, tech. rep. ATLAS-CONF-2011-128, 2011, URL: https://cds.cern.ch/record/1383793.
[89] ATLAS Collaboration, *ATLAS Liquid Argon Calorimeter: Technical Design Report*,

ATLAS-TDR-2; CERN-LHCC-96-041, 1996,
URL: https://cds.cern.ch/record/331061.
[90] ATLAS Collaboration, *ATLAS Tile Calorimeter: Technical Design Report*,
ATLAS-TDR-3; CERN-LHCC-96-042, 1996,
URL: https://cds.cern.ch/record/331062.
[91] G. Barr, R. Devenish, R. Walczak, and T. Weidberg,
Particle Physics in the LHC Era, Oxford University Press, 2016,
ISBN: 9780198748557.
[92] ATLAS Collaboration,
ATLAS Calorimeter Performance: Technical Design Report,
ATLAS-TDR-1; CERN-LHCC-96-040, 1996,
URL: https://cds.cern.ch/record/331059.
[93] ATLAS Collaboration, *ATLAS Muon Spectrometer: Technical Design Report*,
ATLAS-TDR-10; CERN-LHCC-97-022, CERN, 1997,
URL: https://cds.cern.ch/record/331068.
[94] T. Kawamoto et al., *New Small Wheel Technical Design Report*, tech. rep.,
ATLAS New Small Wheel Technical Design Report, 2013,
URL: https://cds.cern.ch/record/1552862.
[95] ATLAS Collaboration,
ATLAS Magnet System: Magnet Project Technical Design Report, Volume 1,
ATLAS-TDR-6; CERN-LHCC-97-018, 1997,
URL: https://cds.cern.ch/record/338080.
[96] A. M. Rodriguez Vera and J. Antunes Pequenao,
ATLAS Detector Magnet System, General Photo, 2021,
URL: https://cds.cern.ch/record/2770604.
[97] A. R. Martínez, *The Run-2 ATLAS Trigger System*,
J. Phys. Conf. Ser. **762** (2016) 012003, ed. by L. Salinas and C. Torres.
[98] *ATLAS level-1 trigger: Technical Design Report*, (1998).
[99] *ATLAS high-level trigger, data acquisition and controls: Technical design report*,
(2003).
[100] M. Abolins et al., *The ATLAS Data Acquisition and High Level Trigger system*,
JINST **11** (2016) P06008.
[101] G. Aad et al., *Operation of the ATLAS trigger system in Run 2*,
JINST **15** (2020) P10004, arXiv: 2007.12539 [physics.ins-det].
[102] J. Pequenao and P. Schaffner,
How ATLAS detects particles: diagram of particle paths in the detector, 2013,
URL: https://cds.cern.ch/record/1505342.
[103] ATLAS Collaboration,
Early Inner Detector Tracking Performance in the 2015 Data at $\sqrt{s} = 13$ *TeV*,
ATL-PHYS-PUB-2015-051, 2015, URL: https://cds.cern.ch/record/2110140.
[104] ATLAS Collaboration, *Performance of the ATLAS track reconstruction
algorithms in dense environments in LHC Run 2*, Eur. Phys. J. C **77** (2017) 673,
arXiv: 1704.07983 [hep-ex].
[105] ATLAS Collaboration, *Performance of the reconstruction of large impact
parameter tracks in the inner detector of ATLAS*, ATL-PHYS-PUB-2017-014,
2017, URL: https://cds.cern.ch/record/2275635.
[106] ATLAS Collaboration, *Performance of the ATLAS Silicon Pattern Recognition
Algorithm in Data and Simulation at* $\sqrt{s} = 7$ *TeV*, ATLAS-CONF-2010-072,
2010, URL: https://cds.cern.ch/record/1281363.

[107] ATLAS Collaboration, *Performance of primary vertex reconstruction in proton–proton collisions at $\sqrt{s} = 7$ TeV in the ATLAS experiment*, ATLAS-CONF-2010-069, 2010, URL: https://cds.cern.ch/record/1281344.

[108] ATLAS Collaboration, *Vertex Reconstruction Performance of the ATLAS Detector at $\sqrt{s} = 13$ TeV*, ATLAS-PHYS-PUB-2015-026, 2015, URL: https://cds.cern.ch/record/2037717.

[109] ATLAS Collaboration, *Performance of the ATLAS Inner Detector Track and Vertex Reconstruction in High Pile-Up LHC Environment*, ATLAS-CONF-2012-042, 2012, URL: https://cds.cern.ch/record/1435196.

[110] ATLAS Collaboration, *Jet reconstruction and performance using particle flow with the ATLAS Detector*, Eur. Phys. J. C **77** (2017) 466, arXiv: 1703.10485 [hep-ex].

[111] ATLAS Collaboration, *Jet energy scale measurements and their systematic uncertainties in proton–proton collisions at $\sqrt{s} = 13$ TeV with the ATLAS detector*, Phys. Rev. D **96** (2017) 072002, arXiv: 1703.09665 [hep-ex].

[112] M. Cacciari, G. P. Salam, and G. Soyez, *The anti-k_t jet clustering algorithm*, Journal of High Energy Physics **2008** (2008) 063.

[113] ATLAS Collaboration, *Tagging and suppression of pileup jets*, ATL-PHYS-PUB-2014-001, 2014, URL: https://cds.cern.ch/record/1643929.

[114] ATLAS Collaboration, *Performance of b-jet identification in the ATLAS experiment*, JINST **11** (2016) P04008, arXiv: 1512.01094 [hep-ex].

[115] ATLAS Collaboration, *Performance of the ATLAS Secondary Vertex b-tagging Algorithm in 900 GeV Collision Data*, ATLAS-CONF-2010-004, 2010, URL: https://cds.cern.ch/record/1273194.

[116] ATLAS Collaboration, *Calibration of light-flavour b-jet mistagging rates using ATLAS proton–proton collision data at $\sqrt{s} = 13$ TeV*, ATLAS-CONF-2018-006, 2018, URL: https://cds.cern.ch/record/2314418.

[117] ATLAS Collaboration, *Electron and photon performance measurements with the ATLAS detector using the 2015–2017 LHC proton–proton collision data*, JINST **14** (2019) P12006, arXiv: 1908.00005 [hep-ex].

[118] ATLAS Collaboration, *Electron reconstruction and identification in the ATLAS experiment using the 2015 and 2016 LHC proton–proton collision data at $\sqrt{s} = 13$ TeV*, Eur. Phys. J. C **79** (2019) 639, arXiv: 1902.04655 [hep-ex].

[119] ATLAS Collaboration, *Muon reconstruction performance of the ATLAS detector in proton–proton collision data at $\sqrt{s} = 13$ TeV*, The European Physical Journal C **76** (2016).

[120] ATLAS Collaboration, *Muon reconstruction and identification efficiency in ATLAS using the full Run 2 pp collision data set at $\sqrt{s} = 13$ TeV*, Eur. Phys. J. C **81** (2021) 578, arXiv: 2012.00578 [hep-ex].

[121] ATLAS Collaboration, *SUSY Object Definitions (Rel 21)*, URL: https://twiki.cern.ch/twiki/bin/viewauth/AtlasProtected/SusyObjectDefinitionsr2113TeV#Electrons.

[122] ATLAS Collaboration, *Performance of missing transverse momentum reconstruction with the ATLAS detector in the first proton–proton collisions at $\sqrt{s} = 13$ TeV*, ATL-PHYS-PUB-2015-027, 2015, URL: https://cds.cern.ch/record/2037904.

[123] ATLAS Collaboration,
Performance of missing transverse momentum reconstruction with the ATLAS detector using proton–proton collisions at $\sqrt{s} = 13$ TeV,
Eur. Phys. J. C **78** (2018) 903, arXiv: 1802.08168 [hep-ex].
[124] ATLAS Collaboration, *Luminosity determination in pp collisions at $\sqrt{s} = 13$ TeV using the ATLAS detector at the LHC*, (2022),
arXiv: 2212.09379 [hep-ex].
[125] G. Avoni et al., *The new LUCID-2 detector for luminosity measurement and monitoring in ATLAS*, JINST **13** (2018) P07017.
[126] ATLAS Collaboration, *Public Luminosity measurements of the ATLAS detector*, last accessed 28.03.2021, URL: https://twiki.cern.ch/twiki/bin/view/AtlasPublic/LuminosityPublicResultsRun2.
[127] L. Harland-Lang, A. Martin, P. Motylinski, and R. Thorne,
Parton distributions in the LHC era: MMHT 2014 PDFs,
Eur. Phys. J. C **75** (2015) 204, arXiv: 1412.3989 [hep-ph].
[128] Y. L. Dokshitzer,
Calculation of the Structure Functions for Deep Inelastic Scattering and e+ e- Annihilation by Perturbation Theory in Quantum Chromodynamics.,
Sov. Phys. JETP **46** (1977) 641.
[129] V. N. Gribov and L. N. Lipatov,
Deep inelastic e p scattering in perturbation theory,
Sov. J. Nucl. Phys. **15** (1972) 438.
[130] G. Altarelli and G. Parisi, *Asymptotic Freedom in Parton Language*,
Nucl. Phys. B **126** (1977) 298.
[131] A. Hoecker,
Physics at the LHC Run-2 and Beyond. Physics at the LHC Run-2 and Beyond, (2017) 153, Lecture notes from the 2016 European School of High-Energy Physics, 15-28 June 2016, Skeikampen, Norway (61 pages, 56 figures), arXiv: 1611.07864.
[132] T. Gleisberg et al., *Event generation with SHERPA 1.1*, JHEP **02** (2009) 007,
arXiv: 0811.4622 [hep-ph].
[133] S. Frixione, P. Nason, and C. Oleari, *Matching NLO QCD computations with parton shower simulations: the POWHEG method*, JHEP **11** (2007) 070,
arXiv: 0709.2092 [hep-ph].
[134] S. Alioli, P. Nason, C. Oleari, and E. Re, *A general framework for implementing NLO calculations in shower Monte Carlo programs: the POWHEG BOX*,
JHEP **06** (2010) 043, arXiv: 1002.2581 [hep-ph].
[135] T. Sjöstrand et al., *An introduction to PYTHIA 8.2*,
Comput. Phys. Commun. **191** (2015) 159, arXiv: 1410.3012 [hep-ph].
[136] S. Agostinelli et al., GEANT4 – *a simulation toolkit*,
Nucl. Instrum. Meth. A **506** (2003) 250.
[137] J. Alwall, M. Herquet, F. Maltoni, O. Mattelaer, and T. Stelzer,
MadGraph 5 : Going Beyond, JHEP **06** (2011) 128, arXiv: 1106.0522 [hep-ph].
[138] S. Mrenna and P. Skands, *Automated parton-shower variations in PYTHIA 8*,
Phys. Rev. D **94** (2016) 074005, arXiv: 1605.08352 [hep-ph].
[139] R. D. Ball et al., *Parton distributions with LHC data*,
Nucl. Phys. B **867** (2013) 244, arXiv: 1207.1303 [hep-ph].
[140] ATLAS Collaboration, *ATLAS Pythia 8 tunes to 7 TeV data*, tech. rep.,
CERN, 2014, URL: https://cds.cern.ch/record/1966419.

[141] M. Beneke, P. Falgari, S. Klein, and C. Schwinn,
Hadronic top-quark pair production with NNLL threshold resummation,
Nucl. Phys. B **855** (2012) 695, arXiv: 1109.1536 [hep-ph].

[142] M. Cacciari, M. Czakon, M. Mangano, A. Mitov, and P. Nason,
Top-pair production at hadron colliders with next-to-next-to-leading logarithmic soft-gluon resummation, Phys. Lett. B **710** (2012) 612,
arXiv: 1111.5869 [hep-ph].

[143] P. Bärnreuther, M. Czakon, and A. Mitov, *Percent-Level-Precision Physics at the Tevatron: Next-to-Next-to-Leading Order QCD Corrections to* $q\bar{q} \to t\bar{t} + X$,
Phys. Rev. Lett. **109** (2012) 132001, arXiv: 1204.5201 [hep-ph].

[144] M. Czakon and A. Mitov, *NNLO corrections to top-pair production at hadron colliders: the all-fermionic scattering channels*, JHEP **12** (2012) 054,
arXiv: 1207.0236 [hep-ph].

[145] M. Czakon and A. Mitov, *NNLO corrections to top pair production at hadron colliders: the quark-gluon reaction*, JHEP **01** (2013) 080,
arXiv: 1210.6832 [hep-ph].

[146] M. Czakon, P. Fiedler, and A. Mitov, *Total Top-Quark Pair-Production Cross Section at Hadron Colliders Through* $O(\alpha_S^4)$, Phys. Rev. Lett. **110** (2013) 252004,
arXiv: 1303.6254 [hep-ph].

[147] M. Czakon and A. Mitov, *Top++: A program for the calculation of the top-pair cross-section at hadron colliders*, Comput. Phys. Commun. **185** (2014) 2930,
arXiv: 1112.5675 [hep-ph].

[148] S. Frixione, P. Nason, and G. Ridolfi, *A positive-weight next-to-leading-order Monte Carlo for heavy flavour hadroproduction*, JHEP **09** (2007) 126,
arXiv: 0707.3088 [hep-ph].

[149] P. Nason,
A new method for combining NLO QCD with shower Monte Carlo algorithms,
JHEP **11** (2004) 040, arXiv: hep-ph/0409146.

[150] R. D. Ball et al., *Parton distributions for the LHC run II*, JHEP **04** (2015) 040,
arXiv: 1410.8849 [hep-ph].

[151] N. Kidonakis, *Two-loop soft anomalous dimensions for single top quark associated production with a* W^- *or* H^-, Phys. Rev. D **82** (2010) 054018,
arXiv: 1005.4451 [hep-ph].

[152] N. Kidonakis, *Top Quark Production*, 2014, arXiv: 1311.0283 [hep-ph].

[153] J. Alwall et al., *The automated computation of tree-level and next-to-leading order differential cross sections, and their matching to parton shower simulations*,
Journal of High Energy Physics **2014** (2014).

[154] E. Bothmann et al., *Event generation with Sherpa 2.2*,
SciPost Phys. **7** (2019) 034, arXiv: 1905.09127 [hep-ph].

[155] S. Schumann and F. Krauss,
A parton shower algorithm based on Catani–Seymour dipole factorisation,
JHEP **03** (2008) 038, arXiv: 0709.1027 [hep-ph].

[156] S. Catani, L. Cieri, G. Ferrera, D. de Florian, and M. Grazzini,
Vector Boson Production at Hadron Colliders: A Fully Exclusive QCD Calculation at Next-to-Next-to-Leading Order,
Physical Review Letters **103** (2009).

[157] C. Anastasiou, L. J. Dixon, K. Melnikov, and F. Petriello,
High precision QCD at hadron colliders: Electroweak gauge boson rapidity

distributions at next-to-next-to leading order, Phys. Rev. D **69** (2004) 094008, arXiv: hep-ph/0312266.

[158] R. D. Cousins, J. T. Linnemann, and J. Tucker, *Evaluation of three methods for calculating statistical significance when incorporating a systematic uncertainty into a test of the background-only hypothesis for a Poisson process*, Nucl. Instrum. Meth. A **595** (2008) 480, arXiv: physics/0702156 [physics.data-an].

[159] M. Baak et al., *HistFitter software framework for statistical data analysis*, Eur. Phys. J. C **75** (2015) 153, arXiv: 1410.1280 [hep-ex].

[160] G. Cowan, K. Cranmer, E. Gross, and O. Vitells, *Asymptotic formulae for likelihood-based tests of new physics*, Eur. Phys. J. C **71** (2011) 1554, arXiv: 1007.1727 [physics.data-an].

[161] K. Cranmer, *Practical Statistics for the LHC*, *2011 European School of High-Energy Physics*, 2014 267, arXiv: 1503.07622 [physics.data-an].

[162] ATLAS Collaboration, *Jet energy resolution in proton–proton collisions at $\sqrt{s} = 7$ TeV recorded in 2010 with the ATLAS detector*, Eur. Phys. J. C **73** (2013) 2306, arXiv: 1210.6210 [hep-ex].

[163] ATLAS Collaboration, *ATLAS b-jet identification performance and efficiency measurement with $t\bar{t}$ events in pp collisions at $\sqrt{s} = 13$ TeV*, Eur. Phys. J. C **79** (2019) 970, arXiv: 1907.05120 [hep-ex].

[164] ATLAS Collaboration, *ATLAS Run 1 searches for direct pair production of third-generation squarks at the Large Hadron Collider*, Eur. Phys. J. C **75** (2015) 510, arXiv: 1506.08616 [hep-ex].

[165] A. Giammanco, *Single top quark production at the LHC*, Reviews in Physics **1** (2016) 1, ISSN: 2405-4283.

[166] ATLAS Collaboration, *Performance of the ATLAS trigger system in 2015*, Eur. Phys. J. C **77** (2017) 317, arXiv: 1611.09661 [hep-ex].

[167] ATLAS Collaboration, *Performance of the missing transverse momentum triggers for the ATLAS detector during Run-2 data taking*, Journal of High Energy Physics **2020** (2020).

[168] ATLAS Collaboration, *Performance of electron and photon triggers in ATLAS during LHC Run 2*, Eur. Phys. J. C **80** (2020) 47, arXiv: 1909.00761 [hep-ex].

[169] ATLAS Collaboration, *Performance of the ATLAS muon triggers in Run 2*, JINST **15** (2020) P09015, arXiv: 2004.13447 [hep-ex].

[170] ATLAS Collaboration, *Object-based missing transverse momentum significance in the ATLAS Detector*, ATLAS-CONF-2018-038, 2018, URL: https://cds.cern.ch/record/2630948.

[171] G. Arnison et al., *Further Evidence for Charged Intermediate Vector Bosons at the SPS Collider*, Phys. Lett. B **129** (1983) 273.

[172] C. G. Lester and D. J. Summers, *Measuring masses of semiinvisibly decaying particles pair produced at hadron colliders*, Phys. Lett. B **463** (1999) 99, arXiv: hep-ph/9906349.

[173] A. Barr, C. Lester, and P. Stephens, *m(T2): The Truth behind the glamour*, J. Phys. G **29** (2003) 2343, arXiv: hep-ph/0304226.

[174] I. Neutelings, *Third-generation leptoquark searches in CMS*, Phenomenology Symposium 2021. Pittsburgh., URL: https://indico.cern.ch/event/982783/contributions/4363894/.

[175] P. Konar, K. Kong, K. T. Matchev, and M. Park, *Dark matter particle spectroscopy at the LHC: generalizing M T2 to asymmetric event topologies*, Journal of High Energy Physics **2010** (2010).

[176] F. Cascioli, S. Kallweit, P. Maierhöfer, and S. Pozzorini, *A unified NLO description of top-pair and associated Wt production*, The European Physical Journal C **74** (2014).

[177] J. K. Anders, *Searches for direct pair production of third generation squarks, and dark matter, in final states containing b−jets and $E_{\mathrm{T}}^{\mathrm{miss}}$ using the ATLAS detector at the LHC*, Presented 07 Jun 2017, 2017, URL: https://cds.cern.ch/record/2291836.

[178] ATLAS Collaboration, *Search for new phenomena in events with two opposite-charge leptons, jets and missing transverse momentum in pp collisions at $\sqrt{s}$13 TeV with the ATLAS detector*, Journal of High Energy Physics **2021** (2021).

[179] ATLAS Collaboration, *A search for R-parity-violating supersymmetry in final states containing many jets in $\sqrt{s} = 13$ TeV pp collisions with the ATLAS detector*, tech. rep., CERN, 2023, URL: https://cds.cern.ch/record/2867658.

[180] CMS Collaboration, *Search for Pair-Produced Resonances Each Decaying into at Least Four Quarks in Proton–Proton collisions at $\sqrt{s} = 13$ TeV*, Phys. Rev. Lett. **121** (2018) 141802, arXiv: 1806.01058 [hep-ex].

[181] M. R. Kauth, J. H. Kühn, P. Marquard, and M. Steinhauser, *Gluino pair production at the LHC: The threshold*, Nuclear Physics B **857** (2012) 28.

[182] G. Aad et al., *Measurement of hadronic event shapes in high-p_T multijet final states at $\sqrt{s}$ = 13 TeV with the ATLAS detector*, JHEP **01** (2021) 188, [Erratum: JHEP 12, 053 (2021)], arXiv: 2007.12600 [hep-ex].

[183] G. Parisi, *Super Inclusive Cross-Sections*, Phys. Lett. B **74** (1978) 65.

[184] J. F. Donoghue, F. E. Low, and S.-Y. Pi, *Tensor Analysis of Hadronic Jets in Quantum Chromodynamics*, Phys. Rev. D **20** (1979) 2759.

[185] A. Badea et al., *Solving combinatorial problems at particle colliders using machine learning*, Phys. Rev. D **106** (2022) 016001, arXiv: 2201.02205 [hep-ph].

[186] A. Badea, *Search for massive particles producing all hadronic final states in proton-proton collisions at the LHC with the ATLAS detector*, Presented 07 Jul 2023, Harvard University, 2023, URL: http://cds.cern.ch/record/2872562.

[187] ATLAS Collaboration, *Search for New Particles in Two-Jet Final States in 7 TeV Proton–Proton Collisions with the ATLAS Detector at the LHC*, Phys. Rev. Lett. **105** (2010) 161801, arXiv: 1008.2461 [hep-ex].

[188] ATLAS Collaboration, *Search for new phenomena in the dijet mass distribution using pp collision data at $\sqrt{s} = 8$ TeV with the ATLAS detector*, Phys. Rev. D **91** (2015) 052007, arXiv: 1407.1376 [hep-ex].

[189] ATLAS Collaboration, *Search for new phenomena in dijet mass and angular distributions from pp collisions at $\sqrt{s} = 13$ TeV with the ATLAS detector*, Phys. Lett. B **754** (2016) 302, arXiv: 1512.01530 [hep-ex].

[190] ATLAS Collaboration, *Search for new resonances in mass distributions of jet pairs using 139 fb^{-1} of pp collisions at $\sqrt{s} = 13$ TeV with the ATLAS detector*, JHEP **03** (2020) 145, arXiv: 1910.08447 [hep-ex].

[191] ATLAS Collaboration, *Search for new resonances in mass distributions of jet pairs using 139 fb^{-1} of pp collisions at $\sqrt{s} = 13$ TeV with the ATLAS detector*, JHEP **03** (2020) 145, arXiv: 1910.08447 [hep-ex].

[192] CMS Collaboration, *Search for Resonances in the Dijet Mass Spectrum from 7 TeV pp Collisions at CMS*, Phys. Lett. B **704** (2011) 123, arXiv: 1107.4771 [hep-ex].

[193] CMS Collaboration, *Search for dijet resonances in proton–proton collisions at $\sqrt{s} = 13$ TeV and constraints on dark matter and other models*, Phys. Lett. B **769** (2017) 520, arXiv: 1611.03568 [hep-ex].

[194] CMS Collaboration, *Search for resonant and nonresonant production of pairs of dijet resonances in proton-proton collisions at $\sqrt{s} = 13$ TeV*, JHEP **07** (2023) 161, arXiv: 2206.09997 [hep-ex].

[195] *High-Luminosity Large Hadron Collider (HL-LHC) : Preliminary Design Report*, (2015), ed. by G Apollinari, I Béjar Alonso, O Brüning, M Lamont, and L Rossi.

[196] I. Zurbano Fernandez et al., *High-Luminosity Large Hadron Collider (HL-LHC): Technical design report*, **10/2020** (2020), ed. by I. Béjar Alonso et al.

[197] P. Vankov, *ATLAS Upgrade for the HL-LHC: meeting the challenges of a five-fold increase in collision rate*, tech. rep., Presented at the 2011 Hadron Collider Physics symposium (HCP-2011), Paris, France, November 14-18 2011, 3 pages, 3 figures: CERN, 2012, arXiv: 1201.5469.

[198] F. Sánchez Muñoz, *ATLAS ITk Pixel Detector Overview*, J. Phys. Conf. Ser. **2374** (2022) 012061.

[199] ATLAS Collaboration, *ATLAS Inner Tracker Pixel Detector: Technical Design Report*, ATLAS-TDR-030; CERN-LHCC-2017-021, 2017, URL: https://cds.cern.ch/record/2285585.

[200] ATLAS Collaboration, *ATLAS Inner Tracker Strip Detector: Technical Design Report*, ATLAS-TDR-025; CERN-LHCC-2017-005, 2017, URL: https://cds.cern.ch/record/2257755.

[201] ATLAS Collaboration, *Letter of Intent for the Phase-II Upgrade of the ATLAS Experiment*, tech. rep. LHCC-I-023, CERN-LHCC-2012-022, 2012.

[202] ATLAS Collaboration, *Expected tracking and related performance with the updated ATLAS Inner Tracker layout at the High-Luminosity LHC*, tech. rep., CERN, 2021, URL: http://cds.cern.ch/record/2776651.

[203] G.-F. Dalla Betta et al., *Development of a new generation of 3D pixel sensors for HL-LHC*, Nucl. Instrum. Meth. A **824** (2016) 386, ed. by M. G. Bisogni, M. Grassi, M. Incagli, R. Paoletti, and G. Signorelli, arXiv: 1612.00624 [physics.ins-det].

[204] L. Franconi, *The Opto-electrical conversion system for the data transmission chain of the ATLAS ITk Pixel detector upgrade for the HL-LHC*, J. Phys. Conf. Ser. **2374** (2022) 012105.

[205] A. I. Collaboration, *Optoboard System Documentation*, Internal Documentation, URL: https://optoboard-system.docs.cern.ch/.

[206] C. Chen et al., *A gigabit transceiver for the ATLAS inner tracker pixel detector readout upgrade*, Journal of Instrumentation **14** (2019) C07005, URL: https://dx.doi.org/10.1088/1748-0221/14/07/C07005.

[207] P. Moreira, *The lpGBT: a radiation tolerant ASIC for Data, Timing, Trigger and Control Applications in HL-LHC*, TWEPP 2019, 2019, URL: https://indico.cern.ch/event/799025/contributions/3486153/.

[208] J. Troska et al., *The VTRx+, an optical link module for data transmission at HL-LHC*, PoS **TWEPP-17** (2017) 048, URL: https://cds.cern.ch/record/2312396.

[209] G. Ripamonti et al., *2.5V step-down DCDCs: a radiation-hard solution for power conversion*, PoS **370** (2020) 071.

[210] ATLAS Collaboration, *Radiation simulation public results.Phase II ITk Inclined Duals (April 2018).*, URL: https://twiki.cern.ch/twiki/bin/view/AtlasPublic/RadiationSimulationPublicResults#Phase_II_ITk_Inclined_Duals_Apri.

[211] A. Ferrari, P. R. Sala, A. Fasso, and J. Ranft, *FLUKA: A multi-particle transport code (Program version 2005)*, (2005).

[212] S. Agostinelli et al., *GEANT4–a simulation toolkit*, Nucl. Instrum. Meth. A **506** (2003) 250.

[213] S. Braccini, *The new bern PET cyclotron, its research beam line, and the development of an innovative beam monitor detector*, AIP Conference Proceedings **1525** (2013), ISSN: 0094-243X.

[214] J. Anders et al., *A facility for radiation hardness studies based on a medical cyclotron*, JINST **17** (2022) P04021, arXiv: 2201.04176 [physics.ins-det].

[215] M. Auger et al., *A detector based on silica fibers for ion beam monitoring in a wide current range*, Journal of Instrumentation **11** (2016).

[216] C. Belver-Aguilar et al., *Development of Novel Non-Destructive 2D and 3D Beam Monitoring Detectors at the Bern Medical Cyclotron*, *Proc. IBIC'20* (Santos, Brazil), International Beam Instrumentation Conference 9, JACoW Publishing, Geneva, Switzerland, 2020 78, ISBN: 978-3-95450-222-6, URL: https://www.jacow.org/ibic2020/papers/tupp32.pdf.

[217] F. Ravotti, *Dosimetry Techniques and Radiation Test Facilities for Total Ionizing Dose Testing*, IEEE Transactions on Nuclear Science **65** (2018) 1440.

[218] A. Holmes-Siedle and L. Adams, *Handbook of Radiation Effects; 2nd ed.* OUP Oxford, 2002.

[219] J. F. Ziegler, M. Ziegler, and J. Biersack, *SRIM – The stopping and range of ions in matter (2010)*, Nuclear Instruments and Methods in Physics Research Section B: Beam Interactions with Materials and Atoms **268** (2010) 1818, 19th International Conference on Ion Beam Analysis, ISSN: 0168-583X.

[220] L. Halser, *Irradiation studies at the Bern cyclotron for the ATLAS ITk upgrade*, J. Phys. Conf. Ser. **2374** (2022) 012052.
[221] T. S. Bird, *Definition and Misuse of Return Loss [Report of the Transactions Editor-in-Chief]*, IEEE Antennas and Propagation Magazine **51** (2009) 166.
[222] Keysight Technologies, *S-Parameter Design*, (2020), URL: https://www.keysight.com/us/en/assets/7018-06743/application-notes/5952-1087.pdf.
[223] K. Moustakas et al., *A Clock and Data Recovery Circuit for the ALTAS/CMS HL-LHC Pixel Front End Chip in 65 nm CMOS Technology*, (2020).
[224] A. Ilg, *Novel Analysis Techniques and High-Speed Readout to Search for New Physics*, PhD Thesis, 2021, URL: https://cds.cern.ch/record/2779858.
[225] M. Daas et al., *BDAQ53, a versatile pixel detector readout and test system for the ATLAS and CMS HL-LHC upgrades*, Nuclear Instruments and Methods in Physics Research Section A: Accelerators, Spectrometers, Detectors and Associated Equipment **986** (2021) 164721.
[226] A. Lopez Solis et al., *A search for top-squark pair production, in minimal flavour violating supersymmetry, in final states containing a t-quark, c-quark and missing transverse momentum using the full Run 2 dataset collected by the ATLAS detector*, tech. rep., CERN, 2023, URL: https://cds.cern.ch/record/2863797.
[227] J. C. Pati and A. Salam, *Lepton Number as the Fourth Color*, Phys. Rev. D **10** (1974) 275, [Erratum: Phys.Rev.D 11, 703–703 (1975)].
[228] G. Steigman and M. S. Turner, *Cosmological Constraints on the Properties of Weakly Interacting Massive Particles*, Nucl. Phys. B **253** (1985) 375.
[229] CMS Collaboration, *Search for pair-produced multijet resonances using data scouting*, 2023, URL: https://cds.cern.ch/record/2866497.
[230] S. Juillerat, *Irradiation studies on the Optosystem of the ATLAS ITk Pixel data transmission chain*, Bachelor Thesis, Albert Einstein Center for Fundamental Physics, University of Bern, 2022.
[231] J. Montejo Berlingen and F. Meloni, *SUSY August 2023 Summary Plot Update*, tech. rep., CERN, 2023, URL: https://cds.cern.ch/record/2866203.
[232] J. L. Feng, I. Galon, F. Kling, and S. Trojanowski, *ForwArd Search ExpeRiment at the LHC*, Phys. Rev. D **97** (2018) 035001, arXiv: 1708.09389 [hep-ph].
[233] A. Ariga et al., *FASER's physics reach for long-lived particles*, Phys. Rev. D **99** (2019) 095011, arXiv: 1811.12522 [hep-ph].
[234] C. Ahdida et al., *SND@LHC*, (2020), arXiv: 2002.08722 [physics.ins-det].
[235] A. Boyarsky, O. Mikulenko, M. Ovchynnikov, and L. Shchutska, *Searches for new physics at SND@LHC*, JHEP **03** (2022) 006, arXiv: 2104.09688 [hep-ph].
[236] J. L. Feng et al., *The Forward Physics Facility at the High-Luminosity LHC*, J. Phys. G **50** (2023) 030501, arXiv: 2203.05090 [hep-ex].
[237] H. Abreu et al., *Search for Dark Photons with the FASER detector at the LHC*, (2023), arXiv: 2308.05587 [hep-ex].

Appendix A

Energy Loss in Twinax Cable

This study was conducted to ensure that the 16.7 MeV protons from the Bern cyclotron penetrate two layers of Twinax cable, which is made of various materials. An illustration of the cross-section of the Molex Twinax cable is shown in Figure A.1. The two differential lines are routed in parallel, while the grounding wire is above the horizontal line between the two signal lines. Table A.1 summarises the material properties of each part of the cable.

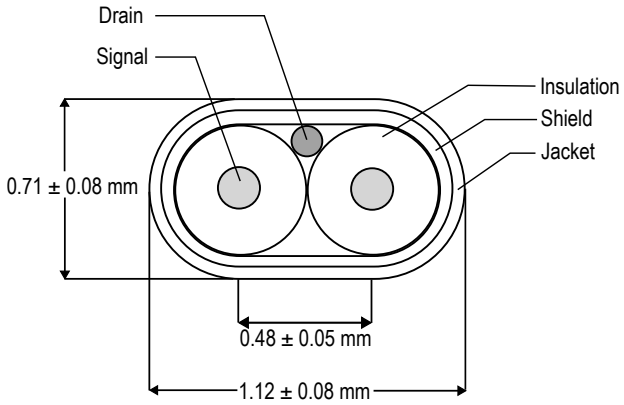

Figure A.1: Schematics of the Molex Twinax cable cross-section with dimension and components. Inspired from Molex data sheet.

Part	Material	Thickness [mm]	Density [g/cm^3]
Jacket	Polyester	0.018	1.06
Shield	Aluminium	0.023	2.7
Insulation	Polyolefin	0.5	0.9
Drain Wire	Bare Copper	0.13	8.96
Conductor (Signal)	Bare Copper	0.16	8.96

Table A.1: Materials and their properties of the Molex Twinax cable.

In order to simulate the energy loss of 16.7 MeV protons in the different layers of the Twinax cable, it was assumed that the protons hit the long and of the cable. Figure A.2 illustrates the path of incoming protons that was assumed for this study. This path crosses the conductor, which is the part of the cable where most of the proton's energy is deposited. All other paths through two (or three) layers of Twinax cable are subject to lower energy loss. Therefore, this path is considered the "worst case" and used as a reference for the study presented here. In each layer, the protons deposit a fraction of their energy, which has an effect on the energy dependent energy loss in the following

layer. Therefore, for each layer, the remaining energy was calculated and used to extract the energy loss in the next layer. Table A.2 summarises all steps of the simulation with energy going in, energy lost (per mm and in total), and remaining energy of the protons after each component of up to three Twinax cable layers. All values were obtained with SRIM [219]. The energy loss increases with decreasing proton energy, as expected. For more dense materials, such as copper, the energy loss is generally larger. From the listed results, one concludes, that 16.7 MeV protons can penetrate through two layers of Twinax cable but would be stopped in the conductor of the third layer. Therefore, the spool for irradiating 6 m long Twinax cables is designed such that two layers can be rolled up.

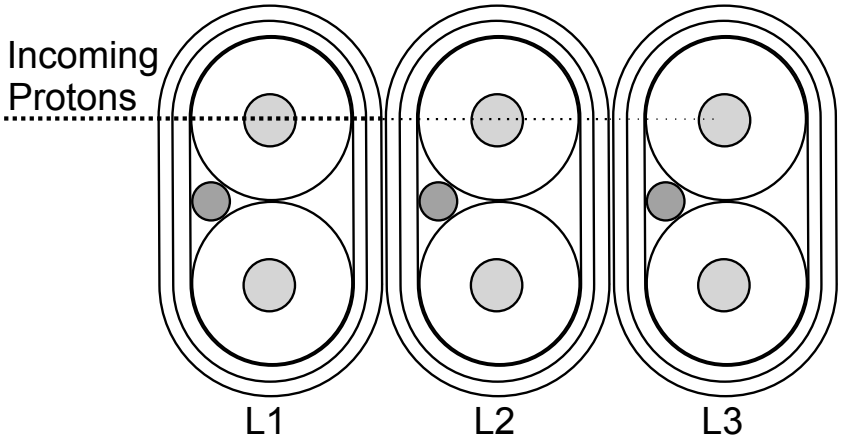

Figure A.2: Illustration of three layers of Twinax cable and the path incoming 16.7 MeV protons are taking. This path is used for the simulations summarised in Table A.2.

	E_{in} [MeV]	$\mathrm{d}E/\mathrm{d}x$ [MeV/mm]	Loss [MeV]	E_{out} [MeV]
L1: Jacket	16.70	3.20	0.06	16.5
L1: Shielding	16.5	6.18	0.14	15.8
L1: Insulator	16.5	2.98	0.74	15.8
L1: Conductor	15.8	17.29	2.77	13.0
L1: Insulator	13.0	3.62	0.91	12.1
L1: Shielding	12.1	7.91	0.18	11.9
L1: Jacket	11.9	4.21	0.08	11.8
L2: Jacket	11.8	4.24	0.08	11.7
L2: Shielding	11.7	8.12	0.19	11.5
L2: Insulator	11.5	4.00	1.00	10.5
L2: Conductor	10.5	23.40	3.74	6.8
L2: Insulator	6.8	6.14	1.5	5.3
L2: Shielding	5.3	14.85	0.34	5.0
L2: Jacket	5.0	8.47	0.15	4.8
L3: Jacket	4.8	8.75	0.16	4.6
L3: Shielding	4.6	16.50	0.38	4.2
L3: Insulator	4.2	0.90	0.23	4.0
L3: Conductor	4.0	46.02	7.36	-3.4
L3: Insulator	0	0	0	0
L3: Shielding	0	0	0	0
L3: Jacket	0	0	0	0

Table A.2: Results from the energy loss simulation in each layer of the Twinax cable. The table is divided into three parts, which corresponds to three layers of Twinax cable (L1, L2, L3) through which protons are passing. After each component of each layer, the remaining energy (E_{out}) is calculated and used as ingoing energy for the next component. The energy loss, $\mathrm{d}E/\mathrm{d}x$ [MeV/mm], and the deposited energy in MeV, are given for each part of each layer. One observes that protons only pass through two full layers of Twinax cable and have no remaining energy left after the conductor. All values are simulated with SRIM [219].

Declaration of Consent

Erklärung

gemäss Art. 18 PromR Phil.-nat. 2019

Name/Vorname: Lea Halser

Matrikelnummer: 19-123-645

Studiengang: Doktorat Physik

Bachelor ☐ Master ☐ Dissertation ☑

Titel der Arbeit: Exploring the Limits of the Standard Model with the ATLAS Experiment at the LHC

LeiterIn der Arbeit: Prof. Dr. Michele Weber

Ich erkläre hiermit, dass ich diese Arbeit selbständig verfasst und keine anderen als die angegebenen Quellen benutzt habe. Alle Stellen, die wörtlich oder sinngemäss aus Quellen entnommen wurden, habe ich als solche gekennzeichnet. Mir ist bekannt, dass andernfalls der Senat gemäss Artikel 36 Absatz 1 Buchstabe r des Gesetzes über die Universität vom 5. September 1996 und Artikel 69 des Universitätsstatuts vom 7. Juni 2011 zum Entzug des Doktortitels berechtigt ist. Für die Zwecke der Begutachtung und der Überprüfung der Einhaltung der Selbständigkeitserklärung bzw. der Reglemente betreffend Plagiate erteile ich der Universität Bern das Recht, die dazu erforderlichen Personendaten zu bearbeiten und Nutzungshandlungen vorzunehmen, insbesondere die Doktorarbeit zu vervielfältigen und dauerhaft in einer Datenbank zu speichern sowie diese zur Überprüfung von Arbeiten Dritter zu verwenden oder hierzu zur Verfügung zu stellen.

Ort/Datum

Bern, 31. August 2023

Unterschrift